

**NEWCASTLE UNIVERSITY**

**DISPERSION AND DEPOSITION OF  
HEAVY PARTICLES IN  
TURBULENT FLOWS**

by

**Chunyu Jin**

A thesis submitted in partial fulfillment for the  
degree of Doctor of Philosophy

in the

**School of Mechanical and Systems Engineering**

(viva on 5th March, 2012)

# Declaration of Authorship

I, CHUNYU JIN, declare that this thesis titled, ‘DEPOSITION OF HEAVY PARTICLES IN TURBULENT FLOWS’ and the work presented in it are my own. I confirm that:

- This work was done wholly or mainly while in candidature for a research degree at this University.
- Where any part of this thesis has previously been submitted for a degree or any other qualification at this University or any other institution, this has been clearly stated.
- Where I have consulted the published work of others, this is always clearly attributed.
- Where I have quoted from the work of others, the source is always given. With the exception of such quotations, this thesis is entirely my own work.
- I have acknowledged all main sources of help.
- Where the thesis is based on work done by myself jointly with others, I have made clear exactly what was done by others and what I have contributed myself.

Signed:

---

Date:

---

*“Nothing is static, nothing is final, everything is held provisionally.”*

Jocelyn Bell Burnell,  
a British astrophysicist who missed out a Nobel Prize.

# Abstract

For nearly 40 years, engineers, researchers and scientists from the nuclear industry across the World have been trying to understand the behaviors of deposition, bounce and re-suspension of heavy, radioactive particles suspended as a dilute secondary phase in the cooling circuits of primary reactor systems. The aim is to understand the mechanism of transport and deposition of such particles through large, complex geometry systems, so that the risk of dispersal of radioactive particles may be assessed, and confirmed to be acceptably small both in closed containers and in the atmosphere in the case of an accident scenario.

The first part of the present work addresses the challenge of robustly and efficiently predicting the behaviors of rigid and spherical particles (referred to as heavy particles) within turbulent boundary layers, the underlying physics of which is the controlling factor on particle deposition in smooth pipes and ducts. In the second component of work we study the deposition and bounce of heavy particles suspended in turbulent flows across heat exchanger tube banks, using Large Eddy Simulation (LES). It was originally proposed to extend the boundary layer work to this application, but it was quickly identified that the deposition mechanisms here are governed by the high core flow turbulence, rather than boundary layer phenomena, so that LES provides the only realistic modelling approach. In both cases the dispersed heavy particles are expressed in a Lagrangian framework solved in an independently developed large-scale parallel code; whilst the fluid phase is described in an Eulerian framework, either based on correlations from published Direct Numerical Simulation (DNS) for the boundary layer models, or from Computational Fluid Dynamics (CFD) simulations for both the boundary layer and tube-bank models, making use of the unstructured-grid based Navier-Stokes solver ANSYS FLUENT.

Underpinning this work we implement a complete stochastic Lagrangian particle tracking module, based on a robust and efficient particle localization algorithm which can determine and update the cell containing each particle as the particles move through an unstructured finite volume grid overlying the flow domain. The module can handle correctly the interactions of particles with complex boundaries, and uses a novel numerical scheme for interpolating the carrier-phase velocity field seen by the particles from cell-centred values obtained from CFD computation. It implements a Gear three-level implicit scheme to compute the particle velocity, which is more robust, accurate and efficient than the conventional explicit and implicit schemes. The module has been fully

parallelized using MPI (Message Passing Interface) settings on a Linux cluster consisting of 20 single CPU node, and further been successfully integrated with both the steady and unsteady ANSYS FLUENT solvers, complete replacing the built-in Lagrangian particle tracking model provided by ANSYS FLUENT. The algorithm and numerical schemes have been validated against analytical solutions of particle transport in a two-dimensional straining shear flow and other cases.

For turbulent boundary layer flows, a simpler but more promising stochastic quadrant model, inspired by the discrete random walk model of Kallio and Reeks and the quadrant analysis of Wu and Willmarth, is developed in order to account for the effects of near wall large-scale coherent structures, e.g. sweeps and ejections, on particle transport. The input parameters for the stochastic quadrant model are deduced from the corresponding statistics obtained from a Large Eddy Simulation (LES) of a fully developed channel flow. The model is applied to the prediction of deposition of heavy particles in a turbulent boundary layer; both using a Kallio and Reeks correlation based model of the flow, and also a Reynolds-Averaged Navier-Stokes (RANS) flow solution of using ANSYS FLUENT, the latter flow model having the potential to be extended to complex duct geometries. These solutions are compared to those of by solving an alternative Langevin equation of Dehbi, or continuous random walk model, which satisfies the fully mixed condition and describes the fluid velocity fluctuations seen by heavy particles.

Prior to the current work no systematic investigation of the potential errors in particle deposition in turbulent boundary layers due to the modified hydrodynamic forces experienced by particles when very close to the wall has been carried out, possibly because of the complexity of the correlations involved. The effect is explored with the present stochastic quadrant model, using recently published composite correlations of Zeng and Balachandar for the particle drag coefficient  $C_D$  and lift coefficient  $C_L$  for near wall particles. This work provides an important first confirmation that for practical cases hydrodynamic effects can reasonably be neglected for particle deposition in turbulent boundary layers.

The boundary layer methods developed in the first part of this thesis are applicable to the prediction of heavy particle deposition in fairly complex duct geometries, but are shown to be inappropriate for flow over tube-banks, where the boundary layers are no longer the rate limiting feature. Consequently the parallel Lagrangian stochastic particle tracking model is extended to study the particle impaction efficiency on tube banks in a turbulent flow in the framework of Large Eddy Simulation (LES). The flow field, obtained from Large Eddy Simulation with the dynamic Smagorinsky sub-grid scale model within

ANSYS FLUENT, is fully validated against existing experimental data. As far as the dispersed particle phase is concerned, the energy losses when particles impact on and generally, but not always, rebound from cylinders within the tube-bank is taken into account using an empirical critical-impact velocity model. The efficiency of particle impaction is measured for particles of three Stokes number, and the results are compared with existing experimental data.

# Acknowledgements

There are many people to whom I own deepest gratitude for their support and understanding during my years in Newcastle. With the help from many confident but humble engineers, physicists and mathematicians, I am deeply grateful for sharpening my understanding of fluid dynamics as well as for learning the elegant and joyful way of living.

I especially want to thank Dr Ian Potts and Professor Mike W. Reeks who introduced me to the world of numerical simulation and mathematical modelling of dispersion and deposition of inertial particles in turbulent flows when I came abroad with the desire of doing fluid experiments. I am indebted to them for the full support, great guidance and understanding along the way I built up my sense of conducting research and became devoted to the field of turbulent dispersed particulate flows. I very much appreciate the opportunities provided by them to attend many conferences and meetings, which allows me to discuss my work with other researchers and to enlarge my horizon. They may not aware that I have learnt enormous knowledge from them over the past few years.

I am also grateful to my two examiners, Dr David C. Swailes, and Dr Abdel Dehbi for their insightful discussions of the many problems I encountered in my research. I thank them for taking time to review, comment and improve my thesis.

The code provided by Dr Ed Wynn helped to get me started into the complex world of user defined functions (UDF) with ANSYS FLUENT, his methodology was ultimately abandoned though.

Moreover, I would like to thank my friends in Newcastle who helped to make the demanding research seem joyful. Special thanks to Sui Wang and his family, Fred Zhang for sharing my joy and sadness, offering instant help whenever needed. Andy Bragg, Mahyar Mahinzaeim and Suhaimi Haji Abdul Wahab shared the office T4 with me during the past few years. I have also benefited a great deal from the kindness of Prof. Yuri Sergeev, Yasmine Ammar, Elena Meneguz, Peter van Dijk, Rutger IJzermans, Zhongxu Hu and William Waugh. I am grateful to have them as my lifelong friends.

Last, but never the least, I would never had made it this far without the consistent love and unconditional support of my parents, parents in-law and my three sisters. They provided me long-distance support and understanding and are truly a source of inspiration. I save greatest appreciation to my wonderful wife Bin Yang, for all the love, support and

encouragement, especially during the period of my prolonged and stressful thesis writing in Paris.

None of this research would have been possible without generous funding from British Energy (Part of EDF).

# Contents

<b>Declaration of Authorship</b>	<b>i</b>
<b>Abstract</b>	<b>iii</b>
<b>Acknowledgements</b>	<b>vi</b>
<b>List of Figures</b>	<b>xii</b>
<b>List of Tables</b>	<b>xvii</b>
<b>1 Introduction</b>	<b>1</b>
1.1 Background and motivation . . . . .	1
1.2 Thesis outline . . . . .	4
REFERENCES . . . . .	7
<b>2 Eulerian-Lagrangian methods for dispersed particulate flows</b>	<b>9</b>
2.1 Introduction . . . . .	9
2.2 Governing equations and boundary conditions . . . . .	12
2.2.1 Continuous phase . . . . .	12
2.2.2 Dispersed particle phase . . . . .	13
2.3 Finite Volume Method (FVM) for Navier-Stokes equations . . . . .	15
2.3.1 Formulation of the Finite Volume Method (FVM) . . . . .	16
2.3.1.1 The general transport equation . . . . .	16
2.4 Forces acting on rigid spherical particles . . . . .	17
2.4.1 Viscous drag force . . . . .	17
2.4.2 Shear-induced lift force . . . . .	20
2.5 Particle response time and Stokes number . . . . .	21
2.6 Turbulent particle dispersion in CFD modelling frameworks . . . . .	23
2.6.1 Discrete Random Walk (DRW) models . . . . .	24
2.6.1.1 Eddy lifetime $\tau_e$ and length scale $l_e$ . . . . .	27
2.6.1.2 The pros and cons of DRW models . . . . .	31
2.6.2 Continuous Random Walk (CRW) models . . . . .	33

2.6.2.1	One-dimensional models . . . . .	33
2.6.2.2	Connection with the Fokker-Planck equation . . . . .	34
2.6.2.3	Determination of the coefficients . . . . .	37
2.6.2.4	Drift correction with the well-mixed condition . . . . .	38
REFERENCES	. . . . .	40

<b>3</b>	<b>Implementation of the Eulerian-Lagrangian method for heavy particles deposition in ANSYS FLUENT</b>	<b>47</b>
3.1	Introduction . . . . .	47
3.2	Background on heavy particles deposition . . . . .	48
3.3	Preliminary results from the Discrete -Phase Model (DPM) . . . . .	51
3.3.1	Particle deposition using the standard $k - \varepsilon$ model . . . . .	53
3.3.2	Particle deposition using the standard $k - \varepsilon$ turbulence model accounting for the inhomogeneous and anisotropic feature of fully developed turbulent boundary layers . . . . .	54
3.3.3	Serious deficiencies concerning the standard Fluent Discrete Particle Model for studying particle deposition in Boundary Layers	59
3.4	Self-implementation of the Lagrangian particle tracking approach in the colocated unstructured grid based Navier-Stokes solver in ANSYS FLUENT . . . . .	62
3.4.1	A particle localization algorithm for unstructured grids . . . . .	62
3.4.1.1	Identifying the initial host cell . . . . .	64
3.4.1.2	Updating the host cell . . . . .	65
3.4.2	Velocity interpolation based on the reconstruction of velocity gradient . . . . .	68
3.4.3	An implicit ODE solver for the particle equation of motion . . . . .	72
3.5	Validations . . . . .	74
3.5.1	Case 1: Irrotational straining flow . . . . .	74
3.5.1.1	The transport of a particle in a two-dimensional symmetric shear flow . . . . .	74
3.5.1.2	UDF patch of the two-dimensional symmetric shear flow in ANSYS FLUENT . . . . .	78
3.5.1.3	Comparison of Lagrangian particle tracking . . . . .	78
3.5.2	Case 2: Sinusoidal flow . . . . .	80
3.5.2.1	The transport of a particle in a sinusoidally modulated flow . . . . .	80
3.5.3	Application of the self-implemented Lagrangian particle tracking scheme UDF to the prediction of particle deposition in turbulent boundary layers . . . . .	82
3.6	Parallelization of the stochastic Lagrangian particle tracking model using MPI . . . . .	84
3.6.1	An abstract data type for particles . . . . .	86
3.6.2	The procedure for parallelization . . . . .	87
3.6.3	Test of speed-up performance and particle data transfer . . . . .	88
3.7	Conclusion . . . . .	90



---

6.2.3	Flow configuration of in-line tube banks . . . . .	170
6.3	Results and discussion . . . . .	172
6.3.1	Instantaneous flow field . . . . .	173
6.3.2	Surface pressure characteristics . . . . .	174
6.3.3	Drag and lift coefficients . . . . .	177
6.3.4	Shear-layer instability and vortex shedding . . . . .	181
6.3.5	Correlation length for vortex shedding . . . . .	182
6.4	Concluding remarks . . . . .	183
	REFERENCES . . . . .	186
<b>7</b>	<b>An LES study of particle deposition within an in-line array tube-banks</b>	<b>206</b>
7.1	Introduction . . . . .	206
7.2	Overview of numerical simulations . . . . .	210
7.2.1	Mathematical formulation of LES . . . . .	210
7.2.2	Flow configuration of in-line tube banks . . . . .	210
7.2.3	Calculation of particle trajectories . . . . .	212
7.2.4	A particle-wall collision model . . . . .	214
7.3	Results and discussion . . . . .	217
7.3.1	Results on the carrier phase . . . . .	217
7.3.2	Results for the particle phase . . . . .	221
	7.3.2.1 Sample particle trajectories and bounce upon impact . . . . .	221
	7.3.2.2 Deposition efficiency on tube-banks . . . . .	222
	7.3.2.3 Deposition fraction across the tube-banks . . . . .	224
7.4	Concluding remarks . . . . .	230
	REFERENCES . . . . .	232
<b>8</b>	<b>Conclusions and future work</b>	<b>235</b>
8.1	Conclusions . . . . .	235
8.1.1	Conclusions on the stochastic quadrant model . . . . .	236
8.1.2	Conclusions on the wall effects on particle deposition . . . . .	237
8.1.3	Conclusions on the LES study of inertial deposition of heavy particles onto tube-banks . . . . .	238
8.2	Future work . . . . .	240
	REFERENCES . . . . .	243

# List of Figures

2.1	Drag Coefficient $C_D$ as a function of the particle Reynolds number $Re_p$ for a rigid spherical particle . . . . .	19
2.2	A particle in a uniform simple shear flow. . . . .	21
2.3	Schematic show of heavy particles trajectories in a free-shear vortex flow for various non-dimensional particle response time (Stokes number) $St$ . The solid line denotes the continuous fluid streak lines, whilst the dashed lines denote heavy particle trajectories. . . . .	23
2.4	particle interaction with a succession of eddies in a turbulent flow field. . . . .	24
2.5	Five realizations of Brownian motion (Wiener process) $W(t)$ . . . . .	35
3.1	Summary of experimental measurements on particle deposition from fully developed turbulent pipe flow. . . . .	50
3.2	Results on particle deposition from fully developed turbulent pipe flow using the DPM with the standard $k - \epsilon$ model and compared against experiments. . . . .	53
3.3	Curve fit of non-dimensional r.m.s of velocity fluctuations within turbulent boundary layers. Dehbi (2008) . . . . .	56
3.4	Results for particle deposition from the implementation of the DRW model of Kallio and Reeks (1989), implemented as a UDF coupled with the standard k-epsilon model in ANSYS Fluent, compared against those from the default standard $k - \epsilon$ model and experiments. . . . .	57
3.5	Results for particle deposition from a stand-alone C code implementation of the grid-free model of Kallio and Reeks (1989), compared with those from the default Fluent $k - \epsilon$ model, a Fluent UDF implementation of the model of Kallio and Reeks (1989), and experiment. . . . .	58
3.6	Debugging the default wall boundary condition on particle deposition, It is not possible to alter the capture condition directly via a Fluent DPM UDF, so an artificial strategy of applying a large wall-directed force to any particle coming within one particle radius of a wall surface was implemented. The effectiveness of this somewhat inelegant solution is shown by the trajectory of similar particle marked "Modified". . . . .	60
3.7	Debugging the fluid velocity interpolation scheme . . . . .	61
3.8	Flow chart for studying particle deposition using self-developed Lagrangian particle tracking module . . . . .	63
3.9	Identifying the cell which contains the particle initial position . . . . .	65
3.10	Updating the host cell through face-neighbouring cells search. (simple case) . . . . .	66

3.11	Updating the host cell through face-neighbouring cells search. (complex case) . . . . .	67
3.12	Computational stencil for the determination of second order derivatives of fluid variables. . . . .	70
3.13	Contour of stream function of the 2-d symmetric shear flow with $\alpha = 2$ . . . . .	75
3.14	Computational mesh used for the 2-d symmetric shear flow with $\alpha = 2$ in ANSYS FLUENT. . . . .	79
3.15	Patched contour of velocity magnitude and vector plot for the 2-d symmetric shear flow with $\alpha = 2$ in ANSYS FLUENT. . . . .	79
3.16	Inertial particle trajectory obtained using RK4 and Gear2 scheme and compared against the analytical solution for particle trajectory in a irrotational flow. . . . .	80
3.17	Computed errors of fluid particle trajectory obtained in a prescribed velocity field using different interpolation scheme and compared against the analytical solution. . . . .	82
3.18	Comparison of particle deposition prediction from various implementations of the discrete random walk model, based on the basic model of Kallio and Reeks (1989) . . . . .	84
3.19	One-dimensional computational domain decomposition . . . . .	86
3.20	Test of speed-up performance to each node with $10^6$ particles. . . . .	89
3.21	Trajectory of specimen particles computed by the stochastic parallel Lagrangian particle tracking module coupled with a Large Eddy Simulation of a channel flow . . . . .	89
4.1	Scatter plot of $u'$ and $v'$ at $y^+ = 50$ resolved by LES, categorised in terms of quadrant analysis. . . . .	104
4.2	Profiles of $v'$ and $\langle v'_i \rangle$ as a function of $y^+$ at $Re_\tau = 180$ in each of the four quadrants. . . . .	105
4.3	Profiles of momentum fluxes as a function of $y^+$ at $Re_\tau = 180$ in each of the four quadrants. . . . .	106
4.4	Probability density function (pdf) for $\langle v'_i \rangle$ obtained by LES and a comparison with a half normal distribution (HND) . . . . .	107
4.5	Diagram describing the Markov chain modelling motions in the four quadrants. . . . .	108
4.6	Relative probability of four quadrants as a function of $y^+$ . . . . .	109
4.7	Non-dimensional wall normal fluid velocity and Lagrangian time integral time scale as a function of $y'$ within turbulent boundary layers. . . . .	110
4.8	Mean fluid velocity profiles from the inlet and middle plane. Both based on $u_\tau$ and compared with the $U^+$ data of Kim et al. (1987). . . . .	113
4.9	Comparison of dimensionless particle deposition velocity as a function of dimensionless particle response time with experimental measurements and different models in turbulent boundary layers. The results from the stochastic quadrant are model compared against the benchmark experimental measurements from Liu and Agarwal (1974), against the theoretical curve fit by McCoy and Hanratty (1977). In addition, the numerical results from Guingo and Minier (2008) are presented. . . . .	114

4.10	Comparison of dimensionless particle deposition velocity as a function of dimensionless particle response time with experimental measurements and different models in turbulent boundary layers. The results from a CRW model are compared to the benchmark experimental measurements from Liu and Agarwal (1974), and the theoretical curve fit by McCoy and Hanratty (1977). In addition, the CRW results are compared with numerical results from various models (e.g. Guingo and Minier (2008); Dehbi (2008b); Hanratty and Mito (2006)). . . . .	115
4.11	Particle preferential concentration profile as a function of $y^+$ . . . . .	117
4.12	Mean wallward drift velocity and sampled wall-normal fluid velocity, (a) $St = 2$ , (b) $St = 5$ . . . . .	119
4.13	Mean wallward drift velocity and sampled wall-normal fluid velocity, (a) $St = 2$ , (b) $St = 5$ . . . . .	120
4.14	Root mean square (r.m.s) of velocity fluctuations, (a) $St = 2$ , (b) $St = 5$ . . . . .	121
4.15	Root mean square (r.m.s) of velocity fluctuations, (a) $St = 10$ , (b) $St = 20$ . . . . .	122
4.16	Particle residence time in the region of $y^+ < 3$ versus particle deposition velocity (a) $St = 2$ , (b) $St = 5$ . . . . .	124
4.17	Probability density function (pdf) of non-dimensional impact velocities of particles, $St = 5$ . . . . .	125
4.18	Probability density function (pdf) of non-dimensional impact velocities of particles, (a) $St = 10$ , (b) $St = 20$ . . . . .	126
5.1	Drag Coefficient $C_D$ as a function of the particle Reynolds number $Re_p$ for a rigid spherical particle . . . . .	136
5.2	Comparison of corrections for $C_D$ , (a) $Re_p < 1$ , (b) $Re_p > 1$ . . . . .	141
5.3	Comparison of corrections for $C_L$ , (a) $C_{Ls}$ for a particle in a shear flow adjacent to a wall, and compared to the Saffman lift coefficient, (b) $C_{Lt}$ for a particle translating through still fluid next to a wall. . . . .	145
5.4	Deposition comparison with the standard drag law $C_D$ and near-wall corrections from Zeng et al. (2009) . . . . .	148
5.5	Comparison of mean streamwise particle velocities with the standard drag law $C_D$ and near-wall corrections from Zeng et al. (2009) and compared to the fluid velocities (a) $St = 2$ , (b) $St = 5$ . . . . .	150
5.6	Comparison of mean streamwise particle velocities with the standard drag law $C_D$ and near-wall corrections from Zeng et al. (2009) and compared to the fluid velocities (a) $St = 10$ , (b) $St = 20$ . . . . .	151
5.7	Comparison of wall-normal particle r.m.s velocities with the standard drag law $C_D$ and near-wall corrections from Zeng et al. (2009) and compared to the fluid r.m.s. velocities (a) $St = 2$ , (b) $St = 5$ . . . . .	152
5.8	Comparison of wall-normal particle r.m.s velocities with the standard drag law $C_D$ and near-wall corrections from Zeng et al. (2009) and compared to the fluid r.m.s. velocities (a) $St = 10$ , (b) $St = 20$ . . . . .	153
5.9	Deposition comparison with the standard drag law $C_D$ and Saffman lift coefficient $C_L$ and $C_{Ls}$ with near-wall corrections from Zeng et al. (2009) . . . . .	154

5.10	Comparison of mean streamwise particle velocities with the standard drag law $C_D$ , with $C_L$ and inclusion of near-wall corrections on $C_L$ from Zeng et al. (2009) and compared to the fluid velocities (a) $St = 2$ , (b) $St = 5$ . . . . .	155
5.11	Comparison of mean streamwise particle velocities with the standard drag law $C_D$ , with $C_L$ and inclusion of near-wall corrections on $C_L$ from Zeng et al. (2009) and compared to the fluid velocities (a) $St = 10$ , (b) $St = 20$ . . . . .	156
5.12	Comparison of wall-normal r.m.s velocities with the standard drag law $C_D$ , with $C_L$ and inclusion of near-wall corrections on $C_L$ from Zeng et al. (2009) and compared to the fluid velocities (a) $St = 2$ , (b) $St = 5$ . . . . .	157
5.13	Comparison of wall-normal r.m.s velocities with the standard drag law $C_D$ , with $C_L$ and inclusion of near-wall corrections on $C_L$ from Zeng et al. (2009) and compared to the fluid velocities (a) $St = 10$ , (b) $St = 20$ . . . . .	158
6.1	Configuration of the four-column in-line tube banks . . . . .	191
6.2	Configuration of the four-row in-line tube bank, The $x$ - axis indicates the freestream flow direction; $y$ - and $z$ -axis respectively indicate the transverse and spanwise direction. . . . .	192
6.3	Computational domain and mesh in the $x - y$ plane . . . . .	193
6.4	The filtered flow structure development across the four-in-line tube banks, iso-surface of the second invariant of velocity gradient tensor, colored by the resolved turbulent kinetic energy (TKE) . . . . .	194
6.5	Vortex motion around cylinders at the middle plane cut . . . . .	195
6.6	Averaged mean $C_p$ as a function of angle from the front stagnation point, (a) <b>C1</b> , (b) <b>C2</b> , (c) <b>C3</b> , (d) <b>C4</b> . . . . .	196
6.7	surface fluctuating pressure distribution as a function of angle from the front stagnation point over 30 non-dimensional time units,(a) <b>C1</b> , (b) <b>C2</b> , (c) <b>C3</b> , (d) <b>C4</b> . . . . .	197
6.8	Time history of $\overline{C_D}$ , (a) <b>C1,C2</b> (b) <b>C3,C4</b> . . . . .	198
6.9	Time history of $C'_L$ , (a) <b>C1,C2</b> (b) <b>C3,C4</b> . . . . .	199
6.10	Instantaneous velocity vector map in the middle plane of flow domain (a) <b>C1</b> , (b) <b>C2</b> , (c) <b>C3</b> , (d) <b>C4</b> . . . . .	200
6.11	Time histories of velocity signal fluctuations behind cylinder <b>C1</b> and the corresponding power spectrum density. . . . .	201
6.12	Time histories of velocity signal fluctuations behind cylinder <b>C2</b> and the corresponding power spectrum density. . . . .	202
6.13	Time histories of velocity signal fluctuations behind cylinder <b>C3</b> and the corresponding power spectrum density. . . . .	203
6.14	Time histories of velocity signal fluctuations behind cylinder <b>C4</b> and the corresponding power spectrum density. . . . .	204
6.15	Auto-correlation of streamwise and crosswise velocity fluctutations as a function of spanwise length (a) <b>C1</b> , (b) <b>C2</b> , (c) <b>C3</b> , (c) <b>C4</b> , . . . . .	205

7.1	Contour of the $y^+$ value of each cell associated with its correspondingly nearest wall-adjacent cell face in a turbulent flow across in-line tube-banks. UDM-2 stands for $y^+$ . . . . .	209
7.2	Configuration of four by five pairs of in-line tube banks. . . . .	211
7.3	A side view of computational mesh used for the LES with a close look-up around a cylinder. . . . .	212
7.4	Critical sticking velocity on a steel cylinder as a function of alumina particle radius. . . . .	216
7.5	Coefficient of restitution $e$ as a function of alumina particle incident normal velocity upon a steel cylinder. . . . .	216
7.6	Instantaneous velocity magnitude based on the normalised $Q$ -criterion = $8 \times 10^{-2}$ . . . . .	217
7.7	Mean pressure distribution on the middle cylinder surface. Definition of $\bar{C}_p$ based on Shim et al. (1988). (a) the first pair tube banks, (b) the second pair tube banks. . . . .	218
7.8	Mean pressure distribution on the middle cylinder surface. Definition of $\bar{C}_p$ based on Shim et al. (1988). (a) the third pair tube banks, (b) the fourth pair tube banks. . . . .	219
7.9	Comparison of mean pressure distribution on the middle cylinder surface from the second, third and fourth pair of tube-banks . . . . .	220
7.10	Sample particle trajectories and bounce upon impact on cylinders for particles $St = 0.35$ . . . . .	222
7.11	Fraction of total deposition particles across tube-banks for particles $St = 0.35$ (a) each pair of tube-banks, (b) each tube-banks. . . . .	226
7.12	Fraction of total deposition particles across tube-banks for particles $St = 0.086$ (a) each pair of tube-banks, (b) each tube-banks. . . . .	227
7.13	Fraction of total deposition particles across tube-banks for particles $St = 0.0075$ (a) each pair of tube-banks, (b) each tube-banks. . . . .	228
7.14	Deposition particles on tube-banks (a) $St = 0.0075$ , (b) $St = 0.35$ . . . . .	229

# List of Tables

6.1	Comparison of results for r.m.s pressure distribution $C'_p$ . . . . .	177
6.2	Comparison of results for $\bar{C}_D$ and $C'_L$ . . . . .	179
6.3	Comparison of $St$ with the universal Strouhal number . . . . .	183
7.1	Comparison of deposition efficiency of particles of $St = 0.35$ onto the individual cylinders from the first column tube-banks with the deposition efficiency on a single cylinder . . . . .	223
7.2	Comparison of deposition efficiency of particles of $St = 0.35, 0.086$ and $0.0075$ onto each pair of the tube-banks . . . . .	224

***Dedicated to***  
***my grandfather***

***Chen Liyun***

# Chapter 1

## Introduction

### 1.1 Background and motivation

Particle-laden turbulent flows are involved in a wide variety of fields. Atmospheric sciences and environmental pollution, sediment transport in rivers, spray drying and fouling of heating exchangers are just a few areas where the behavior of small particles suspended in a fluid is of vital importance (see [Crowe et al. \(1998\)](#); [Crowe \(2006\)](#); [Friedlander \(2000\)](#)). In the past forty years, with concerns about the consequences of accidents in nuclear reactors, a great deal of research effort has been devoted towards the modelling and calculation of the deposition/plate-out, resuspension, dispersal and of radioactive particles both in the reactor coolant system and containment and their possible release to the atmosphere.

Though the design of the civil advanced gas-cooled reactors (CAGRs), which is unique to the UK, is capable of preventing large-scale failure and fission-attached radioactive dust release even in accident scenarios, significant quantities of radioactive dust may be deposited in the primary system and available for release due to resuspension. Some may result from a dropped fuel during on-loading refuelling operations. The radioactive dust generated by dropped fuel will be transported and suspended in the coolant gas circuit, and plate-out onto surfaces in the primary system. The high-pressure coolant gas renders enough momentum for releasing radioactive dust from the primary system to the outside

environment in the event of a breach of the reactor coolant system and a loss-of-coolant accident (LOCA) (see [Hewitt and Collier \(2000\)](#); [Allelein et al. \(2008\)](#)).

In order to assess the magnitude of the release it is crucial to know the mechanism by which the radioactive dust deposit/plate-out, and resuspended during transient flows from the containment surfaces. This normally involves a series of complex deposition processes including turbulent diffusion, turbophoresis, thermophoresis, inertial impaction, interception, gravitational settling, Brownian motion and the effects of surface roughness, etc. However, in effective assessments of deposition of radioactive dust, it is frequently assumed that the deposition rate is limited by the transport of dust particles through the turbulent boundary layer adjacent to depositing surface. This assumption significantly simplifies all the related computations of radioactive particles suspended in the complex containers. Based on this idea, the industrial code CIRCD, developed by [Reeks \(1991\)](#) in British Energy (part of EDF), has been successfully applied to the analysis of the transport, deposition or plate-out on the container surfaces and resuspension from transient flows of radioactive dust in the gas-coolant circuit.

Focusing on transport of particles in turbulent boundary layers, [Kallio and Reeks \(1989\)](#) first demonstrated that a discrete random walk (DRW) boundary model is capable of predicting the inertial deposition of a wide spectrum of particles from turbulent flows when compared to the benchmark experimental measurements of particle deposition in a turbulent pipe flow by [Liu and Agarwal \(1974\)](#). The central idea of [Kallio and Reeks \(1989\)](#) is to account for the turbulence effect on the particle motions through simulating random particle-eddy-interaction within turbulent boundary layers. This idea has attracted a great deal of attention and been employed by [Greenfield \(1998\)](#) for studying particle deposition. More recently, [Dehbi \(2008a\)](#) implemented this approach into the CFD code ANSYS FLUENT as a proper stochastic boundary layer particle-eddy interaction model for the prediction of particle deposition in turbulent pipe flows.

Near wall coherent-structures (CS) have received much attention in recent years due to their critical role in turbulence generation and maintenance, which offers important mechanisms on the transfer and segregation of inertial particles within turbulent boundary layers (see [Marchioli and Soldati \(2002\)](#)). The term coherent-structures (CS) refers to

a wide variety of spatially coherent events that are usually identified in turbulent flows using flow visualization or analysis of velocity signals measured experimentally and numerically. They play an important role on the turbulent transport process and has also been investigated as a potential engineering model used in the nuclear CFD code Saturne for the prediction of inertial particle deposition in turbulent flows by [Guingo and Minier \(2008\)](#). However, the above model utilized artificial parameters needing fine tuning and is also too complex to be used in the practical safety assessment calculations.

One way to simplify the loosely defined near wall coherent-structures is make use of the approach of quadrant analysis proposed by [Willmarth and Lu \(1972\)](#). Later, [Wei and Willmarth \(1991\)](#) used the quadrant analysis to study the wall-normal velocity fluctuations within a turbulent boundary layer measured by LDA, and proposed to use the mechanism of turbulent momentum transport normal to the wall for understanding suspended sediment transport. The momentum transport mechanism is directly associated with sweeps and ejections which produce large  $-\rho\overline{u'v'}$  turbulent shear stresses. Sweeps involve wall-ward directed high velocity fluid and cause particles to be transported toward the wall; whilst ejections involve the ejection of low velocity fluid away from the wall region and therefore cause particles to be migrated away from the wall. This was established by DNS calculations of particle-laden channel flows from [Marchioli and Soldati \(2002\)](#).

Another way to simulate the inhomogeneous and anisotropic feature of turbulent boundary layers is based on the Langevin equation, which simulates the turbulent fluid velocity fluctuations along the particles trajectories. This methodology was employed by [Dehbi \(2008b\)](#) to study inertial deposition of particles in turbulent flows through the implementation of user-defined-functions (UDF) in ANSYS FLUENT.

From the practical engineering modelling point of view, this thesis presents a simple but more promising stochastic quadrant model of near wall coherent-structures for studying inertial deposition of particles in a CFD modelling framework. The model, inspired by the discrete random walk (DRW) model of [Kallio and Reeks \(1989\)](#) and the quadrant analysis of [Willmarth and Lu \(1972\)](#), is developed to account for the effects of large scale

near wall coherent structures, e.g. sweeps and ejections, on particle transport within turbulent boundary layers.

## 1.2 Thesis outline

The principal objective of this thesis is to investigate dispersion and deposition of heavy particles suspended in turbulent flows as a dilute second dispersed phase in a CFD modelling framework.

Chapter 2 describes the Eulerian-Lagrangian approach for turbulent dispersed particulate flows. The governing equations for the fluid and particle phase are described in the Eulerian and Lagrangian framework respectively. The Finite-Volume-Method (FVM) used in the present CFD modelling framework is also briefly reviewed. The two important forces acting on rigid spherical particles, the drag force and lift force, are presented. On the basis of the RANS modelling framework it then describes the detailed theory concerning discrete random walk (DRW) eddy-interaction and continuous random walk (CRW) model.

Chapter 3 presents an implementation of the Eulerian-Lagrangian method for investigating heavy particle deposition in the CFD modelling framework ANSYS FLUENT. It first discusses the background on heavy particle deposition from turbulent flows. Underpinning the idea both employed in CIRCD and proposed by [Kallio and Reeks \(1989\)](#), the eddy-interaction model was applied to study particle deposition through UDFs in the CFD modelling framework ANSYS FLUENT. Through this, multiple shortcomings inherent in the discrete phase model (DPM) provided by ANSYS FLUENT were revealed. However, these deficiencies are beyond the range of UDFs. Therefore, a complete stochastic Lagrangian particle tracking module was implemented in ANSYS FLUENT. This is based on a robust and efficient particle localization algorithm proposed by [Haselbacher et al. \(2007\)](#), which can determine and update the cell containing each particle as the particles move through an unstructured finite volume grid overlying the flow domain. It then presents a novel numerical scheme for interpolating the carrier-phase velocity field seen by the particles on structured grids. The module uses a Gear

three-level implicit scheme to compute the particle velocity, which is more robust, accurate and efficient than the conventional explicit and implicit schemes. It was further been successfully integrated with both the steady and unsteady ANSYS FLUENT solvers, complete replacing the built-in Lagrangian particle tracking model provided by ANSYS FLUENT. The algorithm and numerical schemes have been validated against analytical solutions of particle transport in a two-dimensional straining shear flow and other cases. Finally the parallelization of this module using MPI (Message Passing Interface) is described and its corresponding performance presented.

Chapter 4 deals with inertial deposition of heavy particles in a real turbulent boundary layer, which is based on a simpler but more promising stochastic quadrant model of near wall coherent-structures. The stochastic quadrant model is formulated mathematically and its related statistics are presented. The performance of the model in predicting deposition rates is evaluated through comparing against experimental measurements and those from the continuous random walk. Various statistics related to the particle phase are presented as well.

Chapter 5 presents an investigation of the wall effects on the hydrodynamic forces acting on a particle in the very near wall region and the corresponding effects on particle deposition. This is achieved through employing composite correlations for the drag coefficient  $C_D$  and lift coefficient  $C_L$  in the particle equation of motion. These correlations are based on very recent research from [Zeng et al. \(2009\)](#). These new correlations are examined by comparing the results with those from the standard correlations.

Chapter 6 is concerned with a large eddy simulation (LES) study of a turbulent flow over a tube bank. The dynamic Smagorinsky subgrid scale model based LES takes advantage of the Werner and Wengle wall layer model in order to mitigate the forbidding computational cost for such a complex flow. The LES methodology in simulating turbulent flows across tube-banks is assessed carefully by comparisons with available experimental measurements.

To understand further the deposition process of particles onto complex geometries, Chapter 7 presents an LES study of the inertial deposition of heavy particles within tube-banks in a turbulent flow. An empirical particle-wall collision model that considers

the energy loss upon impaction is implemented to address particle rebound from the cylinder surfaces. The results both on the fluid phase and particle phase are presented and discussed.

Chapter 8 summarizes these investigations and discusses the general features of future work.

## REFERENCES

- H. J. Allelein, A. Auvinen, J. Ball, S. Güntay, L. E. Herranz, A. Hidaka, A. Jones, M. Kissane, D. Powers, and G. Weber. State of the art report on nuclear aerosols. *CSNI Report, Draft, April*, pages 309–346, 2008.
- C. T. Crowe. *Multiphase flow handbook*. CRC Press, 2006.
- C. T. Crowe, M. Sommerfeld, and Y. Tsuji. *Multiphase flows with particles and droplets*. CRC Press, New York, 1998.
- A. Dehbi. A CFD model for particle dispersion in turbulent boundary layer flows. *Nuclear Engineering and Design*, 238(3):707–715, 2008a.
- A. Dehbi. Turbulent particle dispersion in arbitrary wall-bounded geometries: A coupled CFD-Langevin-equation based approach. *International Journal of Multiphase Flow*, 34(9):819–828, 2008b.
- S. K. Friedlander. *Smoke, Dust, and Haze: Fundamentals of Aerosol Dynamics*, 59 New York: Oxford University Press. 2000.
- C. Greenfield. *Numerical modelling of transport phenomena in reactors*. PhD thesis, Bristol Univesity, 1998.
- M. Guingo and J. P. Minier. A stochastic model of coherent structures for particle deposition in turbulent flows. *Physics of Fluids*, 20(5), 2008.
- A. Haselbacher, F. M. Najjar, and J. P. Ferry. An efficient and robust particle-localization algorithm for unstructured grids. *Journal of Computational Physics*, 225(2):2198–2213, 2007.

- G. F. Hewitt and J. G. Collier. *Introduction to nuclear power*. Hemisphere Pub, 2000.
- G. A. Kallio and M. W. Reeks. A numerical simulation of particle deposition in turbulent boundary layers. *International Journal of Multiphase Flow*, 15(3):433–446, 1989.
- B. Y. H. Liu and J. K. Agarwal. Experimental observation of aerosol deposition in turbulent flow. *Journal of Aerosol Science*, 5(2):145–148, IN1–IN2, 149–155, 1974.
- C. Marchioli and A. Soldati. Mechanisms for particle transfer and segregation in a turbulent boundary layer. *Journal of Fluid Mechanics*, 468:283–315, 2002.
- M. W. Reeks. CIRCD a computer code for calculating the deposition half-lives of gas borne particles in gas-cooled reactor circuits. *TD/STB/REP/0268, RPTG/P(91)18*, 1991.
- T. Wei and W. W. Willmarth. Examination of v-velocity fluctuations in a turbulent channel flow in the context of sediment transport. *Journal of Fluid Mechanics*, 223: 241–252, 1991.
- W. W. Willmarth and S. S. Lu. Structure of the reynolds stress near the wall. *Journal of Fluid Mechanics*, 55(01):65–92, 1972.
- L. Zeng, F. Najjar, S. Balachandar, and P. Fischer. Forces on a finite-sized particle located close to a wall in a linear shear flow. *Physics of Fluids*, 21:033302, 2009.

# Chapter 2

## Eulerian-Lagrangian methods for dispersed particulate flows

### 2.1 Introduction

To predict turbulent dispersed particulate flows, two general approaches are possible. One treats the carrier phase as a continuum and the dispersed particulate phase as individual particles. This approach, which predicts the particle trajectories in a fluid phase by solving their equations of motion, is usually known as the Eulerian-Lagrangian approach. For example, this approach was used by many researchers (e.g. [Maxey \(1987\)](#); [Kallio and Reeks \(1989\)](#); [McLaughlin \(1989\)](#); [Elghobashi \(1991\)](#); [Squires and Eaton \(1990, 1991\)](#); [Wang and Squires \(1996b\)](#); [Uijtewaal and Oliemans \(1996\)](#); [Marchioli and Soldati \(2002\)](#); [Narayanan et al. \(2003\)](#); [Dehbi \(2008a,b, 2009, 2010, 2011\)](#); [Dehbi and Martin \(2011\)](#); [Guingo and Minier \(2008\)](#); [Chibbaro and Minier \(2008\)](#); [Guha \(2008\)](#)). The another approach treats the particulate phase like the carrier flow as a fluid continuum, and solves the appropriate mass, momentum and energy equations for both the carrier and dispersed phases simultaneously. It is normally referred to as the Eulerian-Eulerian or two-fluid approach. The Eulerian-Eulerian approach is also seen in the following work for studying the near wall behavior of inertial particles in turbulent flows.(e.g. [Clever and Yates \(1975\)](#); [Reeks \(1991, 1992\)](#); [Swales and Reeks \(1994\)](#); [Devenish et al. \(1999\)](#);

[Young and Leeming \(1997\)](#); [Guha \(1997, 2008\)](#); [Sergeev et al. \(2002\)](#); [Zaichik et al. \(2008\)](#) )

In this thesis, the Eulerian-Lagrangian approach has been chosen for modelling the deposition and dispersion of inertial particles in turbulent flows. This approach has the advantage that, albeit an approximation, allows the simulation of millions of particles suspended in a turbulent flow. The key feature of the Eulerian-Lagrangian approach is that the exchanges of mass, momentum and energy between the continuous carrier phase and the dispersed particulate phase are modelled, rather than directly resolved. Otherwise, it would result in a significantly computational cost. This therefore requires some assumptions for the development of mathematical models.

Here, the point-particle approximation (e.g. [Prosperetti and Tryggvason \(2007\)](#); [Balachandar and Eaton \(2010\)](#)) is used to model the transport of the dispersed particle phase. Under this approximation, individual particles are represented in terms of their position and velocity and have no spatial dimensions under most circumstances except that they tend to interact with another surface, i.e. the solid wall boundary. Nevertheless, this approximation requires the dispersed particulate phase to satisfy certain requirements, one of which is that the size of the particle is less than smallest length scale in the underlying turbulent flow field. On the other hand, the point-particle approximation has established a wide range of applications and proved to be a useful tool for modelling a great deal of complex systems, especially those consisted of a huge amount of particles.

Moreover, in this thesis, it is assumed that the dispersed particulate phase has very low volume fraction so that it does not affect the behavior of the continuous carrier phase. This is referred to as one-way coupling. Furthermore, there is no mass and energy transfer from the carrier phase to the dispersed particle phase. Particle-particle collisions are insignificant. These assumptions hence allow us to focus on the behaviors of dilute dispersed particles in turbulent flow fields.

Thanks to the development of numerical techniques in Computational Fluid Dynamics (CFD) (e.g. [Versteeg and Malalasekera \(2007\)](#), Finite-Volume-Method (FVM) for the Navier-Stokes equations on unstructured grids (e.g. [Barth and Jespersen \(1989\)](#); [Mathur and Murthy \(1997\)](#)) has been very successful in addressing the single carrier-phase

turbulent flow and has been implemented into commercial CFD codes such as ANSYS FLUENT. Apart from using state-of-the-art numerical techniques for solving the Navier-Stokes equations robustly and efficiently for the continuous carrier-phase, ANSYS FLUENT allows users to incorporate User-Defined-Functions via the mechanism of loading a dynamically linked shared-object library. This functionality allows users to custom ANSYS FLUENT and can significantly enhance its modelling capabilities. Therefore, to avoid reinventing the tool, the Finite-Volume Method(FVM) based Navier-Stokes solver ANSYS FLUENT is justifiably used to solve the governing equations of the continuous fluid phase and to achieve acceptable flow fields instead of using a research academic code. In this regard, commercial CFD codes have been used by the researchers for studying turbulent dispersed two-phase flows (e.g. [Greenfield \(1998\)](#); [Tian and Ahmadi \(2007\)](#); [Horn and Schmid \(2008\)](#); [Dehbi \(2008a,b, 2009\)](#); [Mehel et al. \(2010\)](#)). More importantly, this thesis focuses mainly on the investigation of the deposition of inertial particles onto the adjacent wall surface exposed to a turbulent flow in the Computational Fluid Dynamics (CFD) modelling framework. In this regard the preference here has been to develop independently stochastic Lagrangian particle tracking models which can be coupled to the Navier-Stokes solver, rather than using the default general-purpose oriented Lagrangian particle tracking model provided by ANSYS FLUENT.

This chapter is structured as follows: section [2.2](#) defines the governing equations and boundary conditions for the continuous and dispersed particle phase; the Finite Volume Method (FVM) employed by ANSYS FLUENT is briefly reviewed in section [2.3](#); two significant forces, e.g. the drag and shear-induced lift force, acting on a rigid spherical particle are discussed in section [2.4](#); section [2.5](#) gives the definitions of particle response time and Stokes number that determines the dispersion characteristics of heavy particles in turbulent flows. Finally, the theory on discrete random walk (DRW) and continuous random walk (CRW) models used in CFD modelling frameworks to study turbulent dispersed particle flow is presented in section [2.6](#).

## 2.2 Governing equations and boundary conditions

### 2.2.1 Continuous phase

In view of the prominent role played by the incompressible single-phase Navier-Stokes equations in the study of particle-laden turbulent flows, it is useful to review them here. The derivation of Navier-Stokes is based on the conservation laws for mass, momentum.

Let  $\rho(\mathbf{x}, t)$  and  $\mathbf{u}(\mathbf{x}, t)$  denote the fluid density and velocity fields of the continuous phase at position  $\mathbf{x}$  and time  $t$ , the continuity equation is given as

$$\frac{\partial \rho}{\partial t} + \nabla \cdot (\rho \mathbf{u}) = 0. \quad (2.1)$$

In this thesis we consider incompressible flows of constant property (i.e., flows in which  $\rho$  is independent both of  $\mathbf{x}$  and of  $t$ ). In this case the evolution equation Eq. (2.1) reduces to

$$\nabla \cdot \mathbf{u} = 0. \quad (2.2)$$

Eq. (2.2) embodies the idea that each elemental volume of fluid particle conserves its volume as it moves in the flow.

In a similar form, the momentum equation is given as:

$$\frac{\partial}{\partial t}(\rho \mathbf{u}) + \nabla \cdot (\rho \mathbf{u} \mathbf{u}) = \nabla \cdot \boldsymbol{\sigma} + \rho \mathbf{f}, \quad (2.3)$$

where  $\mathbf{f}$  denotes an external force per unit volume acting on the fluid. The stress tensor  $\boldsymbol{\sigma}$  can be decomposed into a pressure  $p$  and viscous part  $\boldsymbol{\tau}$ :

$$\boldsymbol{\sigma} = -p\mathbf{I} + \boldsymbol{\tau}, \quad (2.4)$$

where  $\mathbf{I}$  denotes the identity tensor  $\delta_{ij}$ . This work deals with Newtonian fluids, for which the viscous part of the stress tensor  $\boldsymbol{\sigma}$  is given by

$$\boldsymbol{\tau} = 2\mu \mathbf{e}, \quad \mathbf{e} = \frac{1}{2}(\nabla \mathbf{u} + \nabla \mathbf{u}^T), \quad (2.5)$$

where  $\mu$  denotes the coefficient of dynamics viscosity,  $\mathbf{e}$  is the rate of strain tensor, and the superscript  $T$  represents the transpose; in component form, it can be written as:

$$e_{ij} = \frac{1}{2} \left( \frac{\partial u_i}{\partial x_j} + \frac{\partial u_j}{\partial x_i} \right), \quad (2.6)$$

where  $\mathbf{x} = (x_1, x_2, x_3)$ . With Eq. (2.3), the momentum equation (2.5) may be written for a Newtonian incompressible fluid as:

$$\frac{\partial \mathbf{u}}{\partial t} + \nabla \cdot (\mathbf{u}\mathbf{u}) = -\frac{1}{\rho} \nabla p + \nu \nabla^2 \mathbf{u} + \mathbf{f}. \quad (2.7)$$

where  $\nu = \mu/\rho$  is the kinematic viscosity.

When it comes to the boundary conditions for the Navier-Stokes equations (2.2) and (2.7), the only case needed to be considered in this thesis is the most common type of boundary for the continuous phase —the rigid impermeable static wall. This type of boundary condition amounts to

$$\left. \begin{aligned} \mathbf{u} \cdot \hat{\mathbf{n}} &= 0, & \text{impermeable condition} \\ \mathbf{u} \times \hat{\mathbf{n}} &= 0, & \text{no slip condition} \end{aligned} \right\} \quad (2.8)$$

where  $\hat{\mathbf{n}}$  is the unit normal to the wall surface.

### 2.2.2 Dispersed particle phase

To determine the trajectories of individual particles with radius  $a_p$  and density  $\rho_p$ , which move in an arbitrary flow field  $\mathbf{u}(\mathbf{x}, t)$  of a fluid with dynamic viscosity  $\mu$  and density  $\rho$ . The acceleration of the particle is described by the equation of motion, which is written in a Lagrangian frame of reference in terms of the Newton's second law of motion in the

form of proposed by [Maxey and Riley \(1983\)](#):

$$\begin{aligned} \frac{d\mathbf{x}_p}{dt} &= \mathbf{u}_p & (2.9) \\ m_p \frac{d\mathbf{u}_p}{dt} &= (m_p - m_f)\mathbf{g} + m_f \left( \frac{D\mathbf{u}}{Dt} \right)_{\mathbf{x}=\mathbf{x}_p(t)} - \frac{m_f}{2} \frac{d}{dt} \left( \mathbf{u}_p - \left( \mathbf{u} + \frac{a_p^2}{10} \nabla^2 \mathbf{u} \right)_{\mathbf{x}=\mathbf{x}_p(t)} \right) \\ &\quad - 6\pi a_p^2 \mu \int_0^t \frac{d/d\tau \left( \mathbf{u}_p - \left( \mathbf{u} + \frac{a_p^2}{6} \nabla^2 \mathbf{u} \right)_{\mathbf{x}=\mathbf{x}_p(\tau)} \right)}{\sqrt{\pi(t-\tau)\rho/\mu}} d\tau \\ &\quad - 6\pi a_p \mu \left( \mathbf{u}_p - \left( \mathbf{u} + \frac{a_p^2}{6} \nabla^2 \mathbf{u} \right)_{\mathbf{x}=\mathbf{x}_p(t)} \right), & (2.10) \end{aligned}$$

where  $\mathbf{x}_p$  denotes the position vector of the particle,  $\mathbf{u}_p$  is the velocity of the particle,  $\mathbf{g}$  is the acceleration vector of gravity,  $m_p = 4\pi\rho_p a_p^3/3$  is the mass of the particle,  $m_f = 4\pi\rho a_p^3/3$  represents the mass of the fluid displaced by the particle volume. Moreover, the two terms  $\left( \mathbf{u} + \frac{a_p^2}{10} \nabla^2 \mathbf{u} \right)_{\mathbf{x}=\mathbf{x}_p(t)}$  and  $\left( \mathbf{u} + \frac{a_p^2}{6} \nabla^2 \mathbf{u} \right)_{\mathbf{x}=\mathbf{x}_p(t)}$  represent the average velocity of the fluid over the particle volume and the average velocity of the fluid over the particle surface, respectively. Eq. (2.10) was deduced for situations in which the particle Reynolds number  $Re_p = 2|\mathbf{u}_p - \mathbf{u}|a_p/\nu = O(1)$ , i.e. the surrounding flow field around the particle is assumed to be a Stokes flow.

The terms of on the right hand side of Eq. (2.10) represent buoyancy, a force due to the acceleration of the undisturbed fluid, the virtual mass force due to the inertia of adjacent fluid displaced by the particle motion, the Basset history force resulting from unsteady relative acceleration, and the quasi steady viscous drag force due to the relative velocity difference between the particle and the surrounding fluid, respectively.

Divided by the particle mass  $m_p$  for the Eq. (2.10), the following equations are obtained in terms of the force balance per unit mass:

$$\frac{d\mathbf{x}_p}{dt} = \mathbf{u}_p \quad (2.11)$$

$$\begin{aligned} \frac{d\mathbf{u}_p}{dt} = & \left(1 - \frac{\rho}{\rho_p}\right)\mathbf{g} + \frac{\rho}{\rho_p} \left(\frac{D\mathbf{u}}{Dt}\right)_{\mathbf{x}=\mathbf{x}_p(t)} - \frac{1}{2} \frac{\rho}{\rho_p} \frac{d}{dt} \left(\mathbf{u}_p - \left(\mathbf{u} + \frac{a_p^2}{10} \nabla^2 \mathbf{u}\right)_{\mathbf{x}=\mathbf{x}_p(t)}\right) \\ & - \frac{a_p}{\tau_p} \int_0^t \frac{d/d\tau \left(\mathbf{u}_p - \left(\mathbf{u} + \frac{a_p^2}{6} \nabla^2 \mathbf{u}\right)_{\mathbf{x}=\mathbf{x}_p(\tau)}\right)}{\sqrt{\pi(t-\tau)\rho/\mu}} d\tau \\ & - \frac{1}{\tau_p} \left(\mathbf{u}_p - \left(\mathbf{u} + \frac{a_p^2}{6} \nabla^2 \mathbf{u}\right)_{\mathbf{x}=\mathbf{x}_p(t)}\right) \end{aligned} \quad (2.12)$$

where  $\tau_p$  denotes the particle response time given by:

$$\tau_p = \frac{2}{9} \frac{\rho_p}{\rho} \frac{a_p^2}{\nu} \quad (2.13)$$

which represents the time required by a particle for adjusting itself to the velocity change of surrounding fluid.

Moreover, perfectly absorbing (sticky) conditions on a solid surface for the particle are considered. This corresponds to the situation when the distance from the particle center to the adjacent wall surface is less than its radius and the particle sticks to the wall and the computation for the particle is complete. However, this simple boundary condition is not correctly implemented in ANSYS FLUENT. This point will be elaborated on later.

## 2.3 Finite Volume Method (FVM) for Navier-Stokes equations

The Finite Volume Method (FVM) is quite popular for solving the Navier-Stokes equations in Computational Fluid Dynamics (CFD) frameworks for a couple of reasons:

1. It ensures that the discretization of governing equations is conservative.

2. It can be easily adapted to unstructured meshes. Using the finite volume formulation, the integral forms of the conservative laws are satisfied to a great extent of approximation for all control volumes of the underlying computational grid.

The Navier-Stokes equations solver in ANSYS FLUENT is a three-dimensional finite volume unstructured-grid based collocated solver that is capable of solving incompressible, compressible, isothermal and non-isothermal flow problems.

## 2.3.1 Formulation of the Finite Volume Method (FVM)

### 2.3.1.1 The general transport equation

Eq: 2.7 may be rearranged to a general transport equation with an appropriate choice of a general flow property variable  $\phi$ ,  $\Gamma$  and  $S_\phi$ .  $\phi$  may be a scalar, vector or tensor field. Then Eq: 2.7 may be rewritten as:

$$\underbrace{\frac{\partial \rho \phi}{\partial t}}_{\text{unsteady term}} + \underbrace{\nabla \cdot (\rho \phi \mathbf{u})}_{\text{convective term}} = \underbrace{\nabla \cdot (\Gamma \nabla \phi)}_{\text{diffusive term}} + \underbrace{S_\phi}_{\text{source term}}, \quad (2.14)$$

where  $\Gamma$  denotes the diffusivity and  $S_\phi$  the source term. One can average Eq: 2.14 by integrating it over a three dimensional control volume,  $\Omega_i$ , of cell  $i$ ,

$$\int_{\Omega_i} \frac{\partial \rho \phi}{\partial t} dV + \int_{\Omega_i} \nabla \cdot (\rho \phi \mathbf{u}) dV = \int_{\Omega_i} \nabla \cdot (\Gamma \nabla \phi) dV + \int_{\Omega_i} S_\phi dV, \quad (2.15)$$

Applying the divergence theorem, Eq: 2.15 may be written as follows:

$$\int_{\Omega_i} \frac{\partial \rho \phi}{\partial t} dV + \int_{\partial \Omega_i} (\rho \phi \mathbf{u}) \cdot \mathbf{n} dS = \int_{\partial \Omega_i} (\Gamma \nabla \phi) \cdot \mathbf{n} dS + \int_{\Omega_i} S_\phi dV, \quad (2.16)$$

where the vector  $\mathbf{n}$  is normal to surface element  $dS$  of the entire bounding surface  $\partial \Omega_i$  of  $\Omega_i$ .

Eq: 2.16 is the basis of the formulation of finite volume method (FVM). Choosing appropriate properties for  $\phi$ ,  $\Gamma$  and  $S_\phi$ , the generic transport equation can be transformed into the continuity and momentum equations.

## 2.4 Forces acting on rigid spherical particles

In this work, only situations where particles are suspended in incompressible, isothermal flows are considered, the particle response time  $\tau_p$  hence is a constant, provided that the properties of the particle is given. Further, particles studied in this work are of much higher density than the surrounding fluid, e.g.  $\rho_p \gg \rho$ . The particle radius is small so that  $a_p^2 |\nabla^2 \mathbf{u}| \ll |\mathbf{u}|$ . The Basset history force is justifiably neglected in terms of the assumption that the accelerations of the flow field are sufficiently small. When a particle moves into the near wall region, it will experience the well-known Saffman lift force (Saffman (1965, 1968)) resulting from the mean velocity gradient seen by the particle. Moreover, the gravity is not considered throughout this study since it does not affect the particle deposition both onto vertical surfaces and onto the tube-banks in a turbulent flow. Based on these assumptions, which are applicable to this thesis, the Eq. (2.10) can be simplified considerably as:

$$\frac{d\mathbf{u}_p}{dt} = \frac{1}{\tau_p}(\mathbf{u} - \mathbf{u}_p) + \mathbf{f}_L \quad (2.17)$$

where  $\mathbf{u}$  is the instantaneous fluid velocity seen by the particle. The first term on the right hand side of Eq. (2.17) denotes the Stokes drag force resulting from the velocity difference between the particle and surrounding fluid; the second term  $\mathbf{f}_L$  denotes the lift force, i.e., the well-known Saffman lift force resulting from the shear of the underlying flow. This force shall be elaborated further in the following section.

### 2.4.1 Viscous drag force

The Stokes drag force accounted for by the first term in Eq. (2.17) is applicable only when  $Re_p \ll 1$ . Nevertheless, the situation encountered in this thesis is not necessarily found to be the case. For example, when a particle moves in the near wall region within turbulent boundary layers, the particle Reynolds number is being of the order of magnitude  $O(10)$  (see Kallio and Reeks (1989)). Hence, the Reynolds number effect on the drag force needs to be addressed appropriately. The extension of the Stokes drag force to higher

particle Reynolds numbers is normally based on the introduction of a drag coefficient  $C_D$  given by

$$C_D = \frac{\mathbf{F}_D}{\frac{1}{2}\rho(\mathbf{u} - \mathbf{u}_p)^2 A}, \quad (2.18)$$

where  $A = \pi/4d_p^2$  is the cross-section area of a spherical particle with density  $\rho_p$  and diameter  $d_p$ . The drag force then may be rearranged for per unit particle mass as:

$$\mathbf{F}_D = \frac{3}{4}C_D \frac{\rho}{\rho_p d_p} (\mathbf{u} - \mathbf{u}_p) |\mathbf{u} - \mathbf{u}_p|, \quad (2.19)$$

Then substituting Eq. (2.13) into Eq. (2.19), which in turn can be simplified as:

$$\mathbf{F}_D = \frac{1}{\tau_p} \frac{C_D Re_p}{24} (\mathbf{u} - \mathbf{u}_p). \quad (2.20)$$

Where  $C_D$  is a function of the particle Reynolds number  $Re_p$  as defined in section 2.2.2.

There has been a plethora of experimental investigations that have resulted in empirical correlations for  $C_D$  of rigid spherical particles at intermediate and high Reynolds number. Figure 2.1 shows the dependence of  $C_D$  of a rigid spherical particle upon  $Re_p$ . From this figure, it can be observed that there are several regimes which are associated with different flow characteristics around the rigid spherical particle.

First, when the particle Reynolds number  $Re_p$  is less than 0.1, viscous effect is dominating and analytic solution for  $C_D$  from the Stokes equations may be presented as:

$$C_D = \frac{24}{Re_p}. \quad (2.21)$$

This regime is also known as the Stokes flow as shown in Fig. 2.1. When  $Re_p$  is in the range of [0.1, 0.4], the drag force follows the Oseen expression (see Oseen (1910, 1913)) and decreases monotonically with  $Re_p$  but diverges from both the Stokes and Oseen expression.

As the  $Re_p$  increases, there is a transition regime (i.e.  $0.4 < Re_p < 1000$ ), where inertial effects become of increasing importance.

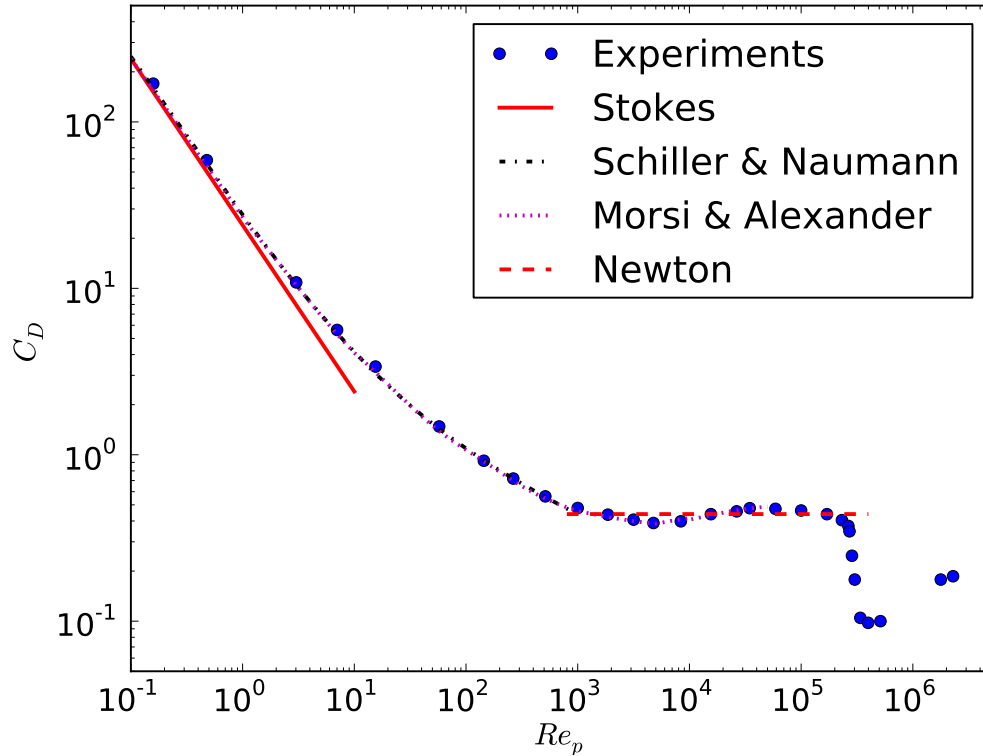


Figure 2.1: Drag Coefficient  $C_D$  as a function of the particle Reynolds number  $Re_p$  for a rigid spherical particle

When  $Re_p > 1000$ , the flow is fully turbulent and  $C_D$  remains almost constant up to the critical Reynolds number ( $Re_p \approx 3.0 \times 10^5$ ). This regime is also known as the Newton-regime with  $C_D$  attains a value between 0.42 and 0.44. At the critical particle Reynolds number  $Re_{crit}$ , there is a drastic decrease in  $C_D$  due to turbulent transition from a laminar to a turbulent boundary layer around the spherical particle. However, this regime is not relevant to the study in this thesis.

It is convenient in analytical and numerical investigations to use algebraic expressions for the  $C_D$ . For the non-linear regime various correlations have been proposed. [Schiller and Naumann \(1933\)](#); [Morsi and Alexander \(1972\)](#) are the two among most frequently used correlations. The correlation developed by [Schiller and Naumann \(1933\)](#) is relatively simple and takes the form following

$$C_D = \frac{24}{Re_p} (1 + 0.15 Re_p^{0.687}) = \frac{24}{Re_p} f(Re_p) \quad (2.22)$$

Morsi and Alexander (1972) proposed the following expression, which accounts for a wide range of  $Re_p$  with sufficiently high accuracy:

$$C_D = c_1 + \frac{c_2}{Re_p} + \frac{c_3}{Re_p^2}, \quad (2.23)$$

where  $c_1, c_2, c_3$  are constants and provided by Morsi and Alexander (1972). Eq. (2.23) exhibits the correct asymptotic behavior at low as well as high values of  $Re_p$ . It can be observed from Fig 2.1 that these two correlations fit  $C_D$  very well up to  $Re \approx 1000$  and display no discrepancies within these regime.

## 2.4.2 Shear-induced lift force

A particle moving in a shear flow experiences a transverse lift force due to the non-uniform fluid velocity over the particle and the resulting non-uniform pressure distribution on the particle. Saffman (1965, 1968) derived the following expression for the steady-state lift force (named Saffman lift force) on a not-rotating rigid spherical particle in a uniform simple shear flow as shown in Figure 2.2:

$$\mathbf{f}_L = 1.615\mu d_p \sqrt{Re_G}(\mathbf{u} - \mathbf{u}_p), \quad (2.24)$$

where  $Re_G$  is the shear Reynolds number (see McLaughlin (1991)) defined as

$$Re_G = \frac{d_p^2}{\nu} \frac{du}{dy}, \quad (2.25)$$

which depends on the mean fluid velocity gradient measured at the particle center. In the case when a particle is moving within the viscous sub-layer, the mean streamwise velocity gradient seen by it, is greater than zero in the wall-normal direction. If the particle lags the surrounding fluid, it experiences the Saffman lift force directed away from wall. Hence, it will reduce the chance of deposition of a particle. On the other hand, if the particle leads the surrounding fluid, the Saffman lift force exerted on the particle points toward the wall and will increase the chance of deposition of a particle.

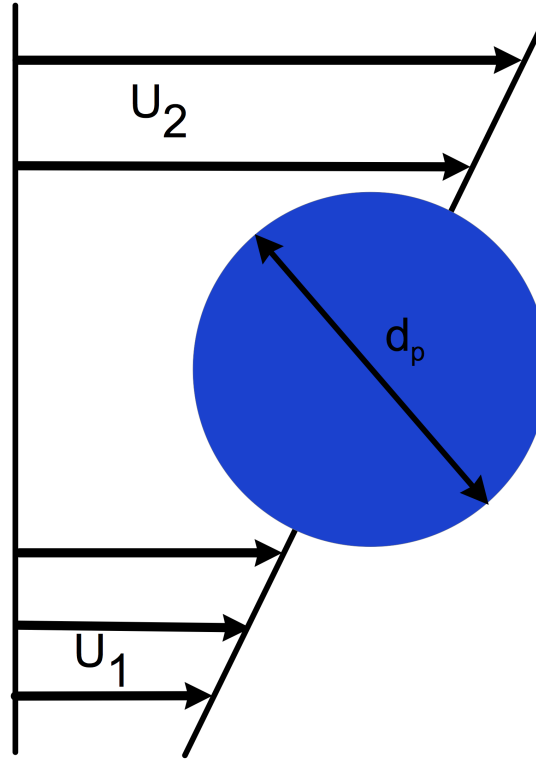


Figure 2.2: A particle in a uniform simple shear flow..

## 2.5 Particle response time and Stokes number

The response time of a particle is defined as

$$\tau_p = \frac{\rho_p d_p^2}{18\mu}, \quad (2.26)$$

where  $\rho_p$  is the density of the particle and  $d_p$  the diameter of the particle,  $\mu$  is the dynamics viscosity of the continuous phase. The response time of a particle represents a characteristic time scale for velocity changes of the particle. Similarly, a characteristic time scale for velocity changes in the continuous phase may be defined.

As far as a characteristic time scale  $\tau_f$  of the continuous phase is concerned, there are various definitions according to the most interesting scale in the underlying flow. A characteristic time scale for the macroscopic motion of the continuous phase, e.g. in a flow over tube banks may be defined as:

$$\tau_f = \frac{L_c}{U_c} \quad (2.27)$$

where  $L_c$  is a characteristic length scale of the flow, e.g. the cylinder diameter  $D$ , and  $U_c$  denotes a characteristic velocity, e.g. the mean inlet velocity  $U_0$ .

For a fully turbulent boundary layer, the characteristic time scale  $\tau_f$  is normally defined as

$$\tau_f = \frac{v}{u_\tau^2}, \quad (2.28)$$

where  $u_\tau$  is the wall friction velocity and given by

$$u_\tau = \sqrt{\frac{\tau_w}{\rho}}, \quad (2.29)$$

where  $\tau_w$  denotes the wall shear stress.

The Stokes number is defined in terms of the ratio of the particle response time  $\tau_p$  to the characteristic time scale in the underlying flow  $\tau_f$  defines, which is an important dimensionless parameter governing the dynamics of particles in a turbulent flow and given by,

$$St = \frac{\tau_p}{\tau_f}. \quad (2.30)$$

In this work, when the concern is particle deposition within turbulent boundary layers,  $St$  may be estimated as:

$$St = \frac{\rho_p d_p^2 u_\tau^2}{\rho 18\nu^2} \quad (2.31)$$

In the case of particle deposition on tube-banks in a turbulent flow field,  $St$  is defined as

$$St = \frac{\rho_p d_p^2 U_{inlet}}{18\mu D} \quad (2.32)$$

One may note that, if  $St \ll 1$ , the particle response time is much smaller than the characteristic time associated with the underlying flow. In this case, the particle will have enough time to respond to velocity changes in the continuous phase. Hence, the particle will completely follow the motions of the continuous phase and there is velocity equilibrium between the dispersed and continuous phase; On the other hand, if  $St \gg 1$ , then the particle essentially will have no time to adjust to the fluid velocity changes and the motion of the dispersed particles and of the continuous phase may be totally uncorrelated. This may be schematically shown in in Figure 2.3.

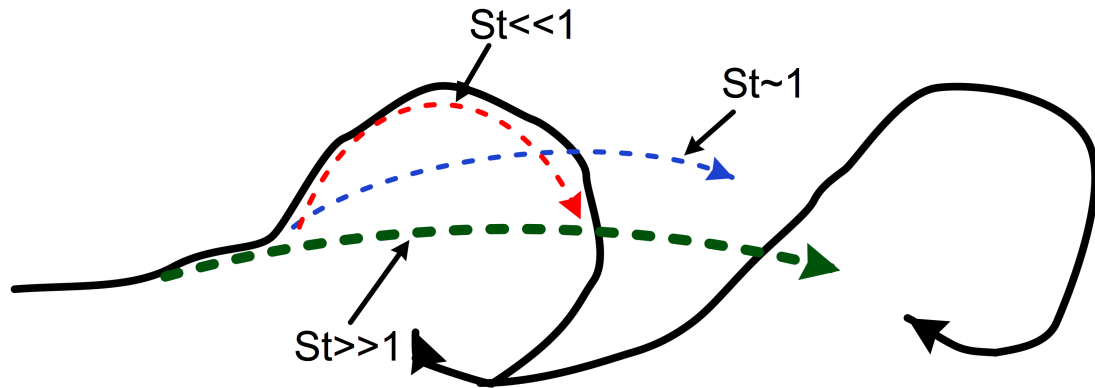


Figure 2.3: Schematic show of heavy particles trajectories in a free-shear vortex flow for various non-dimensional particle response time (Stokes number)  $St$ . The solid line denotes the continuous fluid streak lines, whilst the dashed lines denote heavy particle trajectories.

## 2.6 Turbulent particle dispersion in CFD modelling frameworks

While there has been a plethora of work which employs computationally expensive methods, e.g. either Large Eddy Simulation (LES) (e.g. Wang and Squires (1996b,a); Uijttewaal and Oliemans (1996); Kuerten and Vreman (2005); Kuerten (2006); Berrouk et al. (2008)) or Direct Numerical Simulation (DNS) (e.g. McLaughlin (1989); Uijttewaal and Oliemans (1996); Zhang and Ahmadi (2000); Portela and Oliemans (2003); Marchioli and Soldati (2002); Narayanan et al. (2003); Marchioli et al. (2003); Picciotto et al. (2005); Marchioli et al. (2008b,a)) to investigate the dispersion and deposition of inertial particle in turbulent flows, they focused primarily on the behavior of point-like particles in idealized flow geometries i.e. fully developed channel flows. As a matter of fact, the accuracy of the Lagrangian particle tracking, to a great extent, depends on the accurate characterization of turbulence in the underlying flow field. In many practical circumstances, it is usually calculated in a RANS (Reynolds-Averaged Navier-Stokes equation) modelling framework to establish an appropriate averaged flow field, instead of using LES, not to even mention DNS. Furthermore, using a RANS modelling framework does not resolve small length and temporal scales which influence the dispersed particle transport. Therefore, in order to account for turbulent particle transport, the turbulence

in the fluids has to be modelled appropriately. In this regard, two widely modelling approaches have been demonstrated to be quite successful. One is referred to as the discrete random walk model (DRW) or eddy interaction model (e.g. [Hutchinson et al. \(1971\)](#); [Gosman and Ioannides \(1983\)](#); [Kallio and Reeks \(1989\)](#); [Graham and James \(1996\)](#); [Graham \(1996, 1998, 2004\)](#); [Dehbi \(2008a\)](#)); another is known as the continuous random walk (CRW) based on the Langevin equation (e.g. [Bocksell and Loth \(2006\)](#); [Dehbi \(2008b, 2009, 2011\)](#); [Dehbi and Martin \(2011\)](#); [Guingo and Minier \(2008\)](#); [Chibbaro and Minier \(2008\)](#)).

### 2.6.1 Discrete Random Walk (DRW) models

The central idea behind DRW models is that the turbulence in the underlying flow may be described as a series of discretized random eddies, among which particles successively interact those encountered along their trajectories. A sketch of this is shown in Figure (2.4).

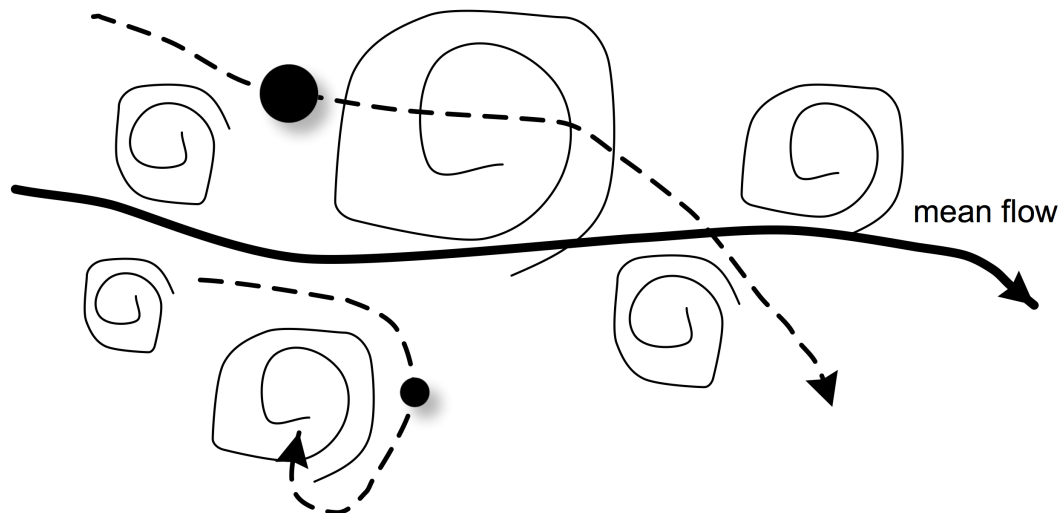


Figure 2.4: particle interaction with a succession of eddies in a turbulent flow field.

Each eddy is characterized by an eddy length  $l_e$  and eddy life time  $\tau_e$  as it moves at the mean fluid velocity. Furthermore, it is assumed that each eddy contributes a random fluctuating velocity to the fluid velocity in addition to the mean fluid velocity interpolated

at the particle position. This may be expressed as:

$$u_e = U + u'_e, \quad (2.33)$$

where  $u_e$  is the instantaneous eddy velocity seen by the particle,  $U$  is mean velocity of the flow and the fluctuating component  $u'_e$ , which is usually kept constant during an eddy life time  $\tau_e$ .

Moreover, in order to reproduce a flow with the same characteristics of the underlying flow, the eddy velocity fluctuation  $u'_e$  is computed from a Gaussian distribution  $N[0, u']$ . The fluid velocity fluctuation  $u'$  is a function of local turbulence conditions (e.g. the particle distance away from the wall).

When particles are dispersed by the underlying turbulent flow, they move according to the mean flow velocity and local fluctuations generated by individual eddies encountered along the trajectories.

Assuming the only force acting on a particle is the drag force and obeys the linear Stokes drag law, the particle motion may be expressed in the form

$$\frac{du_p}{dt} = \frac{1}{\tau_p}(u_e - u_p). \quad (2.34)$$

Within each eddy,  $u_e$  remains constant in space and time. Given the particle initial velocity  $u_p(0)$  at the very beginning of an interaction, one can obtain a general solution of  $u_p$  by analytically solving Eq. (2.34) as

$$u_p(t) = u_e - (u_e - u_p(0))e^{-\frac{t}{\tau_p}}, \quad (2.35)$$

Eq. (2.35) may be rewritten as

$$u_r = u_p(t) - u_e = -(u_e - u_p(0))e^{-\frac{t}{\tau_p}}, \quad (2.36)$$

where  $u_r$  is the relative velocity between the particle and eddy. Supposing the particle stop distance  $l_s$  equal to  $\tau_p u_p$  when a particle moves in a quiescent fluid (see [Young and](#)

Hanratty (1991)), we then can evaluate the eddy interaction time  $t_i$  that is the time spent by a particle within an eddy as follows:

- if  $|u_r|\tau_p < l_e$ , the particle is captured by the eddy and interacts with it until it decays. Under this circumstances,  $t_i = \tau_e$ .
- if  $|u_r|\tau_p > l_e$ , the particle crosses the eddy at an eddy crossing time  $t_c$  before the eddy decays. In this case,  $t_i = \min(t_c, \tau_e)$ .

The eddy crossing time  $t_c$  may be calculated by integrating Eq. (2.36) and by setting it equal to  $l_e$

$$t_c = -\tau_p \log \left( 1 - \frac{l_e}{|u_r(0)|\tau_p} \right), \quad (2.37)$$

in which  $u_r(0) = u_p(0) - u_e$ , represents the relative particle/eddy velocity at the start of a particle/eddy interaction. Eq: (2.37) is valid only if  $l_e/(|u_r(0)|\tau_p) < 1$ , and if this condition holds, it indicates the particle crosses the current eddy before it decays. Hence  $t_i$  is set equal to  $t_c$ . This phenomenon is usually referred to as the crossing trajectory effect (see Yudine (1959); Csanady (1963); Wells and Stock (1983)). If this inequality does not hold, it implies that the particle is captured by the current eddy. Therefore  $t_i$  is set equal to the current eddy lifetime  $\tau_e$ .

In the case of a small particle response time, the particle is normally be captured by the eddies. The particle/eddy interaction time thus can be set to equal the eddy lifetime and the particle follows the fluid. Then the particle velocities quickly approach the fluid velocities. In this case, the turbulent dispersion of rigid spherical particles will be similar to that of fluid particles. In the case of a large particle response time, the particle/eddy interaction time will be more often equal to the particle crossing time. In such circumstances, the interaction time may be independent of the eddy lifetime.

For practical implementation, the discrete random walk model requires:

1. The mean fluid velocity,  $U$ , and the r.m.s value  $u'$ ;
2. Values of the eddy time  $\tau_e$  and the eddy length  $l_e$ .

In RANS simulations, apart from the mean fluid velocity  $U$ , information on the turbulence is only available in statistical averaged terms. For example, turbulent kinetic energy and energy dissipation rate in simulations with the  $k - \varepsilon$  turbulence model, or Reynolds stresses and dissipation from a Reynolds stress model.

### 2.6.1.1 Eddy lifetime $\tau_e$ and length scale $l_e$

The selection of appropriate values of eddy lifetime  $\tau_e$  and length scale  $l_e$  is crucial for the success of discrete random walk model in the determination of the behaviors of turbulent dispersed particles. In the widely-used model of [Gosman and Ioannides \(1983\)](#), it is assumed that the eddy length and lifetime are set according to the following relations:

$$l_e = C_\mu^{3/4} \frac{k^{3/2}}{\varepsilon}, \quad \tau_e = \sqrt{\frac{3}{2}} C_\mu^{3/4} \frac{k}{\varepsilon}, \quad (2.38)$$

where  $k$  denotes the turbulent kinetic energy,  $\varepsilon$  represents the rate of dissipation and  $C_\mu$  is a constant used in the  $k - \varepsilon$  turbulence model. In this study, both the eddy lifetime  $\tau_e$  and the eddy length scale  $l_e$  are deterministic functions of the distance away from the wall boundary in the computational domain.

[Kallio and Reeks \(1989\)](#) used a random distribution of eddy lifetime  $\tau_e$  for predicting particle deposition in an inhomogeneous turbulent boundary layer. Moreover, [Wang and Stock \(1992\)](#) demonstrated that the correct choice of eddy lifetime distribution in the eddy interaction model ensures the following self-consistent dispersion properties of fluid particles in homogeneous, isotropic and stationary turbulence (see [Taylor \(1921\)](#)):

$$\langle u'^2 \rangle_{T_L} = \frac{1}{2} \frac{d \langle y^2(t) \rangle}{dt}, \quad (2.39)$$

where  $u'$  represents the r.m.s fluctuation velocity,  $T_L$  denotes the integral Lagrangian time scale,  $y(t)$  is the displacement of a fluid particle relative to its mean motion, and  $\langle \rangle$  indicates an ensemble average over all realizations of all the particle trajectories. The above expression 2.39 denotes the diffusivity of fluid particles.

The integral Lagrangian time scale is a measure that how long the particle velocity at the present time will influence its future velocity. It is determined according to the following expression

$$T_L = \int_0^t R_L(\tau) d\tau, \quad (2.40)$$

where  $R_L(\tau)$  is the Lagrangian correlation coefficient, which describes how the particle velocity are temporally related along the particle trajectory. It is defined as

$$R_L(\tau) = \frac{\langle u(t)u(t+\tau) \rangle}{\langle u_0^2 \rangle}. \quad (2.41)$$

In a homogeneous, isotropic and stationary turbulence  $u(t)$  equals  $u_0$ . Hence, it is critical to determine  $R(\tau)$  for evaluating  $T_L$ . The problem is that, on the one hand, there is no theoretical form for  $R_L(\tau)$ ; on the other hand, experimental measurements of Lagrangian quantities are difficult to obtain. Therefore, there is not a great deal of information about  $R_L(\tau)$ . Nevertheless, two important asymptotic results are available by making use of the following properties of the correlation coefficient  $R_L(\tau)$ :

$$R_L(0) = 1, \quad R_L(t) \rightarrow 0, \quad \text{as } t \rightarrow \infty. \quad (2.42)$$

The two results represents for the limiting case  $t \rightarrow 0$  and  $t \rightarrow \infty$ , respectively:

1. short time limit  $t \ll T_L$ : if  $t$  is small enough, the correlation coefficient  $R_L(\tau)$  may be approximated by unity,  $R_L(\tau) = 1$ . Then, one may obtain

$$\langle y^2(t) \rangle = \langle u_0^2 \rangle t^2. \quad (2.43)$$

The above expression (2.43) indicates that the distance covered by the representative particle is equal to its velocity multiplied by the time elapsed at short diffusion time.

2. long time limit  $t \gg T_L$ : Given a time long enough for allowing the correlation coefficient  $R_L(\tau)$  to have fallen to zero, the integral of Eq: (2.40) is cut off and

equal to  $T_L$ . Then, one may get

$$\langle y^2(t) \rangle \sim 2 \langle u_0^2 \rangle T_L t. \quad (2.44)$$

Eq: (2.44) suggests that the r.m.s particle displacement is proportional to the square root of the time elapsed, which corresponds to the same result obtained by Taylor (1921) who analysed the classical random walk of discontinuous movements.

To match the above two diffusion properties of fluid particles in a homogeneous, isotropic and stationary turbulent field, Wang and Stock (1992) proposed that, if the eddy lifetime is randomly distributed in terms of a probability density function (PDF)  $f(t_e)$ , then a time averaged form of  $R_L(\tau)$  may be estimated by:

$$R_L(\tau) = \frac{\int_{\tau}^{\infty} (t_e - \tau) f(t_e) dt_e}{T_e}, \quad (2.45)$$

where the denominator is the mean of random eddy time interval  $t_e$  and given by:

$$T_e = \int_0^{\infty} t_e f(t_e) dt_e. \quad (2.46)$$

Eq: (2.45) may be rewritten using integration by parts as:

$$R_L(\tau) = \frac{\int_{\tau}^{\infty} \phi(t_e) dt_e}{\int_0^{\infty} \phi(t_e) dt_e}, \quad (2.47)$$

where

$$\phi(t_e) = \int_{t_e}^{\infty} f(t_1) dt_1, \quad (2.48)$$

according to  $f(t_e)$  denotes the PDF of eddy lifetime,  $\phi(t_e)$  is the probability that the random eddy lifetime is greater than  $t_e$ , i.e.  $\phi(t_e) = P(t > t_e)$ .

If the characteristic eddy lifetime is defined as constant (e.g. Hutchinson et al. (1971); Gosman and Ioannides (1983); Fluent (2009)), then the PDF of  $f(t_e)$  is a delta function, i.e.  $f(t_e) = \delta(t_e - T_e)$ , where  $T_e$  is the constant mean value of eddy lifetime. In this case,

the Lagrangian auto-correlation coefficient takes the form:

$$R_L = \begin{cases} 1 - \frac{\tau}{T_e}, & \tau \ll T_e, \\ 0 & \tau \gg T_e, \end{cases} \quad (2.49)$$

then the integral Lagrangian time scale  $T_L$  defined in Eq: (2.40) may be found to be  $T_L = 0.5T_e$  by integrating Eq: (2.47). Accordingly, in order to ensure the self-consistency dispersion properties proposed in [Kallio and Reeks \(1989\)](#), the eddy lifetime  $T_e$  is chosen as:

$$T_e = 2T_L. \quad (2.50)$$

An exponential distribution,

$$f(t_e) = \frac{1}{T_e} e^{-t_e/T_e}, \quad (2.51)$$

was used to describe the PDF of the eddy lifetime in [Kallio and Reeks \(1989\)](#). This distribution yields a more realistic description of the correlation coefficient  $R_L(\tau)$ , which can be found to be by integrating Eq: (2.47):

$$R_L(\tau) = e^{-\tau/T_e}. \quad (2.52)$$

In this case, one may obtain  $T_L = T_e$ . Therefore, choice of  $T_e = T_L$  yields self-consistency dispersion properties for random eddy lifetime.

The same procedure can be applied to study the eddy length scale  $l_e$ . Considering fluid velocity fluctuation auto-correlation along a particle path,  $G(\tau)$ , we can define it according to homogeneity in space and time domain as

$$G(\tau) = \langle u_f(\mathbf{x}, t) u_f(\mathbf{x} + \mathbf{U}_s \tau + \boldsymbol{\varepsilon}(\tau), t + \tau) \rangle = u'^2 R_f^p(\tau), \quad (2.53)$$

where  $\mathbf{x} + \mathbf{U}_s \tau + \boldsymbol{\varepsilon}(\tau)$  is the position of particle at time  $t + \tau$  due to setting velocity and random velocity fluctuations.  $R_f^p(\tau)$  denotes the fluid velocity auto-correlation along a particle path and  $R_f^p(0) = 1$ .

In the limit of very heavy particle ( $\mathbf{U}_s \tau \gg \varepsilon(\tau)$ ), the turbulence seen by the particle can be assumed to be “frozen” in time and Eq: (2.53) may be rewritten as:

$$G(\tau) = u'^2 R_E(\mathbf{U}_s \tau, 0), \quad (2.54)$$

with Eq: (2.53), one obtains:

$$R_E(\mathbf{U}_s \tau, 0) = R_f^p(\tau), \quad (2.55)$$

where  $R_E$  represents the Eulerian fluid velocity auto-correlation, and given by

$$R_E(\mathbf{x}, t) = \frac{\langle u_f(\mathbf{x}_0, t) u_f(\mathbf{x}_0 + \mathbf{x}, t_0 + t) \rangle}{\langle u_f^2(\mathbf{x}_0, t_0) \rangle}, \quad (2.56)$$

$R_E(\mathbf{x}, t)$  in Eq: (2.56) is assumed to be independent of  $t_0$  and  $x_0$  in a homogeneous, isotropic and stationary turbulent field.

Integrating both sides of Eq: (2.55) with respect to  $\tau$ , one gives:

$$\int_0^\infty R_f^p(\tau) d\tau = \frac{1}{\mathbf{U}_s} \int_0^\infty R_E(\mathbf{x}, 0) d\mathbf{x} = \frac{\Lambda_E}{\mathbf{U}_s}, \quad (2.57)$$

where  $\Lambda_E$  denotes the Eulerian length-scale of the flow field. Similarly, employing the same procedure proposed by Wang and Stock (1992), it can be demonstrated that, if the eddy length scale  $l_e$  is kept constant in DRW,  $l_e = 2\Lambda_E$ ; whilst  $l_e$  obeys an exponential distribution,  $l_e = \Lambda_E$ . Then, both cases can reproduce the self-consistency dispersion properties of heavy particles.

In this thesis, specifying the eddy lifetime that obeys an exponential distribution is adopted for studying the deposition and dispersion of heavy particles in turbulent boundary layers.

### 2.6.1.2 The pros and cons of DRW models

DRW models are widely used for modelling turbulent dispersed particulate flows in CFD modelling frameworks. The advantages of DRW models lie in its conceptual simplicity,

in that it merely requires the length, time and velocity scales of the flow to reconstruct the turbulence effect on the particle dispersion. In DRW models, the motion of the dispersed particulate phase in a turbulent flow field is determined by simulating the interactions of particles with a succession of random discrete eddies. The eddy velocity is determined according to the sum of the interpolated average fluid velocity and a random velocity fluctuation. The random velocity fluctuation is normally characterized by the turbulent velocity fluctuations and random eddy time scales according to a function of the local turbulence conditions.

Although DRW models enjoy a huge popularity and great success in a wide range of turbulent particle-dispersion applications, they fail in a few cases. This was partly summarized by [Graham \(1998\)](#).

1. They yield contrary results to analytical solutions and experimental measurements, which show that the dispersion of heavy particles increases with increasing particle inertia and is stronger than that of fluid particles. This is also known as the inertia effect (see [Reeks \(1977\)](#); [Wells and Stock \(1983\)](#)). This results from the fact that the particle/eddy interaction time in DRW models never exceeds the eddy lifetime.
2. The crossing trajectory effect (e.g. [Yudine \(1959\)](#); [Csanady \(1963\)](#); [Wells and Stock \(1983\)](#)) may not be properly accounted for, since the turbulent dispersed particles may move faster than the encountered eddies along the path. Under this circumstance, eddies are crossed by particles in a relatively shorter time that results in a reduced turbulent dispersion effect on the particle motion.
3. DRW models fail to account for the “continuity effect” proposed by [Csanady \(1963\)](#), whereby the particle dispersion in the direction of gravitational drift is stronger than the counterpart at the right angle to this direction.
4. It has been demonstrated by [MacInnes and Bracco \(1992\)](#) that DRW models cause serious spurious drift of heavy particle in inhomogeneous turbulence. The

unphysical accumulation of particles results from the fact that sampling velocity fluctuations in each eddy attains constant values, which causes particles drift relative to the mean flow from regions with higher turbulence intensity to lower ones.

Corresponding modifications with respect to the cons of DRW can be consulted in [Graham \(1998\)](#) and [MacInnes and Bracco \(1992\)](#).

## 2.6.2 Continuous Random Walk (CRW) models

Continuous random walk (CRW) models have proved to be a successful and versatile tool in the study of the dispersion of fluid particles and deposition of heavy particles in turbulent flows (see [Bocksell and Loth \(2006\)](#); [Dehbi \(2008b\)](#)), and these models avoid unphysical infinite accelerations experienced by particles when using the discrete random walk models.

### 2.6.2.1 One-dimensional models

The CRW approach is based on the Langevin equation, which was proposed by [Langevin \(1908\)](#) to give an alternative description of the Brownian motion. For simplicity, the acceleration of a Brownian particle in one dimension can be expressed as

$$\frac{du}{dt} = -\alpha u + \sigma \xi(t), \quad (2.58)$$

in which  $u$  denotes a Brownian particle velocity,  $t$  is time, and  $\alpha$  represents a damping coefficient associated with viscous drag on the particle suspended in a fluid,  $\xi(t)$  represents what is called white noise resulting from irregular, unsymmetrical and stochastic molecular bombardment on the particle,  $\sigma$  may be interpreted as an amplified factor to  $\xi(t)$ . Physically speaking, the first term on the right hand side of Eq: (2.58) may be called the local drift term of random velocity  $u$ , whilst the second term may be called the diffusion term. If  $\alpha$  attains constant value, then  $u$  is modelled by the stationary Brownian motion process or called Ornstein-Uhlenbeck (OU) process ([Gardiner \(2004\)](#));

van Kampen (2007)). Eq: (2.58) in fact is a stochastic differential equation (SDE) in disguise and may be rewritten as:

$$\left. \begin{aligned} du &= -\alpha u dt + \sigma dW(t), \\ dx &= u dt. \end{aligned} \right\} \quad (2.59)$$

where  $W(t)$  denotes a Brownian motion or Wiener process that satisfies the following properties:

1.  $W(t)$  is continuous;
2.  $W(0) = 0$ ;
3. For  $s < t$  the stochastic variable  $W(t) - W(s)$  has the Gaussian distribution  $N[0, \sqrt{t-s}]$ ;
4.  $W(t)$  has independent increments, i.e. if  $r < s \leq t < u$  then  $W(u) - W(t)$  and  $W(s) - W(r)$  are independent random variables.

Figure (2.5) shows five realizations of the Brownian paths.

### 2.6.2.2 Connection with the Fokker-Planck equation

The Langevin equation is mainly concerned with the properties of individual realizations of fluid particle trajectories with drift and diffusion. Whereas the alternative is to discover the statistics of a sufficient large number of particle paths: their mean and variance, or more generally, the time evolution of the probability density distribution (PDF) of a stochastic process. The time evolution of the PDF is normally governed by the Fokker-Planck equation, which can be used to obtain the coefficients  $\alpha$  and  $\sigma$  appearing in equation 2.58 according to the corresponding Eulerian statistics of the turbulent flow field.

Assume  $P(x, u, t)$  denotes the probability density function of phase-space (i.e.  $(x, u$ -space)) distribution of all the fluid particles described by Eq: 2.58, the evolution of the

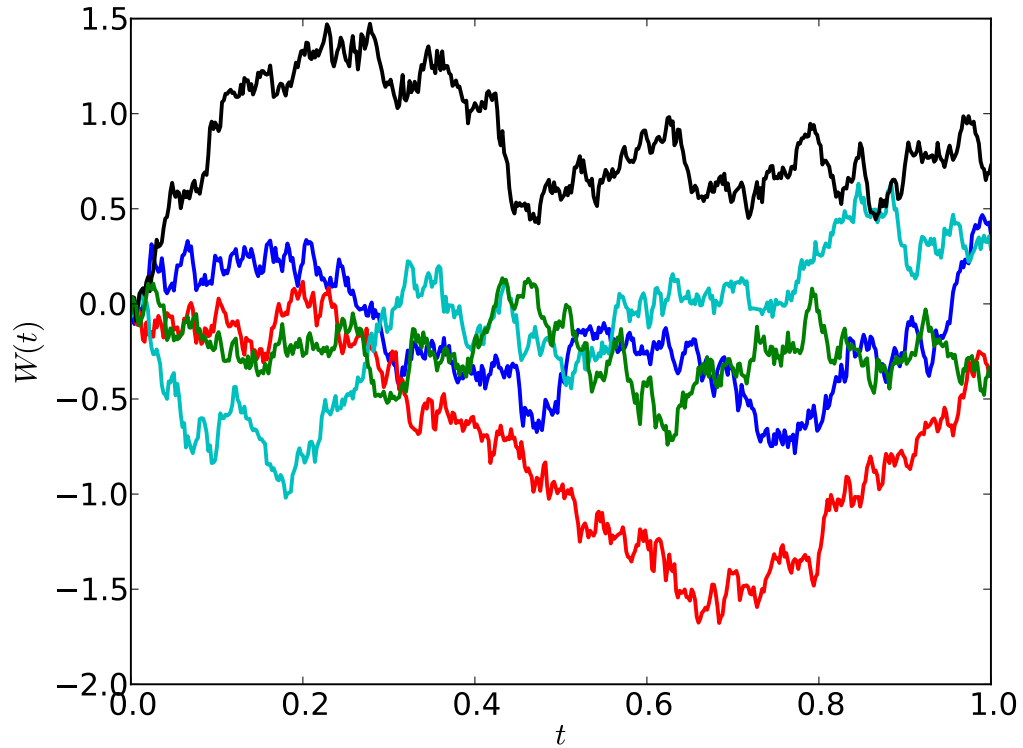


Figure 2.5: Five realizations of Brownian motion (Wiener process)  $W(t)$

distribution  $P(x, u, t)$  may be given:

$$\frac{\partial P(x, u, t)}{\partial t} + u \frac{\partial P(x, u, t)}{\partial x} = -\frac{\partial}{\partial u} [-\alpha u P(x, u, t)] + \frac{1}{2} \frac{\partial^2}{\partial u^2} [\sigma^2 P(x, u, t)]. \quad (2.60)$$

This is called the backward Kolmogorov equation (see [Risken \(1996\)](#)). Here, the Itô formula is used to drive Eq: 2.60 as

$$dP(x, u, t) = \frac{\partial P}{\partial t} dt + \frac{\partial P}{\partial x} dx + \frac{\partial P}{\partial u} du + \frac{1}{2} \frac{\partial^2 P}{\partial x^2} (dx)^2 + \frac{1}{2} \frac{\partial^2 P}{\partial u^2} (du)^2. \quad (2.61)$$

According to Eq: 2.59

$$\left. \begin{aligned} (du)^2 &= \alpha^2 u^2 (dt)^2 + \sigma^2 (dW)^2 - 2\alpha u \sigma (dt)(dW), \\ (dx)^2 &= u^2 (dt)^2. \end{aligned} \right\} \quad (2.62)$$

The term containing  $(dt)^2$  above is negligible compared to the  $dt$ -term, and it can also be

shown that the term  $(dt)(dW)$  is negligible compared to the  $dt$ -term. Furthermore, it is known that  $(dW)^2 = dt$ , and substituting all this into Eq: 2.61 gives the following:

$$dP(x, u, t) = \frac{\partial P}{\partial t} dt + u \frac{\partial P}{\partial x} dt + (-\alpha u) \frac{\partial P}{\partial u} dt + \sigma \frac{\partial P}{\partial u} dW + \frac{1}{2} \sigma^2 \frac{\partial^2 P}{\partial u^2} dt. \quad (2.63)$$

Integrating the both sides of the above equation, and assuming there is no any source, one obtains:

$$\int \frac{\partial P}{\partial t} dt + \int u \frac{\partial P}{\partial x} dt + \int (-\alpha u) \frac{\partial P}{\partial u} dt + \int \sigma \frac{\partial P}{\partial u} dW + \int \frac{1}{2} \sigma^2 \frac{\partial^2 P}{\partial u^2} dt = 0. \quad (2.64)$$

By the martingale property of Itô integrals (see Øksendal (2003)) that

$$\mathbf{E} \left\{ \int \cdot dW \right\} = 0, \quad (2.65)$$

Hence Eq: 2.64 may be written as:b

$$\int \left[ \frac{\partial P}{\partial t} + u \frac{\partial P}{\partial x} + (-\alpha u) \frac{\partial P}{\partial u} dt + \frac{1}{2} \sigma^2 \frac{\partial^2 P}{\partial u^2} \right] dt = 0. \quad (2.66)$$

Now one can obtain Eq: 2.60. Similarly,  $P(x, u, t)$  satisfies the forward Kolmogorov or Fokker-Planck equation:

$$\frac{\partial P(x, u, t)}{\partial t} + u \frac{\partial P(x, u, t)}{\partial x} = \frac{\partial}{\partial u} [\alpha u P(x, u, t)] + \frac{1}{2} \frac{\partial^2}{\partial u^2} [\sigma^2 P(x, u, t)]. \quad (2.67)$$

Eq: 2.67 may also be written as:

$$\frac{\partial P(x, u, t)}{\partial t} + u \frac{\partial P(x, u, t)}{\partial x} = \frac{\partial}{\partial u} \left[ \alpha u P(x, u, t) + \frac{1}{2} \sigma^2 \frac{\partial P(x, u, t)}{\partial u} \right]. \quad (2.68)$$

Eq: 2.68 is also known as the PDF transport equation that has the following physical interpretation for a one-dimensional flow: the material derivative of the probability distribution function  $P(x, u, t)$  is balanced by the flux of  $\left\{ \alpha u P(x, u, t) + \frac{1}{2} \sigma^2 \frac{\partial P(x, u, t)}{\partial u} \right\}$  in the  $u$  direction that is a probability distribution being carried by a mean velocity  $\alpha u$  due to the drift and a diffusion with coefficient  $\frac{1}{2} \sigma^2$ .

### 2.6.2.3 Determination of the coefficients

The determination of the coefficient  $\sigma$  in Eq: 2.59 with an initial condition  $u(0) = u_0$  is relatively simple. According to the theory of linear ODE, the solution of Eq: 2.59 may be conjectured as:

$$u_t = e^{-\alpha t} u_0 + \sigma \int_0^t e^{-\alpha(t-s)} dW(s). \quad (2.69)$$

Eq: 2.69 is of several interesting features. First, one can see that as  $t \rightarrow \infty$  the influence of the initial value  $u(0) = u_0$  decays exponentially, which corresponds to that the velocity of fluid particle has short memory. Second,  $\mathbf{E}[u(t)] = e^{-\alpha t} u_0$  since the  $dW(s)$  integral has mean zero, so the mean  $\mathbf{E}[u(t)]$  also goes to zero rapidly.

Moreover, both sides of Eq: 2.69 times  $u(0)$  and runs an ensemble average for a large number of fluid particles  $u(t)$  one may obtain the following:

$$\langle u(t)u(0) \rangle = \langle u(0)^2 \rangle e^{-\alpha t}. \quad (2.70)$$

Looking back to the Eqs: 2.41 and 2.51 for the correlation coefficient  $R_L(\tau)$ , one finds

$$\alpha = \frac{1}{T_L}. \quad (2.71)$$

According to the Itô isometry for a stochastic process  $X(t)$  (see Øksendal (2003)):

$$\mathbf{E} \left[ \left( \int_0^T X(t) dW(t) \right)^2 \right] = \mathbf{E} \left[ \int_0^T X(t)^2 dt \right], \quad (2.72)$$

one may compute the variance of  $u(t)$ ,  $\langle u(t)^2 \rangle$  from Eq: 2.69 as:

$$\langle u(t)^2 \rangle = e^{-2\alpha t} \langle u(0)^2 \rangle + \sigma^2 \int_0^t e^{-2\alpha(t-s)} ds = e^{-2\alpha t} \langle u(0)^2 \rangle + \frac{\sigma^2}{2\alpha} (1 - e^{-2\alpha t}). \quad (2.73)$$

From this calculation, it has

$$\langle u(t)^2 \rangle \rightarrow \frac{\sigma^2}{2\alpha}, \quad (2.74)$$

Then one can find for a stationary turbulence:

$$\sigma = \sqrt{2\alpha \langle u(t)^2 \rangle} = \sqrt{\frac{2 \langle u(0)^2 \rangle}{T_L}}. \quad (2.75)$$

#### 2.6.2.4 Drift correction with the well-mixed condition

For the Eq: 2.68, assuming that the convection term  $u \frac{\partial P(x,u,t)}{\partial x}$  and drift term  $\alpha u \frac{\partial P(x,u,t)}{\partial u}$  equals to zero, one obtains:

$$\frac{\partial P(x,u,t)}{\partial t} = \frac{1}{2} \sigma^2 \frac{\partial^2 P(x,u,t)}{\partial u^2}. \quad (2.76)$$

This is a diffusion equation. With an initial condition  $P(x,u,t) = \delta_0(x,u)$  (the Dirac delta function), the long time equilibrium solution for  $P(x,u,t)$  is a Gaussian distribution namely

$$P(x,u,t) = \frac{1}{\sqrt{2\pi}\sigma_x} \exp\left[-\frac{1}{2} \left(\frac{u}{\sigma_x}\right)^2\right] \quad (2.77)$$

satisfies Eq: 2.76 for diffusion with  $\sigma_x$  denoting the variance of the Eulerian fluid velocity. In Thomson (1987), the above equation is also assumed to satisfy the Fokker-Planck equation 2.68.

In order to satisfy the well-mixed condition proposed by Thomson (1987) in an inhomogeneous flow field, e.g. a fully turbulent boundary layer, the Langevin equation 2.59 need modifications to account for the mean pressure gradient that exists in the fluid. The following equations result from Eq: 2.68 and define the well-mixed condition:

$$\alpha_1 P = \frac{\partial}{\partial x} \left( \frac{\sigma^2}{2} P \right) + \phi(x,u,t), \quad (2.78a)$$

$$\frac{\partial \phi}{\partial u} = -\frac{\partial P}{\partial t} - \frac{\partial}{\partial x} (uP). \quad (2.78b)$$

where  $\alpha_1$  is used to substitute  $\alpha u$  in Eq: 2.68. Moreover,

$$\phi \rightarrow 0 \quad \text{as} \quad |u| \rightarrow \infty. \quad (2.79)$$

To obtain  $\alpha_1$ , substituting the partial derivatives of Eq: 2.77 with respect to  $t, u, x$ , one finds:

$$\alpha_1 = -\frac{u}{T_L} + \frac{\phi}{P}. \quad (2.80)$$

Now one need to find out a solution for the “drift correction” represented by second term in the above equation  $\phi/P$ .

Thomson (1987) and Rodean (1996) gave the following expression:

$$\frac{\phi}{P} = \frac{1}{2} \frac{\partial \sigma_x^2}{\partial x} + \frac{1}{2\sigma_x^2} \left( \frac{\partial \sigma_x^2}{\partial t} \right) u + \frac{1}{2\sigma_x^2} \left( \frac{\partial \sigma_x^2}{\partial x} \right) u^2. \quad (2.81)$$

With stationary conditions, the second term in the above equation may be set to zero.

Then substituting Eqs: 2.81 and 2.80 into Eq: 2.59 yields

$$du = -\frac{u}{T_L} dt + \frac{1}{2} \left[ 1 + \left( \frac{u}{\sigma_x} \right)^2 \right] \frac{\partial \sigma_x^2}{\partial x} dt + \left( \frac{2\sigma_x^2}{T_L} \right)^{1/2} dW(t). \quad (2.82)$$

This is the model for one-dimensional (wall-normal) diffusion in stationary inhomogeneous turbulence. Eq: (2.82) can be normalized as

$$d \left( \frac{u}{\sigma_x} \right) = - \left( \frac{u}{\sigma_x} \right) \frac{1}{T_L} dt + \frac{\partial \sigma_x}{\partial x} dt + \left( \frac{2}{T_L} \right)^{1/2} dW(t). \quad (2.83)$$

Bocksell and Loth (2006) further considered the inertial effect in the drift correction term, and following this Eq: (2.83) can be rewritten as

$$d \left( \frac{u}{\sigma_x} \right) = - \left( \frac{u}{\sigma_x} \right) \frac{1}{T_L} dt + \left( \frac{1}{1+St} \right) \frac{\partial \sigma_x}{\partial x} dt + \left( \frac{2}{T_L} \right)^{1/2} dW(t), \quad (2.84)$$

where  $St$  is the particle Stokes number. Eq: (2.84) is the basis that is adopted to account for the wall-normal fluctuations of fluid velocity seen by heavy particles along their trajectories.

## REFERENCES

- S. Balachandar and J. K. Eaton. Turbulent dispersed multiphase flow. *Annual Review of Fluid Mechanics*, 42:111–133, 2010.
- T. J. Barth and D. C. Jespersen. The design and application of upwind schemes on unstructured meshes. In *27th Aerospace Sciences Meeting*, volume 89, 1989.
- A. S. Berrouk, D. E. Stock, D. Laurence, and J. J. Riley. Heavy particle dispersion from a point source in turbulent pipe flow. *International Journal of Multiphase Flow*, 34(10):916–923, 2008.
- T. L. Bocksell and E. Loth. Stochastic modeling of particle diffusion in a turbulent boundary layer. *International Journal of Multiphase Flow*, 32(10-11):1234–1253, 2006.
- S. Chibbaro and J. P. Minier. Langevin PDF simulation of particle deposition in a turbulent pipe flow. *Journal of Aerosol Science*, 39(7):555–571, 2008.
- J. W. Cleaver and B. Yates. A sub layer model for the deposition of particles from a turbulent flow. *Chemical Engineering Science*, 30(8):983–992, 1975.
- G. T. Csanady. Turbulent diffusion of heavy particles in the atmosphere. *Journal of Atmospheric Sciences*, 20:201–208, 1963.
- A. Dehbi. A CFD model for particle dispersion in turbulent boundary layer flows. *Nuclear Engineering and Design*, 238(3):707–715, 2008a.
- A. Dehbi. Turbulent particle dispersion in arbitrary wall-bounded geometries: A coupled CFD-Langevin-equation based approach. *International Journal of Multiphase Flow*, 34(9):819–828, 2008b.

- A. Dehbi. A stochastic langevin model of turbulent particle dispersion in the presence of thermophoresis. *International Journal of Multiphase Flow*, 35(3):219–226, 2009.
- A. Dehbi. Validation against dns statistics of the normalized langevin model for particle transport in turbulent channel flows. *Powder Technology*, 200(1-2):60–68, 2010.
- A. Dehbi. Prediction of Extrathoracic Aerosol Deposition using RANS-Random Walk and LES Approaches. *Aerosol Science and Technology*, 45(5):555–569, 2011.
- A. Dehbi and S. Martin. Cfd simulation of particle deposition on an array of spheres using an euler/lagrange approach. *Nuclear Engineering and Design*, 2011.
- B. J. Devenish, D. C. Swailes, Y. A. Sergeev, and V. N. Kurdyumov. A pdf model for dispersed particles with inelastic particle–wall collisions. *Physics of Fluids*, 11(7):1858–1868, 1999.
- S. Elghobashi. Particle-laden turbulent flows: direct simulation and closure models. *Applied scientific research*, 48(3):301–314, 1991.
- A. Fluent. 12.0 documentation. *ANSYS Inc*, 2009.
- C. Gardiner. *Handbook of Stochastic Methods: for Physics, Chemistry and the Natural Sciences*. 2004.
- A. D. Gosman and E. Ioannides. Aspects of computer simulation of liquid-fueled combustors. *Journal of energy*, 7(6):482–490, 1983.
- D. I. Graham. On the inertia effect in eddy interaction models. *International Journal of Multiphase Flow*, 22(1):177–184, 1996.
- D. I. Graham. Development of particle dispersion characteristics from arbitrary initial conditions in isotropic turbulence. *Journal of Fluid Mechanics*, 501:149–168, 2004.
- D. I. Graham. Improved eddy interaction models with random length and time scales. *International Journal of Multiphase Flow*, 24(2):335–345, 1998.
- D. I. Graham and P. W. James. Turbulent dispersion of particles using eddy interaction models. *International Journal of Multiphase Flow*, 22(1):157–175, 1996.

- C. Greenfield. *Numerical modelling of transport phenomena in reactors*. PhD thesis, Bristol Univesity, 1998.
- A. Guha. Transport and deposition of particles in turbulent and laminar flow. *Annual Review of Fluid Mechanics*, 40:311–341, 2008.
- A. Guha. A unified eulerian theory of turbulent deposition to smooth and rough surfaces. *Journal of Aerosol Science*, 28(8):1517–1537, 1997.
- M. Guingo and J. P. Minier. A stochastic model of coherent structures for particle deposition in turbulent flows. *Physics of Fluids*, 20(5), 2008.
- M. Horn and H. J. Schmid. A comprehensive approach in modeling lagrangian particle deposition in turbulent boundary layers. *Powder Technology*, 186(3):189–198, 2008.
- P. Hutchinson, G. F. Hewitt, and A. E. Dukler. Deposition of liquid or solid dispersions from turbulent gas streams: a stochastic model. *Chemical Engineering Science*, 26(3): 419–439, 1971.
- G. A. Kallio and M. W. Reeks. A numerical simulation of particle deposition in turbulent boundary layers. *International Journal of Multiphase Flow*, 15(3):433–446, 1989.
- J. G. M. Kuerten. Subgrid modeling in particle-laden channel flow. *Physics of Fluids*, 18 (2):025108, 2006.
- J. G. M Kuerten and A. W. Vreman. Can turbophoresis be predicted by large-eddy simulation? *Physics of Fluids*, 17:011701, 2005.
- P. Langevin. On the theory of brownian motion. *CR Acad. Sci. Paris*, 146:530–533, 1908.
- J. M. MacInnes and F. V. Bracco. Stochastic particle dispersion modeling and the tracer-particle limit. *Physics of Fluids A: Fluid Dynamics*, 4:2809, 1992.
- C. Marchioli and A. Soldati. Mechanisms for particle transfer and segregation in a turbulent boundary layer. *Journal of Fluid Mechanics*, 468:283–315, 2002.

- C. Marchioli, A. Giusti, M. Vittoria Salvetti, and A. Soldati. Direct numerical simulation of particle wall transfer and deposition in upward turbulent pipe flow. *International Journal of Multiphase Flow*, 29(6):1017–1038, 2003.
- C. Marchioli, MV Salvetti, and A. Soldati. Some issues concerning Large-Eddy Simulation of inertial particle dispersion in turbulent bounded flows. *Physics of Fluids*, 20:040603, 2008a.
- C. Marchioli, A. Soldati, J. G. M. Kuerten, B. Arcen, A. Tanière, G. Goldensoph, K. D. Squires, M. F. Cargnelutti, and L. M. Portela. Statistics of particle dispersion in direct numerical simulations of wall-bounded turbulence: Results of an international collaborative benchmark test. *International Journal of Multiphase Flow*, 34(9):879–893, 2008b.
- S. R. Mathur and J. Y. Murthy. A pressure-based method for unstructured meshes. *Numerical heat transfer. Part B, fundamentals*, 31(2):195–215, 1997.
- M. R. Maxey. Gravitational settling of aerosol particles in homogeneous turbulence and random flow fields. *Journal of Fluid Mechanics*, 174(1):441, 1987.
- M. R. Maxey and J. J. Riley. Equation of motion for a small rigid sphere in a nonuniform flow. *Physics of Fluids*, 26:883, 1983.
- J. B. McLaughlin. Aerosol particle deposition in numerically simulated channel flow. *Physics of Fluids A: Fluid Dynamics*, 1:1211, 1989.
- J. B. McLaughlin. Inertial migration of a small sphere in linear shear flows. *Journal of Fluid Mechanics*, 224:261–274, 1991.
- A. Mehel, A. Tanière, B. Oesterlé, and J. R. Fontaine. The influence of an anisotropic langevin dispersion model on the prediction of micro-and nanoparticle deposition in wall-bounded turbulent flows. *Journal of Aerosol Science*, 41(8):729–744, 2010.
- S. A. Morsi and A. J. Alexander. An investigation of particle trajectories in two-phase flow systems. *Journal of Fluid Mechanics*, 55(02):193–208, 1972.

- C. Narayanan, D. Lakehal, L. Botto, and A. Soldati. Mechanisms of particle deposition in a fully developed turbulent open channel flow. *Physics of Fluids*, 15(3):763–775, 2003.
- B. K. Øksendal. *Stochastic differential equations: an introduction with applications*. Springer Verlag, 2003.
- C. W. Oseen. Über die stokes'sche formel und über eine verwandte aufgabe in der hydrodynamik. *Ark. Mat. Astron. Fysik*, 6(29), 1910.
- C. W. Oseen. Über den goltigkeitsbereich der stokesschen widerstandsformel. *Ark. Mat. Astron. Fysik*, 9(19), 1913.
- M. Picciotto, C. Marchioli, M. W. Reeks, and A. Soldati. Statistics of velocity and preferential accumulation of micro-particles in boundary layer turbulence. *Nuclear Engineering and Design*, 235(10-12):1239–1249, 2005.
- L. M. Portela and R. V. A. Oliemans. Eulerian-lagrangian dns/les of particle-turbulence interactions in wall-bounded flows. *International Journal for Numerical Methods in Fluids*, 43(9):1045–1065, 2003.
- A. Prosperetti and G. Tryggvason. *Computational Methods for Multiphase Flow*. Cambridge University Press, 2007.
- M. W. Reeks. On the dispersion of small particles suspended in an isotropic turbulent fluid. *Journal of Fluid Mechanics*, 83(3):529–546, 1977.
- M. W. Reeks. On a kinetic equation for the transport of particles in turbulent flows. *Physics of Fluids A: Fluid Dynamics*, 3:446, 1991.
- M. W. Reeks. On the continuum equations for dispersed particles in nonuniform flows. *Physics of Fluids A: Fluid Dynamics*, 4:1290, 1992.
- H. Risken. *The Fokker-Planck Equation: Methods of Solutions and Applications*. Springer Series in Synergetics. Springer, 2nd ed. 1989. 3rd printing edition, 1996.
- H. C. Rodean. *Stochastic Lagrangian models of turbulent diffusion*, volume 45. American Meteorological Society, 1996.

- P. G. Saffman. The lift on a small sphere in a slow shear flow. *Journal of Fluid Mechanics*, 22(02):385–400, 1965.
- P. G. Saffman. Corrigendum to the lift of a small sphere in a slow shear flow. *Journal of Fluid Mechanics*, 32, 1968.
- L. Schiller and A. Naumann. A drag coefficient correlation. *Vdi Zeitung*, 77:318–320, 1933.
- Y. A. Sergeev, R. S. Johnson, and D. C. Swailes. Dilute suspension of high inertia particles in the turbulent flow near the wall. *Physics of Fluids*, 14(3):1042–1055, 2002.
- K. D. Squires and J. K. Eaton. Particle response and turbulence modification in isotropic turbulence. *Physics of Fluids A: Fluid Dynamics*, 2:1191, 1990.
- K. D. Squires and J. K. Eaton. Preferential concentration of particles by turbulence. *Physics of Fluids A: Fluid Dynamics*, 3:1169, 1991.
- D. C. Swailes and M. W. Reeks. Particle deposition from a turbulent flow. i. a steady-state model for high inertia particles. *Physics of Fluids*, 6:3392, 1994.
- G. I. Taylor. Diffusion by continuous movements. *Proc. London Math. Soc.*, 20(2): 196–211, 1921.
- D. J. Thomson. Criteria for the selection of stochastic models of particle trajectories in turbulent flows. *Journal of Fluid Mechanics*, 180(7):529–556, 1987.
- L. Tian and G. Ahmadi. Particle deposition in turbulent duct flows - comparisons of different model predictions. *Journal of Aerosol Science*, 38(4):377–397, 2007.
- W. S. J Uijtewaal and R. V. A. Oliemans. Particle dispersion and deposition in direct numerical and large eddy simulations of vertical pipe flows. *Physics of Fluids*, 8:2590, 1996.
- N. G. van Kampen. *Stochastic Processes in Physics and Chemistry*. North Holland, 2007.

- H. K. Versteeg and W. Malalasekera. *An introduction to computational fluid dynamics: the finite volume method*. Prentice Hall, 2007.
- L. P. Wang and D. E. Stock. Stochastic trajectory models for turbulent diffusion: Monte carlo process versus markov chains. *Atmospheric Environment. Part A. General Topics*, 26(9):1599–1607, 1992.
- Q. Wang and K. D. Squires. Large eddy simulation of particle deposition in a vertical turbulent channel flow. *International Journal of Multiphase Flow*, 22(4):667–682, 1996a.
- Q. Z. Wang and K. D. Squires. Large eddy simulation of particle-laden turbulent channel flow. *Physics of Fluids*, 8(5):1207–1223, 1996b.
- M. R. Wells and D. E. Stock. The effects of crossing trajectories on the dispersion of particles in a turbulent flow. *Journal of Fluid Mechanics*, 136:31–62, 1983.
- J. Young and A. Leeming. A theory of particle deposition in turbulent pipe flow. *Journal of Fluid Mechanics*, 340:129–159, 1997.
- J. B. Young and T. J. Hanratty. Optical studies on the turbulent motion of solid particles in a pipe flow. *Journal of Fluid Mechanics*, 231:665–688, 1991.
- M. I. Yudine. Physical considerations on heavy particle diffusion. *Adv. Geophys*, 6(185): 41–71, 1959.
- L. Zaichik, V. M. Alipchenkov, and E. G. Sinaiski. *Particles in Turbulent Flows*. Wiley Pub, 2008.
- H. Zhang and G. Ahmadi. Aerosol particle transport and deposition in vertical and horizontal turbulent duct flows. *Journal of Fluid Mechanics*, 406(1):55–88, 2000.

# **Chapter 3**

## **Implementation of the Eulerian-Lagrangian method for heavy particles deposition in ANSYS FLUENT**

### **3.1 Introduction**

This chapter first reviews the theory of heavy particle deposition from turbulent flows. Then it reveals the deficiencies of the existing Discrete Phase Model (DPM) in the unstructured-grid based Navier-Stokes equation solver ANSYS FLUENT for studying the depositions of heavy particles within turbulent boundary layers. After this, it discusses a new implementation of the Eulerian-Lagrangian approach as a User Defined Function (UDF) within ANSYS FLUENT, developed to address these shortcomings. It then shows validations of the new Lagrangian particle tracking model. Furthermore, it discusses the parallelization of the self-developed Lagrangian particle tracking code using the open-source Message Passing Interface (MPI) library. The computational efficiency gains of parallelization allow us to study the deposition of heavy particles onto blunt bodies in a

turbulent flow through complex geometries, such as heater-exchange tube-banks using Large Eddy Simulation (LES) for the carrier phase flow solution..

## 3.2 Background on heavy particles deposition

Heavy particles transport and deposition in turbulent flows has been an experimental, theoretical and computational research topic for more half an century. There are a few comprehensive reviews on this subject (e.g. [Papavergos and Hedley \(1984\)](#); [Guha \(2008\)](#); [Soldati and Marchioli \(2009\)](#)).

It is worthwhile to review here the pioneering work on particle deposition developed by [Friedlander and Johnstone \(1957\)](#), who proposed the concept of “stop distance” and ascribed the deposition to the radial fluctuating component of suspended particles velocity. [Friedlander and Johnstone \(1957\)](#) and [Davies \(1966\)](#) proposed and developed a two-fluid model, which is commonly referred to as the “diffusion/free flight” model, to simulate the deposition of heavy particles. In this model, particles are transported by turbulent diffusion from the bulk flow to an adjacent wall surface and to within one particle stop distance. This stop distance is normally characterized by the particle response time  $\tau_p$  and wall normal velocity fluctuations. In the bulk of the underlying flow, it is assumed that particle transport is governed by a convective-diffusion equation. At the particle stop distance, particles are assumed to separate from the local turbulent fluid motion, and are projected to the wall surface through free-flight in terms of their inertia. As a result, deposition is usually determined by the particle flux through a thin near-wall layer to the adjacent wall surface, after gaining some specified initial velocity. Central to this idea is the concept of the particle “stop distance”; the distance that a particle with a specified momentum will pass into the viscous sublayer without the influence of turbulent fluctuations. The concept of “stop distance” also implies that the particle response time  $\tau_p$  should be the only parameter for determining the deposition rate. In the original gradient transport theory for particle transport in the bulk of flow, there is a difference from the usual theory of convective diffusion because of a special boundary condition: the particle concentration at the stop distance is assumed to vanish. This has a

significant effect on particle deposition rates and results in considerable difficulty in the mathematical theory. Moreover, in order to match existing experimental measurements, the particles free-flight velocity is modelled in a heuristic way. If the free-flight velocity is assumed to equal to the local fluid velocity, deposition rate is usually under-predicted by 1 – 2 orders of magnitude. Despite these underlying issues, the diffusion/free-flight model has a few novel ideas that are still explored in research and industrial applications.

Young and Leeming (1997) summarized many experimental measurements as shown in Figure (3.1). The experimental measurements from Liu and Agarwal (1974) are the most frequently cited and reliable data among all the experiments. The figure shows the deposition rate of a wide spectrum of particles, which is represented by the dimensionless deposition velocity,  $V_{dep+}$ , as a function of dimensionless particle response time  $\tau_{p+}$ . The dimensionless particle deposition velocity is defined as

$$V_{dep+} = \frac{J_w}{\rho_p \bar{c} u_\tau}, \quad (3.1)$$

where  $J_w$  represents the mass flux of particles that get deposited to the wall per unit area and per unit time,  $\rho_p$  is the density of the particle,  $\bar{c}$  denotes the mean particle concentration in the bulk of the flow, and the wall friction velocity  $u_\tau$  is used to non-dimensionalized particle deposition velocity and response time  $\tau_p$ .

It can be observed from figure (3.1) that the deposition rates may be divided into three regimes. In the “diffusional deposition” regime,  $V_{dep+}$  show a monotonically decreasing characteristic as a function of  $\tau_p$ . Within this regime, the particle deposition on to the wall may be well described by a gradient diffusion model, which represents turbulent diffusion in the bulk of the flow and Brownian diffusion in the very thin near wall region directly adjacent to the wall.

In the “diffusion-impaction” regime, there is a dramatic variation in deposition rate of several orders of magnitudes, which corresponds to around a fourfold increase in terms of particle diameter, since  $\tau_p$  is proportional to the square of particle diameter  $d_p$ . As the name “diffusion-impaction” suggests, there exist two mechanisms by which particles from the turbulent core can penetrate the viscous sublayer and deposit. First, relatively heavy particles may shoot through the sublayer to the wall directly because

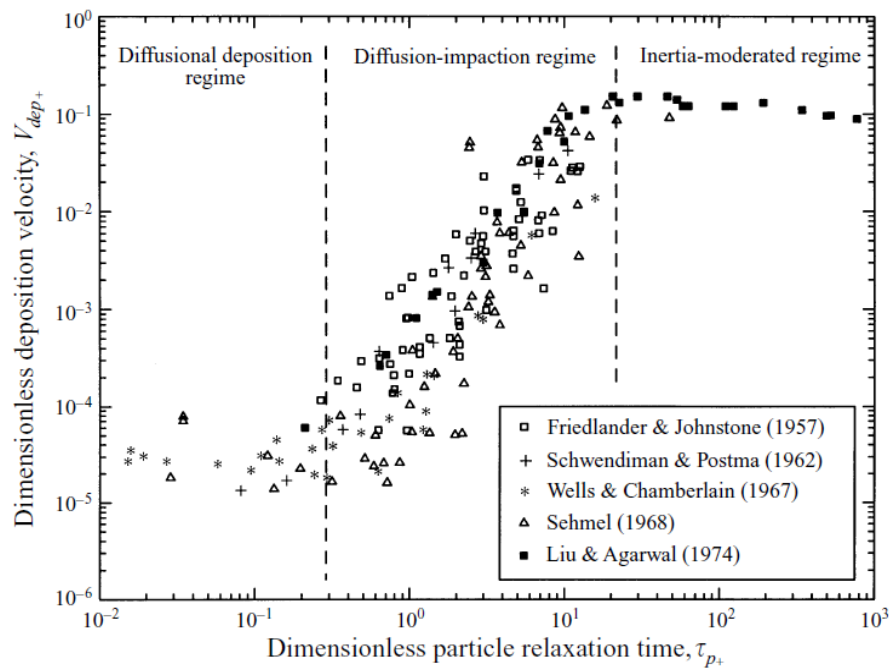


Figure 3.1: Summary of experimental measurements on particle deposition from fully developed turbulent pipe flow. [Young and Leeming \(1997\)](#)

they have greater momentum value than that associated with the r.m.s. value of fluid particles. Second, relatively light particles may be brought to a sufficiently close distance to the wall because of the weak fluid velocity fluctuations within the viscous sublayer. They then may be carried to the wall surface due to their own inertia.

Evidence for both diffusion and impact mechanism based on numerical simulations has been reported by [Chen and McLaughlin \(1995\)](#) and [Narayanan et al. \(2003\)](#). They found that the particle impact velocities striking the wall for dimensionless particle response time  $\tau_{p+} = 5, 10, 15$  may be separated into two groups: Group A with low impact velocities, group B with high impact velocities. Group A is mainly associated with relatively lighter particles with a longer particle residence time within the viscous sublayer, whilst Group B is mostly associated with relatively heavier particles with a larger wall-normal fluctuating velocities and a shorter residence time in the viscous sublayer.

The third regime is referred to as the “inertia-moderated” region. Here the deposition of particles results mainly from their own inertia and large particle velocity fluctuations

acquired from the turbulent core. Hence, the theory of diffusion gradient transport is not applicable for such particles. The reduction in deposition rate with increasing particle size may be ascribed to the fact that the increasing particle inertia results in a decrease in the underlying flow turbulence.

This thesis is concerned primarily with the “diffusion-impact” region that is most challenging of all.

### **3.3 Preliminary results from the Discrete -Phase Model (DPM)**

There is a Discrete-Phase Model (DPM) embedded in ANSYS FLUENT for studying turbulent dispersed particulate flows. Nevertheless, it has a few serious deficiencies when used to study deposition of heavy particles in turbulent boundary layers, which have not been previously reported in the literature. Moreover, the source code of ANSYS FLUENT is not open to the public since it is a commercial software code. On the other hand, ANSYS FLUENT provides an excellent mechanism through which it may load a user-provided shared object. Then, in our case, particle trajectories in a turbulent flow field can be acquired by integrating the particle equation of motion through self-developed codes which acts a share-object code and interacts with the flow field data solved by the unstructured-grid based Navier-Stokes equation solver in ANSYS FLUENT. Moreover, the use of a user provided share object code does not slow down the Navier-Stokes equation solver too much.

In ANSYS FLUENT, the equations that need to be solved by the DPM in order to track a particle in a flow field are as following:

$$d\mathbf{x}_p = \mathbf{u}_p(\mathbf{x}_p; t)dt, \quad (3.2)$$

$$d\mathbf{u}_p = \frac{\mathbf{F}(\mathbf{x}_p; t)}{m_p}dt. \quad (3.3)$$

where  $m_p$  is the mass of the particle. The force  $\mathbf{F}$  is the instantaneous force exerting on a particle suspended in a turbulent flow field, which consists mainly of the drag force due to the difference between the instantaneous fluid and particle velocity and lift force due to the mean velocity gradient in the underlying flow field. With the resolved fluid velocities at every cell centroid available from a converged Reynolds Averaged Navier-Stokes (RANS) or Unsteady Reynolds Averaged Navier-Stokes (URANS) solution, there are four points which are crucial for a successful simulation of deposition of heavy particles in turbulent boundary layers.

1. the spatial interpolation scheme for time-averaged mean fluid velocity;
2. the integration scheme for particle equations of motion [3.2](#) and [3.3](#);
3. the prediction of fluctuating velocity components due to turbulence;
4. boundary handling and particle capture conditions.

At each integration time step, the DPM obtains the discrete, resolved three-dimensional fluid velocities from the Navier-Stokes equations solver. After this, the DPM has to interpolate these velocities to the location of individual particles from the cell centroid at which the discretised fluid velocities are stored, since the particle positions will not coincide exactly with cell centroid. Then the new positions of the particles are calculated using the integration scheme based on the interpolated velocities. Since RANS or URANS simulations only provide the averaged fluid velocities, there is a need for an extra model to account for the influence of flow turbulence. The input velocities for the integration scheme may be divided into a resolved averaged and a fluctuating part. At the end of the DPM step, the boundary interaction handling scheme for a fully absorbing wall should ensure that heavy particles will be captured when the distance from the particle centre to the nearest wall face is less than the particle radius. In the ANSYS FLUENT documentation [Fluent \(2009\)](#), no details are given about the first and fourth points listed above. Therefore, we assumed that these had been fully debugged and correct. Nevertheless, the DPM failed to reproduce the results for particle deposition in turbulent boundary layers when compared against the results resolved by a stand-alone

grid-free Lagrangian particle tracking code. The reasons that the DPM provided by FLUENT fails to reproduce the deposition results shall be elaborated later.

### 3.3.1 Particle deposition using the standard $k - \varepsilon$ model

The first logic step was to apply the default DPM to studying particle deposition using an appropriate turbulence model (e.g. standard  $k - \varepsilon$ ) and compare against the benchmark deposition experiments by Liu and Agarwal (1974) and the curve-fit following available experimental data made by McCoy and Hanratty (1977). The results for particle deposition obtained from running the DPM based on a converged RANS simulation obtained using the standard  $k - \varepsilon$  turbulence model are shown in Figure 3.2.

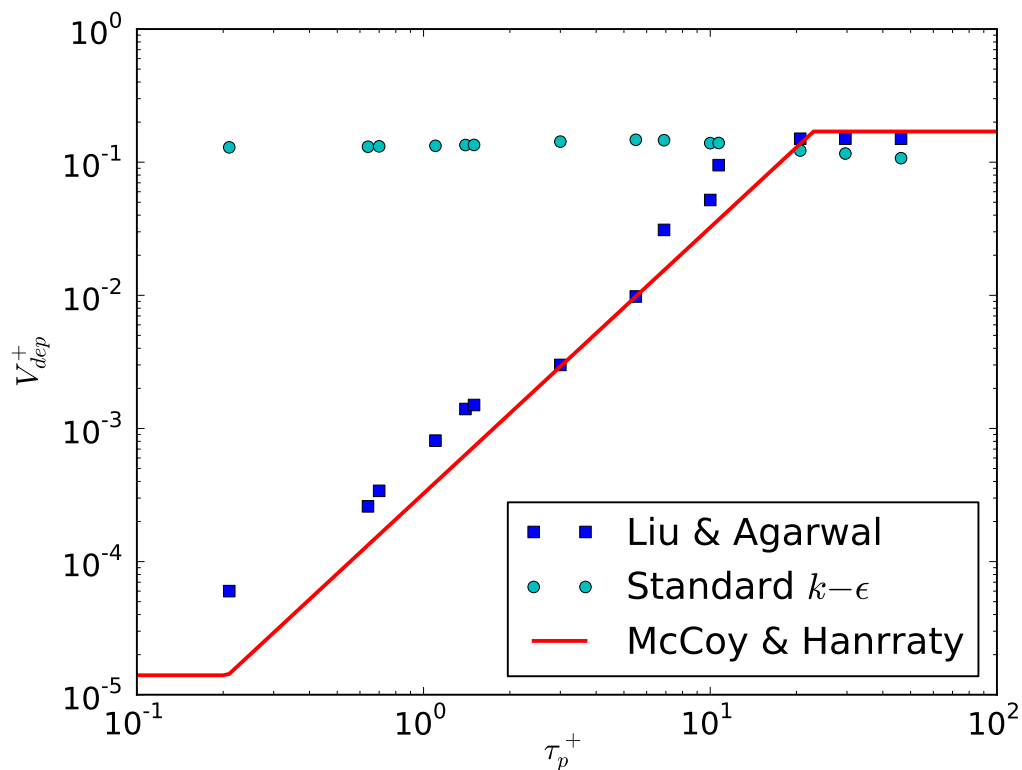


Figure 3.2: Results on particle deposition from fully developed turbulent pipe flow using the DPM with the standard  $k - \varepsilon$  model and compared against experiments.

It can be observed that the deposition rates obtained from the standard  $k - \varepsilon$  model show negligible variation across the whole range of heavy particles studied. This is totally

contradictory to the experimental measurements. The isotropic nature of the standard  $k - \varepsilon$  model is one obvious possible cause of this failure. We recall that the DPM obtains the fluctuating fluid velocities associated with turbulence from the RANS flow field. In the standard  $k - \varepsilon$  model, the r.m.s values of fluctuating fluid velocities are defined as:

$$\sqrt{u'^2} = \sqrt{v'^2} = \sqrt{w'^2} = \sqrt{2k/3}, \quad (3.4)$$

where  $k$  is the turbulent kinetic energy obtained from the standard  $k - \varepsilon$  model. Since the simple  $k - \varepsilon$  model has no mechanism for evaluating the component fluctuations separately, the assumption of isotropy is and the use of Eq: 3.4 is unavoidable. In this case, the turbulence within the turbulent boundary layer in a fully developed pipe flow seen by particles is assumed as the same homogeneous and isotropic as the turbulent core. Hence, so far the prediction of almost same deposition rates for a wide range of particle response time may be explained by the fact that the standard  $k - \varepsilon$  turbulence model does not yield a proper turbulent boundary layer.

Moreover, appropriate grids with adequate resolution have been used to resolve the turbulent flow field, in which the investigation of particle deposition is carried out. An exhaustive comparison study of all the available turbulence models may be carried out to investigate the effect on the particle deposition (see [Tian and Ahmadi \(2007\)](#)), but this is not the main focus of this thesis.

### **3.3.2 Particle deposition using the standard $k - \varepsilon$ turbulence model accounting for the inhomogeneous and anisotropic feature of fully developed turbulent boundary layers**

Based on the methodology for Lagrangian particle tracking in a numerically generated inhomogeneous anisotropic random flow field proposed by [Kallio and Reeks \(1989\)](#), a similar implementation was developed as a ANSYS FLUENT User Defined Function (UDFs) into ANSYS FLUENT to study particle deposition in this Thesis. A similar approach has been employed previously by [Greenfield \(1998\)](#); [Matida et al. \(2000\)](#); [Dehbi \(2008\)](#); [Horn and Schmid \(2008\)](#).

Following the work of [Dehbi \(2008\)](#), a new treatment that accounts for the inhomogeneous and anisotropic feature of fully turbulent boundary layers is adopted. In this implementation, the default model from the standard  $k - \varepsilon$  model with the assumption of isotropic turbulence is retained as long as particle is outside the turbulent boundary layer, i.e. as long as the dimensionless particle distance or the  $y^+$  value of the particle location is greater than 100. If particles move into the turbulent boundary layer, then the values of r.m.s of fluctuating fluid velocities seen by particles are modified in order to account for the anisotropic feature of boundary layer turbulence. For this, the r.m.s. values in three dimension are based on the curve fit based on DNS solutions for a channel flow with  $Re = 13000$  made by [Dehbi \(2008\)](#) as following:

$$\left. \begin{aligned} u'^+ &= \frac{\sqrt{u'^2}}{u_\tau} = \frac{0.40y^+}{1+0.0239(y^+)^{1.496}}, & \text{(streamwise)} \\ v'^+ &= \frac{\sqrt{v'^2}}{u_\tau} = \frac{0.0116(y^+)^2}{1+0.203y^++0.00140(y^+)^{2.421}}, & \text{(wall normal)} \\ w'^+ &= \frac{\sqrt{w'^2}}{u_\tau} = \frac{0.19y^+}{1+0.0361(y^+)^{1.322}}, & \text{(spanwise)} \end{aligned} \right\} \quad (3.5)$$

where  $u_\tau$  is the wall friction velocity that is acquired from the wall shear stress resolved by RANS simulations. The terms in Eq: (3.5) in turn represents the streamwise , wall normal and spanwise r.m.s values of fluctuating fluid velocities, and are graphed in Figure (3.3).

It can be observed from the above figure that the fully developed boundary layer turbulence displays strongly inhomogeneous and anisotropic features, especially for the region when  $y^+ < 10$ .

With this new boundary layer model accounting for the inhomogeneous and anisotropic fluctuating fluid velocities seen by particles, implemented as an appropriate UDF, it is possible to perform investigations of particle deposition from a fully developed turbulent pipe or channel flow. An important point of detail, not elaborated on here, is the need to convert non-dimensional r.m.s values from the local particle  $y^+$  coordinate system to the fixed computational coordinate system.

The results for particle deposition acquired from this model, based on the idea of [Kallio and Reeks \(1989\)](#) and implemented as a Fluent UDF, coupled with the standard  $k - \varepsilon$

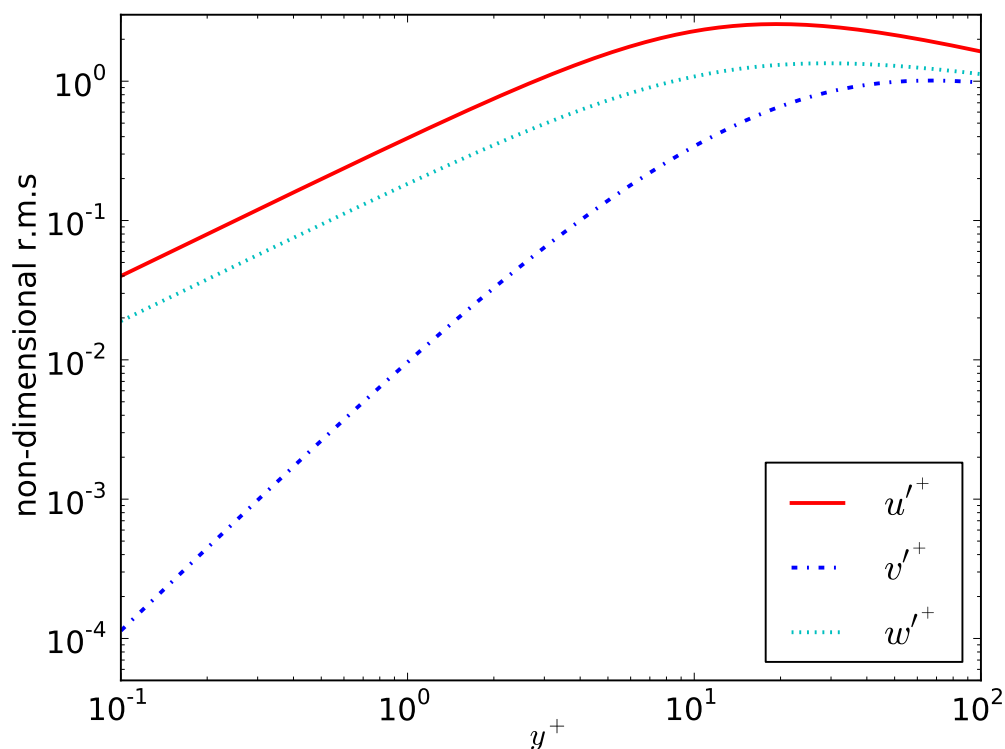


Figure 3.3: Curve fit of non-dimensional r.m.s of velocity fluctuations within turbulent boundary layers. Dehbi (2008)

model in ANSYS FLUENT are shown and compared against those from the default standard  $k - \varepsilon$  model and experiments in Figure 3.4.

It can be observed from figure 3.4 that the results for particle deposition from the improved model are beginning to show a fall-off in deposition rate with decreasing particle relaxation time in the diffusion-impaction region of the graph. Nevertheless, the method still gives an over-prediction by around three-orders of magnitude for small particles.

As a result of these disappointing preliminary results, a stand-alone, grid-free Monte Carlo approach based on Lagrangian particle tracking in a numerically generated random turbulent boundary layer proposed by Kallio and Reeks (1989) was developed in the C programming language to study particle deposition. The results for particle deposition from this stand-alone C code are shown and compared against those from the previous results obtained in this Thesis in Figure 3.5.

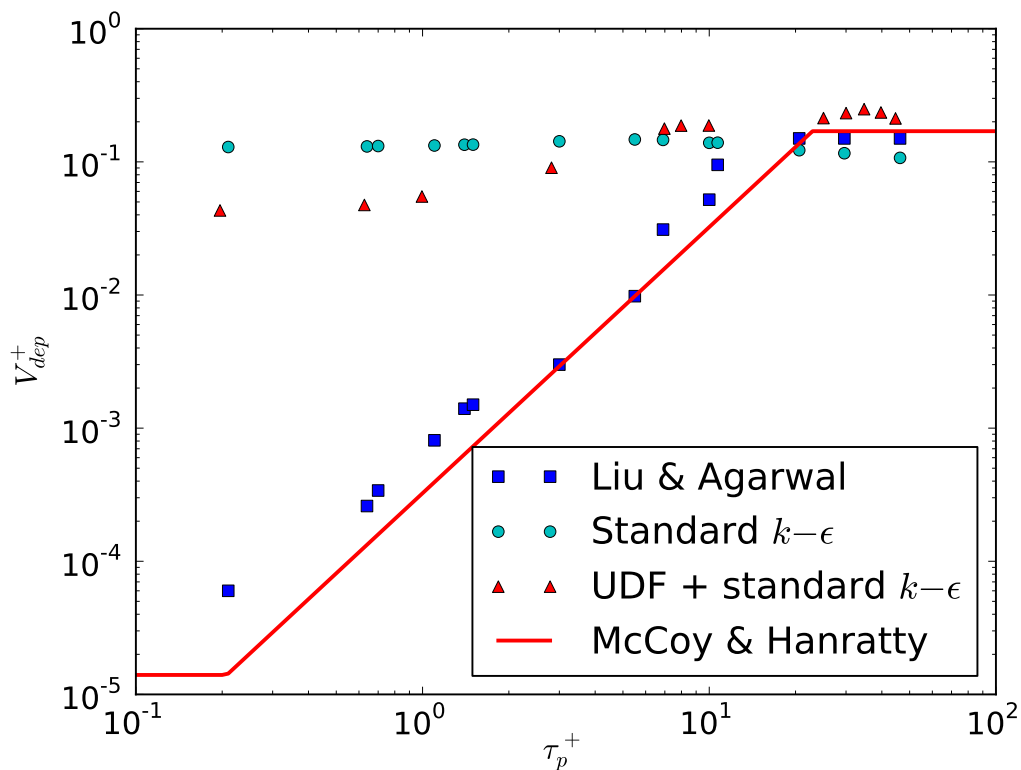


Figure 3.4: Results for particle deposition from the implementation of the DRW model of [Kallio and Reeks \(1989\)](#), implemented as a UDF coupled with the standard  $k-\epsilon$  model in ANSYS Fluent, compared against those from the default standard  $k-\epsilon$  model and experiments.

Interestingly, the stand-alone C code implementation yields better results for particle deposition than the UDF implementation, especially for small particles, i.e.  $\tau_p^+ < 10$ . Moreover, there is fair agreement between the predictions from the stand-alone C code and the experimental measurements, though the code still shows over-predictions for the smallest particles. Another point to note is that a huge discrepancy can be observed from [Figure 3.5](#) between the stand-alone C code and the UDF implementation, both of which are based principally on the same idea and ought to yield similar results.

With regard to the discrepancies and over-predictions from the second UDF implementation, possible options within the ANSYS FLUENT computational framework were to switch to another available sophisticated turbulence model (e.g. [Tian and Ahmadi \(2007\)](#); [Parker et al. \(2008\)](#)) or to change from a discrete random walk (DRW) to continuous random walk (CRW) model (e.g. [Dehbi \(2008\)](#); [Mehel et al. \(2010\)](#)). So, first an

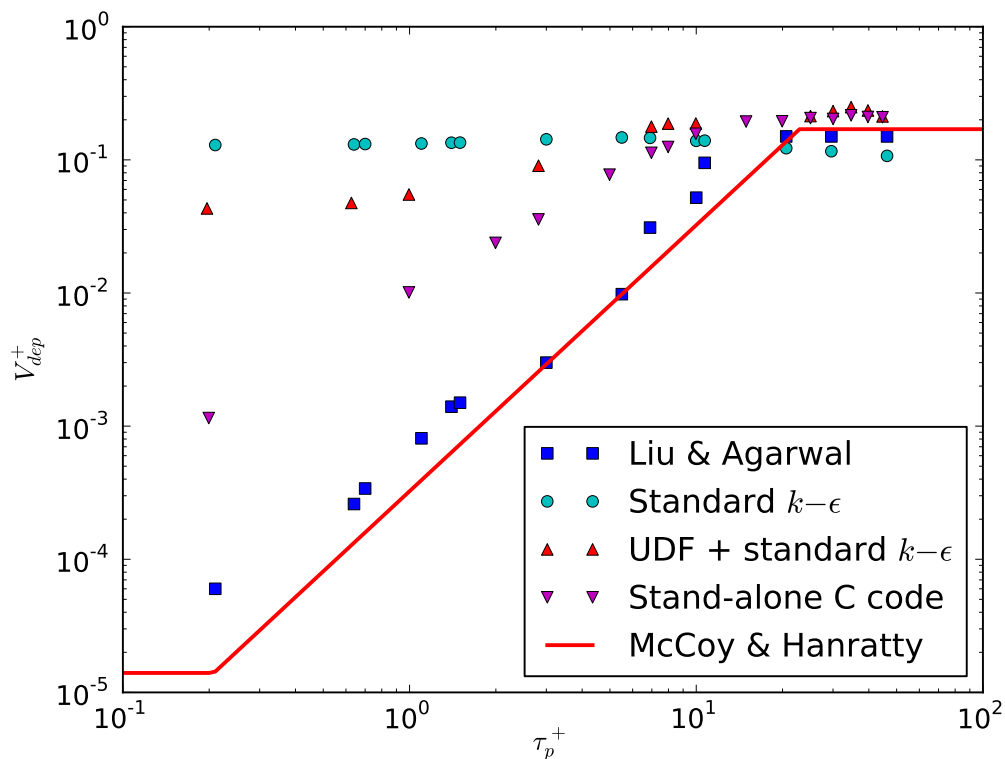


Figure 3.5: Results for particle deposition from a stand-alone C code implementation of the grid-free model of [Kallio and Reeks \(1989\)](#), compared with those from the default Fluent  $k - \epsilon$  model, a Fluent UDF implementation of the model of [Kallio and Reeks \(1989\)](#), and experiment.

successful simulation of a fully developed turbulent pipe flow are carried out with the more sophisticated Reynolds Stress Model (RSM) using a grid in which the  $y^+$  of the first cell centroid adjacent to the wall was 1. The results reported by [Parker et al. \(2008\)](#) for this case could not be reproduced in our study, which showed similar results to the UDF implementation of the model of [Kallio and Reeks \(1989\)](#). The second option of applying Continuous Random Walk models was also investigated briefly, but was not followed through because of lack of time. Instead, a more detailed investigation of the possible sources of error in Fluent's underlying DPM code was carried out, as described next.

### 3.3.3 Serious deficiencies concerning the standard Fluent Discrete Particle Model for studying particle deposition in Boundary Layers

As far as the black box of ANSYS FLUENT's inbuilt discrete phase model (DPM) is concerned, comprehensive debugging investigations with regard to the four critical points discussed in section 3.3 are carried out. The debugging work was based on the exported information associated with the tracked particle trajectories. The first serious issue discovered is concerned with the wall boundary condition handling for particle capture. DPM employs the point particle approach, which means particles have no physical dimensional size. In fact, as long as particles do not touch the wall surface, the assumption of a point particle is reasonable. On the other hand, if the particle distance away from the wall surface is less than its radius, then the particle is captured in terms of perfectly absorbing wall boundary condition adopted in the first part of this Thesis. Nevertheless, the findings demonstrate that ANSYS FLUENT assumes the point particle approach to be valid throughout all the simulation domain, right up to wall boundaries. This is a perceived failure when particles are found to become artificially trapped within less than one particle radius of the wall, and are never recorded as captured, or leave the simulation domain, even when the simulation is based on the Reynolds stresses model with enhanced wall treatment.

The failure of perfectly absorbing wall boundary condition is due to the fact that  $a_p = 0$  is assumed in FLUENT and demonstrated through Figure 3.6. A particle is released from a non-dimensional wall distance  $y^+ = 5$  from some distance away from the inlet of a fully turbulent channel flow. The particle trajectory displays random characteristics under the influence of the underlying turbulence implemented through UDF. Under the default wall boundary condition, the particle surface touches the wall, which should result in capture but, since the particle centroid does not reach the wall, it eventually coasts along the wall surface and leaves the simulation domain. This indicates that the default wall boundary condition in DPM for particle deposition fails. It is not possible to alter the capture condition directly via an UDF, so an artificial strategy of applying a large wall-directed force to any particle coming within one particle radius of a wall surface

was implemented. The effectiveness of this somewhat inelegant solution is shown by the trajectory of similar particle marked “Modified”.

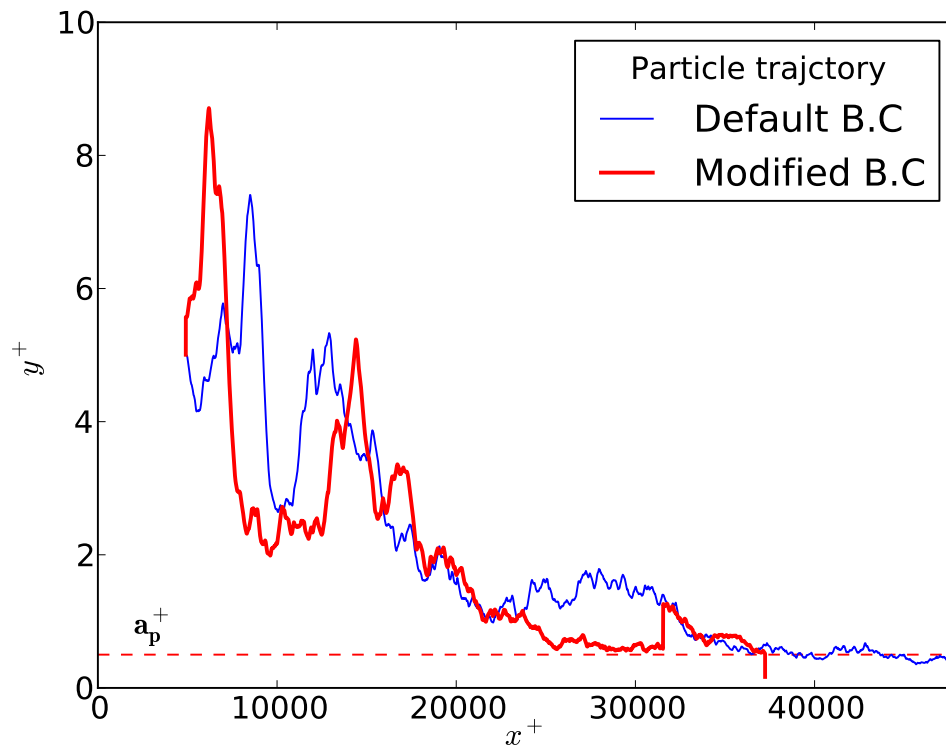


Figure 3.6: Debugging the default wall boundary condition on particle deposition, It is not possible to alter the capture condition directly via a Fluent DPM UDF, so an artificial strategy of applying a large wall-directed force to any particle coming within one particle radius of a wall surface was implemented. The effectiveness of this somewhat inelegant solution is shown by the trajectory of similar particle marked “Modified”.

Another dubious treatment in DPM is concerned with the fluid velocity interpolation from the cell centroid to the particle position. Figure 3.7 shows the interpolated mean fluid velocities seen by particles positioned from a location near the wall surface to  $y^+ = 200$ , and are compared with the standard law of the wall. The mean velocity shown is physical (not dimensionless) velocity so that the mean velocity based on the standard law of the wall is converted to physical mean velocity as well. First, It can be observed that the  $y^+$  value of the first cell centroid is around 30, which meets the requirement of standard  $k - \varepsilon$  turbulence model (e.g. Wilcox (1993)). Second, it can be seen that the mean fluid velocity at the particle position interpolated from the cell centroid is based on a linear interpolation scheme. With this interpolation scheme, the mean fluid

velocities seen by particles whose non-dimensional particle distance is less than the  $y^+$  value of the first cell centroid are greater than the values based on relation of the law of the wall. Hence, the fluid velocities seen by particles may contain physically wrong high values. In this case, the drag force experienced by particles may exhibit similarly wrong behavior, especially in the very near wall region. This may result in over prediction of particle deposition demonstrated in Figure 3.4. Once again, this issue cannot be addressed

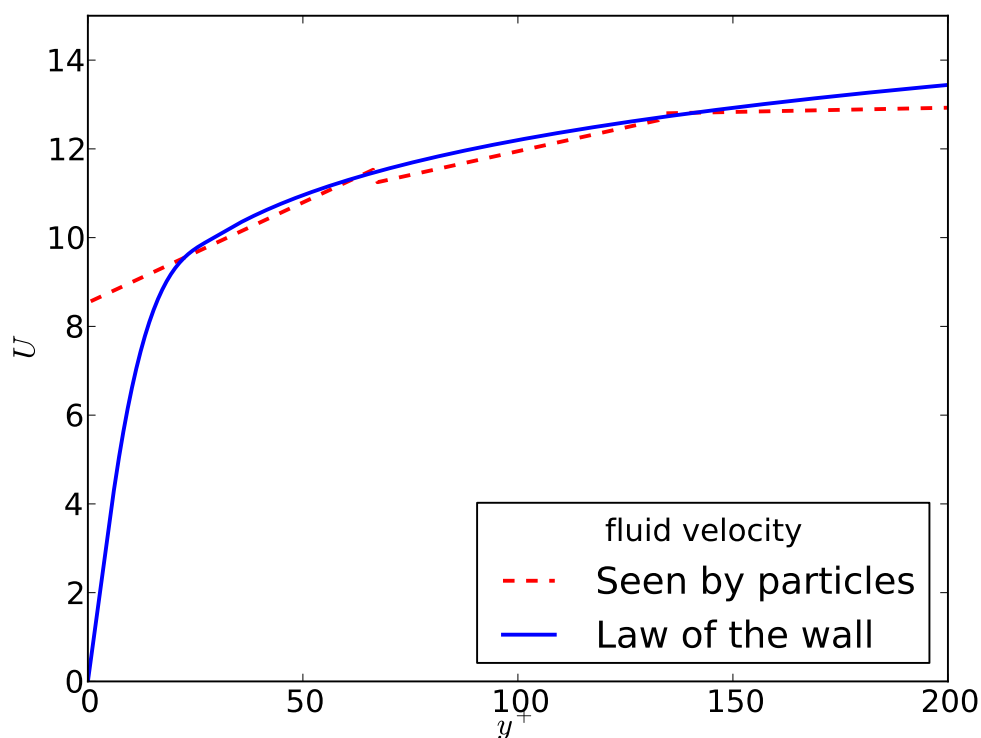


Figure 3.7: Debugging the fluid velocity interpolation scheme

within the framework of Fluent's standard DPM UDFs.

These shortcomings are not criticisms of Fluent alone. Most if not all of the commercial, general purpose, CFD codes routinely use similar approximations. An example of this for the Open Source CFD Code Saturne is shown in [Chibbaro and Minier \(2008\)](#). Two conclusions may be drawn from this. Firstly, in view of these serious but common defects, it is surprising that many recent publications seem to report satisfactory prediction of particle deposition using commercial CFD codes. Secondly, since the standard Fluent DPM UDFs cannot be used to cleanly resolve these issues, a more radical solution is

necessary. This is based on the self-developed stochastic Lagrangian particle module coupled with the steady and unsteady unstructured-grid based Navier-Stokes solver in ANSYS FLUENT. The next section will elaborate the implementation in details.

### **3.4 Self-implementation of the Lagrangian particle tracking approach in the colocated unstructured grid based Navier-Stokes solver in ANSYS FLUENT**

A prerequisite for the Lagrangian prediction of particle deposition from turbulent flows in simple or complex geometries is the accurate determination of the particle trajectories in the underlying flow field. With this purpose, a stochastic Lagrangian particle tracking module has been developed taking advantage of the data structure of the unstructured grid used by the Navier-Stokes equations solver ANSYS FLUENT. The steps involved for studying particle deposition using this module combined with ANSYS FLUENT are shown in Figure 3.8

Since this thesis involves large-scale computations, i.e. the grid used for particle deposition on tube banks in a complex flow through Large Eddy Simulations is of order  $3 \sim 4 \times 10^6$  cells, an efficient algorithm for determining the particle trajectories on such grids has to be implemented.

#### **3.4.1 A particle localization algorithm for unstructured grids**

In turbulent dispersed particulate flows, the evolution of the fluid phase is determined by solving the Navier-Stokes equations in the Eulerian framework, whilst the dispersed particulate phase is determined by the Lagrangian particle tracking approach through solving the particle equations of motion. The solution of the particle equations of motion requires evaluation of the fluid velocities at the particle position. With this aim, two procedures are performed in sequence: First, the cell in which the particle resides is to be determined. Second, the fluid velocity at the particle position is obtained via

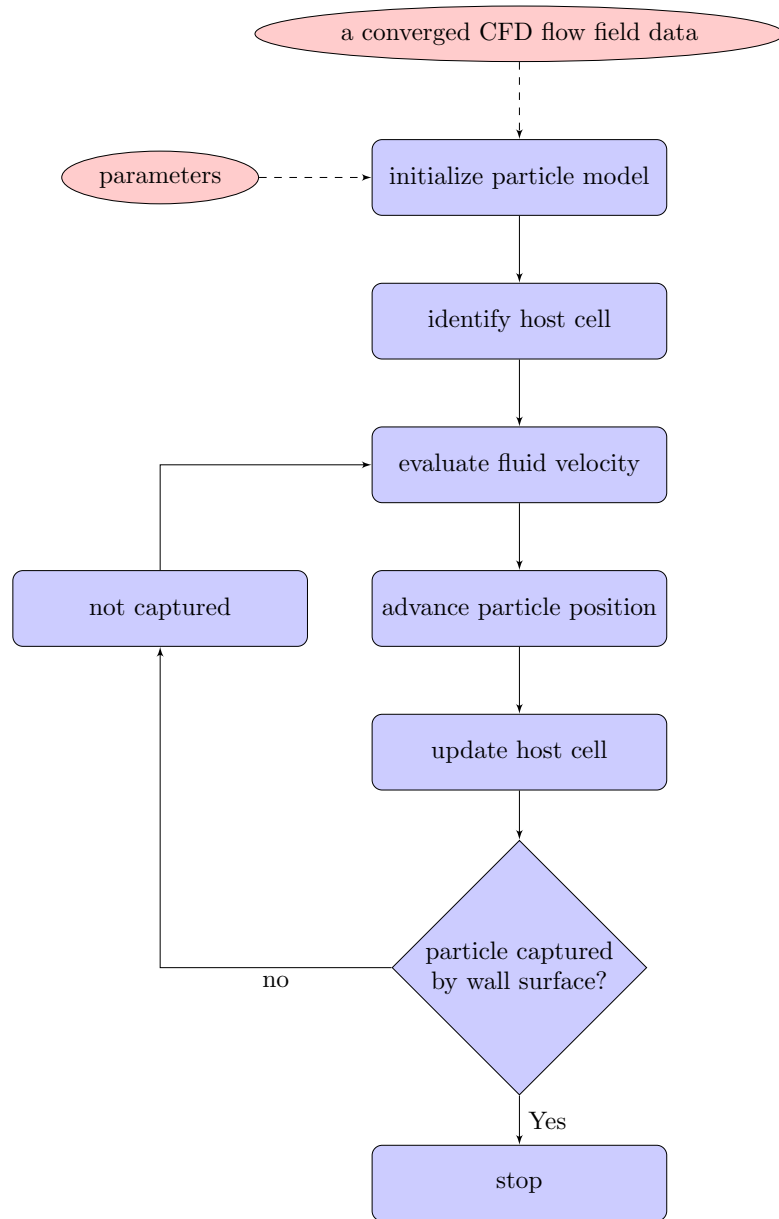


Figure 3.8: Flow chart for studying particle deposition using self-developed Lagrangian particle tracking module

an interpolation scheme from cell centroid stored values resolved by the colocated unstructured-grid based Navier-Stokes solver.

As far as the first step is concerned, a robust and efficient algorithm is required. This step is also known as the particle-localization problem. A formal statement of this is given by [Haselbacher et al. \(2007\)](#) as following: “Given a grid, a particle position, and the cell which contains that particle position, determine the cell which contains a nearby particle position”. Algorithms that solve this problem are often referred to as particle localization algorithms.

A number of particle localization algorithms have been designed for structured or unstructured two-dimensional and three-dimensional grids (e.g. [Seldner and Westermann \(1988\)](#); [Löhner and Ambrosiano \(1990\)](#); [Löhner \(1995\)](#); [Darmofal and Haines \(1996\)](#); [Zhou and Leschziner \(1999\)](#); [Apte et al. \(2003\)](#); [Haselbacher et al. \(2007\)](#)). After a careful study, the particle localization algorithm proposed by [Haselbacher et al. \(2007\)](#) was found to be applicable to the computational framework used in this thesis and was implemented independently.

#### 3.4.1.1 Identifying the initial host cell

Given the particle initial position, the search algorithm can find the cell in which the particle is currently located. For simplicity, the algorithm is described in a two-dimensional setting.

Considering a scenario as shown in [Figure 3.9](#) where a particle is located at a position  $P_p$  in a cell volume, an “in-cell-test” may be performed in terms of the following expression:

$$(\mathbf{P}_c - \mathbf{P}_p) \cdot \mathbf{n} \geq 0, \quad (3.6)$$

where  $\mathbf{P}_c$  is the centroid of the face and  $\mathbf{n}$  is the outward unit normal of the face, and both the centroid of the face and its outward unit normal are available from the data structure of the grid file. If all of the faces of a cell satisfy Equation: [3.6](#), the cell is determined to be the particle initial host cell. So, as far as identifying the initial host

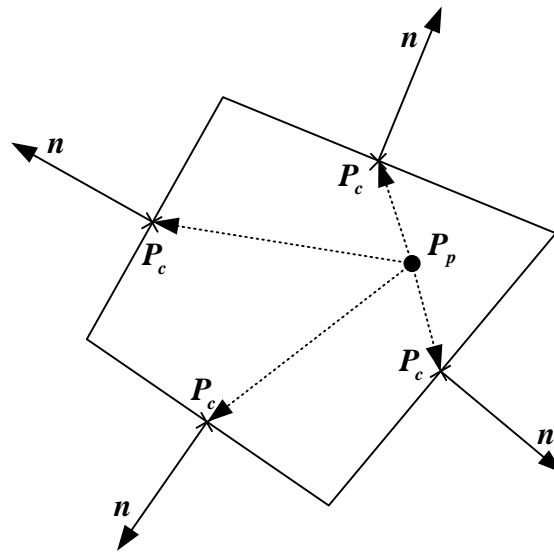


Figure 3.9: Identifying the cell which contains the particle initial position

cell is concerned, the algorithm is an exhaustive search which loops over the whole computational domain for individual particles ( $O(n^2)$ ). This is extremely expensive for a large-scale computation involving millions of particles on millions of cells. Fortunately this operation need only be called once for identifying the particle initial host cell. This also demonstrates that the computational efficiency of the particle localization algorithm is crucial to a Lagrangian particle tracking module.

#### 3.4.1.2 Updating the host cell

The central idea of the particle localization algorithm proposed by [Haselbacher et al. \(2007\)](#) is face-to-neighbouring cell search. Assuming after one integration step, we are given a situation similar to the one shown in Figure 3.10, where a particle is located at position  $\mathbf{P}_0$  and the cell  $C_0$  contains that position, we are to find the cell which contains the updated particle position  $\mathbf{P}_1$ . The displacement vector of the particle hence can be computed as  $P_1 - P_0$ . Then it is needed to find the position  $P_{inter}$  at which the displacement vector  $P_1 - P_0$  intersect with a cell face of the cell  $C_0$ . This problem can

also described as to find the  $\lambda_i \in [0, \infty)$  that satisfies

$$(\mathbf{P}_{inter} - \mathbf{P}_c) \cdot \mathbf{n} = 0, \quad \mathbf{P}_{inter} = \mathbf{P}_0 + \lambda_i(\mathbf{P}_1 - \mathbf{P}_0). \quad (3.7)$$

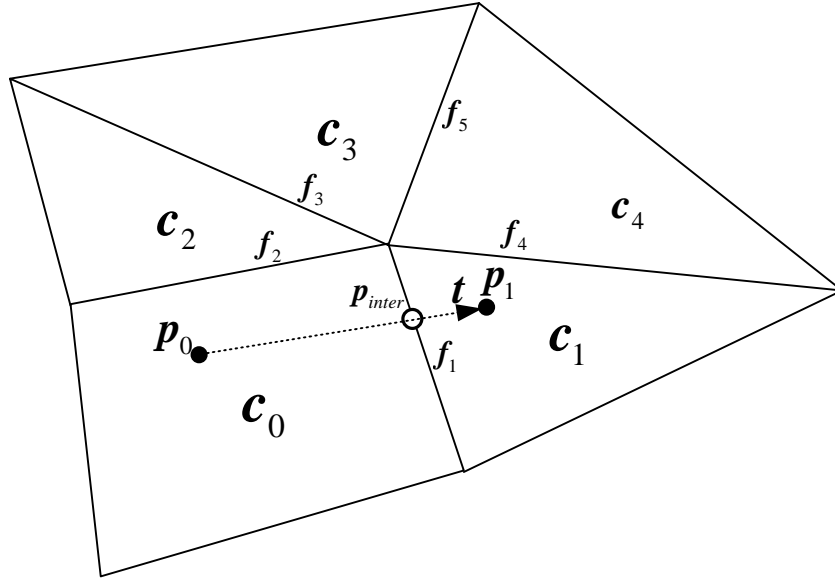


Figure 3.10: Updating the host cell through face-neighbouring cells search. (simple case)

Provided  $(\mathbf{P}_1 - \mathbf{P}_0) \cdot \mathbf{n} \neq 0$ , Equation: 3.7 may be rearranged as:

$$\lambda_i = \frac{(\mathbf{P}_c - \mathbf{P}_0) \cdot \mathbf{n}}{(\mathbf{P}_1 - \mathbf{P}_0) \cdot \mathbf{n}}, \quad ((\mathbf{P}_1 - \mathbf{P}_0) \cdot \mathbf{n} \neq 0) \quad (3.8)$$

Thus, it seems that we must calculate  $\lambda_i$  for all faces to find out which cell face the particle hits first. Nevertheless, it is instructive to analyse the sign of the numerator and denominator of the right hand side of Equation: 3.8. Taking into account the Equation: 3.6 for “in-cell-test” condition that is non-negative if the particle lies in the current cell, the denominator have to be positive in order to ensure  $\lambda_i \in [0, \infty)$ . Moreover, if the

denominator is positive, that indicates that the particle is moving toward the cell face and may hit it. Therefore, it is only necessary to work out all the  $\lambda_i$  values for those faces that satisfy  $(\mathbf{P}_1 - \mathbf{P}_0) \cdot \mathbf{n} > 0$ . Then the particle original position  $\mathbf{P}_0$  may be updated according to the smallest positive  $\lambda_{min}$  and the following expression:

$$\mathbf{P}_0 = \begin{cases} \mathbf{P}_1, & \text{if } \lambda_{min} \geq 1, \\ \mathbf{P}_{dummy} = \mathbf{P}_0 + \lambda(\mathbf{P}_1 - \mathbf{P}_0), & \text{if } \lambda_{min} = \min(1, \max[0, \lambda_i]). \end{cases} \quad (3.9)$$

Correspondingly, the host cell may be updated according to:

$$c_{new} = \begin{cases} c_{old}, & \text{if } \lambda_{min} \geq 1, \\ c_{dummy} \leftarrow f_i, & \text{if } \lambda_{min} \in [0, 1), \end{cases} \quad (3.10)$$

where  $c_{new}$  denotes the updated host cell which contains the updated  $\mathbf{P}_0$ . Here, the information on face-cell connectivity from the data structure of grid file is used to work out the neighbouring cell  $c_{dummy}$  from the intersected cell face  $f_i$ .

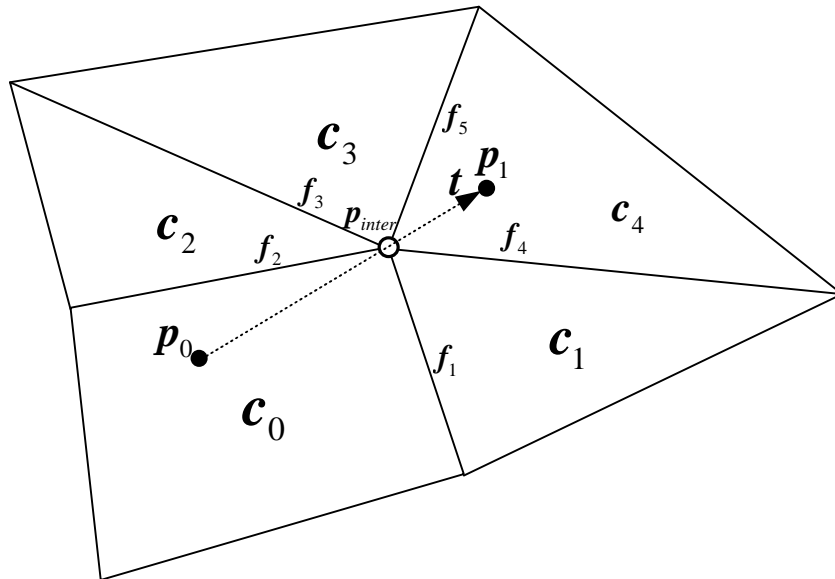


Figure 3.11: Updating the host cell through face-neighbouring cells search. (complex case)

The algorithm also works if a particle crosses to a cell which does not share a common face with the current host cell. For example, Fig 3.11 shows an extreme scenario, in which a particle pass through a vertex to another cell that has no face-cell connection information with the current host cell. With repetition of the algorithm described by Eq: (3.9-3.10), the host cell may be updated through a process

$$\mathbf{P}_0 \rightarrow \mathbf{P}_{inter} \rightarrow \mathbf{P}_{inter} \rightarrow \mathbf{P}_{inter} \rightarrow \mathbf{P}_1; \quad c_o \rightarrow f_2 \rightarrow c_2 \rightarrow f_3 \rightarrow c_3 \rightarrow f_5 \rightarrow c_4.$$

Obviously, in this case the cost of updating the host cell is slightly more expensive than the situation where a particle goes to a direct connected cell. But overall, the computational cost involved in updating host cells is of order  $O(n)$  and much less than that of initialization  $O(n^2)$ .

### 3.4.2 Velocity interpolation based on the reconstruction of velocity gradient

In a CFD modelling framework, the particle position is unlikely coincide with the point where the solution data is stored as part of the computation of the underlying flow field. The Navier-Stokes solver used in this thesis employs a colocated cell-centroid storage unstructured grid based methodology. Therefore, an appropriate numerical methods for the interpolation of the flow solutions to the particle position is required.

In previous research concerned with a dispersed particulate phase, several interpolation approaches, such as Lagrangian polynomials, shape functions, partial Hermite and spectral methods (Kontomaris et al. (1992)), cubic spine interpolation (Yeung and Pope (1988)), Taylor series expansion (Marchioli et al. (2007)) have been extensively studied and applied to the orthogonal and non-orthogonal grids typically used for simple geometries. Nevertheless, less effort has been devoted to the development of higher order interpolation scheme for non-orthogonal unstructured grids used for complex geometries. In such cases, assuming the fluid properties exhibit a linear variation, the interpolation scheme is usually linear and make use of different geometrical weighting procedures.

In applications, the interpolation methods are based on the use of local approximations to acquire estimations from the points on which the underlying solution is computed and

stored. Following [Balachandar and Maxey \(1989\)](#), a useful way to estimate the fluid velocity at the particle location in a three-dimensional domain is given by:

$$\tilde{u}_i(x_p, y_p, z_p, t) = \sum_{x_l} \sum_{y_m} \sum_{z_n} a_i(x_l, y_m, z_n; t) f_l(x_p) g_m(y_p) h_n(z_p), \quad (3.11)$$

where  $\tilde{u}_i$  indicates the estimated Cartesian velocity component at the particle position that is denoted by  $(x_p, y_p, z_p)$ . Equation (3.11) expresses the fluid velocity at the particle position as a weighted summation over the grid of basis functions  $f_l, g_m$  and  $h_n$  and coefficients  $a_i$ . The choice of the basis functions and coefficients depends on the method.

In this thesis, a quadratic fluid velocity interpolation scheme is developed. The scheme is based on least-squares representation of the multi-dimensional Taylor series expansion for the derivatives of flow variables. A similar procedure was developed by [Barth and Jespersen \(1989\)](#), whilst [Potts and Tasri](#) developed a second order extension for gradient-reconstruction of flow field variables on unstructured grids. As far as Lagrangian particle tracking is concerned, the scheme utilizes the resolved fluid velocity to calculate fluid velocity derivatives at cell centroids, which are stored in user-defined memory (UDM), for interpolation of the fluid velocity to the particle location  $(x_p, y_p, z_p)$  after the determination of particle host cell  $c_0$ . The mean fluid velocity components are acquired from the CFD calculations directly. With Taylor series expansion, a scalar value  $\tilde{\phi}$  at a cell  $c_1$  shown in a two-dimensional computational stencil depicted in Fig 3.12 may be given, to second order accuracy as:

$$\begin{aligned} \tilde{\phi}_{c_1} = & \phi_{c_0} + \left( \frac{\partial \phi}{\partial x} \right)_{c_0} \Delta x_1 + \left( \frac{\partial \phi}{\partial y} \right)_{c_0} \Delta y_1 \\ & + \frac{1}{2!} \left( \frac{\partial^2 \phi}{\partial x^2} \right)_{c_0} \Delta x_1^2 + \left( \frac{\partial^2 \phi}{\partial x \partial y} \right)_{c_0} \Delta x_1 \Delta y_1 + \frac{1}{2!} \left( \frac{\partial^2 \phi}{\partial y^2} \right)_{c_0} \Delta y_1^2. \end{aligned} \quad (3.12)$$

In order to determine the five unknown derivatives in Eq: 3.12 for a two-dimensional case, in least squares sense, the number of neighbour cells  $n$  must exceed the number of unknowns. Then an application of Eq: (3.12) to all the cells connected to the cell  $c_0$  gives a system of linear equations for the derivatives at cell  $c_0$ ,

$$\mathbf{Ax} = \mathbf{b}, \quad (3.13)$$

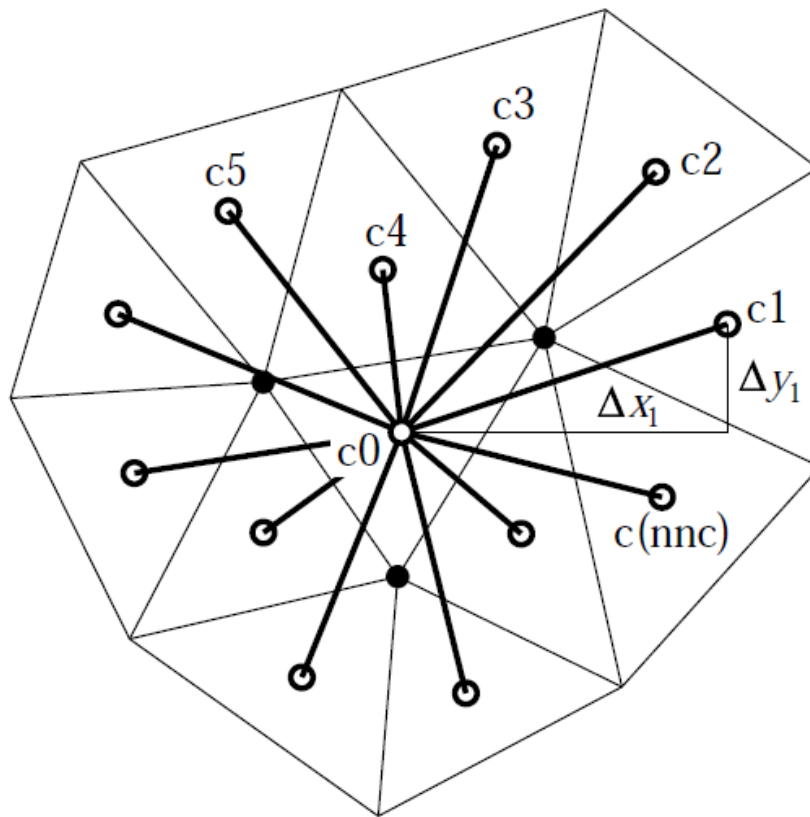


Figure 3.12: Computational stencil for the determination of second order derivatives of fluid variables.

where  $\mathbf{A}$  is a  $nnc \times 5$  matrix of geometrical terms,

$$\mathbf{A} = \begin{bmatrix} \Delta x_1 & \Delta y_1 & 0.5\Delta x_1^2 & \Delta x_1\Delta y_1 & 0.5\Delta y_1^2 \\ \Delta x_2 & \Delta y_2 & 0.5\Delta x_2^2 & \Delta x_2\Delta y_2 & 0.5\Delta y_2^2 \\ \vdots & \vdots & \vdots & \vdots & \vdots \\ \Delta x_{nnc} & \Delta y_{nnc} & 0.5\Delta x_{nnc}^2 & \Delta x_{nnc}\Delta y_{nnc} & 0.5\Delta y_{nnc}^2 \end{bmatrix} \quad (3.14)$$

$\mathbf{x}$  is a five element column vector containing derivatives,

$$\mathbf{x} = \begin{bmatrix} \left(\frac{\partial\phi}{\partial x}\right)_{c0} \\ \left(\frac{\partial\phi}{\partial y}\right)_{c0} \\ \left(\frac{\partial^2\phi}{\partial x^2}\right)_{c0} \\ \left(\frac{\partial^2\phi}{\partial x\partial y}\right)_{c0} \\ \left(\frac{\partial^2\phi}{\partial y^2}\right)_{c0} \end{bmatrix} \quad (3.15)$$

and  $\mathbf{b}$  is an  $nnc$  element column vector of scalar difference values,

$$\mathbf{b} = \begin{bmatrix} \phi_1 - \phi_0 \\ \phi_2 - \phi_0 \\ \vdots \\ \phi_{nnc} - \phi_0 \end{bmatrix} \quad (3.16)$$

Since there are usually more neighbour cells than derivatives ( $nnc > 5$ ), Eq: (3.13) may be solved for derivatives  $\mathbf{x}$  in a least squares fashion.

A general closed-form solution of Eq: (3.13) may be derived through the **QR** decomposition of  $\mathbf{A}$  using the modified Gram-Schmidt process that makes the decomposition of  $\mathbf{A}$  stable (see Galassi et al. (2009)). The general closed-form solution then allows the reconstruction of derivatives of the scalar variable  $\phi$ .

Substituting a velocity component  $U_i$  for  $\phi$ , the local fluid velocity component at the particle position for a two-dimensional case thus may be approximated from the host cell centroid according to:

$$\begin{aligned} U_i|_p &\approx U_i + \left(\frac{\partial U_i}{\partial x}\right)(x_p - x) + \left(\frac{\partial U_i}{\partial y}\right)(y_p - y) \\ &\quad + \frac{1}{2!} \left(\frac{\partial^2 U_i}{\partial x^2}\right)(x_p - x)^2 + \frac{1}{2!} \left(\frac{\partial^2 U_i}{\partial y^2}\right)(y_p - y)^2 \\ &\quad + \left(\frac{\partial^2 U_i}{\partial x\partial y}\right)(x_p - x)(y_p - y). \end{aligned} \quad (3.17)$$

In order to alleviate the computational cost associated with the interpolation of fluid velocity to particle positions and speed up particle tracking, the cell-centroid based

fluid velocity gradients may be computed and stored as UDMS before starting particle tracking. Extension of the method to three dimensions involves more lengthy algebra, but is otherwise straightforward.

### 3.4.3 An implicit ODE solver for the particle equation of motion

In addition to the equation of motion 3.3 used to determine the particle velocity, the displacement of each particle within the simulation domain is evolved according to the kinematic relation 3.2. The non-linear differential equations 3.3 and 3.2 constitute initial value problems (IVPs) that describe the velocity and displacement of a particle in turbulent flows. One hence starts at the initial particle position with all the solution information and marches the differential equation solutions forward in time.

Both equations have the general form of an IVP,

$$\mathbf{y}' = \mathbf{f}(t, \mathbf{y}), \quad 0 \leq t \leq b, \quad \mathbf{y}(0) = \mathbf{c} \quad (3.18)$$

where  $\mathbf{y}$  can represent both the particle position  $\mathbf{x}_p$  and the particle velocity  $\mathbf{u}_p$ , and for Eq: (3.18) numerical solutions may be carried out either with multistep schemes (Adams-Bashforth type) or with multistage schemes (Runge-Kutta type) at discrete time intervals.

Combined with the particle localization algorithm, a three-level, second-order accurate implicit scheme (Gear 2) is implemented as, i.e. for the particle equation of motion 3.3,

$$\sum_{j=0}^k \alpha_j \mathbf{y}_{n-j} = \Delta t \beta_0 \mathbf{f}_n, \quad (3.19)$$

where  $\alpha_0 = 1$ ,  $\alpha_1 = -\frac{4}{3}$ ,  $\alpha_2 = \frac{1}{3}$ ,  $\beta_0 = \frac{2}{3}$ , thus one may obtain

$$\mathbf{y}_n = \frac{1}{3} \left[ 2\mathbf{f}(t_n, \mathbf{y}_n) \Delta t + 4\mathbf{y}_{n-1} - \mathbf{y}_{n-2} \right]. \quad (3.20)$$

It may also be written as:

$$\mathbf{y}_{n-1} + \Delta\mathbf{y} = \frac{1}{3} \left[ 2\mathbf{f}(t_{n-1} + \Delta t, \mathbf{y}_{n-1} + \Delta\mathbf{y})\Delta t + 4\mathbf{y}_{n-1} - \mathbf{y}_{n-2} \right], \quad (3.21)$$

where  $\mathbf{f}$  may be approximated as:

$$\mathbf{f}(t_{n-1} + \Delta t, \mathbf{y}_{n-1} + \Delta\mathbf{y}) \approx \mathbf{f}(t_{n-1}, \mathbf{y}_{n-1}) + \Delta t \frac{\partial \mathbf{f}}{\partial t} \Big|_{t=t_{n-1}, \mathbf{y}=\mathbf{y}_{n-1}} + \Delta\mathbf{y} \frac{\partial \mathbf{f}}{\partial \mathbf{y}} \Big|_{t=t_{n-1}, \mathbf{y}=\mathbf{y}_{n-1}}. \quad (3.22)$$

In the case of the particle equation of motion, i.e.  $\mathbf{y} = \mathbf{u}_p$ , it may be assumed that:

$$\frac{\partial \mathbf{f}}{\partial t} = 0, \quad (3.23)$$

and  $\mathbf{u}_p$  is assumed to be independent of the particle position  $\mathbf{x}_p$ .

Since  $\mathbf{f}$  is a vector, this then requires evaluation of the Jacobian matrix  $\mathbf{f}' = \frac{\partial \mathbf{f}}{\partial \mathbf{y}}$ ,

$$\frac{\partial \mathbf{f}}{\partial \mathbf{u}_p} = \begin{bmatrix} -\frac{1}{\tau_{pc}} & 0 & 0 \\ 0 & -\frac{1}{\tau_{pc}} & 0 \\ 0 & 0 & -\frac{1}{\tau_{pc}} \end{bmatrix}, \quad (3.24)$$

where

$$\frac{1}{\tau_{pc}} = \frac{1}{\tau_p} C_D \frac{Re_p}{24}. \quad (3.25)$$

Finally as far as the particle equation of motion is concerned, i.e.  $\mathbf{y} = \mathbf{u}_p$ , it then may be discretized according to the following formula in terms of the acceleration per unit mass  $\mathbf{f}$  that is substituted by the corresponding Cartesian components,

$$\begin{bmatrix} u_p^n \\ v_p^n \\ w_p^n \end{bmatrix} = B \begin{bmatrix} \frac{2\Delta t}{3\tau_{pc}} u_f^n \\ \frac{2\Delta t}{3\tau_{pc}} v_f^n \\ \frac{2\Delta t}{3\tau_{pc}} w_f^n \end{bmatrix} + \frac{4}{3} B \begin{bmatrix} u_p^{n-1} \\ v_p^{n-1} \\ w_p^{n-1} \end{bmatrix} - \frac{1}{3} B \begin{bmatrix} u_p^{n-2} \\ v_p^{n-2} \\ w_p^{n-2} \end{bmatrix}, \quad (3.26)$$

where B is equal to  $\frac{3\tau_{pc}}{3\tau_{pc} + 2\Delta t}$ .

Similar procedure can be formulated for the lift force component in the particle equation of motion. Further, the second order Adams-Bashforth scheme is used to integrate the

particle kinematic equation 3.3.

Compared to the fourth order schemes (RK45) by [Cash and Karp \(1990\)](#) used in ANSYS FLUENT, Eq: (3.26) requires few function evaluations and consequently less computation cost for updating particle solution per time step. On the other hand, the associated storage overhead is higher as well as it needs more storage.

## 3.5 Validations

This section presents a couple of validations of the stand-alone Lagrangian particle tracking algorithm developed for replacing the default DPM provided by ANSYS FLUENT. The performance of the particle localization algorithm and of several ODE solvers is assessed by comparing the particle trajectory acquired by numerical solutions against analytical solutions.

### 3.5.1 Case 1: Irrotational straining flow

#### 3.5.1.1 The transport of a particle in a two-dimensional symmetric shear flow

The first case is concerned with the motion of particles in a two-dimensional symmetric shear flow in which the trajectory of a particle has a corresponding analytical expression (e.g. [Martin and Meiburg \(1994\)](#); [Reeks \(2005\)](#); [Ammar et al. \(2009\)](#)). The flow field is also known as an irrotational straining flow except at the origin and is given by

$$\left. \begin{aligned} u_1 &= \alpha x_1 \\ u_2 &= -\alpha x_2 \end{aligned} \right\} \quad (3.27)$$

where  $\alpha$  is a positive constant denoting the strain rate,  $-1 < x_i < 1, i = 1, 2$ . Fig 3.13 show the streamlines for a flow with  $\alpha = 2$ .

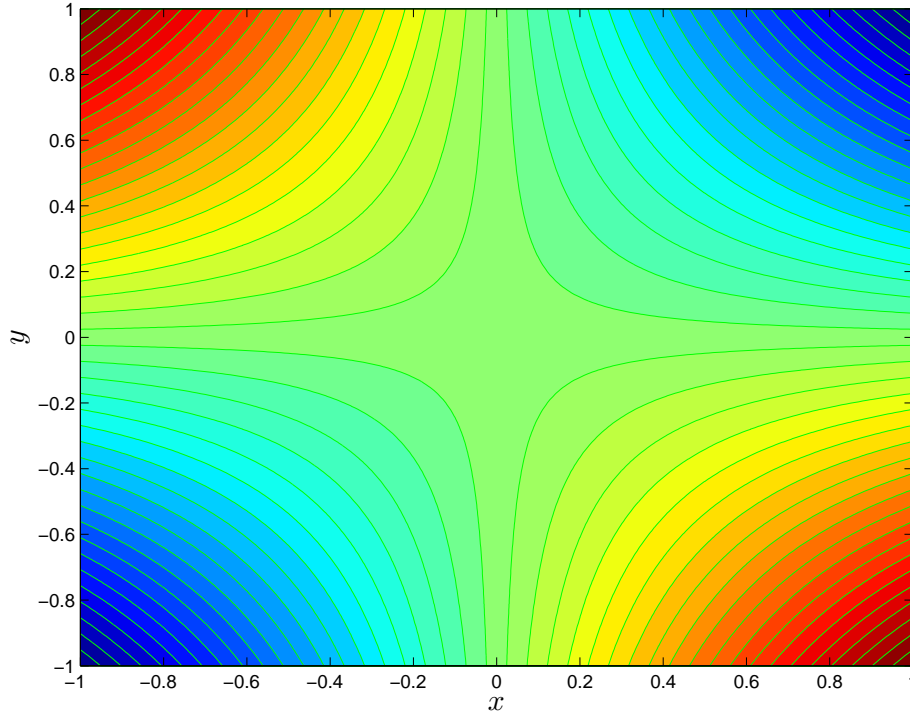


Figure 3.13: Contour of stream function of the 2-d symmetric shear flow with  $\alpha = 2$ .

The acceleration of an inertial particle in such a flow field is governed by the linear set of ordinary differential equations,

$$\left. \begin{aligned} \dot{u}_1^p &= \beta_\tau(u_1 - u_1^p) \\ \dot{u}_2^p &= \beta_\tau(u_2 - u_2^p) \end{aligned} \right\} \quad (3.28)$$

where Stokes drag is assumed and  $\beta_\tau$  is the particle response rate,

$$\beta_\tau = \frac{1}{\tau_p} \quad (3.29)$$

and  $\tau_p$  is the particle response time. In such flow, the Stokes number is defined as

$$St = \frac{\tau_p}{\frac{1}{\alpha}} = \frac{\alpha}{\beta_\tau} \quad (3.30)$$

Eq: 3.28 may be rewritten as

$$\left. \begin{aligned} \ddot{x}_1 &= \beta_\tau(\alpha x_1 - \dot{x}_1) \\ \ddot{x}_2 &= \beta_\tau(\alpha x_2 - \dot{x}_2) \end{aligned} \right\} \quad (3.31)$$

and it may be rearranged as

$$\left. \begin{aligned} \frac{1}{\beta_\tau^2} \ddot{x}_1 + \frac{1}{\beta_\tau} \dot{x}_1 - St x_1 &= 0 \\ \frac{1}{\beta_\tau^2} \ddot{x}_2 + \frac{1}{\beta_\tau} \dot{x}_2 + St x_2 &= 0 \end{aligned} \right\} \quad (3.32)$$

Eq: 3.32 is a set of homogeneous second order linear ordinary differential equation whose characteristic equation is

$$\left. \begin{aligned} \frac{1}{\beta_\tau^2} \lambda^{a2} + \frac{1}{\beta_\tau} \lambda^a - St &= 0 \\ \frac{1}{\beta_\tau^2} \lambda^{b2} + \frac{1}{\beta_\tau} \lambda^b - St &= 0 \end{aligned} \right\} \quad (3.33)$$

According to quadratic formula,

$$\left. \begin{aligned} \lambda^{a}_{1,2} &= \frac{-\beta_\tau \pm \beta_\tau \sqrt{1 + 4St}}{2} \\ \lambda^{b}_{1,2} &= \frac{-\beta_\tau \pm \beta_\tau \sqrt{1 - 4St}}{2} \end{aligned} \right\} \quad (3.34)$$

Thus, for  $x_1$ , the discriminant  $\Delta = \sqrt{1 + 4St}$  is always  $> 0$ , so

$$x_1(t) = C_1 e^{\lambda_1^a t} + C_2 e^{\lambda_2^a t} \quad (3.35)$$

Furthermore,

$$\begin{bmatrix} 1 & 1 \\ \lambda_1^a & \lambda_2^a \end{bmatrix} \begin{bmatrix} C_1 \\ C_2 \end{bmatrix} = \begin{bmatrix} x_0 \\ \alpha x_0 \end{bmatrix} \quad (3.36)$$

where  $x_0$  is the particle starting point  $x$  coordinate. We assume the particle initial velocity equal the carrier phase velocity  $\alpha x_0$  at this particle starting position. Therefore

$$C_1 = \frac{x_0(\lambda_2^a - \alpha)}{\lambda_2^a - \lambda_1^a}$$

$$C_2 = \frac{x_0(\lambda_1^a - \alpha)}{\lambda_1^a - \lambda_2^a}$$

For  $x_2$ , in the second equation, the solution depends on the Stokes number.

When  $St < 1/4$  (subharmonic),  $\Delta > 0$ , so

$$x_2(t) = C_3 e^{\lambda_1^b t} + C_4 e^{\lambda_2^b t} \quad (3.37)$$

Furthermore,

$$\begin{bmatrix} 1 & 1 \\ \lambda_1^b & \lambda_2^b \end{bmatrix} \begin{bmatrix} C_3 \\ C_4 \end{bmatrix} = \begin{bmatrix} y_0 \\ -\alpha y_0 \end{bmatrix} \quad (3.38)$$

where  $y_0$  is the particle starting point  $y$  coordinate, we assume that the particle initial velocity is equal to the carrier phase velocity  $-\alpha y_0$  at this particle starting position. Therefore,

$$C_3 = \frac{y_0(\lambda_2^b + \alpha)}{\lambda_2^b - \lambda_1^b}$$

$$C_4 = \frac{y_0(\lambda_1^b + \alpha)}{\lambda_1^b - \lambda_2^b}$$

Finally, when  $St = 1/4$  (harmonic),  $\Delta = 0$ ,  $\lambda_1^b = \lambda_2^b$

$$x_2(t) = C_5 e^{\lambda_1^b t} + C_6 t e^{\lambda_1^b t} \quad (3.39)$$

Furthermore,

$$C_5 = y_0$$

$$C_6 = -\alpha y_0 - C_5 \lambda_1^b$$

When  $St > 1/4$  (superharmonic),  $\Delta < 0$ ,

$$x_2(t) = e^{Re\{\lambda^b\}t}(C_7 \cos(Im\{\lambda^b\}t) + C_8 \sin(Im\{\lambda^b\}t)) \quad (3.40)$$

where

$$Re\{\lambda^b\} = -\frac{\beta\tau}{2}$$

$$Im\{\lambda^b\} = \frac{\beta\tau\sqrt{-1+4St}}{2}$$

$$C_7 = y_0$$

$$C_8 = \frac{-\alpha y_0 - Re\{\lambda^b\}C_7}{Im\{\lambda^b\}}$$

### 3.5.1.2 UDF patch of the two-dimensional symmetric shear flow in ANSYS FLUENT

The mesh on which this analytically derived flow field is discretised to test the tracking algorithm is shown as in Fig 3.14. The 2-d symmetric shear flow with  $\alpha = 2$  is patched through UDF in ANSYS FLUENT. For example, the macro **F\_PROFILE** (Fluent (2006)) is employed to define the velocity inlet condition for the top and bottom boundary. Then the whole flow field is initialized through the macro **DEFINE\_INIT**. Consequently, a flow solution may be obtained in this way and is shown in Fig 3.15.

### 3.5.1.3 Comparison of Lagrangian particle tracking

After obtaining a steady irrotational flow field, a superharmonic inertial particle with  $\tau_p = 1s$  is introduced into the flow. The corresponding Stokes number is equal to 2 according to Eq: 3.29. The trajectory of such a particle is obtained using the Runge-Kutta RK4 scheme and Gear2 scheme from the initially released position (0.1, 1.0), respectively. The time step used to integrate the equations is  $0.1\tau_p$ . The interpolation of fluid velocity to the particle position in such a coarse resolution is based on the reconstruction gradients of fluid velocities. Based on these settings, the RK4 solution gives an under-shoot prediction when compared against the analytical solution, whilst

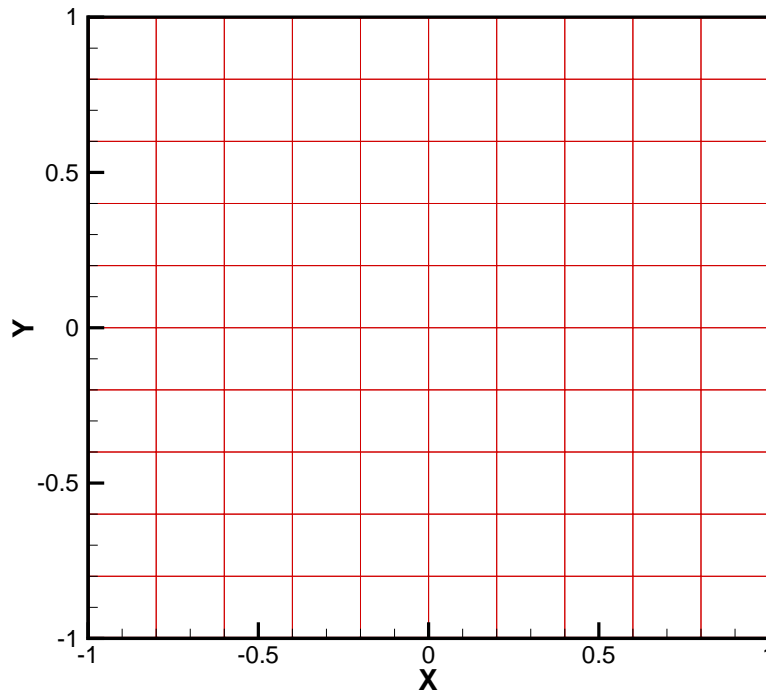


Figure 3.14: Computational mesh used for the 2-d symmetric shear flow with  $\alpha = 2$  in ANSYS FLUENT.

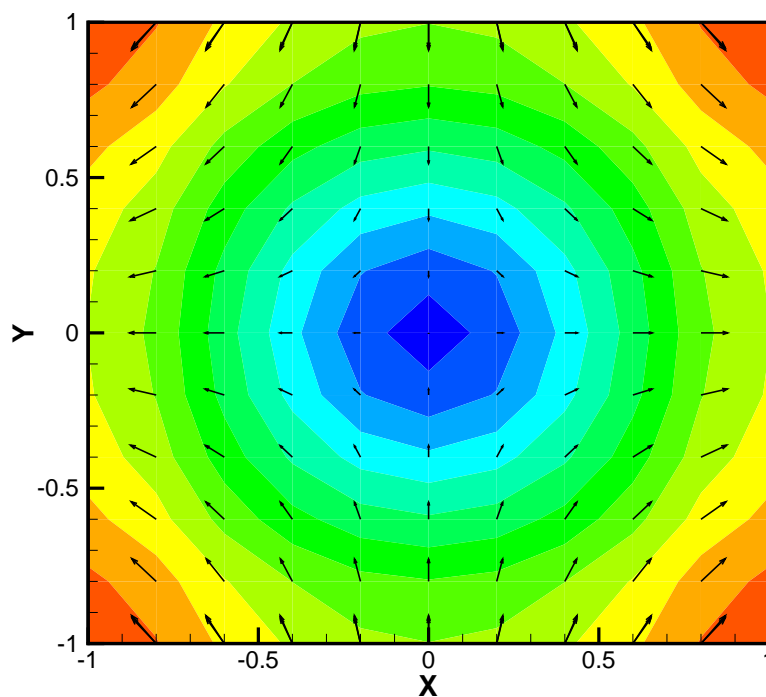


Figure 3.15: Patched contour of velocity magnitude and vector plot for the 2-d symmetric shear flow with  $\alpha = 2$  in ANSYS FLUENT.

the Gear2 solution yields an over-shoot prediction. However, the discrepancy between the Gear2 and exact solution is smaller than that between the RK4 and exact solution. Theoretically, RK4 ought to give a more accurate solution than Gear2. The bigger discrepancy shown by RK4 may result from the error accumulations in the process of interpolation of fluid velocity to the particle position. Nevertheless, Fig 3.16 indicates that Gear2 may be used to integrate the particle equation of motion with good accuracy.

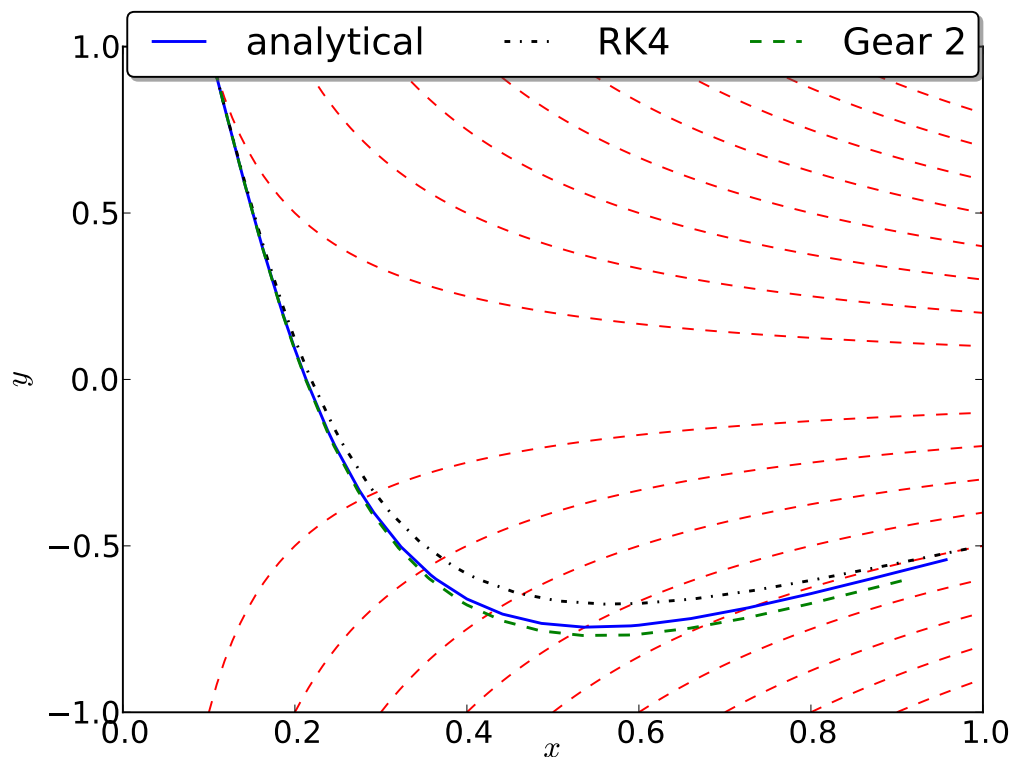


Figure 3.16: Inertial particle trajectory obtained using RK4 and Gear2 scheme and compared against the analytical solution for particle trajectory in a irrotational flow.

## 3.5.2 Case 2: Sinusoidal flow

### 3.5.2.1 The transport of a particle in a sinusoidally modulated flow

The performance of the interpolation scheme of fluid velocity is further assessed by comparing the discrepancy incurred when interpolating a prescribed sinusoidal flow field

where trajectories of fluid particles are known analytically. Such a simple test case is based on the same form of velocity field as the one from [Kontomaris et al. \(1992\)](#):

$$\left. \begin{aligned} U(x, y, z; t) &= U_0, \\ V(x, y, z; t) &= A \sin(k_l x). \end{aligned} \right\} \quad (3.41)$$

The velocity field is periodic, frozen in time. Fluid particles in this flow move sinusoidally in the  $x - y$  plane, and are uniformly translated in the  $x -$  direction. The trajectory of a fluid particle may be derived by an analytic integration of the kinematic equations ( $dx/dt = U_0, dy/dt = A \sin(k_l x)$ ). The solution in terms of particle trajectory  $(x, y)$  at time  $t$  is given by:

$$\left. \begin{aligned} x(t) &= x_0 + U_0 t, \\ y(t) &= y_0 + \frac{A}{k_l U_0} [\cos(k_l x_0) - \cos(k_l x_0 + k_l U_0 t)], \end{aligned} \right\} \quad (3.42)$$

where  $(x_0, y_0)$  denotes the particle initial position. Errors in computed fluid particle trajectory may be quantified by comparing with Eq: [3.42](#).

The parameters of the prescribed flow are chosen as  $U_0 = 5 \text{ m/s}$  and  $A = 20$ , the particle is initially placed at point  $(315.0, 315.0)$  and the wave number  $k_l = 3$  in the  $x -$  direction. The computational box has the dimension  $(630 \times 630)$  and the grid is  $(16 \times 64)$  for a simulation which resolves a wave with five nodes. The simulation procedure is basically the same as the one discussed in section [3.5.1.2](#).

The trajectory of a fluid particle in such a flow is computed numerically and compared against the exact trajectory predicted analytically. Different interpolation schemes, i.e., linear, reconstruction gradient based on ANSYS FLUENT (R\_G\_FLUENT), reconstruction gradient based on UDF (R\_G\_UDF), are applied whilst integrating Eq: [3.42](#) with a second order Adams-Bashforth scheme. Here, it is assumed that the time-stepping error is negligible with respect to the interpolation error as an appropriate time step is employed according to a complete test. It can be observed from Fig [3.17](#) that the linear interpolation scheme which is based on the derivatives of fluid velocity provided by ANSYS FLUENT gives an over-prediction for the sinusoidal variation of the particle trajectory. Whilst the second-order reconstruction gradient scheme, which is solved

via a UDF with UDM storage, reproduces the analytic trajectory almost exactly. The first-order reconstruction gradient scheme implemented via a UDF with UDM storage gives a better predictions that the reconstruction gradient scheme based on standard UDF macros. Moreover, the reconstruction gradient of ANSYS FLUENT fails to compute a smooth fluid trajectory, which implies that the interpolated velocity is not continuous across the interfaces of neighbour cells via this scheme.

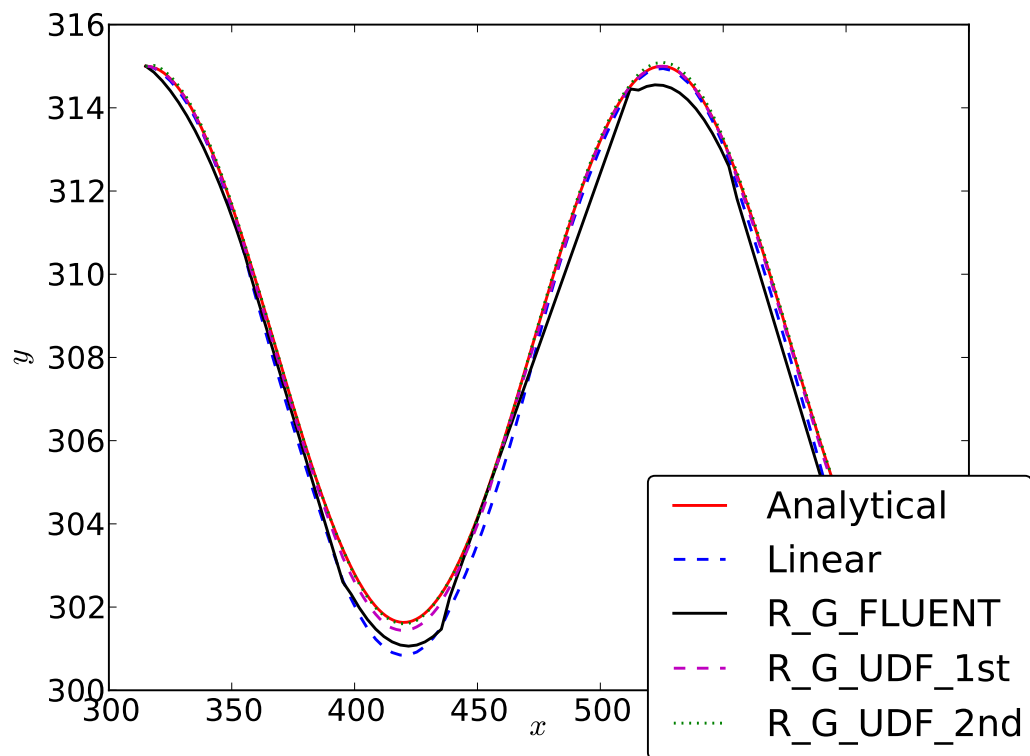


Figure 3.17: Computed errors of fluid particle trajectory obtained in a prescribed velocity field using different interpolation scheme and compared against the analytical solution.

### 3.5.3 Application of the self-implemented Lagrangian particle tracking scheme UDF to the prediction of particle deposition in turbulent boundary layers

Unlike working with ANSYS FLUENTs provided Discrete Particle Model UDF stencils, the new, self-implemented particle tracking UDF allows complete and elegant control of

issues such as particle capture conditions and velocity interpolation to the current particle position. Even with the new velocity interpolation scheme in place, however, it was not possible to achieve good agreement with the stand-alone C-code implementation of the Kallio and Reeks method. The problem is that the deposition curve is extremely sensitive to the near-wall profile for both turbulent velocity perturbations and the mean velocity profile. The latter is not resolved to sufficient accuracy even with the new interpolation scheme and near wall grid refinement. The solution, therefore, was to replace numerical interpolation of the carrier field velocity in the near-wall region ( $y^+ < 35$ ) with a curve-fit based on the law of the wall, in a similar manner to the curve-fits used for the perturbation  $v'$  between  $y^+ = 0$  and  $y^+ = 200$ . This modification could easily be made in the new particle tracking implementation, and resulted in excellent agreement of deposition prediction with the stand-alone C code results based on the idea of [Kallio and Reeks \(1989\)](#), as shown in [Figure 3.18](#). Despite this agreement between the two implementations, both show great deviation from the experimental Liu and Agarwal data than suggested by the original calculations of Kallio and Reeks. The reasons for this are not known.

The UDF implementation has the major advantage, over the stand-alone C code, that it can be used for complex duct geometries, rather than just the simple, flat plate test case.

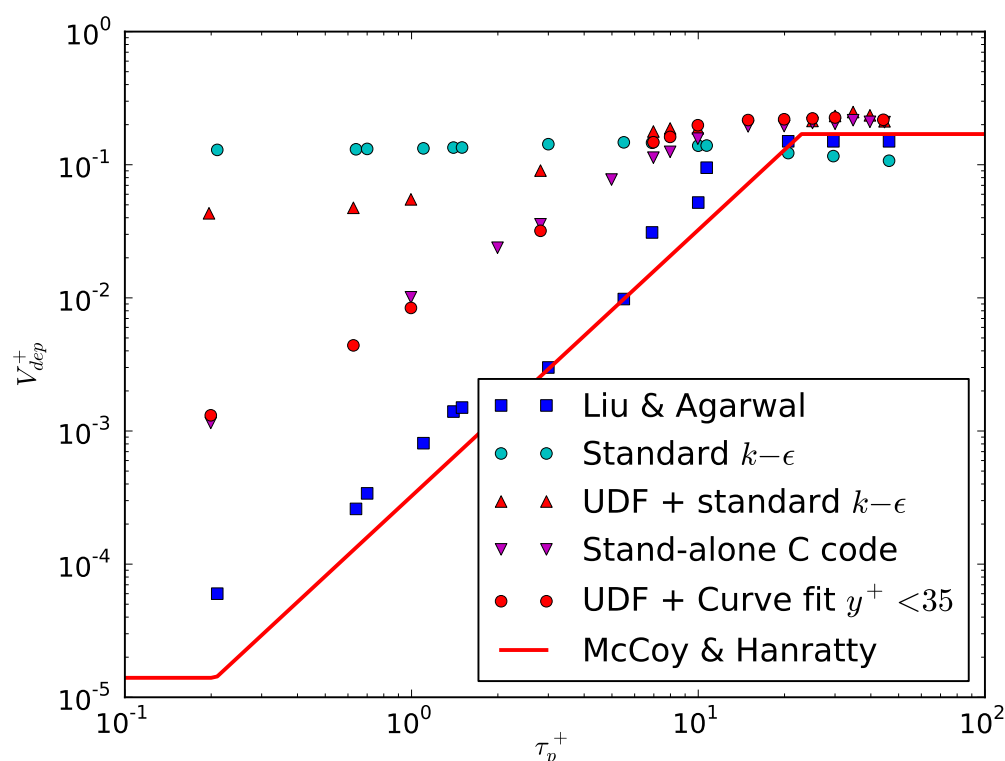


Figure 3.18: Comparison of particle deposition prediction from various implementations of the discrete random walk model, based on the basic model of [Kallio and Reeks \(1989\)](#)

### 3.6 Parallelization of the stochastic Lagrangian particle tracking model using MPI

With the aim of tackling the more computationally challenging problem of particle deposition on heat-exchanger tube banks in turbulent flows with Large Eddy Simulations (LES) of the carrier phase, and in order to take advantage of the available high performance computational facilities in the author's lab, the Lagrangian particle tracking module has been parallelized using the publicly available Message Passing Interface (MPI) library ([MPI Forum \(2009\)](#)) and further coupled with the parallel Navier-Stokes solver in ANSYS FLUENT. It is capable of parallel and/or distributed computation for particle tracking with or without linking to the Navier-Stokes solver in ANSYS FLUENT.

From the computational perspective, Lagrangian particle tracking models are very different from Eulerian models for the carrier phase. Instead of solving a set of partial

differential equations, the trajectories of many particles are obtained by solving the associated governing ordinary differential equations. To some degree, the acquisition of statistically significant predictions of the dispersed particle phase via Lagrangian particle tracking depends mainly on the number of particles.

Parallelization of the Eulerian model for the CFD flow solution, as implemented by ANSYS FLUENT, follows a very different paradigm. Here the computational mesh overlaid on the physical solution domain is divided into a number of connected partitions, each containing an approximately equal number of cells. Each computer node in the parallel machine then takes responsibility for solution of the discretised Navier-Stokes equations in one partition, with common data at the partition boundaries being shared between the appropriate nodes by MPI communication after each solve iteration. Solution data for each partition is only held locally by its associated compute node, which has implications for particle tracking, as particles cross from one partition to another. Figure 3.19 shows a typical one-dimensional computational decomposition used for parallel solution.  $x$  denotes the streamwise (flow) direction, and  $y$  denotes the wall-normal direction and  $z$  the spanwise direction. Particles might migrate from one partition to another partition in the  $z$  direction, and this leads to particle data communications between different computer nodes. The description here is necessarily simplified for brevity: for a more detailed discussion, the reader is referred to the ANSYS FLUENT manuals.

This section focuses on the description of an abstract data type for particles, the procedures for parallelizing the Lagrangian stochastic module based on the standard MPI that supports parallel I/O and block data-communications, on grids used for the simulation of the carrier phase. Moreover, It will show the corresponding performance on a Linux cluster with 20 single CPU nodes based on a parallel random number generator (RNG) SPRNG and the trajectory of a specimen particle in a Large Eddy Simulation (LES) of a channel flow.

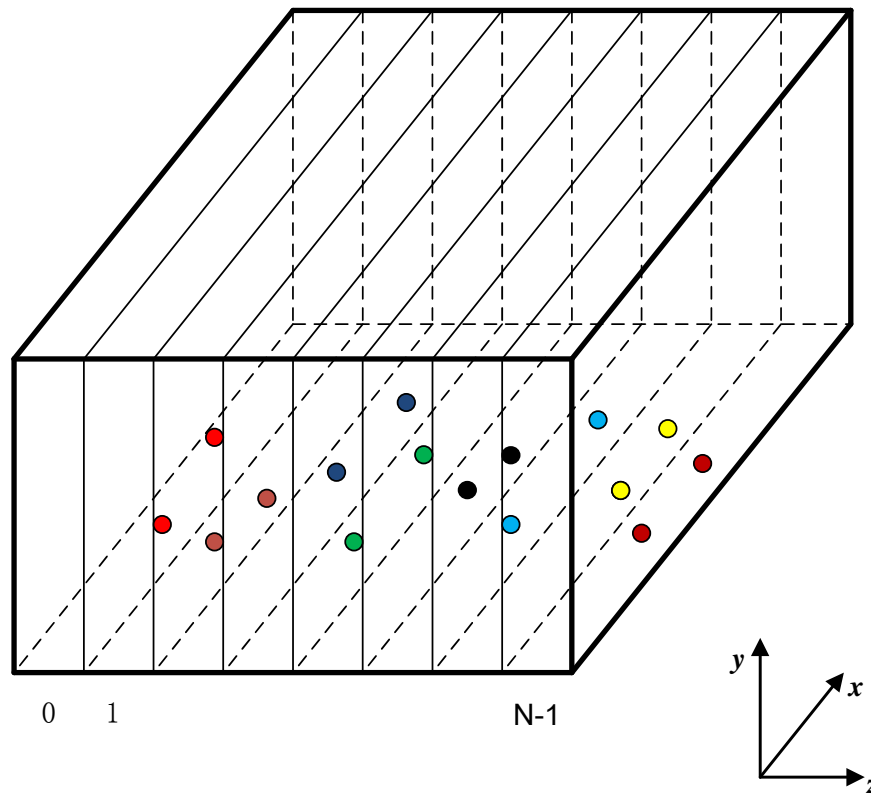


Figure 3.19: One-dimensional computational domain decomposition

### 3.6.1 An abstract data type for particles

Lagrangian particle tracking models are generally well suited for parallelization. The trajectory of particles may be computed independently since they represent independent realizations within a large number of particles. Accordingly, many computation nodes may participate in the computation without data communication with each other. Nevertheless, one data transfer between neighbour partitions in the CFD modelling framework for the carrier phase may be needed to finish a complete realization of a particle trajectory. This is clearly the case when the particle trajectory crosses a boundary between two different CFD mesh partitions. Then the challenge in parallelizing Lagrangian particle tracking model in a CFD modelling framework is that the number of particles to be transferred between grid partitions may vary both in space and time. Hence, an abstract data type for particles is designed as follows:

Listing 3.1: The abstract data type for particles

```
typedef struct particle{
    long ID;          /* identifier for particle */
    int my_rank;      /* identifier for current sub-process/computer node */
    double p_p0[dim]; /* need to update host cell */
    double p_p1[dim];
    double v0[dim];
    double v1[dim];
    double v[dim];
    double a_p[dim];
    long host_cell;
    long old_cell;
    ...
    struct particle *next; /* point to next particle */
}particle;
```

The data structure of linked-list is employed to contain the particles residing on each computer node. Therefore, a pointer may be used to iterate down the particle list. In order to enhance the efficiency of particle tracking and reduce the cost associated with pointer search operations along the particle list, a larger number of particles may be simulated via splitting the particle list into several sub- linked-lists of equal length.

### 3.6.2 The procedure for parallelization

The parallelization of the Lagrangian particle models may be described as follows:

1. If a particle is detected to cross the boundary of the current CFD mesh partition, which results from decomposition of the computational domain in the  $z$  – direction, the index of the corresponding destination partition is determined, the counter of particles to be sent is incremented and the data associated with the particle is stored, ready for transmission, and is then removed from the current particle link list, and the particle is flagged for transfer.
2. Once all particles have been either located or flagged for transfer, the total number of particles which need to be transferred between all partitions is determined via a reduction operation.

3. Tests are carried out to check if the number of particles to be transferred is non-zero. If so each node sends messages containing the number of particles to be transferred for every partition boundary to nodes that contains the corresponding neighbour partition. These messages are clearly different for each sending node. Hence memory has to be allocated to contain the particle data to be sent (e.g. particle ID, velocity and position coordinates) ready for dispatch via the appropriate MPI function call. The migrated particles are removed from the particle link list. On receiving the number of particles to receive, each node allocates corresponding receive buffer memory.
4. The actual data transfer occurs. Then receiving nodes need to unpack the received particle data, using the particle-in-cell test to determine the host cell on the new partition, then appending the data to the particle linked-list on the current node.
5. Finally, the memory allocated for send and receive buffers is freed.

### 3.6.3 Test of speed-up performance and particle data transfer

The speed-up performance of the Lagrangian particle module is tested using 1, 2, 4, and 8 CPUs from a Linux cluster consisting of 20 single CPU nodes. The test is not linked to the Navier-Stokes solver in ANSYS FLUENT so it does not involve communications of particle data. A parallel random number generator SPRNG ([Mascagni and Srinivasan \(2000\)](#)) is adopted for extending the Lagrangian particle module to a stochastic one. The performance of speed-up for the test is shown in Fig 3.20. Finally, a test was carried out to verify the communication of particle data between different computational partitions when the stochastic parallel Lagrangian particle tracking module is coupled with a Large Eddy Simulation of channel using ANSYS FLUENT. Two specimen particles meander in the channel and migrates between different computational partitions as shown in Fig 3.21.

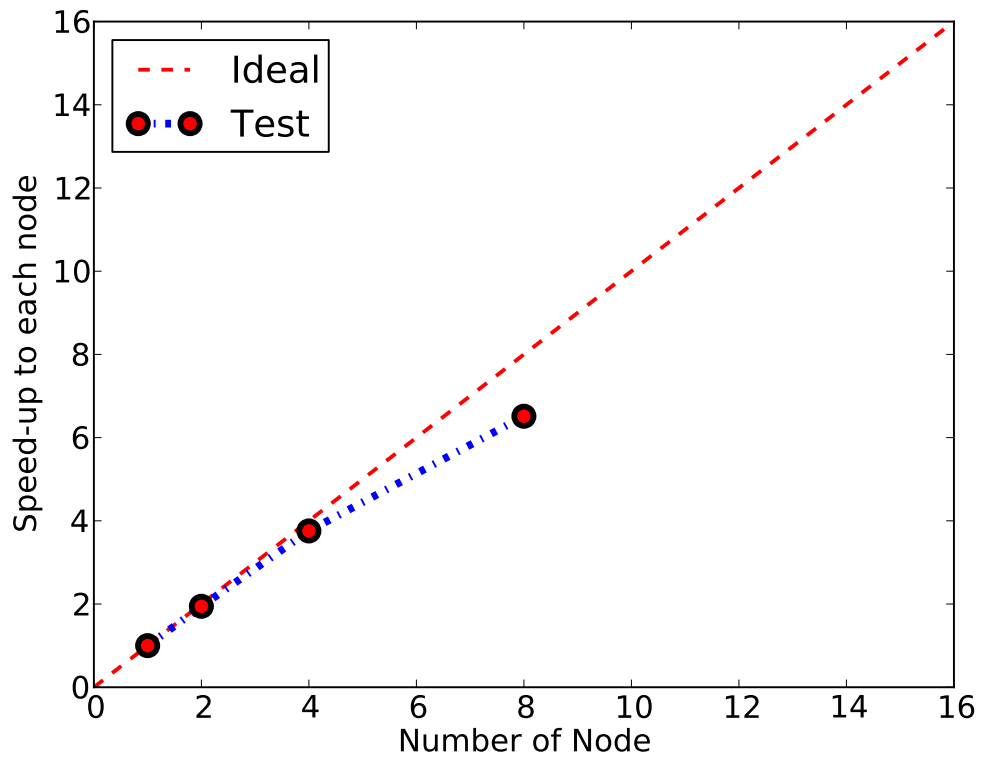


Figure 3.20: Test of speed-up performance to each node with  $10^6$  particles.

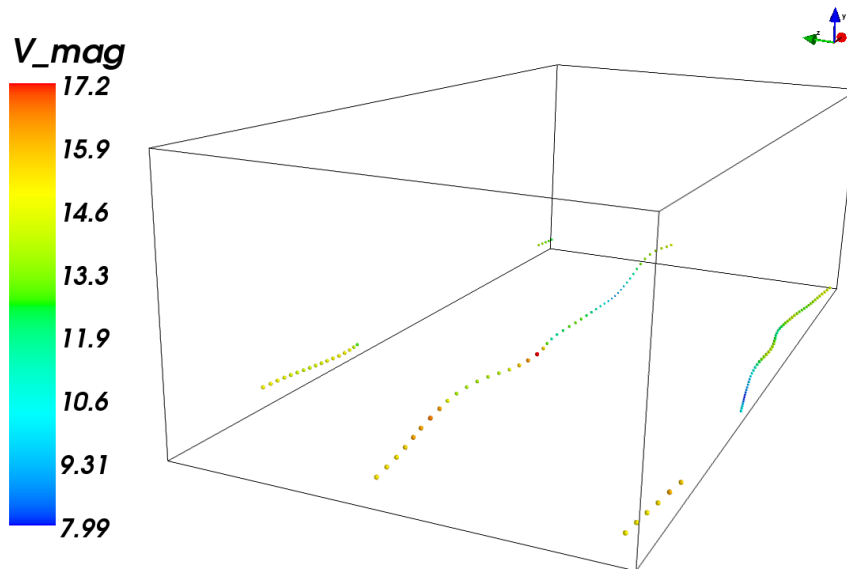


Figure 3.21: Trajectory of specimen particles computed by the stochastic parallel Lagrangian particle tracking module coupled with a Large Eddy Simulation of a channel flow.

### 3.7 Conclusion

In this chapter, first the background of particle deposition in turbulent flows is reviewed. Then a preliminary test applying the default DPM in FLUENT is presented to the problem of particle deposition from a flat plate turbulent boundary layer. The results completely fail to capture the experimentally determined variation in deposition with particle response time. FLUENT's DPM UDFs were then used to replace CFD calculated turbulent velocity fluctuations with a curve-fit to DNS data for the wall region  $0 < y^+ < 200$ , following [Kallio and Reeks \(1989\)](#). This produced only a minor improvement in deposition prediction. Two serious deficiencies associated with FLUENT's standard DPM when applied to particle deposition in boundary layers were then discovered, i.e., the point particle approximation is assumed for the particle-wall interaction and the linear velocity interpolation for the fluid velocity to the particle location violates the no-slip condition, which were not correctable using the standard DPM UDF framework. Therefore, a self-written large-scale parallel stochastic Lagrangian particle tracking module was developed and fully coupled with the steady and unsteady Navier-Stokes equations solver in FLUENT. It involves the implementation of a robust and efficient particle localization algorithm for unstructured grids, an implicit ODE solver (Gear2) for the particle equation, and a second order accurate scheme for interpolation of the fluid to the particle position. The module is validated by comparing particle trajectories acquired by numerical calculations against the exact solutions. This module is then applied to the problem of particle deposition in a turbulent boundary layer on a flat plate, and it is additionally found necessary to replace the interpolation of fluid velocity close to the wall ( $y^+ < 35$ ) by a curve-fit based on the law of the wall to get good agreement with a stand-alone C code, based on the model of [Kallio and Reeks \(1989\)](#). This new implementation, using ANSYS FLUENT, is applicable to prediction of particle deposition in more general, complex geometry problems. Finally, the parallelization of the module using the MPI library is discussed. Further, It has been demonstrated that the parallelized code fully couples with the Large Eddy Simulation model in ANSYS FLUENT. This is a significant advance, since, up to at least Fluent version 13.0, the standard DPM model is not compatible with Fluent's LES model.

## REFERENCES

- Y. Ammar, University of Newcastle upon Tyne. School of Mechanical, and Systems Engineering. *Turbulent agglomeration and break-up of nuclear aerosols*. University of Newcastle upon Tyne, 2009.
- S. V. Apte, K. Mahesh, P. Moin, and J. C. Oefelein. Large-eddy simulation of swirling particle-laden flows in a coaxial-jet combustor. *International Journal of Multiphase Flow*, 29(8):1311–1331, 2003.
- S. Balachandar and M. R. Maxey. Methods for evaluating fluid velocities in spectral simulations of turbulence. *Journal of Computational Physics*, 83(1):96–125, 1989.
- T. J. Barth and D. C. Jespersen. The design and application of upwind schemes on unstructured meshes. In *27th Aerospace Sciences Meeting*, volume 89, 1989.
- J. R. Cash and A. H. Karp. A variable order Runge-Kutta method for initial value problems with rapidly varying right-hand sides. *ACM Transactions on Mathematical Software (TOMS)*, 16(3):201–222, 1990.
- M. Chen and J. B. McLaughlin. A new correlation for the aerosol deposition rate in vertical ducts. *Journal of Colloid and Interface Science*, 169(2):437–455, 1995.
- S. Chibbaro and J. P. Minier. Langevin PDF simulation of particle deposition in a turbulent pipe flow. *Journal of Aerosol Science*, 39(7):555–571, 2008.
- D. L. Darmofal and R. Haimes. An analysis of 3d particle path integration algorithms. *Journal of Computational Physics*, 123(1):182–195, 1996.

- C. N. Davies. Deposition of aerosols from turbulent flow through pipes. *Proceedings of the Royal Society of London. Series A, Mathematical and Physical Sciences (1934-1990)*, 289(1417):235–246, 1966.
- A. Dehbi. A CFD model for particle dispersion in turbulent boundary layer flows. *Nuclear Engineering and Design*, 238(3):707–715, 2008.
- A. Fluent. 6.3 udf manual. *Lebanon, New Hampshire, USA: Fluent Inc*, 2006.
- A. Fluent. 12.0 documentation. *ANSYS Inc*, 2009.
- S. K. Friedlander and H. F. Johnstone. Deposition of suspended particles from turbulent gas streams. *Industrial & Engineering Chemistry*, 49(7):1151–1156, 1957.
- M. Galassi, J. Davies, J. Theiler, B. Gough, G. Jungman, P. Alken, M. Booth, and F. Rossi. GNU Scientific Library Reference Manual, network theory ltd, 2009.
- C. Greenfield. *Numerical modelling of transport phenomena in reactors*. PhD thesis, Bristol Univesity, 1998.
- A. Guha. Transport and deposition of particles in turbulent and laminar flow. *Annual Review of Fluid Mechanics*, 40:311–341, 2008.
- A. Haselbacher, F. M. Najjar, and J. P. Ferry. An efficient and robust particle-localization algorithm for unstructured grids. *Journal of Computational Physics*, 225(2):2198–2213, 2007.
- M. Horn and H. J. Schmid. A comprehensive approach in modeling lagrangian particle deposition in turbulent boundary layers. *Powder Technology*, 186(3):189–198, 2008.
- G. A. Kallio and M. W. Reeks. A numerical simulation of particle deposition in turbulent boundary layers. *International Journal of Multiphase Flow*, 15(3):433–446, 1989.
- K. Kontomaris, T. J. Hanratty, and J. B. McLaughlin. An algorithm for tracking fluid particles in a spectral simulation of turbulent channel flow. *Journal of Computational Physics*, 103(2):231–242, 1992.
- B. Y. H. Liu and J. K. Agarwal. Experimental observation of aerosol deposition in turbulent flow. *Journal of Aerosol Science*, 5(2):145–148, IN1–IN2, 149–155, 1974.

- R. Löhner. Robust, vectorized search algorithms for interpolation on unstructured grids. *Journal of Computational Physics*, 118(2):380–387, 1995.
- R. Löhner and J. Ambrosiano. A vectorized particle tracer for unstructured grids. *Journal of Computational Physics*, 91(1):22–31, 1990.
- C. Marchioli, V. Armenio, and A. Soldati. Simple and accurate scheme for fluid velocity interpolation for eulerian-lagrangian computation of dispersed flows in 3d curvilinear grids. *Computers & Fluids*, 36(7):1187–1198, 2007.
- J. E. Martin and E. Meiburg. The accumulation and dispersion of heavy particles in forced two-dimensional mixing layers. i. the fundamental and subharmonic cases. *Physics of Fluids*, 6(3):1116–1132, 1994.
- M. Mascagni and A. Srinivasan. Algorithm 806: Sprng: A scalable library for pseudo-random number generation. *ACM Transactions on Mathematical Software (TOMS)*, 26(3):436–461, 2000.
- E. A. Matida, K. Nishino, and K. Torii. Statistical simulation of particle deposition on the wall from turbulent dispersed pipe flow. *International Journal of Heat and Fluid Flow*, 21(4):389–402, 2000.
- D. D. McCoy and T. J. Hanratty. Rate of deposition of droplets in annular two-phase flow. *International Journal of Multiphase Flow*, 3(4):319–331, 1977.
- A. Mehel, A. Tanière, B. Oesterlé, and J. R. Fontaine. The influence of an anisotropic langevin dispersion model on the prediction of micro-and nanoparticle deposition in wall-bounded turbulent flows. *Journal of Aerosol Science*, 41(8):729–744, 2010.
- MPI Forum. MPI: A Message-Passing Interface Standard. Version 2.2, September 4th 2009. available at: <http://www.mpi-forum.org> (Dec. 2009).
- C. Narayanan, D. Lakehal, L. Botto, and A. Soldati. Mechanisms of particle deposition in a fully developed turbulent open channel flow. *Physics of Fluids*, 15(3):763–775, 2003.
- P. G. Papavergos and A. B. Hedley. Particle deposition behaviour from turbulent flows. *Chemical Engineering Research and Design*, 62:275–95, 1984.

- S. Parker, T. Foat, and S. Preston. Towards quantitative prediction of aerosol deposition from turbulent flows. *Journal of Aerosol Science*, 39(2):99–112, 2008.
- I. Potts and A. Tasri. Accuracy of Compact-Stencil Interpolation and Differentiation Algorithms for Unstructured Mesh Navier-Stokes Solvers. *Unpublished work*.
- M. W. Reeks. On model equations for particle dispersion in inhomogeneous turbulence. *International Journal of Multiphase Flow*, 31(1):93–114, 2005.
- D. Seldner and T. Westermann. Algorithms for interpolation and localization in irregular 2d meshes. *Journal of Computational Physics*, 79(1):1–11, 1988.
- A. Soldati and C. Marchioli. Physics and modelling of turbulent particle deposition and entrainment: Review of a systematic study. *International Journal of Multiphase Flow*, 35(9):827–839, 2009.
- L. Tian and G. Ahmadi. Particle deposition in turbulent duct flows - comparisons of different model predictions. *Journal of Aerosol Science*, 38(4):377–397, 2007.
- D. C. Wilcox. *Turbulence Modeling for CFD*. DCW Industries Inc., La Cañada, CA, 1993.
- P. K. Yeung and S. B. Pope. An algorithm for tracking fluid particles in numerical simulations of homogeneous turbulence. *Journal of Computational Physics*, 79(2):373–416, 1988.
- J. Young and A. Leeming. A theory of particle deposition in turbulent pipe flow. *Journal of Fluid Mechanics*, 340:129–159, 1997.
- Q. Zhou and M. A. Leschziner. An improved particle-locating algorithm for eulerian-lagrangian computations of two-phase flows in general coordinates. *International Journal of Multiphase Flow*, 25(5):813–825, 1999.

# Chapter 4

## A stochastic quadrant model for particle deposition

### 4.1 Introduction

In this chapter, we propose a simple but more promising stochastic quadrant model of coherent structures for heavy particle deposition, which was inspired by the quadrant analysis proposed by [Willmarth and Lu \(1972\)](#). It is another way to model deposition of heavy particles within fully developed turbulent boundary layers that hopefully can add some further insight or give new ideas to improve the deposition prediction of heavy particles.

From the perspective of numerical modelling, the deposition of particle deposition from turbulent flows is a much studied topic. [Friedlander and Johnstone \(1957\)](#) and [Davies \(1966\)](#) developed gradient diffusion/free-flight theories where the concept of particle stopping distance was proposed. However, in order to obtain agreement between theory and experiments, the initial particle free flight velocity had to be adjusted to get good agreement with the experimental data. [Hutchinson et al. \(1971\)](#) and [Kallio and Reeks \(1989\)](#) employed the Monte-Carlo based Lagrangian particle tracking method for calculating particle deposition. In the work of [Kallio and Reeks \(1989\)](#) the turbulent boundary layer was described as a randomized eddy field with corresponding velocity

and time scales as functions of the particle distance away from the wall. [Swales and Reeks \(1994\)](#) proposed to use the kinetic equation developed by [Reeks \(1991\)](#) as a model to study the deposition of “high inertia” particles in a turbulent duct flow. [Young and Leeming \(1997\)](#) developed a simple approach based on an advection diffusion equation (ADE) to address the particle deposition in turbulent pipe flows, which represents a considerable advance in physical understanding over previous free-flight theories. [Guha \(1997\)](#) developed a unified Eulerian theory, which is based on a Reynolds averaging of the particle continuity and momentum conservation equations, for studying turbulent deposition onto smooth and rough surfaces. [Zaichik et al. \(2010\)](#) developed a simplified Eulerian model called the diffusion-inertia (DIM), which is based on a kinetic equation for the probability density function (PDF) of particle velocity distribution, to investigate the dispersion and deposition of low-inertia particles in turbulent flows. Furthermore, the DIM was incorporated into the nuclear industrial CFD code SATURNE for the deposition of aerosols (e.g. [Nerisson et al. \(2011\)](#)).

Thanks to significant progress achieved in CFD, in particular in the development of sophisticated turbulence models and numerical methods for unstructured grids used for complex geometry, the CFD approach has been used to study the deposition of heavy particles in simple and complex geometries. This is usually described in an Eulerian-Lagrangian calculation framework in which the mean flow field is computed by Eulerian methods, whilst Lagrangian calculations are carried out for a sufficiently large amount of particles to obtain statistically stationary results. This facility has been embedded into most CFD codes though, the stochastic nature of both the turbulence of the underlying flow and the dispersed particulate flow makes the problem of turbulent dispersed particulate flows far more complex than its single-phase counterpart. Therefore, in order to acquire as accurate as possible results on turbulent particle deposition via numerical simulation, additional modelling work needs to be incorporated into the RANS modelling framework to account for the effect of turbulence on the dispersion of particulate phase. Furthermore, the value of the modelling has to be accurately assessed by comparing the results against experimental measurements or data determined by DNS or LES (see [McLaughlin \(1989\)](#); [Brooke et al. \(1992\)](#); [Wang and Squires \(1996\)](#);

Ujttewaal and Oliemans (1996); Zhang and Ahmadi (2000); Narayanan et al. (2003); Marchioli et al. (2003)).

There have been several investigations on extending the existing basic Lagrangian particle tracking method in a RANS modelling framework to address particle deposition, since the default model gives several orders of magnitude over-prediction for the deposition rates. Greenfield (1998) applied the random eddy interaction boundary layer approach proposed by Kallio and Reeks (1989) in CFD code CFX to study deposition of heavy particles. Similar work was performed by Matida et al. (2000) who applied the same model as Kallio and Reeks (1989) for particle deposition in a turbulent pipe flow, in which the Lagrangian time scales seen by small particles were modified in order to make results obtained by numerical simulations match with the experimental measurements from Liu and Agarwal (1974). Dehbi (2008a) implemented the random eddy interaction model as UDFs in ANSYS FLUENT for the investigation of particle deposition, in which fluid velocity fluctuations seen by particles within the turbulent boundary layer are fed in via curve fitted DNS data. The same method was employed by Horn and Schmid (2008) to extend the Lagrangian particle tracking facility in CFX to address particle deposition from turbulent flows. The essence of work by Greenfield (1998), Dehbi (2008a) and Horn and Schmid (2008) was to address an appropriate boundary layer which is not properly resolved in the most-widely used standard  $k - \varepsilon$  turbulence model in a CFD modelling framework. This results from the inherent isotropic assumption used in the standard  $k - \varepsilon$  model to calculate fluctuating fluid velocities  $u'_i = \sqrt{2k/3}$ . However, it is structure and timescale of the near wall turbulence that is critically controlling factor for the deposition of heavy particles. Apart from the simple and efficient standard  $k - \varepsilon$  turbulence model, Tian and Ahmadi (2007) carried out a thorough comparison of the different turbulence models on particle deposition. They demonstrated that the sophisticated Reynolds stress model (RSM) in ANSYS FLUENT coupled with enhanced wall treatment still gives significant over-prediction of deposition rates. Interestingly, Parker et al. (2008) used a different method to work out the particle flux to the wall and obtained very good agreement with the benchmark experimental data from Liu and Agarwal (1974) by means of the same RSM model and Lagrangian particle tracking for studying particle deposition. As far as the above investigations are concerned, the

central idea is to attempt to feed better fluid velocity fluctuations seen by particles within each eddy lifetime modelled than those used in discrete random walk approach in RANS modelling frameworks.

However, there is another way called continuous random walk models based on the Langevin equation to feed fluid velocity fluctuations seen by heavy particles. [Dehbi \(2008b\)](#) developed a normalized Langevin equation based Lagrangian continuous random walk model, which he implemented as UDFs in ANSYS FLUENT to account for the inhomogeneous anisotropic boundary turbulence. [Guingo and Minier \(2008\)](#) proposed a new one-dimensional Langevin boundary layer model of fluid fluctuating velocity which explicitly simulates the interaction of heavy particles with the well-known near wall coherent structures (e.g. sweeps and ejections) into the open source CFD code SATURNE. Similar methodology has been employed by [Chibbaro and Minier \(2008\)](#) who obtained satisfactory prediction of deposition rates with the standard  $k - \varepsilon$  model in SATURNE. In this regard, both [Guingo and Minier \(2008\)](#) and [Chibbaro and Minier \(2008\)](#) demonstrated the important role played by the near wall coherent structures on the transport and deposition of heavy particles within turbulent boundary layers.

Since [Kline et al. \(1967\)](#) first reported the presence of surprisingly well-organized spatially and temporally dependent motions in the near wall region (named bursting), the role played by coherent structures of near wall on the transport and deposition of inertia particle has been the focus of a good fraction of the research efforts before [Guingo and Minier \(2008\)](#). [Owen \(1969\)](#) first suggested that the transport of fine solid particles from a turbulent gas stream to an adjoining surface may result from the sporadic violent eruptions from the viscous sublayer. [Cleaver and Yates \(1975\)](#) proposed a sub-layer model, which takes into account of the role the upsweeps and downsweeps of fluid observed in the near wall region of turbulent flows, in order to obtain a better understanding of the mechanics of particle deposition. The model predictions were in satisfactory agreement with experimental measurements on deposition rates. The sub-layer model of [Cleaver and Yates \(1975\)](#) was used by [Fichman et al. \(1988\)](#) and [Fan and Ahmadi \(1993\)](#) for calculating particle deposition. [Wei and Willmarth \(1991\)](#) carried out a quadrant analysis of LDA measurements of near wall fluid velocity in order to acquire a preliminary understanding of suspended sediment transport. [Kaftori](#)

et al. (1995a,b) demonstrated the importance of coherent wall structures on particle motion in turbulent boundary layer, entrainment and deposition processes via systematic experiments. Marchioli and Soldati (2002) further examined the mechanisms for particle transfer and segregation in turbulent boundary layers through DNS calculation of a channel flow. They revealed that downward sweeps, referred to as  $Q4$  events, cause particles to transfer to the near wall region where particle preferentially accumulate in the low-speed streaks, whilst ejections, referred to as  $Q2$  events bring about the migration of particles to the region of outer flow. Soldati and Marchioli (2009) provided a systematic review and physical insight on the physics and modelling of deposition and entrainment of particles from turbulent flows. It renders ideas for better implementation of models on particle depositions in practical simulation scenarios.

The research efforts of Wei and Willmarth (1991) are particularly worth noting for elucidating the central idea behind the work described in this thesis. They performed the quadrant analysis of Willmarth and Lu (1972) to examine the high-resolution, two-component laser-Doppler anemometer (LDA) measurements of the wall normal fluid velocity fluctuations in a fully developed water channel flow. They found that there is a net upward momentum flux in the range of  $y^+ > 30$  that may be associated with the bursting process occurred in quadrant  $II$ , whilst there is a net downward momentum flux in the range of  $10 \leq y^+ \leq 30$  that may be associated with the sweeps process occurred in quadrant  $IV$ . The net momentum flux results from the positively skewed distribution of the fluctuating wall-normal velocity. Inspired by this idea, the present work proposes another way to model near wall coherent structures and their interaction with particles under a positively skewed distribution of fluctuating wall-normal velocity that hopefully can add new insight or give new ideas to improve the prediction of deposition rates. Moreover, the results are compared against those obtained by solving the Langevin equation used in continuous random walk models which satisfies the well-mixed condition (e.g Thomson (1987)).

The present chapter is structured as follows. First, the stochastic quadrant model is formulated and discussed. We then present the related statistics in four quadrants obtained using a quadrant analysis for the wall-normal fluid velocity fluctuations acquired from an LES of a fully developed channel flow. Finally, results on deposition rates from an

implementation of this stochastic quadrant model are presented, where they are compared with results from benchmark experimental measurements, obtained by solving a one-dimensional Langevin-based continuous random walk (CRW) model and from other CRW models. Several statistics concerning particle phase in the near wall region are also shown.

## 4.2 Modelling methodology

### 4.2.1 Formulation of the stochastic quadrant model

The discrete random walk (also known as Monte-Carlo eddy interaction) model is the basis of the formulation of the present stochastic model. The fluid velocity field in the absence of the dispersed particle phase is determined by a RANS computation with the standard  $k - \varepsilon$  model. The temporal fluctuations of the velocity field are described as a system of discrete eddies, with which the suspended particles interact for a randomized eddy lifetime. In the particle equation of motion Eq: (4.21), the instantaneous fluid velocity is represented by a Reynolds decomposition of averaged and fluctuating components,

$$\mathbf{u} = \bar{\mathbf{U}} + \mathbf{u}', \quad (4.1)$$

The time-averaged fluid velocity  $\bar{\mathbf{U}}$  is acquired from the solution of a RANS calculation for the turbulent flow. Thus it is crucial to model the fluctuating components to account for the effect of turbulence on the dispersion of particles. In this respect, there have been a number of attempts as discussed above (e.g. [Tian and Ahmadi \(2007\)](#); [Dehbi \(2008a,b\)](#); [Guingo and Minier \(2008\)](#); [Chibbaro and Minier \(2008\)](#); [Mehel et al. \(2010\)](#)).

In this work, the attention is confined to the deposition of particles from the fully developed region, in which velocity statistics no longer vary with streamwise coordinate  $x$ . As stated by [Pope \(2000\)](#), the fully developed channel flow can be considered as statistically stationary and one-dimensional, with velocity statistics depending on wall normal direction  $y$  only. In this case, a new approach is proposed here to model the wall-normal fluctuating velocity component denoted by  $v'$  based on quadrant analysis.

Furthermore, the particle tracking is performed by a Lagrangian particle tracking module independent of the discrete phase model (DPM) provided by ANSYS FLUENT.

It is widely considered that the distribution of the wall normal fluctuating velocity is skewed within fully developed turbulent boundary layers (e.g. [Kim et al. \(1987\)](#)). The wall normal fluctuating component can be distinguished as positive or negative according to whether the momentum flux is away from or toward the wall. Thus let  $v'_+$  be a function defined as

$$v'_+ = \begin{cases} v' & \text{if } v' > 0, \\ 0 & \text{if } v' \leq 0 \end{cases} \quad (4.2)$$

and  $v'_-$  defined as

$$v'_- = \begin{cases} v' & \text{if } v' < 0, \\ 0 & \text{if } v' \geq 0. \end{cases} \quad (4.3)$$

It is possible to define the average value of  $v'_+$  and  $v'_-$  as:

$$\langle v'_+ \rangle = \frac{1}{T_+} \int_0^T v'_+ dt \quad (4.4)$$

and

$$\langle v'_- \rangle = \frac{1}{T_-} \int_0^T v'_- dt, \quad (4.5)$$

where  $T$  is the interval of observation time containing the fraction of  $v'_+$  denoted by  $T_+$  and the fraction of  $v'_-$  denoted by  $T_-$ . Then, we have

$$\langle v'_+ \rangle + \langle v'_- \rangle = \frac{1}{T_+} \int_0^T \left( v'_+ + \frac{T_+}{T_-} v'_- \right) dt. \quad (4.6)$$

Accordingly,

$$\frac{1}{T} \int_0^T (v'_+ + v'_-) dt = 0. \quad (4.7)$$

Thus if  $T_+ < T_-$ ,

$$|\langle v'_+ \rangle| > |\langle v'_- \rangle|, \quad (4.8)$$

if  $T_+ > T_-$ ,

$$|\langle v'_+ \rangle| < |\langle v'_- \rangle|. \quad (4.9)$$

Similarly, average momentum flux per unit area can be defined as:

$$\langle v'_+{}^2 \rangle = \frac{1}{T_+} \int_0^T (v'_+)^2 dt \quad (4.10)$$

and

$$\langle v'_-{}^2 \rangle = \frac{1}{T_-} \int_0^T (v'_-)^2 dt. \quad (4.11)$$

According to Eq: (4.8), when  $T_+ < T_-$  we have

$$|\langle v'_+{}^2 \rangle| > |\langle v'_-{}^2 \rangle|, \quad (4.12)$$

and according to Eq: (4.9), when  $T_+ > T_-$

$$|\langle v'_+{}^2 \rangle| < |\langle v'_-{}^2 \rangle|. \quad (4.13)$$

It is obvious that  $|\langle v'_+{}^3 \rangle| > |\langle v'_-{}^3 \rangle|$  when  $T_+ < T_-$ ; whilst  $|\langle v'_+{}^3 \rangle| < |\langle v'_-{}^3 \rangle|$  when  $T_+ > T_-$ . These two cases mean that the wall normal fluctuating component is derived from positively and negatively skewed distributions, respectively. Under the positively skewed distribution, there will be a net upward momentum flux of fluid; whilst under the negatively skewed distribution, there will be a net downward momentum flux of fluid. Thus the imbalance of momentum flux of fluid particle within fully turbulent boundary layers might play an important role on the transport and deposition of heavy particles. The data in [Kim et al. \(1987\)](#) show that the wall normal fluctuating component is of positive skewness in the range of  $0 < y^+ < 10$  and  $y^+ > 30$ .

### 4.2.2 Statistics of $v'$ in each of the four quadrants

Inspired by the quadrant analysis, we classified the wall normal fluctuating velocity and averaged it into the four quadrants according to the instantaneous quadrant of motion. In this sense, the instantaneous velocity of a sufficiently large number of fluid particles at a specified position may be categorized in terms of the sign of the streamwise and wall normal velocity fluctuations. For example, when both  $u'$  and  $v'$  are great than zero,

the instantaneous velocity signal will be categorized into the Quadrant I; in the case of  $u' < 0$  and  $v' > 0$ , this will be put into the quadrant II, and so on. This can be referred to as the criterion of quadrant analysis. Kline et al. (1967) and Willmarth and Lu (1972) suggested that upward momentum fluxes may be primarily associated with the bursting process that resides in Quadrant II, whilst downward momentum fluxes may be mainly associated with sweep events that are come from Quadrant IV. Physically speaking, upward momentum fluxes associated with Quadrant II would cause particles to move away from the wall and downward momentum fluxes associated with Quadrant IV would result in the migration of particles toward the wall.

According to ergodic property, time averages of  $v'$  and momentum flux  $v'^2$  can be defined for each of the four quadrants according to Eq: 4.8 and 4.10 as

$$\langle v'_i \rangle = \frac{1}{T_i} \int_0^T v'_i dt; \quad i = \text{I, II, III, IV} \quad (4.14)$$

and

$$\langle v_i'^2 \rangle = \frac{1}{T_i} \int_0^T v_i'^2 dt; \quad i = \text{I, II, III, IV}, \quad (4.15)$$

where  $T_i$  denotes time spell spent in the quadrant  $i$  by  $v'_i$ , and  $v'_i$  is define as

$$v'_i = \begin{cases} v' & \text{if } v' \text{ satisfies the criterion of quadrant analysis,} \\ 0 & \text{if not.} \end{cases} \quad (4.16)$$

A large eddy simulation (LES) of a fully developed channel flow with  $Re_\tau = 180$  was carried out to obtain the corresponding statistics of  $v'_i$  across the boundary layer. A scatter plot of  $u'$  and  $v'$  with corresponding probability density function (pdf) with 162000 non-dimensional time units is shown in figure 4.1 according to the quadrant analysis. It can be observed that the probability density function of both  $u'$  and  $v'$  are skewed.

In figure 4.2,  $\langle v'_i \rangle$  and  $v'$  as a function of  $y^+$  show that the fluctuating components in the four quadrants are smaller in magnitude than the  $v'$  across the  $y^+$  range shown.  $\langle v'_i \rangle$  in each of the four quadrants is of different magnitude, indicating that there is an asymmetry in the wall normal fluctuating components. Furthermore, the greatest magnitude of  $\langle v'_i \rangle$  is found in quadrant II across most of the  $y^+$  range. Figure 4.3 shows that there is a net

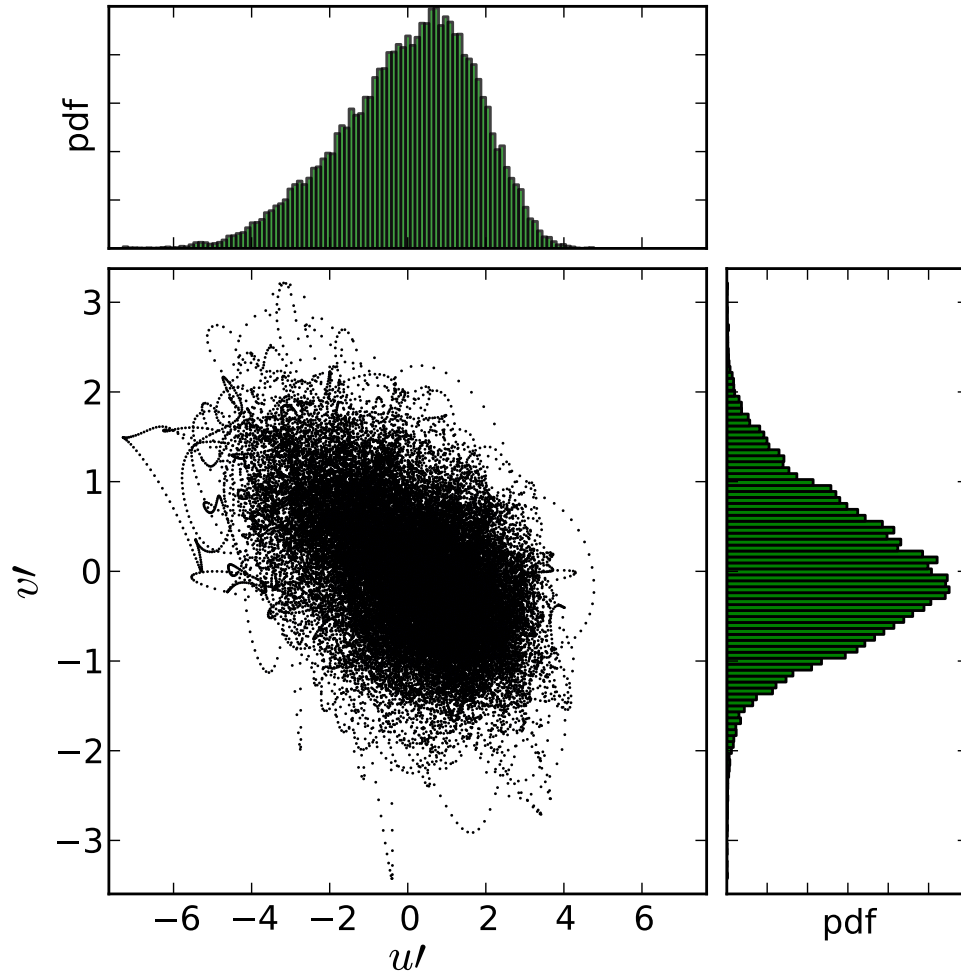


Figure 4.1: Scatter plot of  $u'$  and  $v'$  at  $y^+ = 50$  resolved by LES, categorised in terms of quadrant analysis.

upward momentum flux resulting from quadrant II for the range of  $y^+ > 20$ . However, this situation reverses in the range of  $y^+ < 20$ . The asymmetry of  $\langle v'_i \rangle$  and  $\langle v_i'^2 \rangle$  in each of the four quadrants is a new feature for modelling velocity fluctuations seen by heavy particles. It is particularly interesting for studying the deposition rates.

### 4.2.3 Implementation of the stochastic quadrant model

The imbalance of  $\langle v'_i \rangle$  within four quadrants may be of different importance on the transport and deposition of heavy particles. Events in quadrant II are mainly associated

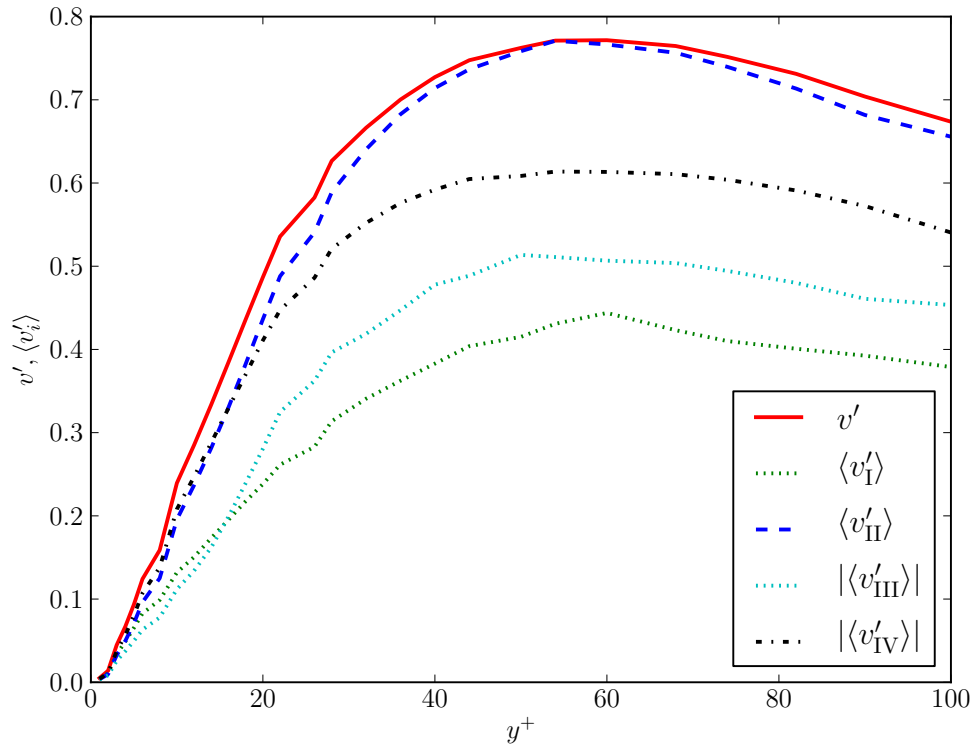


Figure 4.2: Profiles of  $v'$  and  $\langle v'_i \rangle$  as a function of  $y^+$  at  $Re_\tau = 180$  in each of the four quadrants.

with violent ejections of low-speed fluid away from the wall; motions in quadrant IV are primarily associated with an inrush of high-speed fluid toward the wall, also referred to as the sweep event. There are no significant structures associated with quadrant I and III. The upward momentum flux in quadrant II may be a strongly contributing factor on the transport of particles away from the wall and reduce the deposition rates; whilst the inward momentum flux in quadrant IV may be a strongly contributing factor on the transport of particles towards the wall and increase the deposition rates.

The results on  $\langle v'_i \rangle$  and  $\langle v_i'^2 \rangle$  enables us to specify the statistics of wall-normal velocity fluctuations seen by particles in each encountered eddy along their trajectories. For example, curve-fitting of the four profiles of  $\langle v'_i \rangle$  could be achieved easily. However, comparing the shape of  $\langle v'_i \rangle$  against with the shape of  $v'$ , a different scale factor is assumed between  $\langle v'_i \rangle$  and  $v'$ . In figure 4.4 the probability density functions for a half normal distribution and  $\langle v'_i \rangle$  in each of the four quadrants at  $y^+ = 30$  show that they are

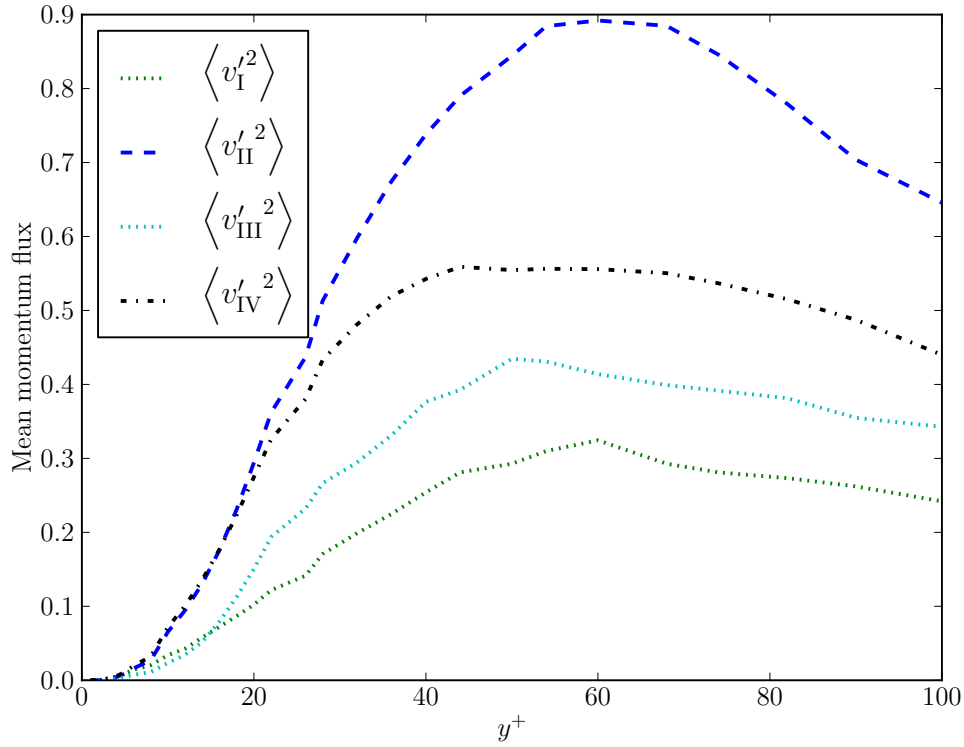


Figure 4.3: Profiles of momentum fluxes as a function of  $y^+$  at  $Re_\tau = 180$  in each of the four quadrants.

in fare agreement with each other, indicating that a half normal distribution may be used to describe the distribution of  $v_i'$ . This probability distribution function is given by

$$f_X(x; \sigma) = \begin{cases} \frac{\sqrt{2}}{\sigma\sqrt{\pi}} \exp\left(-\frac{x^2}{2\sigma^2}\right) & \text{if } x \geq 0, \\ 0 & \text{if } x < 0, \end{cases} \quad (4.17)$$

where  $\sigma$  is set to equal to the value of  $\sqrt{\frac{\pi}{2}} \langle v_i'^2 \rangle^{1/2}$  at the corresponding  $y^+$  location.

The logical next step is to construct a random process, which models eddy motions in the four quadrants. Particles would interact with a random succession of eddies resulting from different quadrants. For this, a homogeneous Markov chain was conceived as a model for the evolution of eddy events in the four quadrants along the particle trajectories. Particles interact with an eddy in quadrant I. After this eddy decays, they would then be able to interact with an eddy resulting from any of the four quadrants with a certain transition probability. Figure 4.5 describes this process. As far as the transition

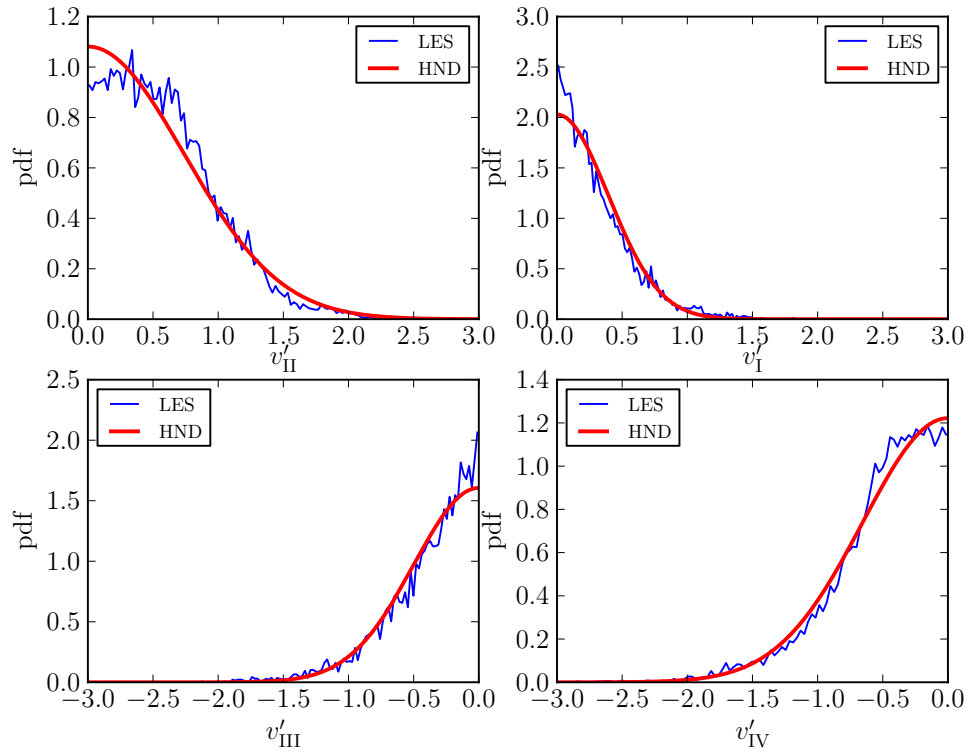


Figure 4.4: Probability density function (pdf) for  $\langle v'_i \rangle$  obtained by LES and a comparison with a half normal distribution (HND)

probabilities are concerned, let  $\mathbf{Q}_i, i = \{I, II, III, IV\}$  be a discrete time Markov chain on  $\{\mathbf{Q}_I, \mathbf{Q}_{II}, \mathbf{Q}_{III}, \mathbf{Q}_{IV}\}$  with transition matrix

$$P = \begin{pmatrix} p_{11} & p_{12} & p_{13} & p_{14} \\ p_{21} & p_{22} & p_{23} & p_{24} \\ p_{31} & p_{32} & p_{33} & p_{34} \\ p_{41} & p_{42} & p_{43} & p_{44} \end{pmatrix}, \quad (4.18)$$

where  $(p_{ij} : i, j \in \{1, 2, 3, 4\})$  denotes the corresponding probability distribution of random eddy events in each quadrant. For eddy events in the four quadrants, Eq: (4.18) is reduced to a “degenerate” transition matrix as

$$P = \begin{pmatrix} p_{11} & p_{22} & p_{33} & p_{44} \end{pmatrix}. \quad (4.19)$$

Figure 4.6 shows variations of the relative probability associated with each of the four

quadrants as a function of  $y^+$ . These probabilities are used as the transition probabilities denoted in Eq: (4.19).

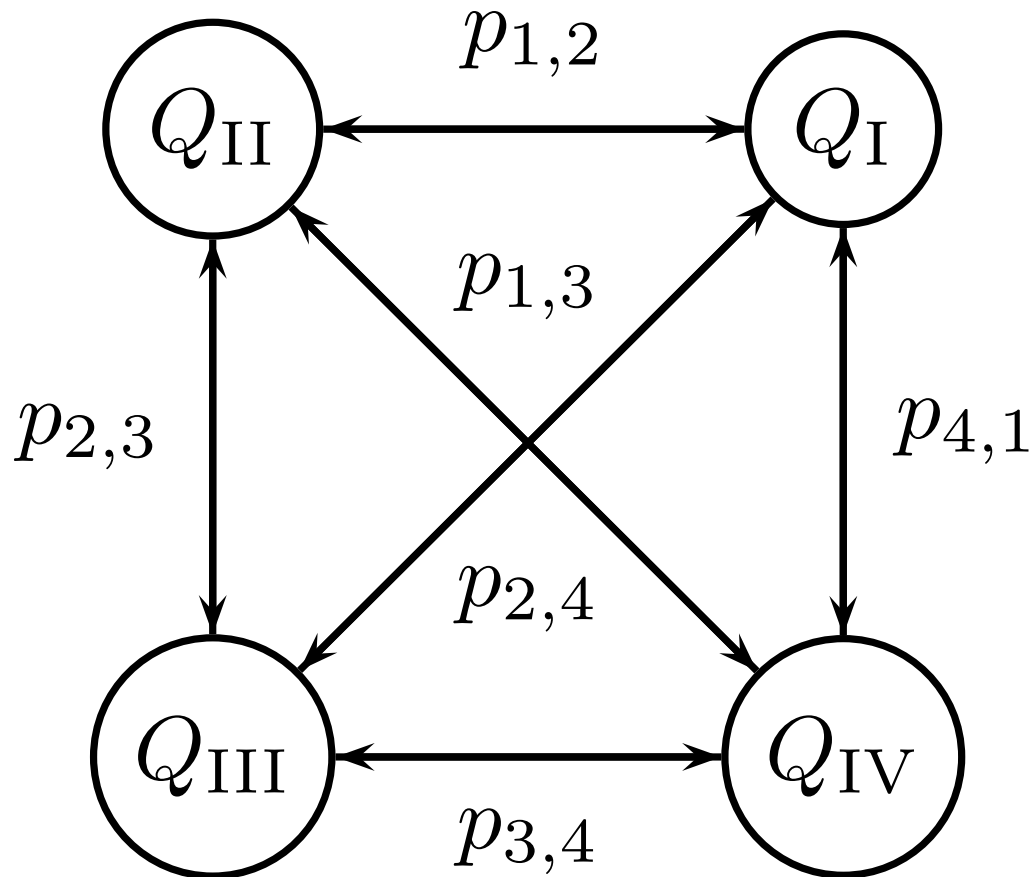


Figure 4.5: Diagram describing the Markov chain modelling motions in the four quadrants.

The time scale of eddies in each of the four quadrants is difficult to estimate from the present study, although [Luchik and Tiederman \(1987\)](#) provided several quantitative techniques to measure time scales associated with burst events. In the present study, the lifetime of eddies in the four quadrants are assumed to equal to the Lagrangian time scale of fluid particles according to their corresponding  $y^+$  position. Figure 4.7 shows the Lagrangian time scale of fluid particles within turbulent boundary layers. This is taken from the curve-fitting of [Kallio and Reeks \(1989\)](#). Furthermore, the Lagrangian

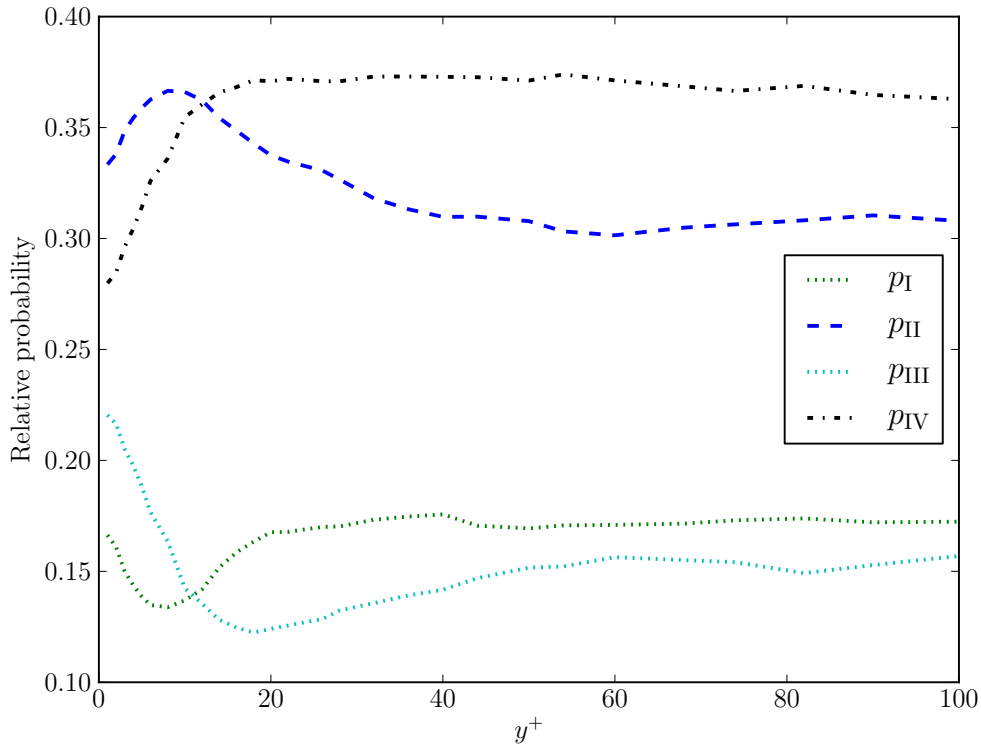


Figure 4.6: Relative probability of four quadrants as a function of  $y^+$ .

time scale is assumed to obey an exponential distribution

$$f_X(x, \lambda) = \lambda e^{-\lambda x}, \quad (4.20)$$

where  $\lambda$  equals to the integral Lagrangian time scale  $T_L$  at the particle position. Figure 4.7 also shows the wall-normal r.m.s profile of fluid velocity.  $\langle v'_i \rangle$  in each of the four quadrants is obtained by multiplying  $v'$  by a scaling factor. In every eddy generated from the four quadrants, fluctuation velocity is sampled from a half normal distribution with having mean  $v'_i$  and a variance corresponding to the particular particle  $y^+$  value in the boundary layer.

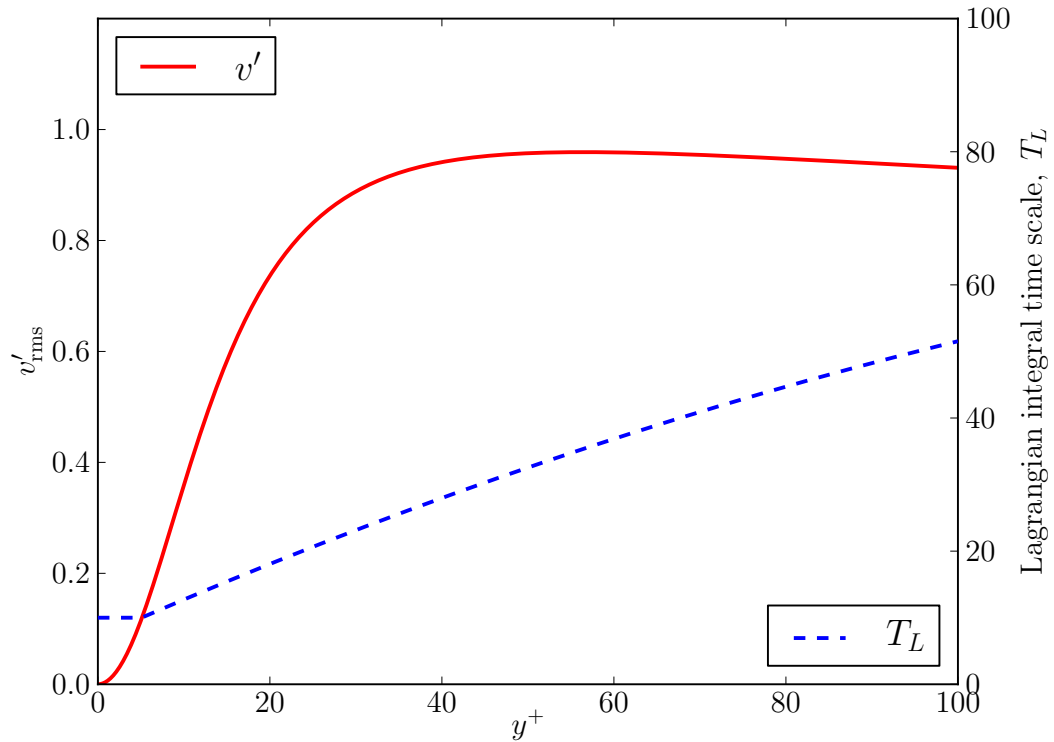


Figure 4.7: Non-dimensional wall normal fluid velocity and Lagrangian time integral as a function of  $y^+$  within turbulent boundary layers.

#### 4.2.4 Governing equations of particle motion

A Lagrangian particle tracking module was developed and coupled with the unstructured mesh Navier-Stokes equation solver in ANSYS FLUENT to calculate trajectories of heavy particles in flow fields. The focus of this work is on the deposition of non-intercollision, rigid, spherical and heavy particles. The ratio of particles density to fluid density is 770, which is the same as the experimental measurements of [Liu and Agarwal \(1974\)](#). The concentration of particles is dilute enough to make one-way coupling assumption. The particle equation of motion discussed by [Maxey and Riley \(1983\)](#) is simplified in this work by taking into account only the drag force. We thus can write the particle equation of motion involving the non-linear form of the drag law with the point particle approximation

$$\frac{d\mathbf{u}_p}{dt} = \frac{1}{\tau_p} C_D \frac{Re_p}{24} (\mathbf{u} - \mathbf{u}_p), \quad (4.21)$$

where  $\mathbf{u}_p$  is the particle velocity and  $\mathbf{u}$  the instantaneous fluid velocity at the particle position,  $\tau_p$  is the particle response time. Previous research effort on particle dispersion in a channel flow (e.g. [Marchioli et al. \(2006\)](#)) has demonstrated that the particle Reynolds number,  $Re_p = |\mathbf{u} - \mathbf{u}_p|d_p/\nu$  does not necessarily remain small enough. Thus, an empirical relation for  $C_D$  from [Morsi and Alexander \(1972\)](#), which is applicable to a wide range of particle Reynolds number with sufficiently high accuracy, is employed.

$$C_D = c_1 + \frac{c_2}{Re_p} + \frac{c_3}{Re_p^2}, \quad (4.22)$$

in which  $c_1, c_2, c_3$  are constants and provided by [Morsi and Alexander \(1972\)](#). The above empirical expression exhibits the correct asymptotic behavior at low as well as high values of  $Re_p$ . A state-of-art composite correlation for drag coefficient and lift coefficient will be investigated in the following work.

The position  $\mathbf{x}_p$  of particles is obtained from the kinematic relationship

$$\frac{d\mathbf{x}_p}{dt} = \mathbf{u}_p \quad (4.23)$$

The boundary condition for the above equation is that the particle is captured by the wall when its center is less than its radius away from the nearest wall. This is not properly treated in the default discrete phase model (DPM) provided by ANSYS FLUENT. Furthermore, this error has a significant effect upon predictions concerning the deposition of heavy particles under investigation.

From a converged RANS computation of an Eulerian velocity field, Eq: (4.23) is integrated in time using the second-order Adams-Bashforth scheme to get particle trajectories, whilst Eq: (4.21) is integrated with the second-order accurate Gear2 (backward differentiation formulae) scheme that is applicable to stiff systems. Fluid velocities are stored at the cell centroid. Since it is only by chance that a particle coincides with the cell centroid, a quadratic scheme based on velocity gradient reconstruction is used to interpolate the fluid velocity to the particle location.

Properties of the dispersed phase are obtained by following the trajectories of  $10^5$  particles. The trajectories of a sufficiently large number of particles are crucial in order

to present significantly statistical results for the dispersed particle phase.

## 4.3 Results and discussions

### 4.3.1 Continuous phase

The stochastic quadrant model was applied to study the transport and deposition of heavy particles in a fully developed turbulent boundary layer. The turbulent boundary layer was resolved using the standard  $k - \varepsilon$  model with enhanced wall treatment in ANSYS FLUENT. The  $y^+$  value of the first cell adjacent to the wall was put at unity. Two points need to be pointed out. First, there is not discernible discrepancy between the inlet and middle plane velocity profiles. Second, the calculated velocity profiles show fair agreement with the DNS data of [Kim et al. \(1987\)](#) across the boundary layer. Given the fact that RANS was employed, the small difference between the calculated and DNS values shown in figure 4.8 is reasonable. As far as there is no discrepancy between the velocity profiles from two planes, this was achieved through a special treatment for the inlet boundary condition. An auxiliary simulation was set up in a small computation domain. Then a converged velocity profiles from the middle plane of this simulation was exported to provide initial velocity condition on the inlet plane. Through this technique, a developing region from the inlet plane was avoided.

### 4.3.2 Dispersed particle phase

#### 4.3.2.1 Particle deposition rates

The prediction of heavy particle deposition rates is of primary interest in this study. The deposition rate in a turbulent boundary layer is usually quantified through a mass transfer coefficient  $K$  defined as

$$K = \frac{J_w}{c}, \quad (4.24)$$

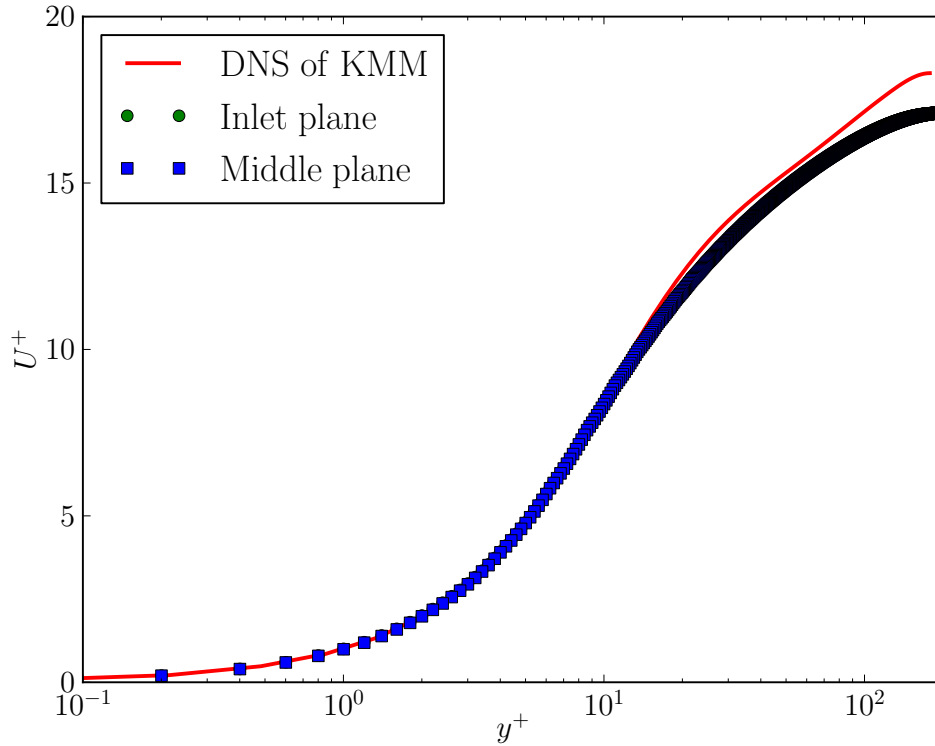


Figure 4.8: Mean fluid velocity profiles from the inlet and middle plane. Both based on  $u_\tau$  and compared with the  $U^+$  data of [Kim et al. \(1987\)](#).

where  $J_w$  represents the particle flux onto the wall surface per unit area and unit time,  $\bar{c}$  is the average particle concentration within the boundary layer. The computation technique proposed by [Kallio and Reeks \(1989\)](#) was used to calculate the non-dimensional particle deposition velocity defined as

$$V_{dep}^+ = \frac{\bar{U}A}{u_\tau P \Delta x} \ln \left( \frac{N_{in}}{N_{out}} \right) \quad (4.25)$$

where  $\bar{U}$  is the average streamwise fluid velocity across the fully developed turbulent boundary layer,  $A$  is the boundary layer cross sectional area,  $P$  the duct perimeter,  $\Delta x$  is the incremental length of section considered, and  $N_{in}$  and  $N_{out}$  are the total number of particles passing through the start and end plane of each section, respectively. The characteristic wall friction velocity  $u_\tau$  was used to obtain the non-dimensional deposition velocity  $V_{dep}^+$ . In this study,  $10^5$  particles were introduced uniformly from the inlet plane.

Computed dimensionless particle deposition velocities are compared with benchmark

experimental measurements (e.g. [Liu and Agarwal \(1974\)](#)), the theoretical curve-fit by [McCoy and Hanratty \(1977\)](#) and the standard  $k - \epsilon$  model in figure 4.9. In particular, the results from [Guingo and Minier \(2008\)](#), who developed a complex stochastic model to account for the geometrical structures in turbulent boundary layers, are included for comparison. It can be observed that very good agreement exists between the present computed results and experimental data in the range of  $St > 5$ . For  $St < 5$ , the stochastic quadrant model gives under-prediction of the deposition rates. Similar phenomena is also observed from the work of [Guingo and Minier \(2008\)](#) who predicted less deposition than obtained in this study. This under-prediction may be directly attributable to the effects of ejection events on particle transport, causing particles to migrate away from the wall region and leading to a over-decrease in their deposition rate.

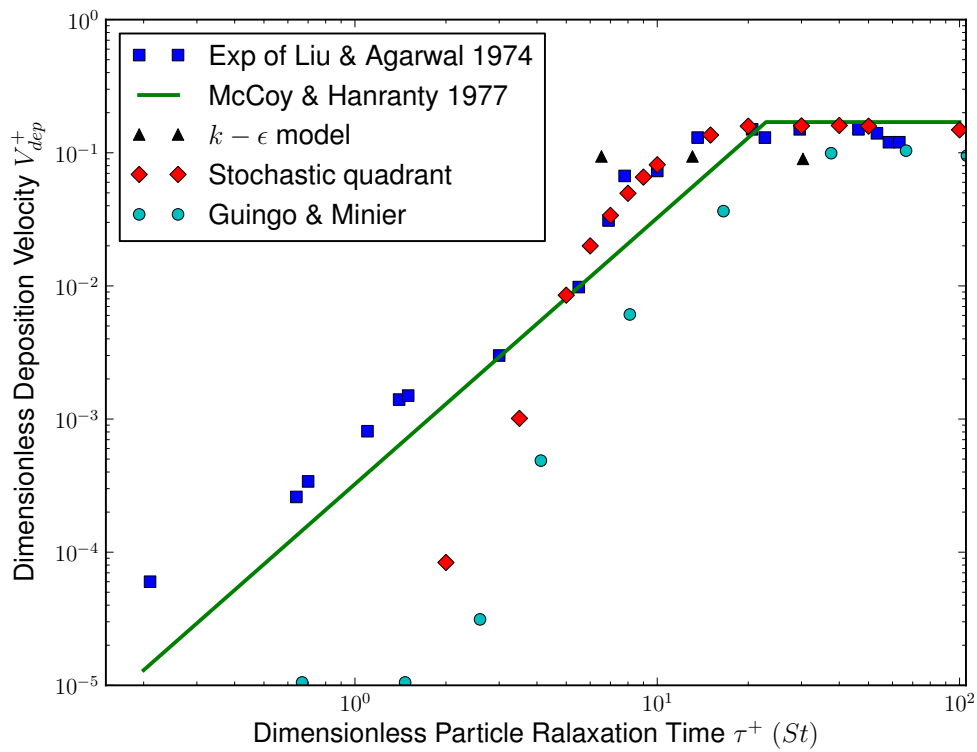


Figure 4.9: Comparison of dimensionless particle deposition velocity as a function of dimensionless particle response time with experimental measurements and different models in turbulent boundary layers. The results from the stochastic quadrant are model compared against the benchmark experimental measurements from [Liu and Agarwal \(1974\)](#), against the theoretical curve fit by [McCoy and Hanratty \(1977\)](#). In addition, the numerical results from [Guingo and Minier \(2008\)](#) are presented.

In this work, an alternatively continuous random walk (CRW) model was applied to repeating the numerical study of particle deposition rates. This model is based on the wall-normal component of normalized Langevin equations in boundary layers (e.g. [Mito and Hanratty \(2002\)](#); [Dehbi \(2008b\)](#)), which takes into account the effect of Stokes number along heavy particle path (see [Bocksell and Loth \(2006\)](#)). The normalized Langevin equation was solved through a second-order accuracy Mil'shtein scheme (see [Mil'shtein \(1978\)](#)). The non-dimensional fluctuating fluid velocity solved this way was converted to a physical velocity. This fluctuating wall-normal fluid velocity was then added into the particle equation of motion in order to account for the turbulence.

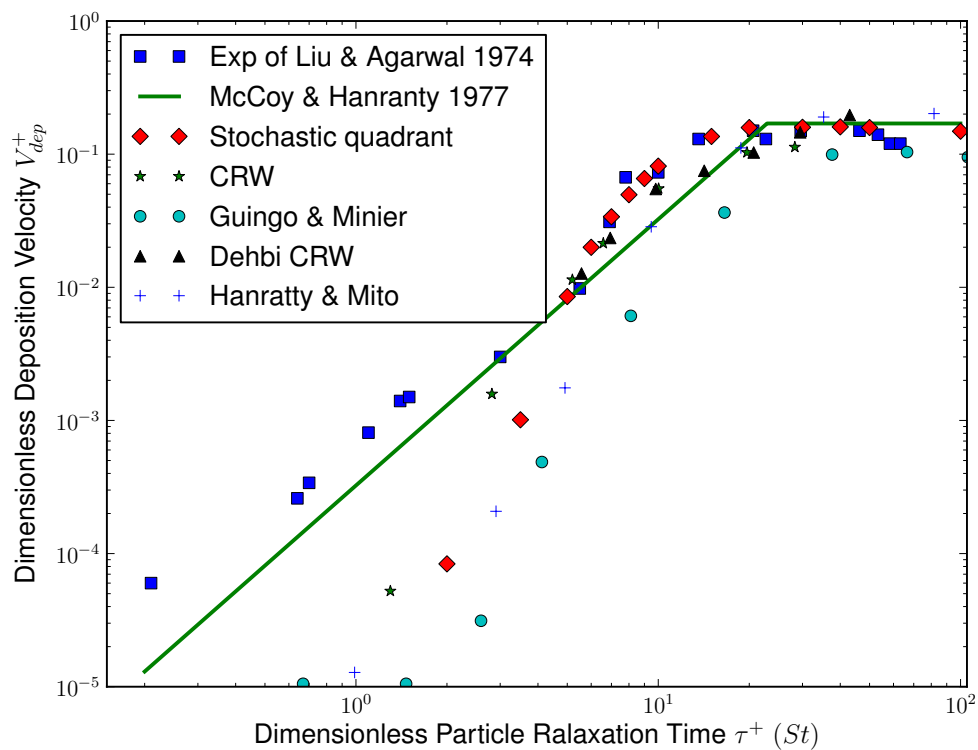


Figure 4.10: Comparison of dimensionless particle deposition velocity as a function of dimensionless particle response time with experimental measurements and different models in turbulent boundary layers. The results from a CRW model are compared to the benchmark experimental measurements from [Liu and Agarwal \(1974\)](#), and the theoretical curve fit by [McCoy and Hanratty \(1977\)](#). In addition, the CRW results are compared with numerical results from various models (e.g. [Guingo and Minier \(2008\)](#); [Dehbi \(2008b\)](#); [Hanratty and Mito \(2006\)](#)).

Results on deposition rates from a CRW model are shown in figure 4.10. There are

a few interesting points to note. Firstly, very similar results can be observed from the present one-dimensional CRW model and [Dehbi \(2008b\)](#)'s work. Secondly, the numerical results from all the models show fair agreement with experiments for large particles. Nevertheless, they all give significant under-predictions on deposition rates for small particles. In contrast to the present one-dimensional CRW and stochastic quadrant model, the CRW model employed by [Dehbi \(2008b\)](#) was solved in three dimensions with curve-fitting DNS database. This may further corroborate the view that the wall-normal fluid fluctuations are a critical control factor on the deposition of heavy particles from fully developed turbulent boundary layer. Thus, as far as practical applications are concerned, it is possible and feasible to feed in only the wall-normal fluid fluctuations for studying particle deposition. On the other hand, compared to CRW models, the stochastic quadrant model is capable of yielding equal quality results on deposition rates, given its relatively simple nature and physical meaning, it is potentially a very promising model for studying deposition of heavy particles from turbulent flows.

#### 4.3.2.2 Preferential mean particle concentration

Figure 4.11 shows preferential mean particle concentration profile as a function  $y^+$  across the boundary layer. Although the present stochastic quadrant model was not corrected for the spurious drift of particles (see [MacInnes and Bracco \(1992\)](#)), this does not affect the preferential mean particle concentration very much since the eddy fluid velocity fluctuation is continuously revised to be that determined by the local turbulence velocity scale according to particle position. It can be noted that there is a significant build-up in concentration for the four classes of particles within the viscous sublayer. The phenomena of build-up of particles has been observed by numerous researchers (e.g. [Kallio and Reeks \(1989\)](#); [Marchioli and Soldati \(2002\)](#); [Narayanan et al. \(2003\)](#)). This is attributed to turbophoresis (see [Reeks \(1983\)](#)). The gradient in wall-normal fluid fluctuations in boundary layer turbulence acts as a driving force and results in a wallward net particle flux. The build-up concentration of particle with  $St = 20$ , is smaller than those of smaller particles with  $St = 2, 5, 10$ . This may result from the fact that they are too heavy particles to follow the relatively quiescent viscous sublayer. On the other hand,

they may move across the viscous sublayer and deposit on the adjacent wall surface, which may also be responsible for the relative reduction of build-up.

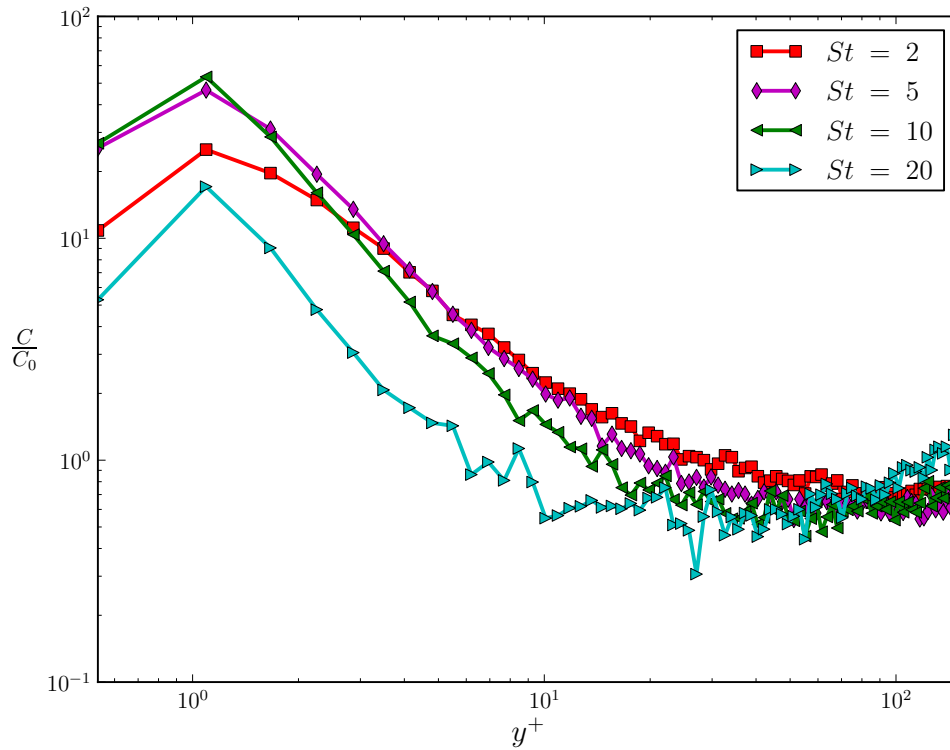


Figure 4.11: Particle preferential concentration profile as a function of  $y^+$ .

#### 4.3.2.3 Mean wallward drift velocity

Figures 4.12 and 4.13 show the mean wallward drift and sampled fluid velocity profiles in the near wall region. It can be observed that for the four sets of particles,  $St = 2, 5, 10$  and  $20$ , have non-zero wallward mean velocity (negative) values. This indicates that the present stochastic quadrant model is capable of predicting the phenomena of turbophoresis. This wallward mean velocity of heavy particles results from primarily the turbulence gradient of boundary layer turbulence as well, which is the prime mechanism that is responsible for the build-up of particles. It is observed that the mean wallward drift velocity of particles varies monotonically with the increase of the particle inertia. Although the wall-normal fluid velocity has zero mean, the sampled mean fluid velocity

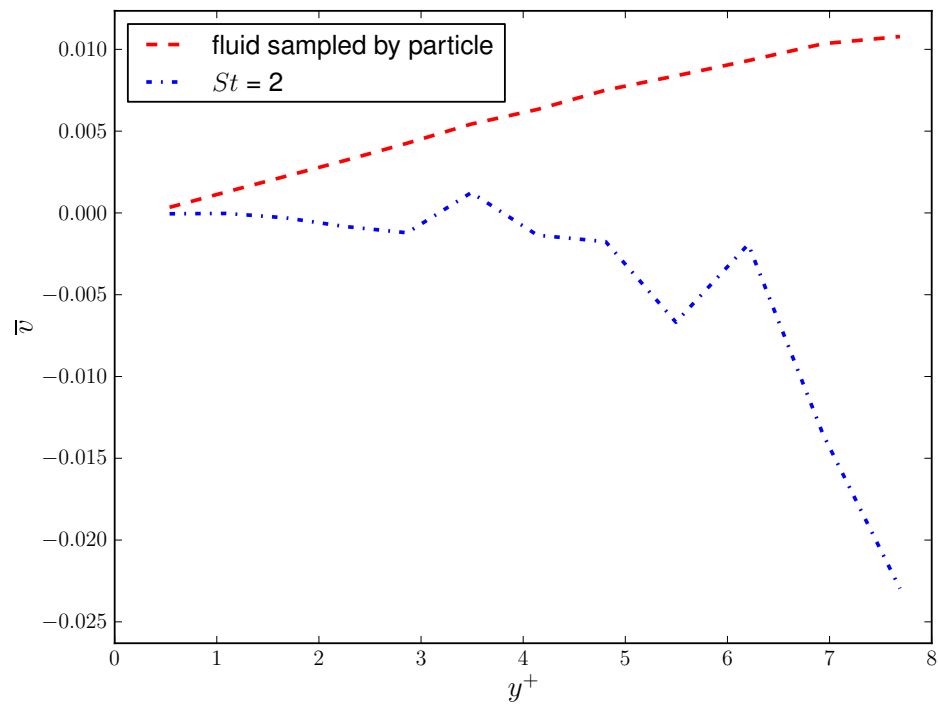
at the particle location has positive values. This may result from the fact that particles sample preferentially events in quadrant II (ejections) characterized by a large positive mean velocity. Since the methodology employed in this study is mainly for industrial applications, it is encouraging that the data quality of mean wallward drift velocity are as good as those obtained by high-fidelity DNS calculations (e.g. [Narayanan et al. \(2003\)](#); [Picciotto et al. \(2005\)](#)).

#### 4.3.2.4 Root mean square (r.m.s.) velocity profiles

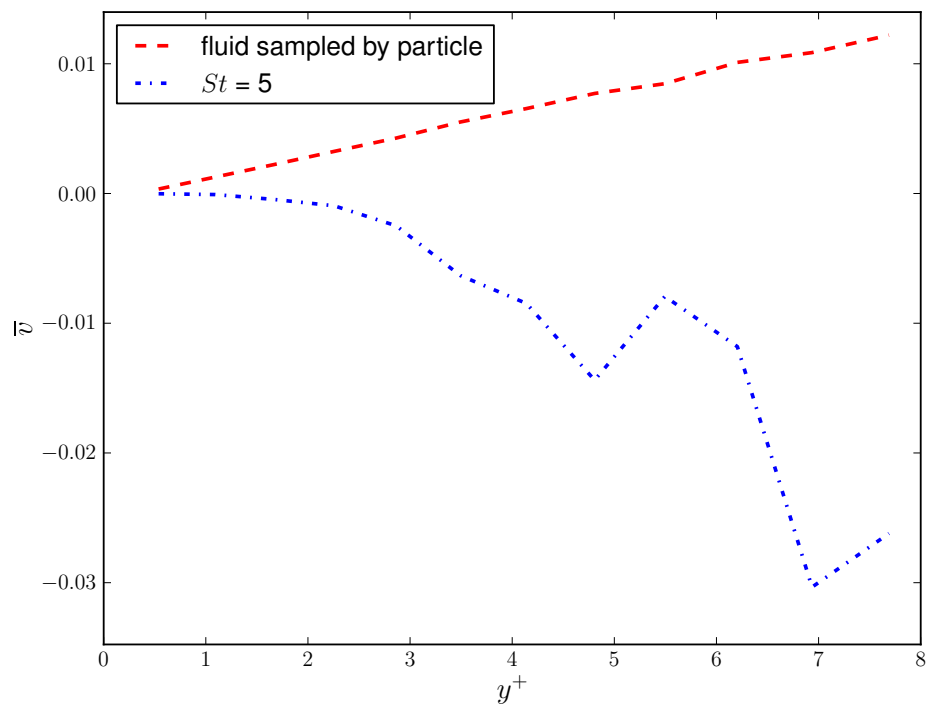
Figures 4.14 and 4.15 show that the r.m.s. of velocity fluctuations of four sets of particles are compared with the fluid velocity fluctuations. It is observed that the r.m.s of particle phase is significantly different from the fluid phase. The difference is increasing with the increase of particle inertia. This results from the fact that the heavier the particles are, the slower their response to the change of surrounding fluid. As far as the noise displayed in the computed particle r.m.s profile is concerned, the reasons may be that the particle phase still has not reached equilibrium or that each sampling bin does not have a sufficient number of representative particles.

#### 4.3.2.5 Mechanisms for particle deposition

The present stochastic model is also applied to study the mechanisms for particle deposition. [Brooke et al. \(1994\)](#); [Narayanan et al. \(2003\)](#) attributed two different mechanisms for particles of different inertia by analysing extensively DNS data-sets. Relatively lighter particles deposit by diffusion mechanism, whilst heavier particles deposit as a result of free-flight. To differentiate the two mechanisms, the concept of particle residence time, which is referred to the continuous time spent by a particle within a certain wall region before depositing, is introduced. Through diffusion, depositing particles have relatively smaller values of deposition velocity and larger values of residence time. Compared to the diffusion counterpart, depositing particles via free-flight mechanism have opposite values. For the deposition velocities and residence time, figure 4.16 shows a scatter plot of wall-normal deposition velocities as a function of particle residence time within the

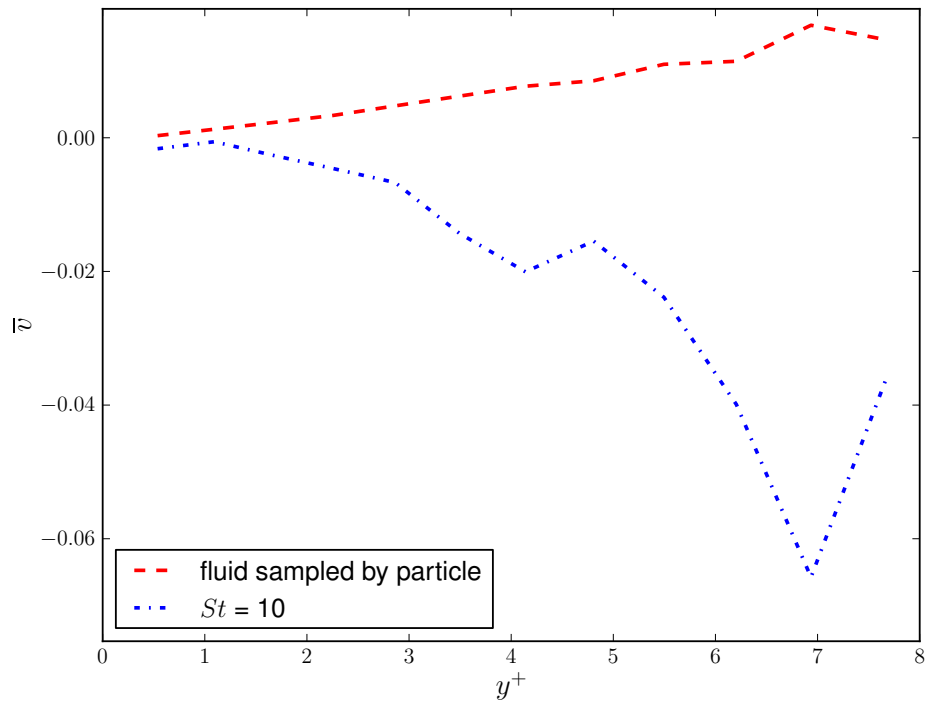


(a)

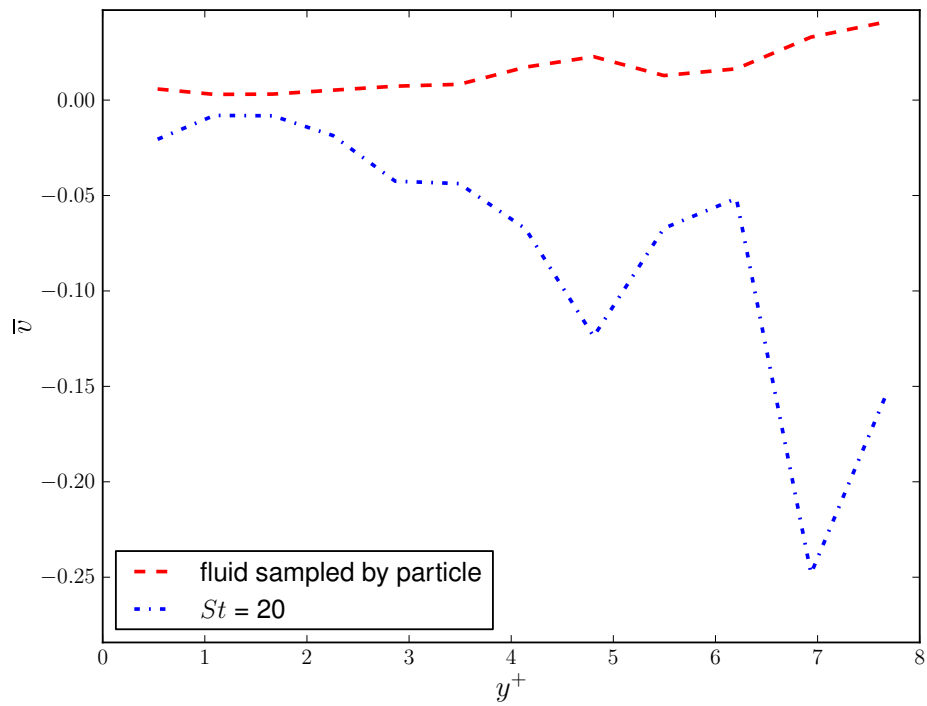


(b)

Figure 4.12: Mean wallward drift velocity and sampled wall-normal fluid velocity, (a)  $St = 2$ , (b)  $St = 5$ .

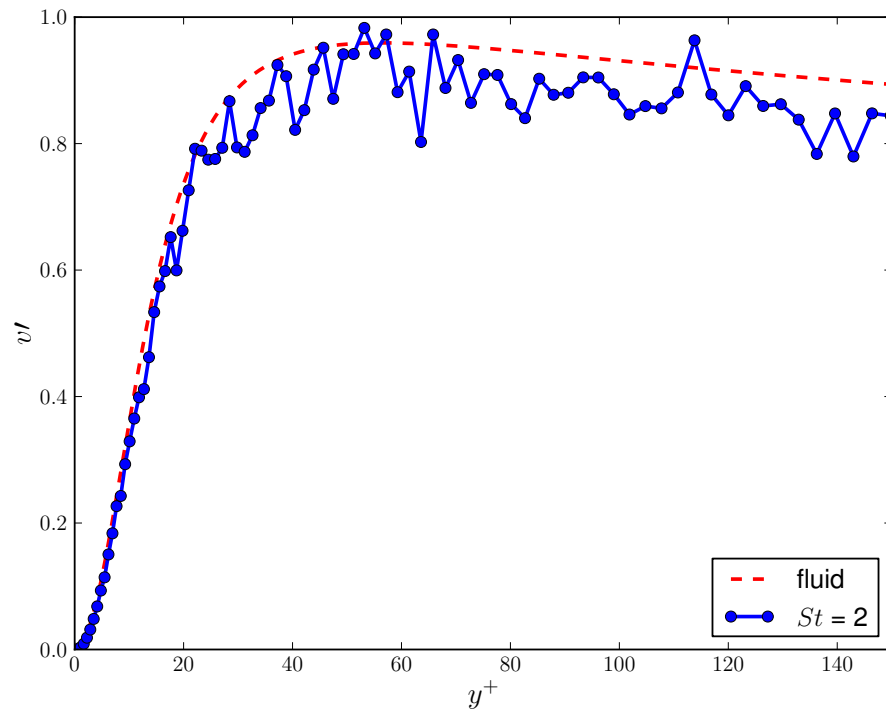


(a)

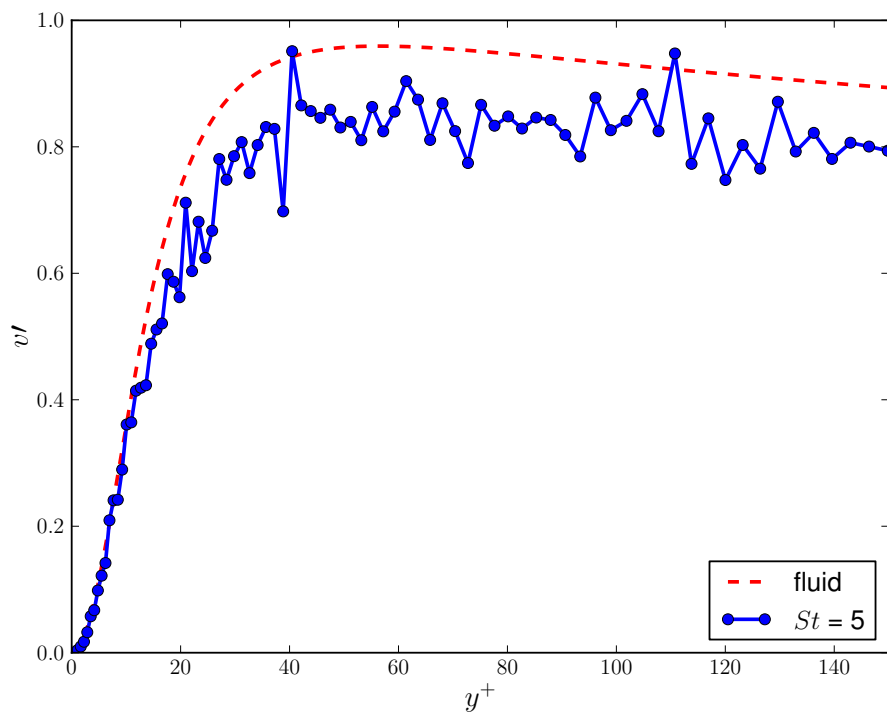


(b)

Figure 4.13: Mean wallward drift velocity and sampled wall-normal fluid velocity, (a)  $St = 2$ , (b)  $St = 5$ .

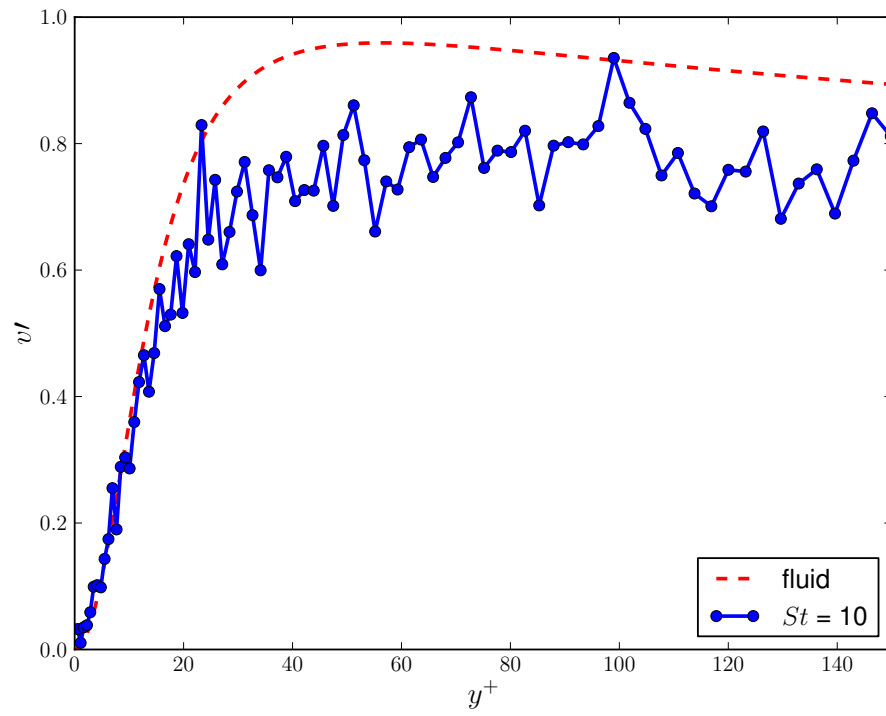


(a)

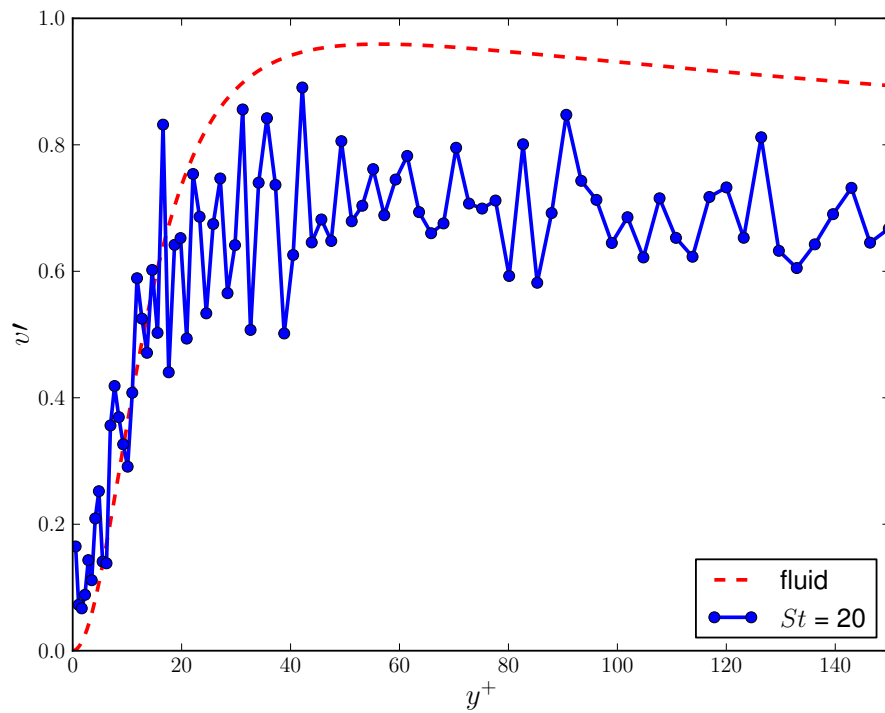


(b)

Figure 4.14: Root mean square (r.m.s) of velocity fluctuations, (a)  $St = 2$ , (b)  $St = 5$ .



(a)



(b)

Figure 4.15: Root mean square (r.m.s) of velocity fluctuations, (a)  $St = 10$ , (b)  $St = 20$ .

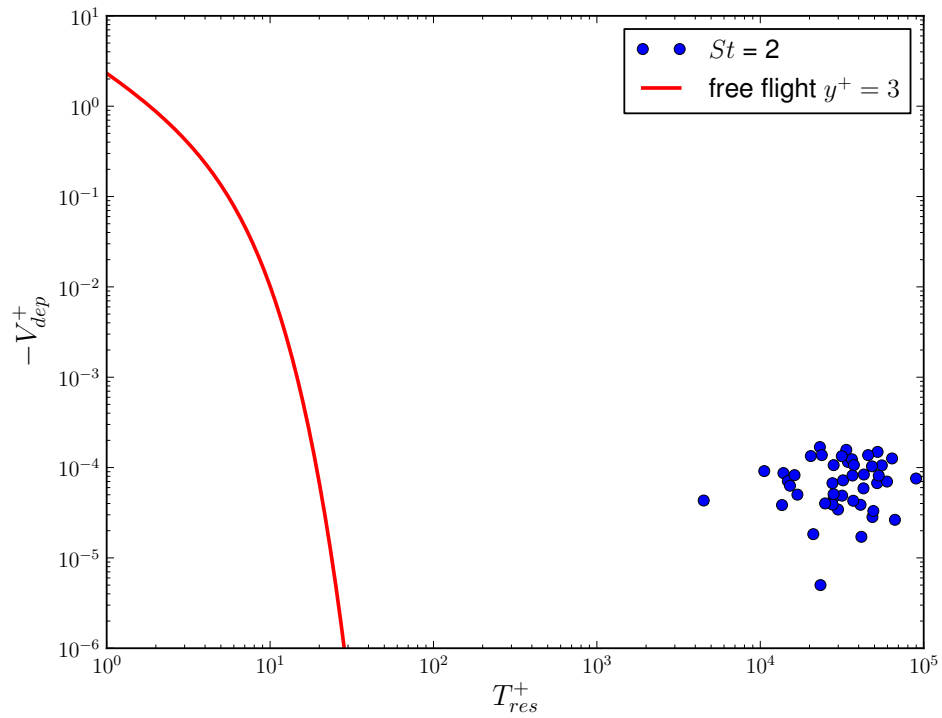
region of  $y^+ < 3$ . The red curve is plotted according to the relation between the wall normal deposition velocity  $V_{dep}^+$  and the residence time  $T_{res}^+$  provided by [Narayanan et al. \(2003\)](#)

$$V_{dep}^+ = \frac{3 - d_p^+ / 2}{\tau^+ \left[ 1 - \exp\left(-\frac{T_{res}^+}{\tau^+}\right) \right]}, \quad (4.26)$$

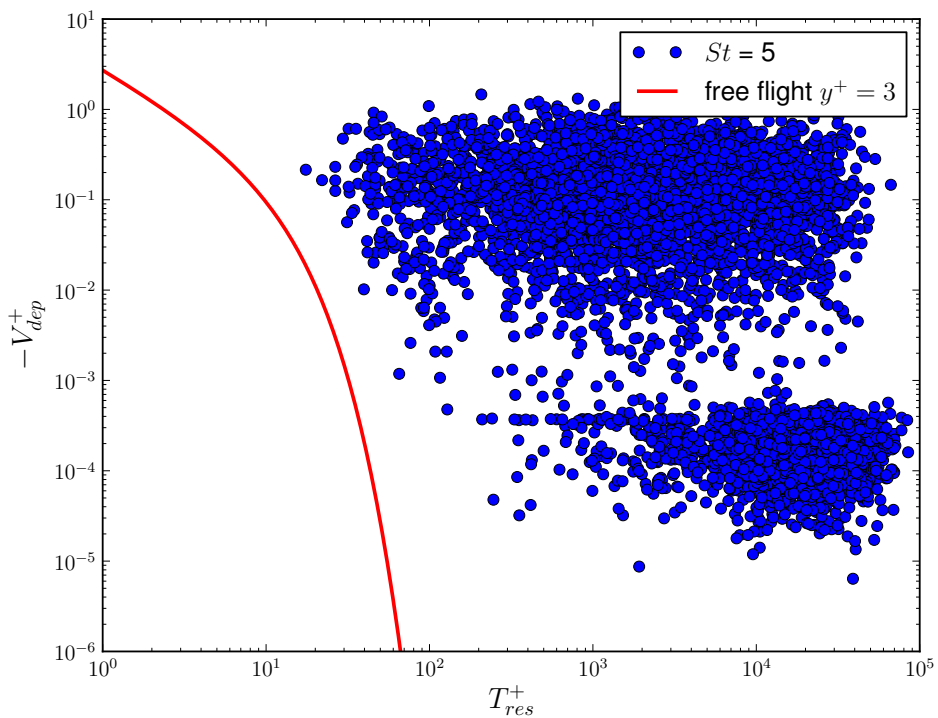
where  $d_p$  is the non-dimensional particle diameter. It can be observed that particles with  $St = 2.0$  get deposited mainly by diffusion as expected. However, the results for  $St = 5$  obtained in the present work are different from DNS data of [Narayanan et al. \(2003\)](#). The results in this work do not follow the relation in Eq: 4.26. However, it can be observed that one population of depositing particles results from diffusion. They are also approaching the curve of free flight. The population of particles with large values of residence time and deposition velocity may get deposition with motions in quadrant IV (sweeps). They then have relatively large deposition velocity. The Lagrangian integral time scales used for motions in quadrant IV may result in the increase of particle residence time.

#### 4.3.2.6 Probability density function (pdf) of impact velocities of particles

Figures 4.17 and 4.18 show the PDF of non-dimensional wall-normal impact velocities of depositing particles onto the wall. It is observed that there is a large increase in probability in the first bin for the three sets of particles. The particles falling in this bin may be associated with the population of depositing particles by diffusion. There also exists long trail of high impact velocities, indicating some of the depositing particles have high deposition velocities. They may be associated with free-flight particles. The PDF of  $St = 20$  is much wider than those of  $St = 5, 10$ , indicating that heavier particles are transported by free-flight across the viscous sublayer before deposition.



(a)



(b)

Figure 4.16: Particle residence time in the region of  $y^+ < 3$  versus particle deposition velocity (a)  $St = 2$ , (b)  $St = 5$ .

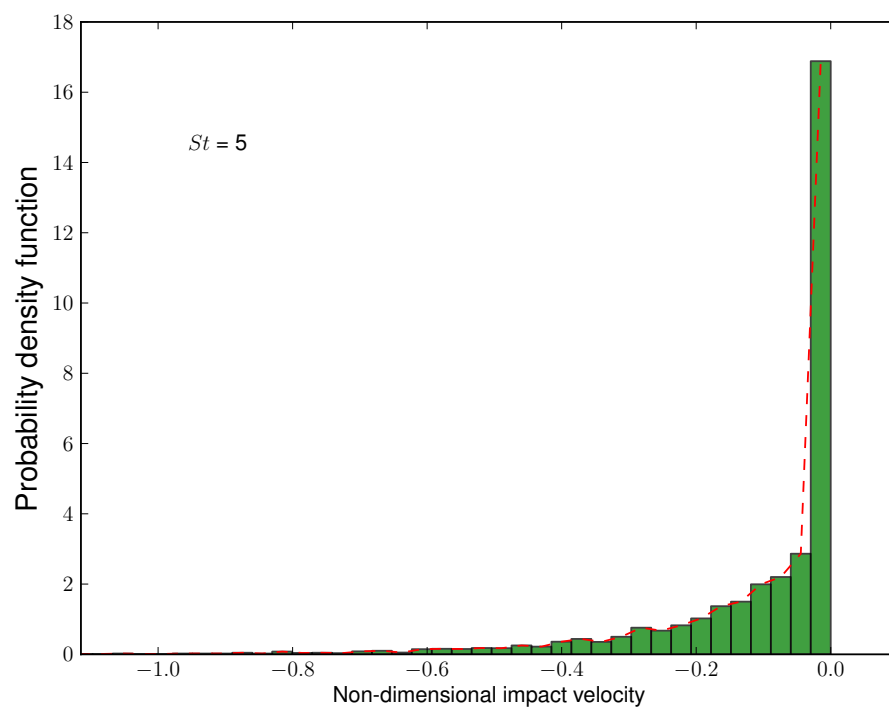
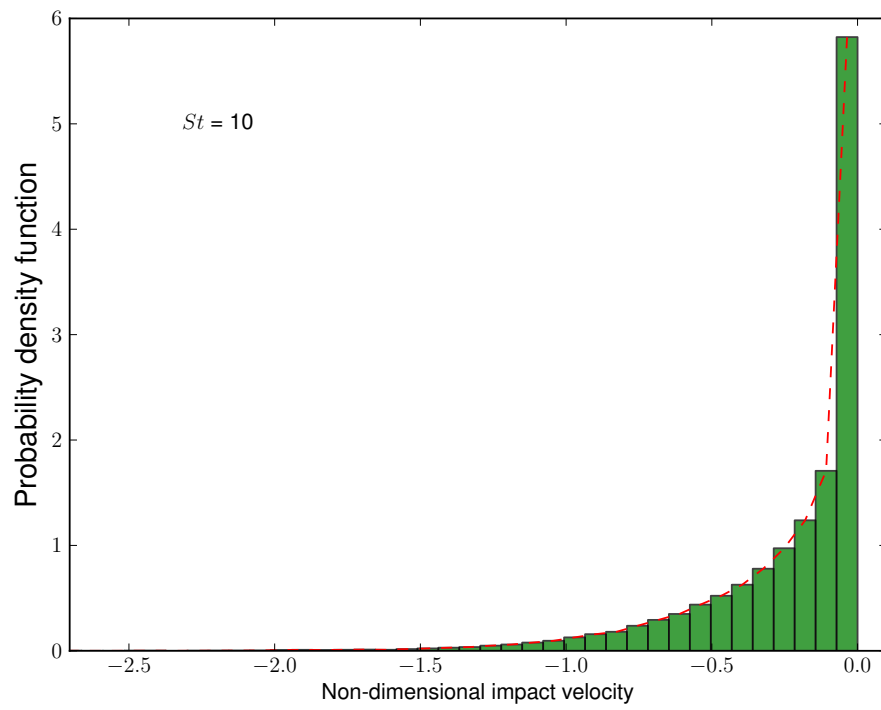
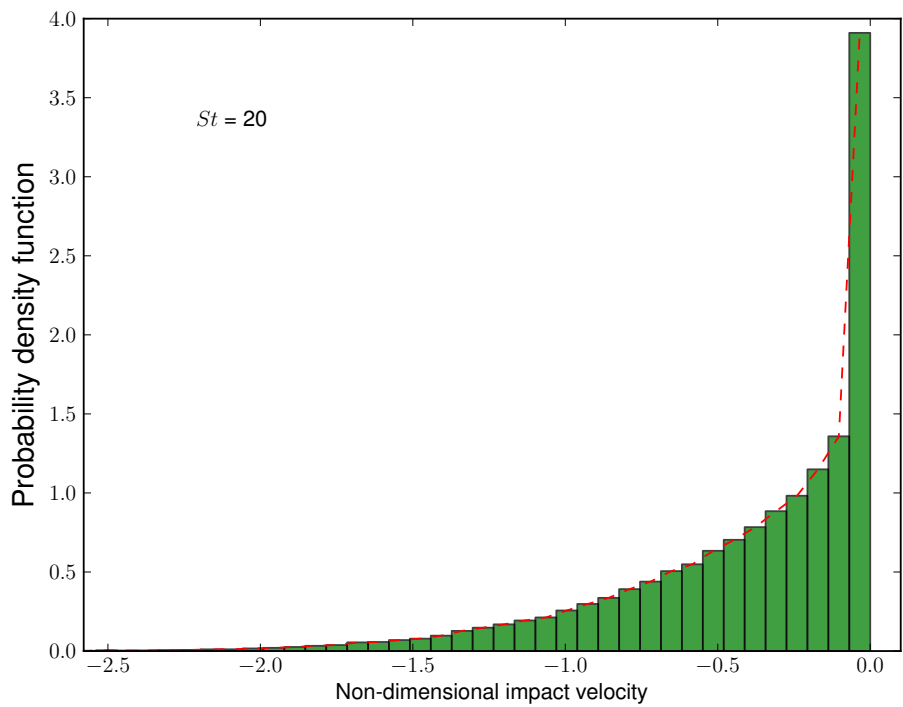


Figure 4.17: Probability density function (pdf) of non-dimensional impact velocities of particles,  $St = 5$ .



(a)



(b)

Figure 4.18: Probability density function (pdf) of non-dimensional impact velocities of particles, (a)  $St = 10$ , (b)  $St = 20$ .

## 4.4 Concluding remarks

A simple stochastic quadrant model was developed for investigating dispersion and deposition of heavy particles in a fully developed turbulent boundary layer. The quadrant model was inspired by the quadrant analysis. The correspondingly detailed statistics of each quadrant are based on a quadrant analysis of the wall-normal fluid velocity fluctuations obtained by an LES of a fully developed channel flow. The turbulent dispersion of heavy particles in fully developed turbulent boundary layer is modelled as interactions of heavy particles with a succession of random eddies found four quadrants in a homogeneous Markov process way. This deals with the skewness of wall-normal fluid velocity fluctuations in developed boundary layers naturally. The model was fully coupled with the steady Navier-Stokes solver in ANSYS FLUENT via a stand-alone Lagrangian stochastic particle tracking module. Deposition rates of heavy particles from turbulent flows is of particular interest to the present stochastic model. This model yields very good predictions of deposition rate for particles  $St > 5$  when compared against benchmark experimental measurements. Prediction of deposition rates at lower values of  $St$  gives under-estimation and may need further improvement. In addition, the deposition rates obtained by the stochastic quadrant model was compared with that acquired by solving a one-dimensional Langevin equation based on a continuous random walk (CRW) model as well as results from multiple CRW models. The discrepancy between deposition rates for particles  $St > 5$  is minor. Of particularly significance is the comparison of the present model with a stochastic model based on the Langevin equation accounting for explicitly the strong sweeps and ejections in boundary layer turbulence. The present model is much simpler and statistically more consistent with experiments.

Most of the predicted statistics of heavy particles are consistent with experiments or DNS calculations. Preferential particle concentration is observed in the near wall region. This indicates that the present stochastic model is capable of predicting turbophoresis responsible for the build-up of particles. The related mean wallward drift velocity is predicted in the viscous sublayer. Predicted r.m.s. profiles of heavy particles wall-normal velocity are typically lower than the counterpart of fluid particles. Mechanisms for particle deposition is explored by observing particle residence time versus deposition

velocity. The population of depositing particles by diffusion is well retrieved. This is also corroborated by a large increase in probability of deposition velocities in the first bin near zero.

The major drawbacks in the present stochastic models lie in the Lagrangian integral time scales for the random eddies occurred in four quadrants and in the inherent spurious drift associated with discrete random walk models. The latter disadvantages may be corrected by adding an appropriately counting component into the eddy fluid velocity fluctuation (see [MacInnes and Bracco \(1992\)](#)). However, the time scales for the events in four quadrants still call for further investigations.

## REFERENCES

- T. L. Bocksell and E. Loth. Stochastic modeling of particle diffusion in a turbulent boundary layer. *International Journal of Multiphase Flow*, 32(10-11):1234–1253, 2006.
- J. W. Brooke, K. Kontomaris, T. J. Hanratty, and J. B. McLaughlin. Turbulent deposition and trapping of aerosols at a wall. *Physics of Fluids A: Fluid Dynamics*, 4:825, 1992.
- J. W. Brooke, T. J. Hanratty, and J. B. McLaughlin. Free-flight mixing and deposition of aerosols. *Physics of Fluids*, 6:3404, 1994.
- S. Chibbaro and J. P. Minier. Langevin PDF simulation of particle deposition in a turbulent pipe flow. *Journal of Aerosol Science*, 39(7):555–571, 2008.
- J. W. Cleaver and B. Yates. A sub layer model for the deposition of particles from a turbulent flow. *Chemical Engineering Science*, 30(8):983–992, 1975.
- C. N. Davies. Deposition of aerosols from turbulent flow through pipes. *Proceedings of the Royal Society of London. Series A, Mathematical and Physical Sciences (1934-1990)*, 289(1417):235–246, 1966.
- A. Dehbi. A CFD model for particle dispersion in turbulent boundary layer flows. *Nuclear Engineering and Design*, 238(3):707–715, 2008a.
- A. Dehbi. Turbulent particle dispersion in arbitrary wall-bounded geometries: A coupled CFD-Langevin-equation based approach. *International Journal of Multiphase Flow*, 34(9):819–828, 2008b.

- F. G. Fan and G. Ahmadi. A sublayer model for turbulent deposition of particles in vertical ducts with smooth and rough surfaces. *Journal of Aerosol Science*, 24(1): 45–64, 1993.
- M. Fichman, C. Gutfinger, and D. Pnueli. A model for turbulent deposition of aerosols. *Journal of Aerosol Science*, 19(1):123–136, 1988.
- S. K. Friedlander and H. F. Johnstone. Deposition of suspended particles from turbulent gas streams. *Industrial & Engineering Chemistry*, 49(7):1151–1156, 1957.
- C. Greenfield. *Numerical modelling of transport phenomena in reactors*. PhD thesis, Bristol Univesity, 1998.
- A. Guha. A unified eulerian theory of turbulent deposition to smooth and rough surfaces. *Journal of Aerosol Science*, 28(8):1517–1537, 1997.
- M. Guingo and J. P. Minier. A stochastic model of coherent structures for particle deposition in turbulent flows. *Physics of Fluids*, 20(5), 2008.
- T. Hanratty and Y. Mito. Use of a stochastic method to describe dispersion and deposition in an idealized annular flow. In *IUTAM Symposium on Computational Approaches to Multiphase Flow*, pages 31–38. Springer, 2006.
- M. Horn and H. J. Schmid. A comprehensive approach in modeling lagrangian particle deposition in turbulent boundary layers. *Powder Technology*, 186(3):189–198, 2008.
- P. Hutchinson, G. F. Hewitt, and A. E. Dukler. Deposition of liquid or solid dispersions from turbulent gas streams: a stochastic model. *Chemical Engineering Science*, 26(3): 419–439, 1971.
- D. Kaftori, G. Hetsroni, and S. Banerjee. Particle behavior in the turbulent boundary layer. i. motion, deposition, and entrainment. *Physics of Fluids*, 7:1095, 1995a.
- D. Kaftori, G. Hetsroni, and S. Banerjee. Particle behavior in the turbulent boundary layer. ii. velocity and distribution profiles. *Physics of Fluids*, 7:1107, 1995b.
- G. A. Kallio and M. W. Reeks. A numerical simulation of particle deposition in turbulent boundary layers. *International Journal of Multiphase Flow*, 15(3):433–446, 1989.

- J. Kim, P. Moin, and R. Moser. Turbulence statistics in fully developed channel flow at low Reynolds number. *Journal of Fluid Mechanics*, 177:133–166, 1987.
- S. J. Kline, W. C. Reynolds, F. A. Schraub, and P. W. Runstadler. The structure of turbulent boundary layers. *Journal of Fluid Mechanics*, 30(04):741–773, 1967.
- B. Y. H. Liu and J. K. Agarwal. Experimental observation of aerosol deposition in turbulent flow. *Journal of Aerosol Science*, 5(2):145–148, IN1–IN2, 149–155, 1974.
- T. S. Luchik and T. W. G. Tiederman. Timescale and structure of ejections and bursts in turbulent channel flows. *Journal of Fluid Mechanics*, 174:529–552, 1987.
- J. M. MacInnes and F. V. Bracco. Stochastic particle dispersion modeling and the tracer-particle limit. *Physics of Fluids A: Fluid Dynamics*, 4:2809, 1992.
- C. Marchioli and A. Soldati. Mechanisms for particle transfer and segregation in a turbulent boundary layer. *Journal of Fluid Mechanics*, 468:283–315, 2002.
- C. Marchioli, A. Giusti, M. Vittoria Salvetti, and A. Soldati. Direct numerical simulation of particle wall transfer and deposition in upward turbulent pipe flow. *International Journal of Multiphase Flow*, 29(6):1017–1038, 2003.
- C. Marchioli, M. Picciotto, and A. Soldati. Particle dispersion and wall-dependent turbulent flow scales: implications for local equilibrium models. *Journal of Turbulence*, (7), 2006.
- E. A. Matida, K. Nishino, and K. Torii. Statistical simulation of particle deposition on the wall from turbulent dispersed pipe flow. *International Journal of Heat and Fluid Flow*, 21(4):389–402, 2000.
- M. R. Maxey and J. J. Riley. Equation of motion for a small rigid sphere in a nonuniform flow. *Physics of Fluids*, 26:883, 1983.
- D. D. McCoy and T. J. Hanratty. Rate of deposition of droplets in annular two-phase flow. *International Journal of Multiphase Flow*, 3(4):319–331, 1977.
- J. B. McLaughlin. Aerosol particle deposition in numerically simulated channel flow. *Physics of Fluids A: Fluid Dynamics*, 1:1211, 1989.

- A. Mehel, A. Tanière, B. Oesterlé, and J. R. Fontaine. The influence of an anisotropic langevin dispersion model on the prediction of micro-and nanoparticle deposition in wall-bounded turbulent flows. *Journal of Aerosol Science*, 41(8):729–744, 2010.
- G. N. Mil'shtein. A method of second order accuracy integration of stochastic differential equations. *Teoriya Veroyatnostei i ee Primeneniya*, 23(2):414–419, 1978.
- Y. Mito and T. J. Hanratty. Use of a modified langevin equation to describe turbulent dispersion of fluid particles in a channel flow. *Flow, turbulence and combustion*, 68(1):1–26, 2002.
- S. A. Morsi and A. J. Alexander. An investigation of particle trajectories in two-phase flow systems. *Journal of Fluid Mechanics*, 55(02):193–208, 1972.
- C. Narayanan, D. Lakehal, L. Botto, and A. Soldati. Mechanisms of particle deposition in a fully developed turbulent open channel flow. *Physics of Fluids*, 15(3):763–775, 2003.
- P. Nerisson, O. Simonin, L. Ricciardi, A. Douce, and J. Fazileabasse. Improved cfd transport and boundary conditions models for low-inertia particles. *Computers & Fluids*, 40(1):79–91, 2011.
- P. R. Owen. Pneumatic transport. *Journal of Fluid Mechanics*, 39(02):407–432, 1969.
- S. Parker, T. Foat, and S. Preston. Towards quantitative prediction of aerosol deposition from turbulent flows. *Journal of Aerosol Science*, 39(2):99–112, 2008.
- M. Picciotto, C. Marchioli, M. W. Reeks, and A. Soldati. Statistics of velocity and preferential accumulation of micro-particles in boundary layer turbulence. *Nuclear Engineering and Design*, 235(10-12):1239–1249, 2005.
- S. B. Pope. *Turbulent Flows*. Cambridge University Press, 2000.
- M. W. Reeks. The transport of discrete particles in inhomogeneous turbulence. *Journal of Aerosol Science*, 14(6):729–739, 1983.
- M. W. Reeks. On a kinetic equation for the transport of particles in turbulent flows. *Physics of Fluids A: Fluid Dynamics*, 3:446, 1991.

- A. Soldati and C. Marchioli. Physics and modelling of turbulent particle deposition and entrainment: Review of a systematic study. *International Journal of Multiphase Flow*, 35(9):827–839, 2009.
- D. C. Swailes and M. W. Reeks. Particle deposition from a turbulent flow. i. a steady-state model for high inertia particles. *Physics of Fluids*, 6:3392, 1994.
- D. J. Thomson. Criteria for the selection of stochastic models of particle trajectories in turbulent flows. *Journal of Fluid Mechanics*, 180(7):529–556, 1987.
- L. Tian and G. Ahmadi. Particle deposition in turbulent duct flows - comparisons of different model predictions. *Journal of Aerosol Science*, 38(4):377–397, 2007.
- W. S. J Uijtewaal and R. V. A. Oliemans. Particle dispersion and deposition in direct numerical and large eddy simulations of vertical pipe flows. *Physics of Fluids*, 8:2590, 1996.
- Q. Wang and K. D. Squires. Large eddy simulation of particle deposition in a vertical turbulent channel flow. *International Journal of Multiphase Flow*, 22(4):667–682, 1996.
- T. Wei and W. W. Willmarth. Examination of v-velocity fluctuations in a turbulent channel flow in the context of sediment transport. *Journal of Fluid Mechanics*, 223:241–252, 1991.
- W. W. Willmarth and S. S. Lu. Structure of the reynolds stress near the wall. *Journal of Fluid Mechanics*, 55(01):65–92, 1972.
- J. Young and A. Leeming. A theory of particle deposition in turbulent pipe flow. *Journal of Fluid Mechanics*, 340:129–159, 1997.
- L. I. Zaichik, N. I. Drobyshvsky, A. S. Filippov, R. V. Mukin, and V. F. Strizhov. A diffusion-inertia model for predicting dispersion and deposition of low-inertia particles in turbulent flows. *International Journal of Heat and Mass Transfer*, 53(1-3):154–162, 2010.
- H. Zhang and G. Ahmadi. Aerosol particle transport and deposition in vertical and horizontal turbulent duct flows. *Journal of Fluid Mechanics*, 406(1):55–88, 2000.

# Chapter 5

## The effects of near wall corrections of hydrodynamic forces on the particle deposition and dispersion in turbulent boundary layers

### 5.1 Introduction

In the Lagrangian particle tracking approach used for modelling particle-laden two-phase flows, rigid, spherical particles are usually approximated as point particles. A complex two-phase problem thus can be significantly simplified through the point particle approximation, i.e. individual particles regarded as mathematical point sources of mass, momentum and energy without physical size. However, this approximation requires further examination, especially the inherent assumption that the size of particles is less than the smallest local length scale in the underlying flow field. On the other hand, the Lagrangian particle tracking approach faces a difficult choice of multiple forces exerted on particles. In this regard, [Maxey and Riley \(1983\)](#) may serve as a theoretical baseline for which forces should be incorporated in the particle equations of motion. For an example, in the scenario when a particle with the ratio of particle density to fluid density

$\rho_p/\rho_f \gg 1$  moves in a steady flow, the added, or virtual, mass force and history force are negligible. The drag force and lift force will determine the motion of particles in the background flow. Then the problem of choosing an appropriate expression for modelling drag and lift force arises.

Numerous expressions for the drag coefficient  $C_D$ , which account for the effect of particle Reynolds number  $Re_p$ , exist. The two most frequently used forms are from [Schiller and Naumann \(1933\)](#) and [Morsi and Alexander \(1972\)](#), respectively. The drag coefficient from [Schiller and Naumann \(1933\)](#) can be written as

$$C_D = \frac{24}{Re_p} \left( 1 + 0.15Re_p^{0.687} \right). \quad (5.1)$$

The above expression reverts to the Stokes relation  $C_D = 24/Re_p$  when  $Re_p \ll 1$ . [Morsi and Alexander \(1972\)](#) proposed the following expression

$$C_D = c_1 + \frac{c_2}{Re_p} + \frac{c_3}{Re_p^2}. \quad (5.2)$$

where  $c_1, c_2, c_3$  are known constants and provided by [Morsi and Alexander \(1972\)](#). Figure 5.1 shows that the expression from [Morsi and Alexander \(1972\)](#) exhibits the correct asymptotic behavior at low as well as high values of  $Re_p$ . Compared to the standard experimental drag-Reynolds-number relationship for rigid, spherical particles, the above two expressions shows no discernible discrepancy. The standard drag correlations from [Schiller and Naumann \(1933\)](#) were used in numerous research efforts that employed sophisticated numerical techniques, i.e. DNS (e.g. [Marchioli and Soldati \(2002\)](#); [Marchioli et al. \(2008\)](#)) or LES (e.g. [Wang and Squires \(1996b,a\)](#)) to solve the incompressible Navier-Stokes equations, coupled with a Lagrangian particle tracking method to study particle-laden two-phase flows. The above two correlations from [Schiller and Naumann \(1933\)](#) and [Morsi and Alexander \(1972\)](#) were all derived for the drag force exerted on a rigid, spherical and steadily moving particle in an unbounded viscous incompressible flow, as was the original Stokes drag law from [Stokes \(1845\)](#). [Chen and McLaughlin \(1995\)](#) were the first to consider the wall effect on the Stokes drag to study particle deposition. The nonlinear drag law was not employed in the work of [Chen and McLaughlin](#)

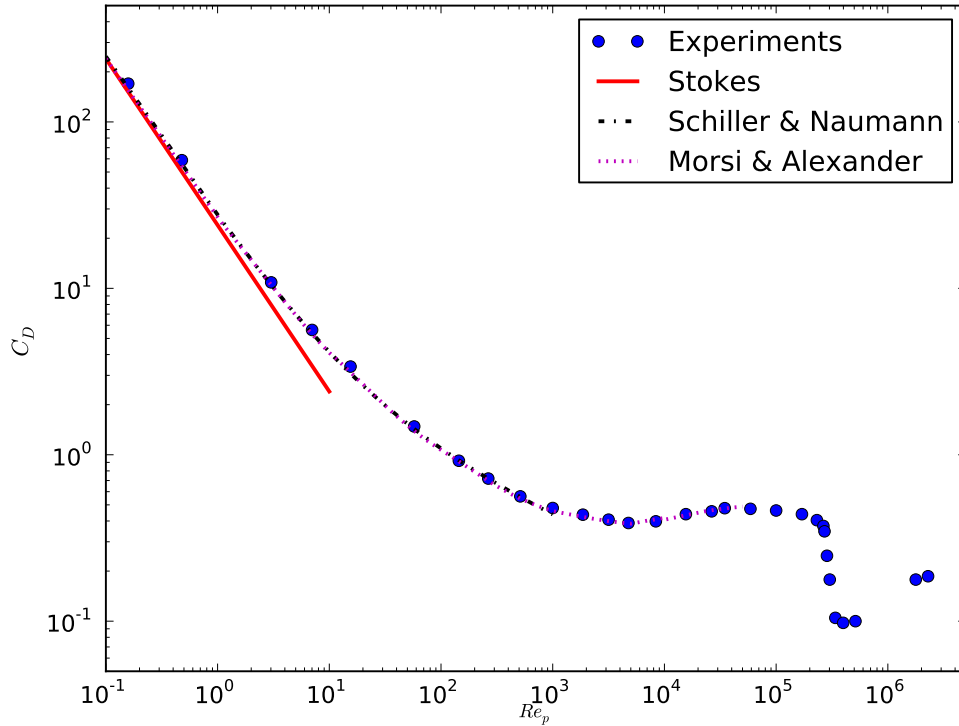


Figure 5.1: Drag Coefficient  $C_D$  as a function of the particle Reynolds number  $Re_p$  for a rigid spherical particle

(1995) as they regarded  $Re_p \ll 1$ , although this is not always the case for deposition of particles (see [Kallio and Reeks \(1989\)](#); [McLaughlin \(1989\)](#); [Marchioli et al. \(2006\)](#)).

The lift force can play a part in the process of particle deposition but is also one of the most difficult forces to be properly modelled. The Saffman lift force, which is the most frequently studied shear-induced lift force, takes the form

$$f_l = 1.615d_p^2(\rho\mu)^{1/2} \left( \left| \frac{du_x}{dy} \right| \right)^{1/2} (u_x - u_{px}), \quad (5.3)$$

where  $\rho$  and  $\mu$  denote the fluid density and dynamics viscosity respectively,  $d_p$  represents the radius of the rigid spherical particle,  $u_{px}$  and  $u_x$  are particle velocity fluid velocity at the particle centroid in the  $x$  – direction and  $du_x/dy$  is the gradient of fluid velocity or the shear rate of the mean flow. Saffman assumed that the particle Reynolds number based on relative velocity,  $Re_p = |u_x - u_{px}|d_p/\nu$ , and that based on velocity gradient  $G$

at the particle centre,  $Re_G = Gd_p^2/\nu$ , are both very much less than 1, and that  $Re_p \ll Re_G$ . According to Eq: 5.3, the relative velocity ( $u_x - u_{px}$ ) between the particle and surrounding fluid and the shear rate determine  $f_l$ , the lift force acting on a rigid spherical particle moving in a unbounded, unidirectional and steady linear shear flow. [Kallio and Reeks \(1989\)](#) employed the relation derived by [Saffman \(1965, 1968\)](#) to account for the lift force exerting on a rigid, spherical particle moving within a fully developed turbulent boundary layer. They observed an increase of deposition rate of heavy particles resulting from the Saffman lift force. [McLaughlin \(1989\)](#) included this same form derived by Saffman for lift force in the particle equation of motion to study aerosol particle deposition in a turbulent channel flow, in which the incompressible three-dimensional Navier-Stokes equations were solved through DNS calculations. [McLaughlin \(1989\)](#) found that the Saffman lift force plays a significant role both in the inertial deposition of particles and in the accumulation of trapped particles within the viscous sublayer where the gradient of streamwise fluid velocity has the highest value across the channel. [McLaughlin \(1991\)](#) and [Mei \(1992\)](#) extended the expression derived by [Saffman \(1965\)](#) to the situation when  $Re_p$  is comparable with, or larger than the square root of  $Re_G$ . [McLaughlin \(1993\)](#); [Cherukat and McLaughlin \(1994\)](#) further developed expressions for the lift force exerted on a particle in a wall-bounded linear shear flow and for the wall-induced lift force when a particle lies in a linear shear flow field near a flat wall. Based on the above research, [Chen and McLaughlin \(1995\)](#) considered wall-induced and shear-induced lift in the particle equation of motion to study particle deposition coupled with a DNS channel flow.

There have been some research efforts to take into account the wall effects on the drag force combined with different expressions for the lift force. [Wang et al. \(1997\)](#) developed an “optimum” form that combines both the shear-induced part and wall-induced part of the lift force on a particle in a wall-bounded shear flow. [Lataste et al. \(2000\)](#) studied the importance of the shear-induced lift force on a particle in a turbulent boundary layer. They found that the shear-induced lift force plays a significant role in the near wall region. Furthermore, they observed that the formulation from [Cherukat and McLaughlin \(1994\)](#) for the lift force gives the best results when compared with experiments. In the DNS calculations of particle-laden channel flows from [Arcen et al. \(2006\)](#), the drag force

was corrected for the presence of a wall, according to the direction of motion the particle, i.e. a particle moving parallel or perpendicular to the wall; the lift force was taken the form derived by [Cherukat and McLaughlin \(1994\)](#). They found that even the inclusion of the most accurate treatment of lift force and drag force for the wall effects does not give rise to significant changes in the statistical properties of the dispersed particle phase, except for the high inertia particles.

[Bagchi and Balachandar \(2003\)](#) studied the effect of turbulence on the drag and lift force acting on a rigid, spherical particle suspended in a free-stream isotropic turbulent flow through DNS calculations. They observed that the standard drag correlation from [Schiller and Naumann \(1933\)](#), based on the instantaneous or mean relative velocity results in a reasonably accurate prediction of the mean drag acquired from DNS calculations. This indicates that the standard drag correlation is applicable to turbulent dispersed particle flow as well. They also demonstrated that the mean drag is insensitive to the fluid velocity measured at the particle center, or acquired by averaging over a fluid volume of the order of the particle size. This confirms that the point particle approach is an acceptable approximation for small particles.

The objective of this chapter is to study the effects of near wall corrections to the hydrodynamic forces on particle deposition and dispersion characteristics in fully developed turbulent boundary layers. Brand new composite correlations for  $C_D$  and  $C_L$  were proposed by [Zeng et al. \(2009\)](#) and [Lee and Balachandar \(2010\)](#), who used DNS with the immersed boundary method (IBM) to fully resolve the flow field around a fixed or moving rigid spherical particle in a wall-bounded shear flow. In order to judge the influence of near wall corrections, three different cases of simulations are performed. The first case is concerned with the standard drag law  $C_D$  and with near wall corrected  $C_D$  from [Zeng et al. \(2009\)](#); the second case focuses on the inclusion of the Saffman lift force with the standard drag law  $C_D$  in the particle equation of motion; the final case studies the inclusion of the wall corrected  $C_L$  with the standard drag law. The comparison is made based on particle deposition rates, mean streamwise particle velocities and wall-normal r.m.s. velocities.

## 5.2 Corrections of hydrodynamic forces

As stated in [Clift et al. \(1978\)](#), in terms of the analytical solutions for flow around rigid and circulating particles, the effect of containing walls is to change the boundary conditions for the equations of motion and continuity of the continuous phase. The corrections for  $C_D$  in presence of containing walls were achieved through either analytical methods (see [Brenner \(1961\)](#); [Goldman et al. \(1967\)](#)) or numerical simulations (see [Zeng et al. \(2009\)](#); [Lee and Balachandar \(2010\)](#)).

### 5.2.1 Near wall correction for the drag force

The drag force resists relative velocity between the particle and surrounding fluid and is therefore defined as

$$\mathbf{F}_D = -\frac{1}{2}\rho_f |\mathbf{u}_p - \mathbf{u}| (\mathbf{u}_p - \mathbf{u}) A_p C_D, \quad (5.4)$$

where  $\rho_f$  is the fluid density,  $A_p$  is the projected area of the particle, equalling  $\pi d_p^2/4$  for a rigid spherical particle, and  $C_D$  is the drag coefficient which is a function of particle Reynolds number  $Re_p$ . When the particle Reynolds number  $Re_p \ll 1$ ,  $C_D$  is given by  $24/Re_p$  so that Eq: 5.4 reverts to the Stokes formula. In this study,  $C_D$  is also dependent upon the distance of the particle center from the wall and so this unbounded flow result requires corrections.

The problem of the approach a rigid spherical particle to a nearby plane wall in a viscous fluid constitutes an entire field of research. [Brenner \(1961\)](#) developed an expression for the corrections to Stokes's law necessitated by the presence of a plane boundary at a finite distance from the particle when the particle moves normal to the wall. It can be written as

$$C_D \cong \left(1 + \frac{9 d_p}{8 2L}\right) \frac{24}{Re_p}, \quad (5.5)$$

where  $L$  is the distance from the center of the particle to the nearby wall. [Goldman et al. \(1967\)](#) further analysed a particle moving parallel to a plane wall through still fluid, and

proposed the following correction

$$C_D = \left[ 1 - \frac{9}{16} \left( \frac{d_p}{2L} \right) + \frac{1}{8} \left( \frac{d_p}{2L} \right)^3 - \frac{45}{256} \left( \frac{d_p}{2L} \right)^4 - \frac{1}{16} \left( \frac{d_p}{2L} \right)^5 \right]^{-1} \frac{24}{Re_p}. \quad (5.6)$$

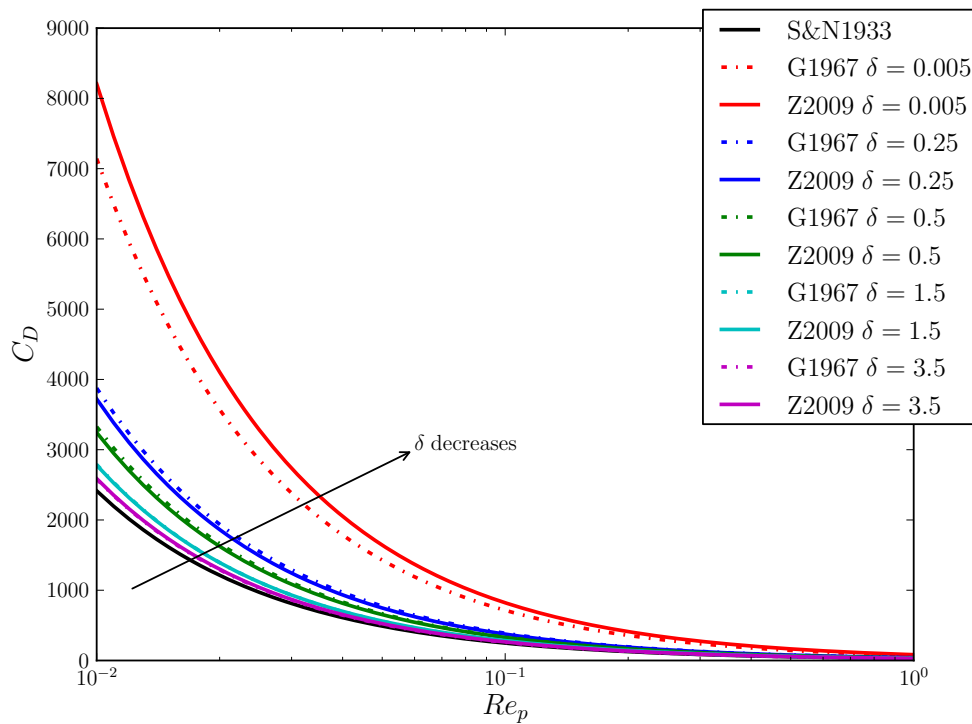
Zeng et al. (2009) proposed a composite drag coefficient for a particle, moving through still fluid, parallel to a plane wall. Further, the drag coefficient is valid for a wide range of  $Re_p$  and distance from the wall. It is given by

$$C_D = \left\{ 1 + 0.15 \left[ 1 - \exp(-\sqrt{\delta}) \right] Re_p^{[0.687 + 0.313 \exp(-2\sqrt{\delta})]} \right\} C_{D0}, \quad (5.7)$$

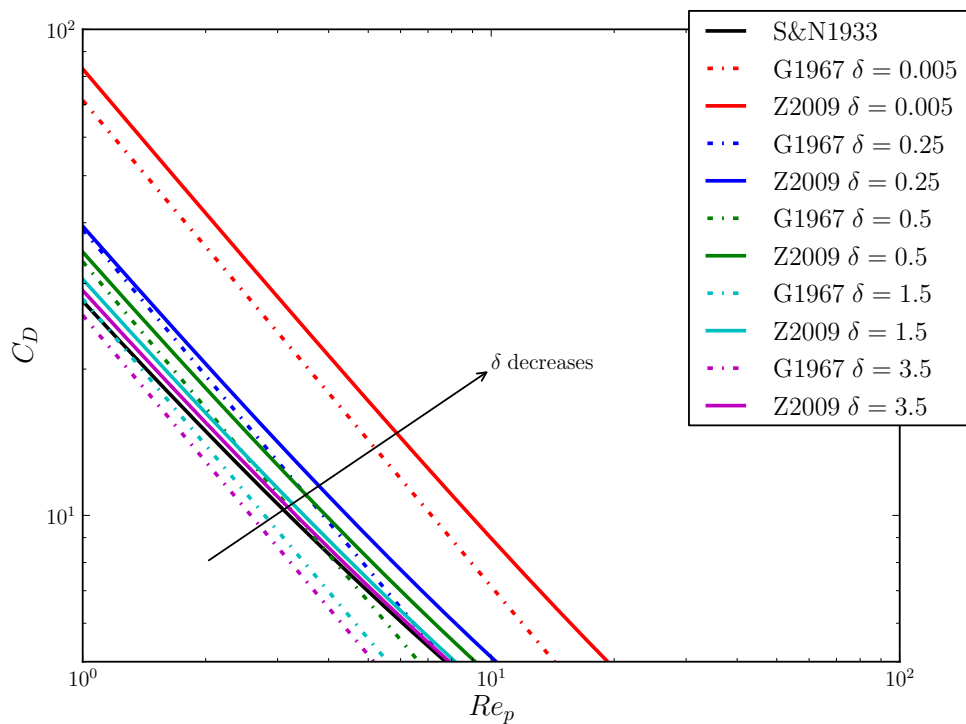
where

$$C_{D0} = \left[ 1.028 - \frac{0.07}{1 + 4\delta^2} - \frac{8}{15} \ln \left( \frac{270\delta}{135 + 256\delta} \right) \right] \frac{24}{Re_p}, \quad \delta = \frac{L}{d_p} - 0.5. \quad (5.8)$$

The above expressions for a particle moving parallel to a wall are shown in figure 5.3 and compared to the standard drag law from Schiller and Naumann (1933). They are plotted as a function of  $Re_p$  for different values of normalised gap between the particle and wall,  $\delta = L/d_p - 0.5$ . It can be seen that as a particle moves closer to a nearby wall, the drag coefficient  $C_D$  rises. In particular,  $C_D$  experiences a significant increase when the gap is vanishingly small (e.g.  $\delta = 0.005$ ). On the other hand, the expressions for  $C_D$  from Goldman et al. (1967) and Zeng et al. (2009) collapse into the standard drag law when the particle moves farther away from the nearby wall. It must be noted that the wall effects would be additionally affected by the shear flow in the vicinity of the wall and the rotation of a particle (see Goldman et al. (1967); Lee and Balachandar (2010)). Whilst being very complete, the composite correlations of Lee and Balachandar (2010) are extremely complex and unwieldy and, although the present author did try to include them in the particle deposition model, the resulting model was not sufficiently robust to provide useful solutions. Since the additional shear and rotation corrections are relatively small, the composite correlation for  $C_D$  from Zeng et al. (2009) is regarded as the most accurate practical representation of drag force acting on a particle moving parallel to a wall for use in the present study. This enabled comparison of particle deposition



(a)



(b)

Figure 5.2: Comparison of corrections for  $C_D$ , (a)  $Re_p < 1$ , (b)  $Re_p > 1$ .

and dispersion characteristics through the inclusion of the composite correlation from [Zeng et al. \(2009\)](#) in the stochastic quadrant model presented in Chapter 4, with results obtained using the standard drag law.

### 5.2.2 Lift force

In this study, it is assumed that each particle attains an equilibrium spin rate and experiences a lift force resulting from vorticity in the underlying carrier-phase. Extending the original Saffman expression for three dimensional flow, and introducing a correction function to account for the Reynolds number dependence of the lift force, Eq: [5.3](#) can become:

$$\mathbf{F}_L = 1.615d_p^2(\rho\mu)^{1/2} \left( \frac{1}{|\boldsymbol{\omega}|} \right)^{1/2} [(\mathbf{u} - \mathbf{u}_p) \times \boldsymbol{\omega}] f(Re_p, Re_G), \quad (5.9)$$

where  $\boldsymbol{\omega}$  is the vorticity of the fluid and the shear Reynolds number  $Re_G$  of the particle is given by:

$$Re_G = \frac{Gd_p^2}{\nu}. \quad (5.10)$$

In a two-dimensional wall bounded linear shear flow,  $|\boldsymbol{\omega}|$  is equal to the shear rate.

Eq: [5.9](#) can be rewritten as

$$\mathbf{F}_L = \frac{1}{2}\rho A_p d_p [(\mathbf{u} - \mathbf{u}_p) \times \boldsymbol{\omega}] \frac{4.1126}{Re_G^{1/2}} f(Re_p, Re_G). \quad (5.11)$$

In the light of the definition of  $C_L$  and from Eq: [5.11](#), the Saffman lift coefficient  $C_{LS}$  is then given by

$$C_{LS} = \frac{4.1126}{Re_G^{1/2}} f(Re_p, Re_G). \quad (5.12)$$

For a creeping flow, the restriction of  $Re_p \ll Re_G^{1/2} \ll 1$  was assumed in the derivation of [Saffman \(1965, 1968\)](#). This condition was relaxed by [McLaughlin \(1991\)](#), and [Mei](#)

(1992), who proposed the following expression for  $f(Re_p, Re_G)$

$$f(Re_p, Re_G) = \begin{cases} \left(1 - 0.3314\alpha^{1/2}\right) \exp\left\{-\frac{Re_p}{10}\right\} + 0.3314\alpha^{1/2} & \text{for } 0 < Re_p \leq 40, \\ 0.0524(\alpha Re_p)^{1/2} & \text{for } Re_p > 40, \end{cases} \quad (5.13)$$

where

$$\alpha = 0.5 \frac{Re_G}{Re_p}. \quad (5.14)$$

In the case of a wall-bounded linear shear flow, the direction of the lift force on a particle is determined by the relative slip velocity from Eq: 5.9, i.e. for a particle moving in a shear flow parallel to a wall, if the particle leads the surrounding fluid, the lift force points to the wall; if particle lags behind the surround fluid, the lift force points away the wall. Hence the lift force causes particles to migrate to the wall or away from the wall.

The presence of a wall has a significant effect on the lift force as well. As far as the shear-induced lift is concerned, Zeng et al. (2009) proposed a composite correlation for  $C_{Ls}$ . The expression reads

$$C_{Ls} = C_{Ls,w} \exp\left\{-0.5\delta \left(\frac{Re_p}{250}\right)^{4/3}\right\} \times \left[\exp\left\{\alpha_{sL}(Re_p)\delta^{\beta_{sL}(Re_p)}\right\} - \lambda_{sL}(\delta, Re_p)\right], \quad (5.15)$$

where

$$\left. \begin{aligned} C_{Ls,w} &= \frac{3.663}{(Re_p^2 + 0.1173)^{0.22}}, \\ \alpha_{sL}(Re_p) &= -\exp\{-0.3 + 0.025 Re_p\}, \\ \beta_{sL}(Re_p) &= 0.8 + 0.01 Re_p, \\ \lambda_{sL}(\delta, Re_p) &= \{1 - \exp\{-\delta\}\} \left(\frac{Re_p}{250}\right)^{5/2}. \end{aligned} \right\} \quad (5.16)$$

Eq: 5.15 is applicable for the circumstance when a stationary particle is positioned in a wall-bounded linear shear flow,  $1 < Re_p < 200$  and even when the particle touches the wall ( $\delta \rightarrow 0$ ). Here, Eq: 5.15 is extended to the situation when  $Re_p < 1$ . This extension seems valid when compared with numerous earlier research efforts focusing on  $Re_p < 1$  (see Zeng et al. (2009)). Figure 5.3a shows that  $C_{Ls}$  results from the combined effect of flow-shear and wall proximity for five dimensionless gap values. Compared to the Saffman lift coefficient with the correction function  $f(Re_p, Re_G)$  set to 1,  $C_{Ls}$

is considerably higher than the Saffman lift coefficient when the gap is vanishingly small. On the other hand, the value of  $C_{L_s}$  is pretty close to the value of the Saffman lift coefficient when  $Re_p \ll 1$  and the gap  $\delta = 3.5$ .

Zeng et al. (2009) proposed a composite lift coefficient  $C_{L_t}$  for a sphere translating through still fluid and parallel to the nearby plane wall. It reads

$$C_{L_t} = f(L, Re_p) + [C_{L_t,w} - f(L = 1/2, Re_p)] \exp \left\{ -11 \left( \frac{\delta}{g(Re_p)} \right)^{1.2} \right\}, \quad (5.17)$$

where

$$f(L, Re_p) = f_0(Re_p) C_{L_t,0}(L^*) L^{f_1(Re_p)}, \quad (5.18)$$

$$\left. \begin{aligned} f_0(Re_p) &= 1 + 0.329 Re_p + 0.00485 Re_p^2 \\ f_1(Re_p) &= -0.9 \tanh(0.022 Re_p) \end{aligned} \right\}, \quad (5.19)$$

$$C_{L_t,0} = \begin{cases} (9/8 + 5.78 \times 10^{-6} L^*) \exp \{-0.292 L^*\} & \text{for } 0 < L^* < 10, \\ 8.94 L^{*-2.09} & \text{for } 10 < L^* < 300, \end{cases} \quad (5.20)$$

$$C_{L_t,w} = 0.313 + 0.812 \exp \{-0.125 Re_p^{0.77}\} \quad (5.21)$$

$$g(Re_p) = 3 \exp \{-0.17 Re_p^{0.7}\}, \quad (5.22)$$

and

$$L^* = \frac{L Re_p}{d_p}. \quad (5.23)$$

Eq: 5.17 is applicable for  $0 < Re_p < 100$  and  $0 < L^* < 300$ . Figure 5.3b shows the curves of  $C_{L_t}$  for five dimensionless gap values almost collapse into a single curve as  $L^*$  decreases below 1.0. Comparing figures 5.3a to 5.3b, it can be observed that the value of  $C_{L_s}$  is much higher than the value of  $C_{L_t}$  when  $Re_p < 1$ . In this study, the shear-induced lift force is considered the dominant lift force. Eq: 5.15 is thus used to study the effects of near wall corrections on the lift force and compare with the Saffman lift force expression for unbounded flow.

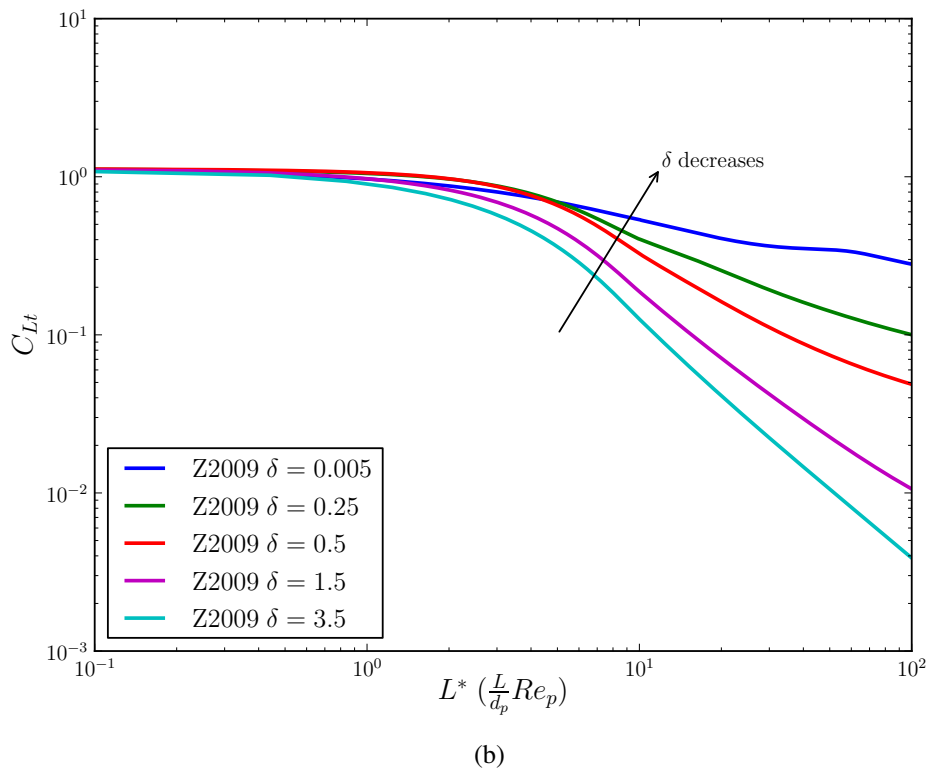
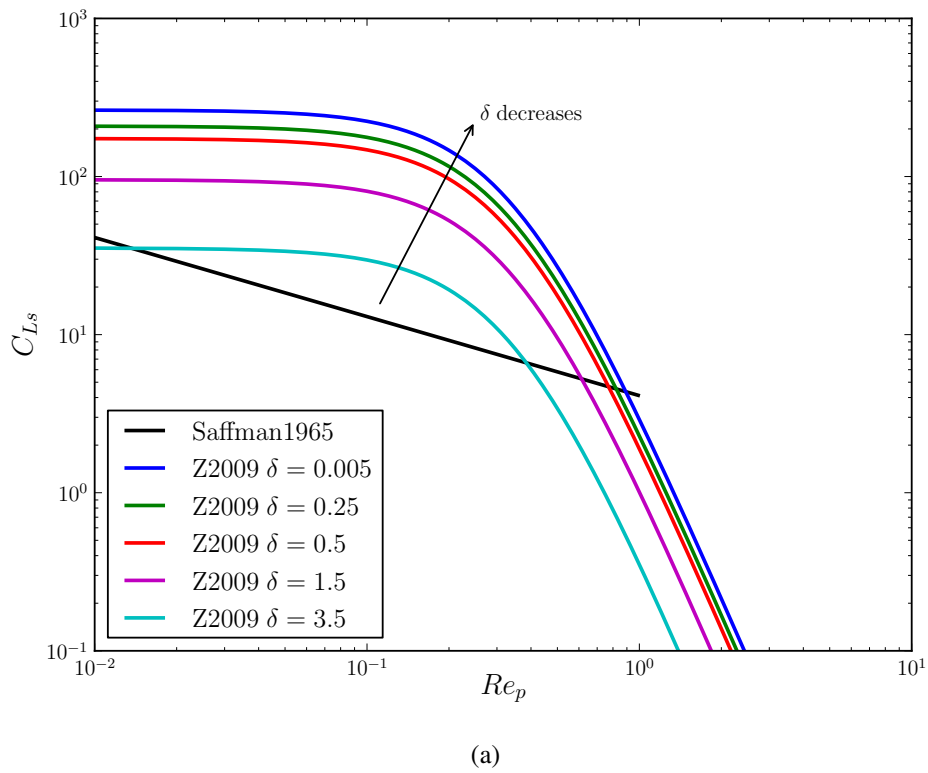


Figure 5.3: Comparison of corrections for  $C_L$ , (a)  $C_{Ls}$  for a particle in a shear flow adjacent to a wall, and compared to the Saffman lift coefficient, (b)  $C_{Lt}$  for a particle translating through still fluid next to a wall.

### 5.3 Modelling methodology

A fully developed turbulent boundary layer at  $Re_\tau = 200$  was solved by a RANS calculation with the standard  $k - \varepsilon$  turbulence model and enhanced-wall treatment, using ANSYS Fluent v.12.0. Particle of various ( $\tau_+$ ) were then tracked through this flow field, using the methodology described in Chapter 4, and deposition and dispersion data were recorded. The size of rigid spherical particles is restricted to smaller than the size of the first wall-adjacent cell  $\Delta y^+ = 1$ . As a consequence, the point particle approach is taken. The volume fraction of the particle phase is small enough so that one-way coupling is assumed. Furthermore, the density ratio of particle to fluid obeys  $\rho_p/\rho_f \gg 1$ , so that the non-linear drag force and shear-induced lift force are considered only. Therefore, the particle equation of motion reads

$$\frac{d\mathbf{u}_p}{dt} = \frac{1}{\tau_p} C_D \frac{Re_p}{24} (\mathbf{u} - \mathbf{u}_p) + \frac{\mathbf{f}_L}{m_p}, \quad (5.24)$$

where  $\mathbf{u}_p, \mathbf{u}$  are the particle velocity and instantaneous fluid velocity at the particle center,  $\tau_p$  is particle response time defined as  $\rho_p d_p^2 / 18\mu$ ,  $\mathbf{f}_L$  is the shear-induced lift force. Both the drag coefficient  $C_D$  and lift coefficient  $C_L$  are corrected for the wall effect.

In RANS calculations, the instantaneous fluid velocity is decomposed into two parts,

$$\mathbf{u} = \bar{\mathbf{U}} + \mathbf{u}', \quad (5.25)$$

where  $\bar{\mathbf{U}}$  is solved by the RANS calculation,  $\mathbf{u}'$  is fluid velocity fluctuations. For a fully developed turbulent boundary layer in this chapter, only the wall normal fluctuation is provided by the stochastic quadrant model presented in Chapter 4 in order to account for the turbulence effect on the particle dispersion.

### 5.4 Results and discussions

The results presented here were obtained from four sets of particles characterized by different particle Stokes number making use of the standard drag  $C_D$ , near-wall correction

of  $C_D$  from [Zeng et al. \(2009\)](#),  $C_L$  from [Saffman \(1965\)](#) and near-wall correction of  $C_L$  from [Zeng et al. \(2009\)](#) in the particle equation of motion, respectively. The Stokes number used were  $St = 2, 5, 10$  and  $20$ , made dimensionless through the characteristic time  $\nu/u_\tau^2$  and particle-to-fluid density ration  $\rho_p/\rho = 770$ . Statistics for the dispersed particle phase were based on  $5 \times 10^4$  particles released initially. The boundary condition of the nearby wall was assumed to perfectly absorbing when the particle centroid was a radius away from the wall surface.

## 5.4.1 Near-wall corrections of $C_D$

### 5.4.1.1 Particle deposition

The effects of near-wall correction of  $C_D$  on the deposition rate of heavy particles were studied first. The results for deposition rates of fourteen sets of heavy particles are shown in figure 5.4 and compared with the experimental measurements from [Liu and Agarwal \(1974\)](#) and the curve-fit of [McCoy and Hanratty \(1977\)](#). While the two expressions from Eqs: 5.2 and 5.7 for  $C_D$  does not yield significant change on the deposition rates for the particles considered, the overall effect of the near-wall correction is that it reduces the deposition rates of small particles and increases the deposition rates of large particles. This may be explained as follows: When a small particle gets into the region within 3.5 times the particle diameter through diffusion, the particle experiences considerably higher drag as a result of the wall-effects and its small  $Re_p$ ; this helps the particle to coast along the vicinity of the near wall and reduces deposition. As far as large particles are concerned, they normally have higher velocity fluctuations in the near wall region. The increase of drag force due to the wall-effects is not strong enough to modify their velocity to the local equilibrium values of fluid velocity. These large particles get deposited by their own inertia. Moreover, the increased drag may prevent particles escaping from the near wall region. For instance, if a particle experiences ejection events resulting form quadrant II, the increased drag may reduce the escape probability of the particle away from the wall along the encountered ejection. Therefore, the near-wall correction of  $C_D$  has opposite effects on the deposition rates.

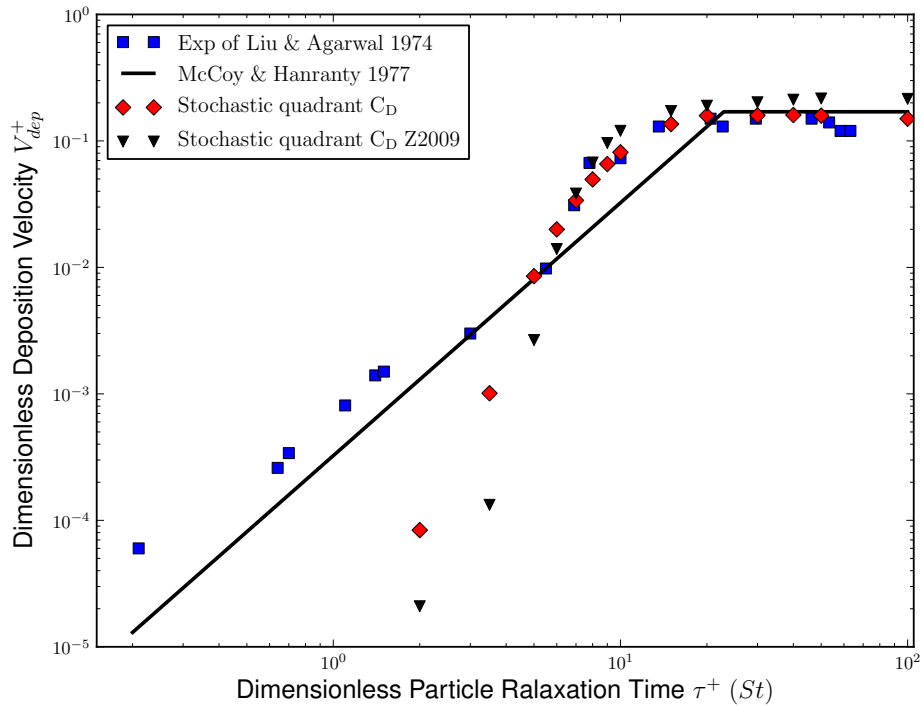


Figure 5.4: Deposition comparison with the standard drag law  $C_D$  and near-wall corrections from Zeng et al. (2009)

#### 5.4.1.2 Mean streamwise and wall normal r.m.s velocities

Figure 5.5 and 5.6 show a comparison of mean streamwise particle velocities as a function of  $y^+$ . The results were obtained from the two expressions for  $C_D$  and are compared with the mean streamwise fluid velocities. It can be observed that there is no discernible difference between the standard drag law  $C_D$  and corrected  $C_D$  for the particles of Stokes number  $St = 2, 5, 10$ . However, The mean streamwise particle velocities for particles of Stokes number  $St = 20$  acquired from the corrected  $C_D$  simulation diverge significantly from the fluid velocities. The standard drag  $C_D$  yields much less divergence from the fluid velocities. In fact, the phenomena that values of streamwise particle velocities are significantly higher than that of fluid velocities in the near wall region is the correct, as confirmed by experiments by Kulick et al. (1994) and numerical simulations from Wang and Squires (1996b). Therefore, the near-wall corrected  $C_D$  produce more correct near-wall behavior for large particles. However, for small particles, the mean streamwise velocities of small particles ( $St = 2, 5$ ) are lower than the counterpart of fluid in the near

wall region. This might result from the fact that the streamwise fluid velocity fluctuations were not incorporated in the present study. From the wall-normal particle and fluid r.m.s velocities shown in Figure 5.7 and 5.8, it can be observed that there is no statistical difference for the two sets of particles of Stokes number  $St = 2, 5$ . The corrected  $C_D$ , however, increases the particle of Stokes number  $St = 20$  wall-normal r.m.s values in the near wall region.

## 5.4.2 Near-wall corrections of $C_L$

### 5.4.2.1 Particle deposition

From figure 5.9, it is evident that the inclusion of lift force into the particle equation of motion does not result in significant change in the deposition rates of particle sizes considered. The two expressions for  $C_L$  produce reduced deposition rates for the smallest particle with Stokes number  $St = 2$ . This contrasts with the previously reported results on the effects of lift force upon particle depositions (see Kallio and Reeks (1989); Wang et al. (1997)). From previous discussions, the present stochastic quadrant model, which does not incorporate the streamwise fluid velocity fluctuations, causing inertial particles to move incorrectly slower than fluid particles in the near-wall region. According to the definition of lift force expressed in Eq 5.11, a positive velocity difference between particles and surrounding fluid results in a lift directed away from the wall. Thus, it reduces the deposition rates of small particles. If, on the other hand, inclusion of streamwise fluid velocity fluctuations in the present stochastic quadrant model did produce the correct near-wall particle behavior, with stream-wise inertial particle velocities exceeding fluid velocities in the near-wall region, then the near-wall corrected  $C_L$  would generate higher deposition rates than the standard lift coefficient  $C_L$  does.

### 5.4.2.2 Mean streamwise and wall normal r.m.s velocities

Figure 5.10 and 5.11 suggest that the inclusion of the lift force in the particle equation of motion does not have any significant effect on the mean streamwise particle velocities

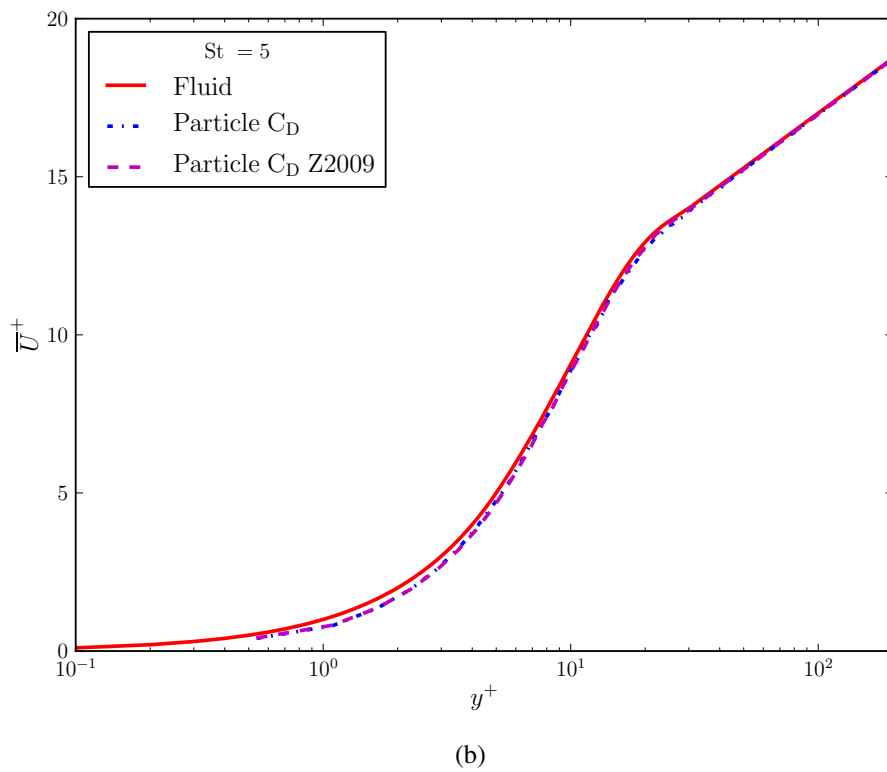
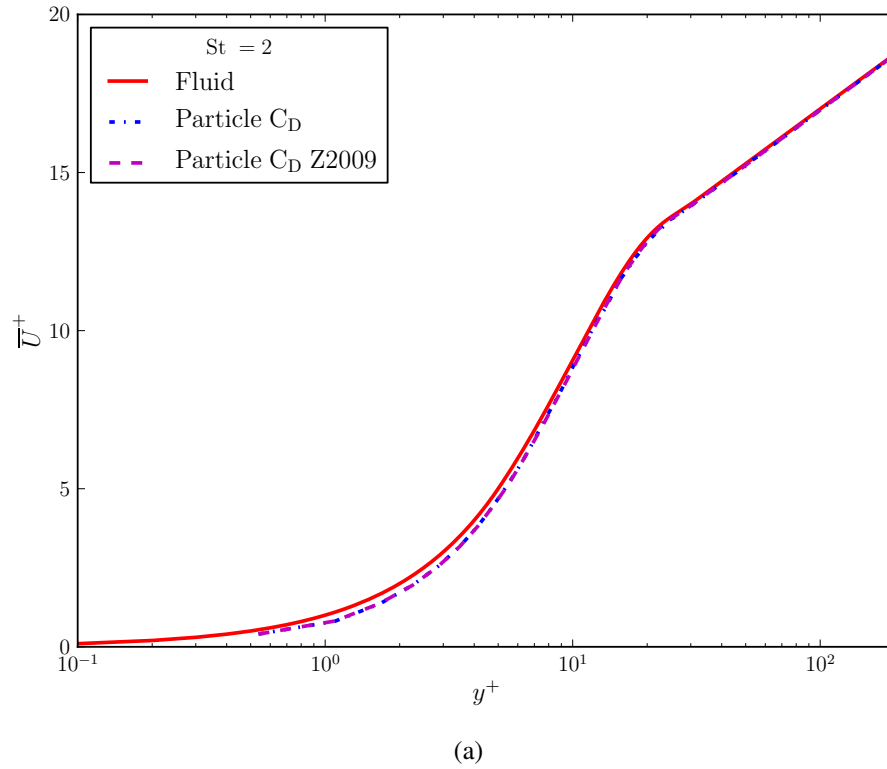


Figure 5.5: Comparison of mean streamwise particle velocities with the standard drag law  $C_D$  and near-wall corrections from Zeng et al. (2009) and compared to the fluid velocities (a)  $St = 2$ , (b)  $St = 5$ .

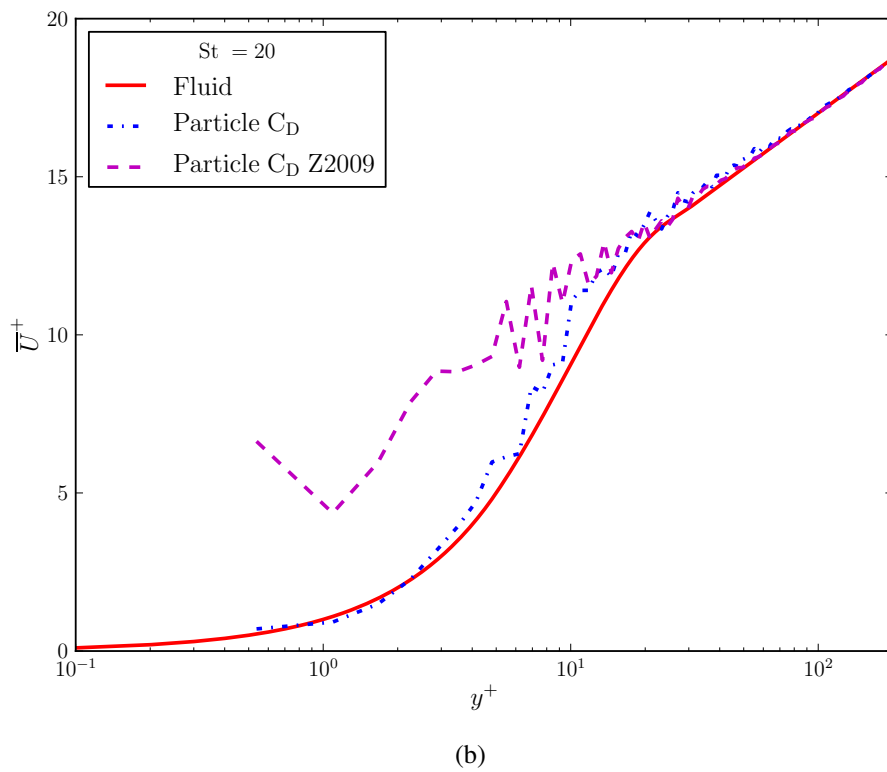
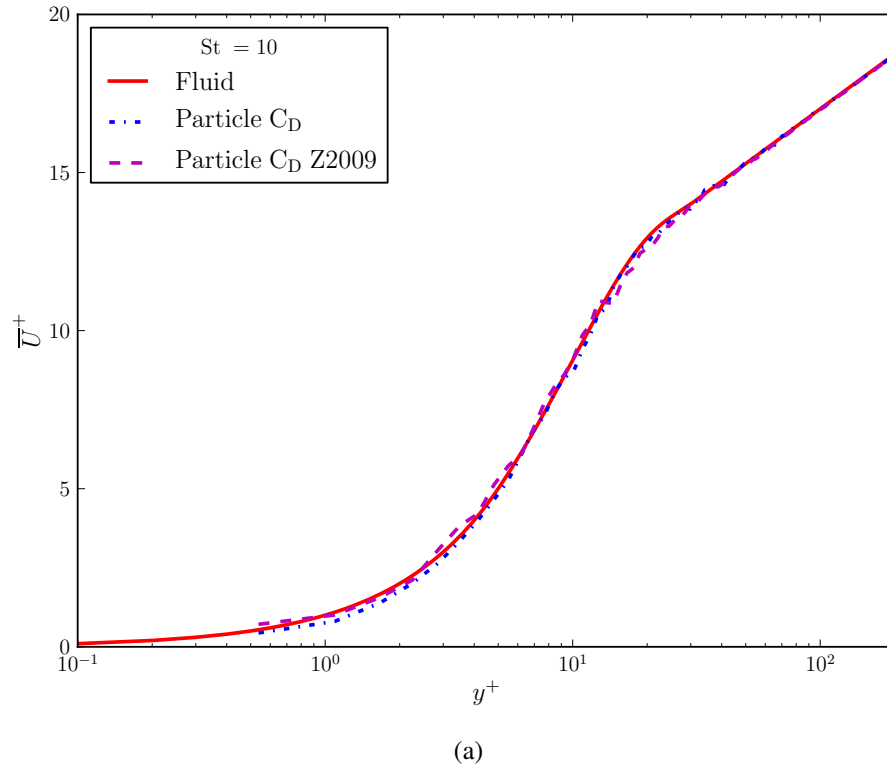
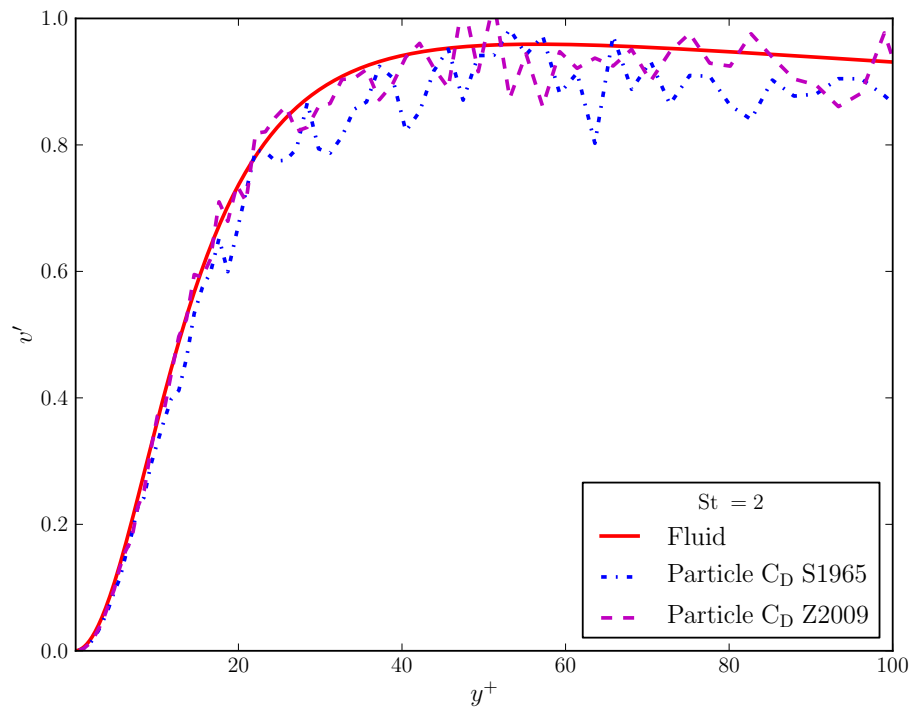
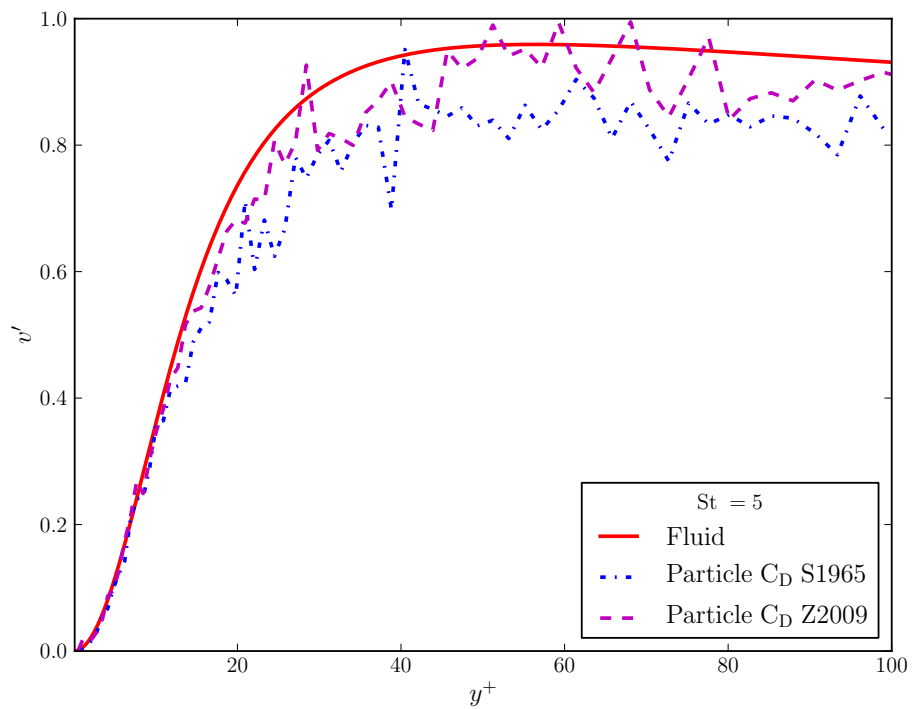


Figure 5.6: Comparison of mean streamwise particle velocities with the standard drag law  $C_D$  and near-wall corrections from Zeng et al. (2009) and compared to the fluid velocities (a)  $St = 10$ , (b)  $St = 20$ .

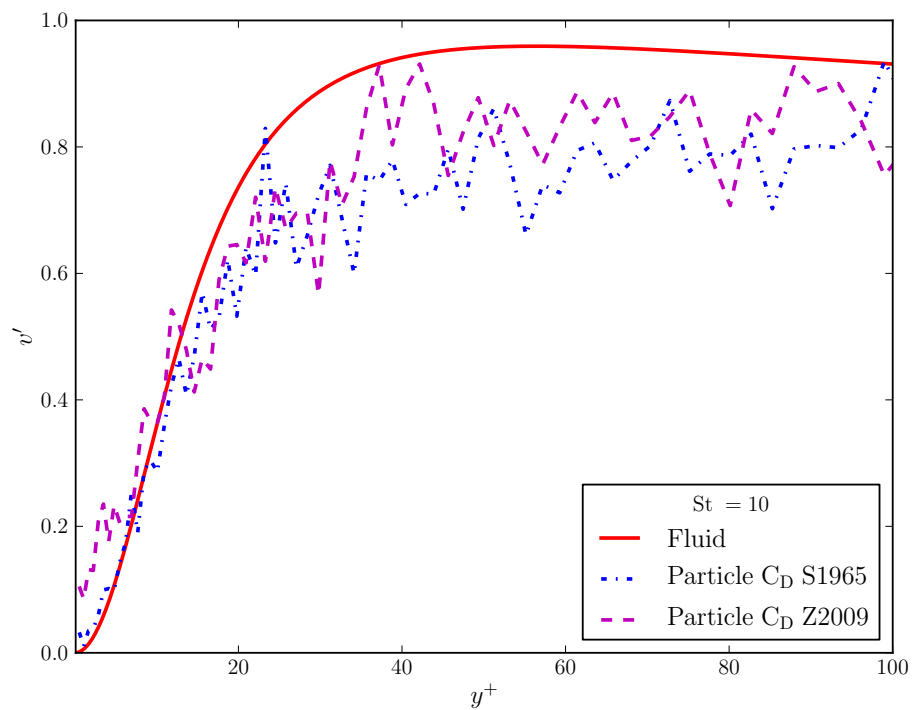


(a)

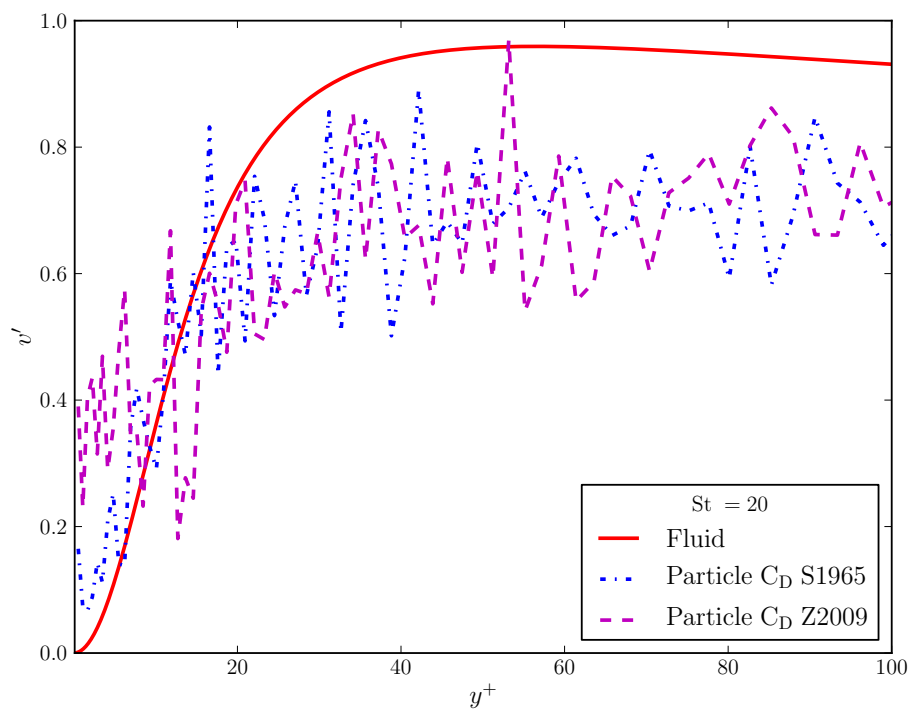


(b)

Figure 5.7: Comparison of wall-normal particle r.m.s velocities with the standard drag law  $C_D$  and near-wall corrections from Zeng et al. (2009) and compared to the fluid r.m.s. velocities (a)  $St = 2$ , (b)  $St = 5$ .



(a)



(b)

Figure 5.8: Comparison of wall-normal particle r.m.s velocities with the standard drag law  $C_D$  and near-wall corrections from Zeng et al. (2009) and compared to the fluid r.m.s. velocities (a)  $St = 10$ , (b)  $St = 20$ .

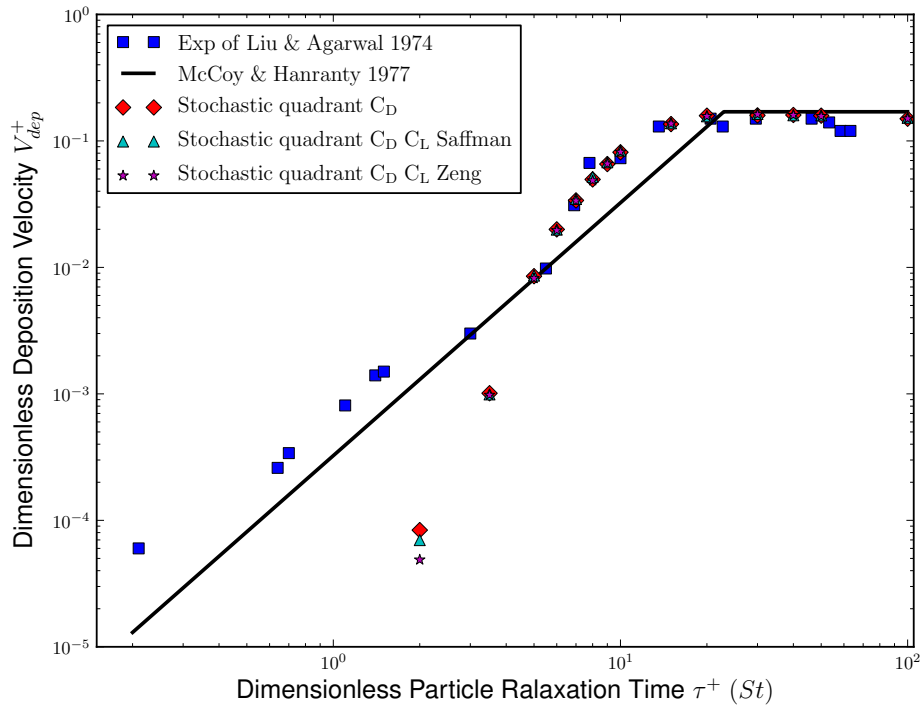
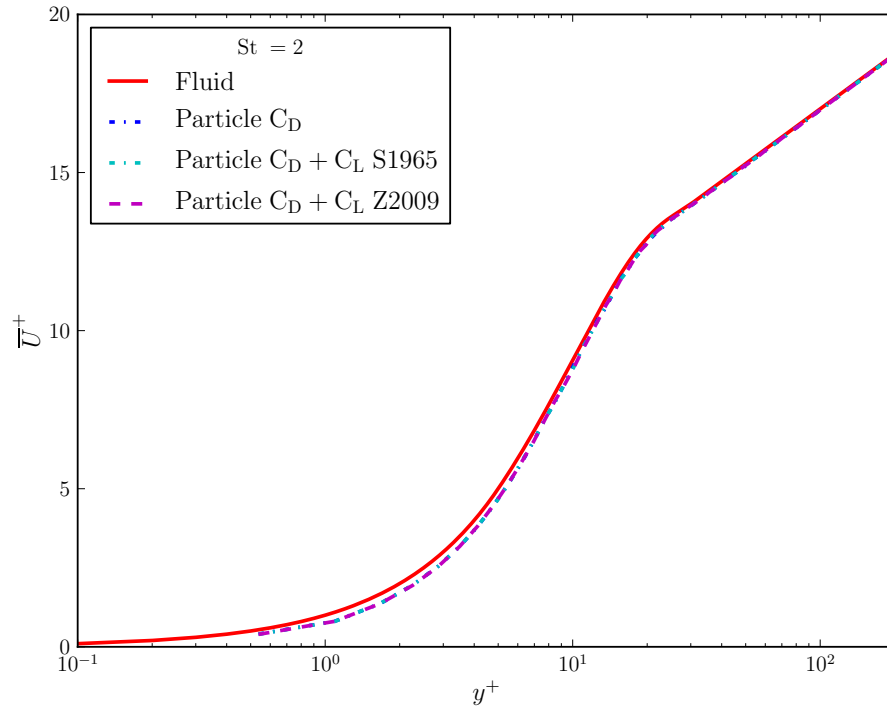
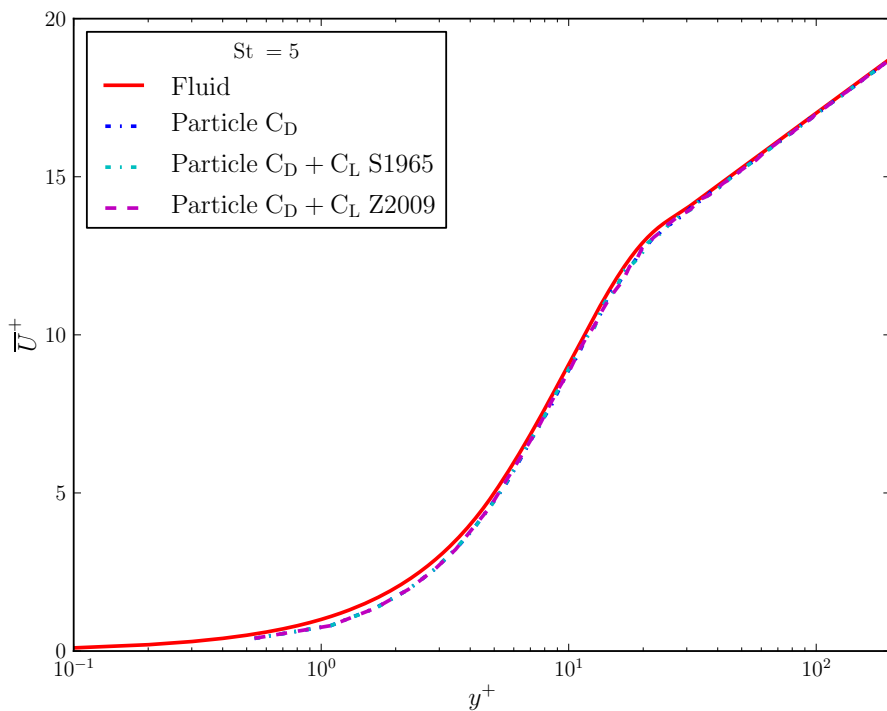


Figure 5.9: Deposition comparison with the standard drag law  $C_D$  and Saffman lift coefficient  $C_L$  and  $C_L$  with near-wall corrections from Zeng et al. (2009)

for Stokes number  $St = 2, 5$  or  $10$ . The near-wall corrected  $C_L$  coupled with the standard drag law  $C_L$  has fair effects on the very near wall behavior of mean streamwise particle velocities at Stokes number  $St = 20$ . A similar conclusion that the wall-normal r.m.s velocities of small particles ( $St = 2, 5, 10$ ) are insensitive to the inclusion of lift force, or of near-wall corrected lift force can be drawn from figures 5.12 and 5.13a. The near-wall corrected  $C_L$  does significantly increase the wall-normal r.m.s velocities of large particles with Stokes number ( $St = 20$ ) in the very near wall region. In fact, Rizk and Elghobashi (1985) reported similar findings that the inclusion of Saffman lift force had a significant effect on the wall-normal r.m.s velocities of the largest particles considered.



(a)



(b)

Figure 5.10: Comparison of mean streamwise particle velocities with the standard drag law  $C_D$ , with  $C_L$  and inclusion of near-wall corrections on  $C_L$  from Zeng et al. (2009) and compared to the fluid velocities (a)  $St = 2$ , (b)  $St = 5$ .

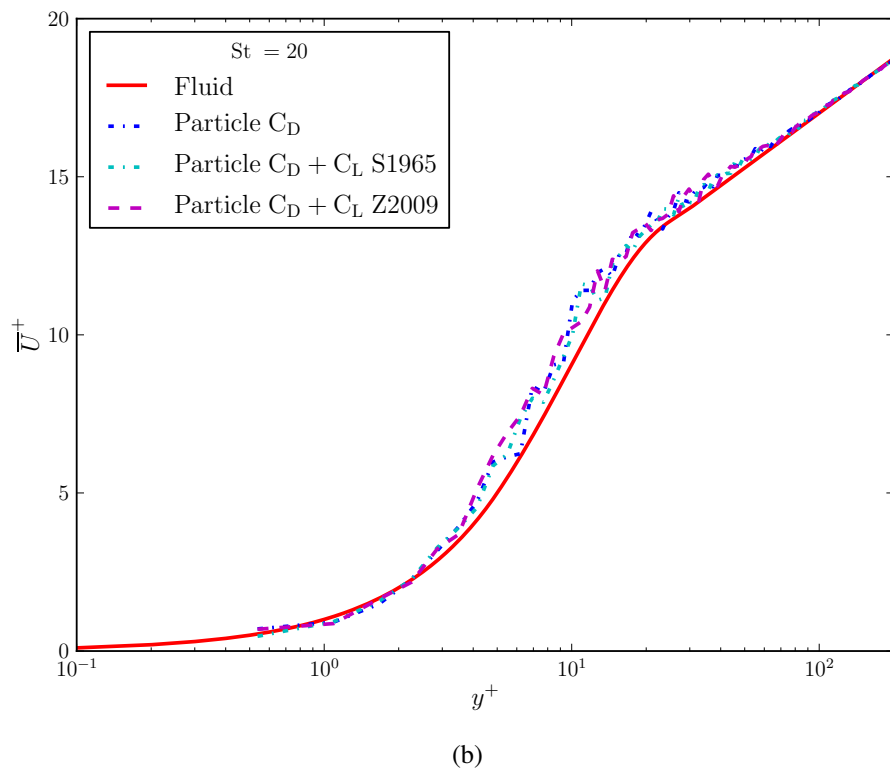
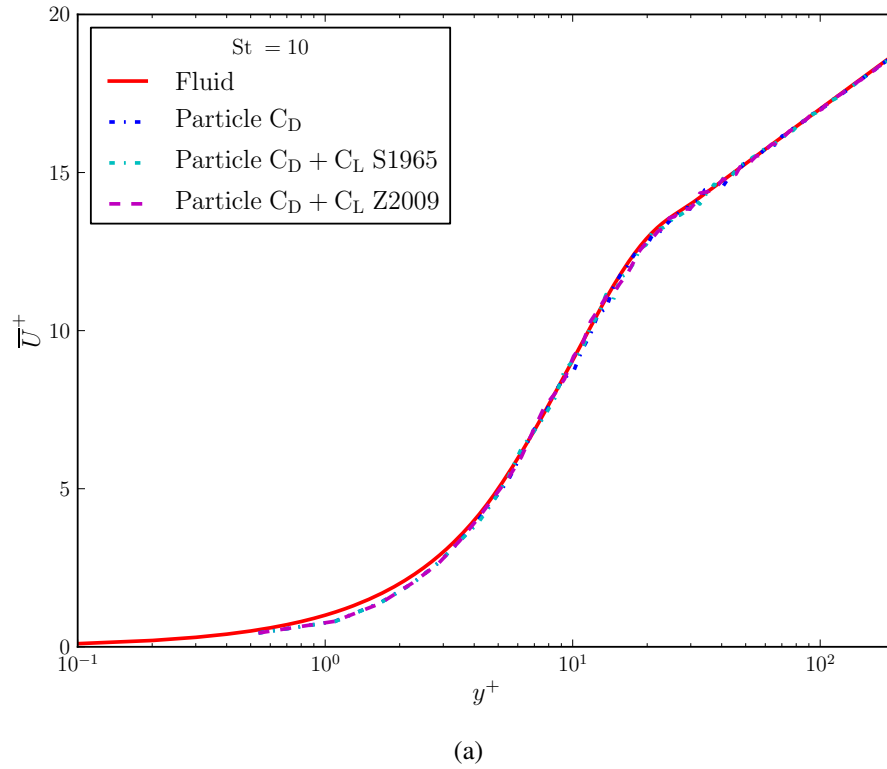
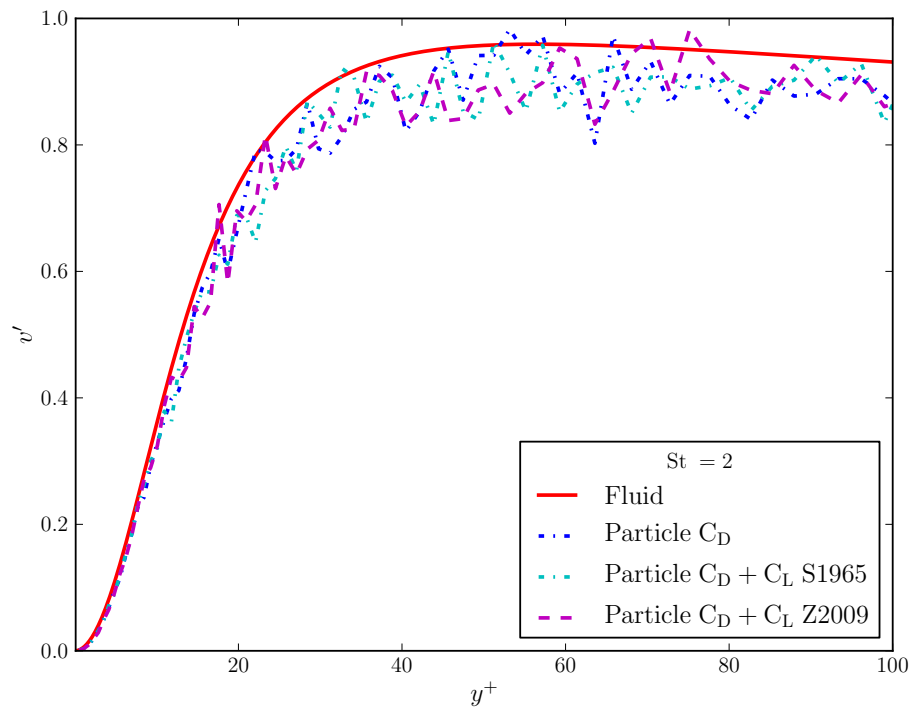
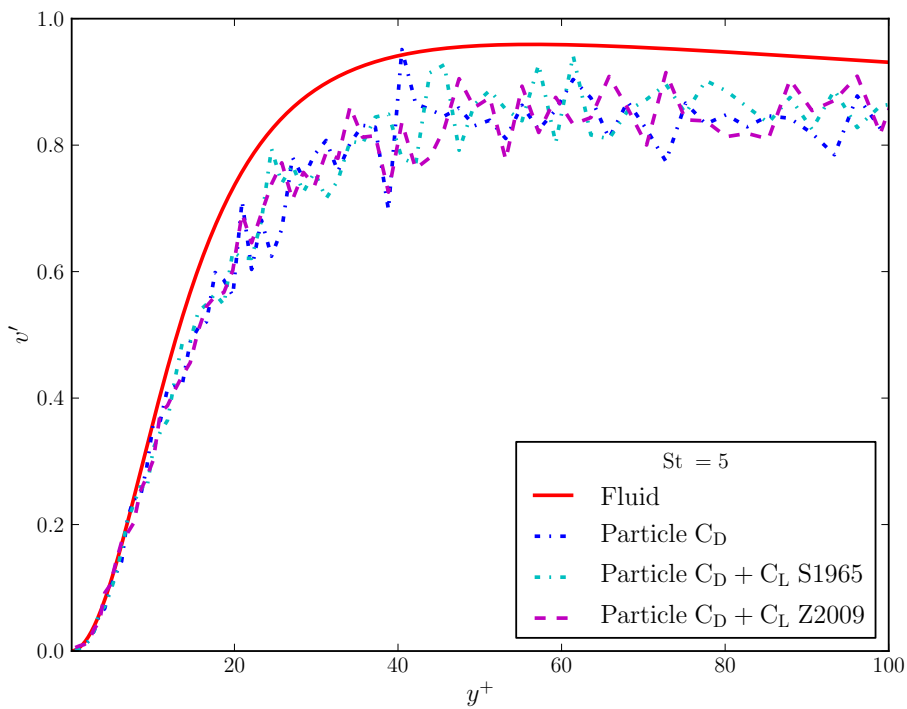


Figure 5.11: Comparison of mean streamwise particle velocities with the standard drag law  $C_D$ , with  $C_L$  and inclusion of near-wall corrections on  $C_L$  from Zeng et al. (2009) and compared to the fluid velocities (a)  $St = 10$ , (b)  $St = 20$ .



(a)



(b)

Figure 5.12: Comparison of wall-normal r.m.s velocities with the standard drag law  $C_D$ , with  $C_L$  and inclusion of near-wall corrections on  $C_L$  from Zeng et al. (2009) and compared to the fluid velocities (a)  $St = 2$ , (b)  $St = 5$ .

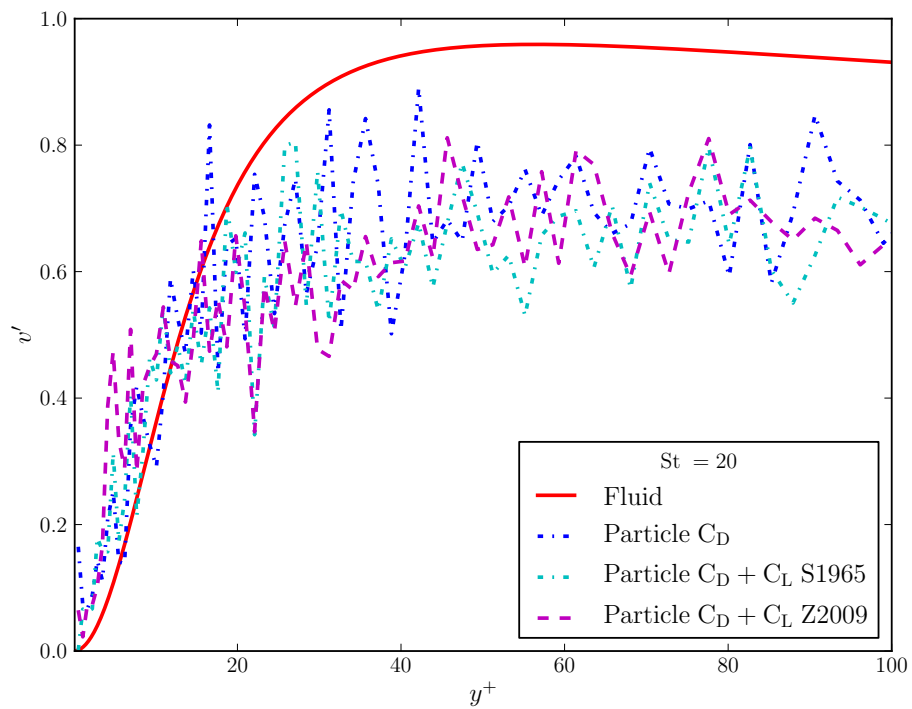
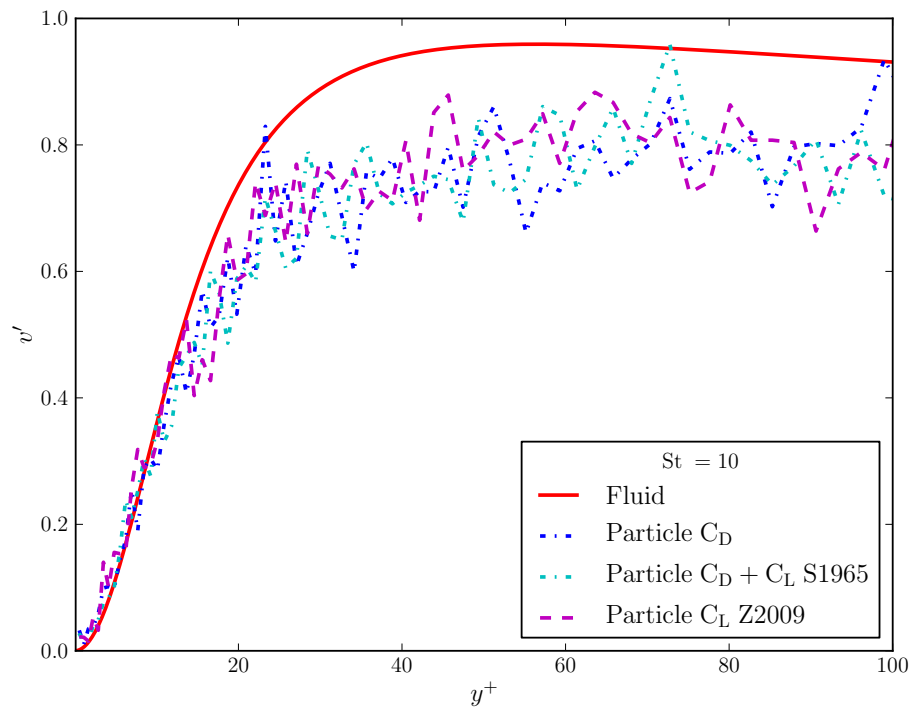


Figure 5.13: Comparison of wall-normal r.m.s velocities with the standard drag law  $C_D$ , with  $C_L$  and inclusion of near-wall corrections on  $C_L$  from Zeng et al. (2009) and compared to the fluid velocities (a)  $St = 10$ , (b)  $St = 20$ .

## 5.5 Concluding remarks

This work investigated the effect of near wall corrections for the drag force, and of the inclusion of Saffman lift force and of near wall corrected lift force on the deposition rates and dispersion characteristics of heavy particles. The near wall corrected drag coefficient  $C_D$  has no significant effects on particle deposition. However, the corrected  $C_D$  provides a greater divergence between particle and fluid stream-wise velocities for large particle ( $St = 20$ ) in the near wall region (see [Kulick et al. \(1994\)](#)). The results for deposition rates obtained from the inclusion of Saffman lift force and near wall corrected lift force must be interpreted with caution since they increase the under-prediction of deposition rates for small particles with Stokes number  $St = 2$  and  $5$ . This may result from the deficiency of the stochastic quadrant model that accounts for the wall-normal velocity fluctuations only. On the other hand, the inclusion of a near wall corrected lift force has only small effects on particle deposition and dispersion characteristics within the near wall region. Given all the results presented, whether the wall effects on the hydrodynamic forces should be included or not depends on specific applications. For instance, making use of the wall-corrected  $C_D$  to study large particles (i.e.  $St > 10$ ) with containing walls provides better particle dispersion characteristics in the near wall region. In general, however, it may be concluded that the inclusion of near wall effects has only a minor effect on particle deposition prediction.

## REFERENCES

- B. Arcen, A. Tanière, and B. Oesterlé. On the influence of near-wall forces in particle-laden channel flows. *International Journal of Multiphase Flow*, 32(12):1326–1339, 2006.
- P. Bagchi and S. Balachandar. Effect of turbulence on the drag and lift of a particle. *Physics of Fluids*, 15:3496, 2003.
- H. Brenner. The slow motion of a sphere through a viscous fluid towards a plane surface. *Chemical Engineering Science*, 16(3-4):242–251, 1961.
- M. Chen and J. B. McLaughlin. A new correlation for the aerosol deposition rate in vertical ducts. *Journal of Colloid and Interface Science*, 169(2):437–455, 1995.
- P. Cherukat and J. B. McLaughlin. The inertial lift on a rigid sphere in a linear shear flow field near a flat wall. *Journal of Fluid Mechanics*, 263:1–18, 1994.
- R. Clift, J. R. Grace, and M. E. Weber. *Bubbles, droplets, and particles*. Academic Press, New York, 1978.
- A. J. Goldman, R. G. Cox, and H. Brenner. Slow viscous motion of a sphere parallel to a plane wall—I Motion through a quiescent fluid. *Chemical Engineering Science*, 22(4):637–651, 1967.
- G. A. Kallio and M. W. Reeks. A numerical simulation of particle deposition in turbulent boundary layers. *International Journal of Multiphase Flow*, 15(3):433–446, 1989.
- J. D. Kulick, J. R. Fessler, and J. K. Eaton. Particle response and turbulence modification in fully developed channel flow. *Journal of Fluid Mechanics*, 277:109–134, 1994.

- J. Lataste, D. Huilier, H. Burnage, and J. Bednar. On the shear lift force acting on heavy particles in a turbulent boundary layer. *Atmospheric environment*, 34(23):3963–3971, 2000.
- H. Lee and S. Balachandar. Drag and lift forces on a spherical particle moving on a wall in a shear flow at finite Re. *Journal of Fluid Mechanics*, 657:89–125, 2010.
- B. Y. H. Liu and J. K. Agarwal. Experimental observation of aerosol deposition in turbulent flow. *Journal of Aerosol Science*, 5(2):145–148, IN1–IN2, 149–155, 1974.
- C. Marchioli and A. Soldati. Mechanisms for particle transfer and segregation in a turbulent boundary layer. *Journal of Fluid Mechanics*, 468:283–315, 2002.
- C. Marchioli, M. Picciotto, and A. Soldati. Particle dispersion and wall-dependent turbulent flow scales: implications for local equilibrium models. *Journal of Turbulence*, (7), 2006.
- C. Marchioli, A. Soldati, J. G. M. Kuerten, B. Arcen, A. Tanière, G. Goldensoph, K. D. Squires, M. F. Cargnelutti, and L. M. Portela. Statistics of particle dispersion in direct numerical simulations of wall-bounded turbulence: Results of an international collaborative benchmark test. *International Journal of Multiphase Flow*, 34(9):879–893, 2008.
- M. R. Maxey and J. J. Riley. Equation of motion for a small rigid sphere in a nonuniform flow. *Physics of Fluids*, 26:883, 1983.
- D. D. McCoy and T. J. Hanratty. Rate of deposition of droplets in annular two-phase flow. *International Journal of Multiphase Flow*, 3(4):319–331, 1977.
- J. B. McLaughlin. Aerosol particle deposition in numerically simulated channel flow. *Physics of Fluids A: Fluid Dynamics*, 1:1211, 1989.
- J. B. McLaughlin. Inertial migration of a small sphere in linear shear flows. *Journal of Fluid Mechanics*, 224:261–274, 1991.
- J. B. McLaughlin. The lift on a small sphere in wall-bounded linear shear flows. *Journal of Fluid Mechanics*, 246:249–265, 1993.

- R. Mei. An approximate expression for the shear lift force on a spherical particle at finite Reynolds number. *International Journal of Multiphase Flow*, 18(1):145–147, 1992.
- S. A. Morsi and A. J. Alexander. An investigation of particle trajectories in two-phase flow systems. *Journal of Fluid Mechanics*, 55(02):193–208, 1972.
- M. A. Rizk and S. E. Elghobashi. The motion of a spherical particle suspended in a turbulent flow near a plane wall. *Physics of Fluids*, 28(3):806–817, 1985.
- P. G. Saffman. The lift on a small sphere in a slow shear flow. *Journal of Fluid Mechanics*, 22(02):385–400, 1965.
- P. G. Saffman. Corrigendum to the lift of a small sphere in a slow shear flow. *Journal of Fluid Mechanics*, 32, 1968.
- L. Schiller and A. Naumann. A drag coefficient correlation. *Vdi Zeitung*, 77:318–320, 1933.
- G. Stokes. On the theories of internal friction of fluids in motion. *Transactions of the Cambridge Philosophical Society*, 8:287, 1845.
- Q. Wang and K. D. Squires. Large eddy simulation of particle deposition in a vertical turbulent channel flow. *International Journal of Multiphase Flow*, 22(4):667–682, 1996a.
- Q. Wang, K. D. Squires, M. Chen, and J. B. McLaughlin. On the role of the lift force in turbulence simulations of particle deposition. *International Journal of Multiphase Flow*, 23(4):749–763, 1997.
- Q. Z. Wang and K. D. Squires. Large eddy simulation of particle-laden turbulent channel flow. *Physics of Fluids*, 8(5):1207–1223, 1996b.
- L. Zeng, F. Najjar, S. Balachandar, and P. Fischer. Forces on a finite-sized particle located close to a wall in a linear shear flow. *Physics of Fluids*, 21:033302, 2009.

# Chapter 6

## An LES study and comparison with experimental measurements of a turbulent flow over an in-line tube-banks

### 6.1 Introduction

Turbulent flows over tube-banks have been traditionally modelled using the Reynolds-Averaged Navier-Stokes (RANS) equations with turbulence models (see [Beale and Spalding \(1999\)](#); [Rollet-Miet et al. \(1999\)](#); [Watterson et al. \(1999\)](#); [Benhamadouche and Laurence \(2003\)](#); [Wang et al. \(2006\)](#)). The flow across tube banks is strongly unsteady, which is characterized by strong vortex shedding and bluff-body wakes. [Rodi \(1997\)](#) has demonstrated the difficulty or even impossibility of accurately simulating the flow phenomena using the RANS methodology with the standard  $k - \varepsilon$  turbulence model. Meanwhile, the astonishingly rapid development of Large-Eddy Simulation (LES) (see [Rogallo and Moin \(1984\)](#); [Mason \(1994\)](#); [Sagaut \(2001\)](#)) has shown the

potential to more accurately simulate simple flow phenomena, as LES resolves the large-scale unsteady motion directly and requires only modelling of the universal small-scale turbulence structures.

It is still a challenging task for numerical simulations to get an accurate prediction of unsteady flow separation at high Reynolds number flow over a single cylinder, not to mention flow across tube-banks, since the flow exhibits strong unsteadiness and complex vortex structures. Whether the dynamic boundary layer around cylinder is accurately resolved with appropriate numerical techniques and resolution (see [Davidson \(2009\)](#); [Breuer \(1998\)](#)) is crucial to the correct prediction of the unstable region where turbulence is generated, the instability of shear layer (see [Bloor \(1964\)](#)) and the physics of the wake (see [Williamson \(1996\)](#); [Jordan \(2003\)](#)). Hence the conventional LES of turbulent flows across a single cylinder and tube-banks is an extremely expensive endeavour for high Reynolds number flows (see [Breuer \(1998, 2000\)](#)).

In recent years, LES has been applied to simulate turbulent flows across in-line and staggered tube-banks (see [Barsamian and Hassan \(1997\)](#); [Hassan and Barsamian \(2004\)](#); [Beale and Spalding \(1999\)](#); [Benhamadouche and Laurence \(2003\)](#); [Bouris and Bergeles \(1999\)](#); [Liang and Papadakis \(2007\)](#); [Lam et al. \(2010\)](#)) and shown feasibility and effectiveness in this application. [Barsamian and Hassan \(1997\)](#) carried out a two-dimensional LES calculation of flow over tube bundle arrays using two subgrid scale models, and studied the power spectra of drag and lift forces. Later extension to three-dimensional LES by [Hassan and Barsamian \(2004\)](#) was used to study velocity profile, power spectra density (PSD) of velocities and forces, auto-correlation functions of streamwise and transverse velocities in a flow past a tube bundle, at Reynolds number 21700 based on the free stream velocity and cylinder diameter. [Rollet-Miet et al. \(1999\)](#) performed an LES based on the Finite Element Method for a turbulent, incompressible flow around a staggered array of tubes, and compared the results with the measurements from [Simonin and Barcouda \(1988\)](#). [Beale and Spalding \(1999\)](#) performed an LES of transient flow in a relatively low Reynolds number regime of  $Re \in [30, 3000]$  based on the gap velocity and cylinder diameter. Both in-line square and staggered-square tube banks were studied in their work to investigate pressure drop, lift, drag and heat transfer.

[Liang and Papadakis \(2007\)](#) employed a Finite-Volume Method (FVM) based LES to study the vortex shedding characteristics inside a staggered tube bundle.

The simulation of turbulent flows over tube bundles can be simplified by modelling only a small element, provided that the cylinders are packed so closely that coherent vortex shedding is suppressed. In this case, the computational domain is reduced to a single periodic circular cylinder with four cylinder quarters around it. Hence periodic boundary conditions are assumed in the streamwise and cross-flow direction. [Benhamadouche and Laurence \(2003\)](#) carried out a comprehensive comparative study of turbulent flow across a single periodic cylinder in a tube bundle with LES, coarse LES and URANS. In their study, LES with a wall function modelling method gave the best results when compared with experimental measurements of [Simonin and Barcouda \(1988\)](#) and DNS results from [Moulinec et al. \(2002\)](#). [Moulinec et al. \(2004b\)](#) conducted a DNS based on the diagonal Cartesian method (DCM) to study turbulent flow past an “element cell” in a tube bundle with four different grids. The Reynolds number was chosen as 6000 based on the bulk velocity and the cylinder diameter. They compared the results for the mean velocity and r.m.s velocity values from the finest mesh with the benchmark data measured by [Simonin and Barcouda \(1988\)](#) and numerical solutions calculated by [Rollet-Miet et al. \(1999\)](#), and showed the feasibility of an “element cell” as an LES computational domain. Following the work of [Moulinec et al. \(2004b\)](#), [Moulinec et al. \(2004a\)](#) further studied the wake turbulence in a “wide element” consisting of 16 circular cylinders using a three-dimensional DNS for  $Re \in [50, 6000]$  based on the bulk velocity.

In the present study, in contrast to previous research work (e.g. [Rollet-Miet et al. \(1999\)](#); [Benhamadouche and Laurence \(2003\)](#); [Moulinec et al. \(2002, 2004a\)](#)), a full scale turbulent flow across an in-line tube bundle is computed with a three-dimensional LES. The numerical technique is based on the Finite-Volume Method (FVM) using wall-layer modelling on unstructured grids with a collocated arrangement for all the unknown flow variables. Particular attention is given to the investigation of detailed statistics around the circular cylinder in the middle of each column within the array, which are compared against with the available experimental data of [Shim \(1985\)](#); [Hill et al. \(1986\)](#); [Shim et al. \(1988\)](#).

The rest of this chapter is structured as follows. The computational methodology and geometry are presented first. Then, a detailed comparison and discussion of mean and r.m.s surface pressure distribution on the middle cylinders from each column are given. In addition to that, the corresponding drag and lift force, frequency analysis of velocity signals and auto-correlations of streamwise and cross-stream velocities in the spanwise direction, which complement the existing experimental measurements, are reported. Finally, conclusions are drawn.

## 6.2 Computational methodology

### 6.2.1 Formulation of the dynamic Smagorinsky model

The governing equations for LES are obtained by spatially filtering the Navier-Stokes equations. In this process, the eddies that are smaller than the filter size used in the simulations are filtered out. Hence, the resulting filtered equations govern the dynamics of large eddies in turbulent flows. A spatially filtered variable that is denoted by an overbar is defined using a convolution product (see [Leonard \(1974\)](#))

$$\bar{\phi}(\mathbf{x}, t) = \int_{\mathcal{D}} \phi(\mathbf{y}, t) G(\mathbf{x}, \mathbf{y}) d\mathbf{y}, \quad (6.1)$$

where  $\mathcal{D}$  is the computational domain, and  $G$  is the filter function that determines the scale of the resolved eddies.

In the current study, the finite-volume discretization employed itself provides the filtering operation as

$$\bar{\phi}(\mathbf{x}, t) = \frac{1}{V} \int_{\mathcal{D}} \phi(\mathbf{y}, t) d\mathbf{y}, \quad \mathbf{y} \in \mathcal{V}, \quad (6.2)$$

where  $V$  is the volume of a computational cell. Hence, the implied filter function,  $G(\mathbf{x}, \mathbf{y})$  in equation (6.2), is a top-hat filter given by

$$G(\mathbf{x}, \mathbf{y}) = \begin{cases} 1/V & \text{for } |\mathbf{x} - \mathbf{y}| \in \mathcal{V}, \\ 0 & \text{otherwise.} \end{cases} \quad (6.3)$$

Filtering the continuity and Navier-Stokes equations, the governing equations for resolved scales in LES are obtained as follows

$$\frac{\partial \bar{u}_i}{\partial x_i} = 0, \quad (6.4)$$

$$\frac{\partial \bar{u}_i}{\partial t} + \frac{\partial \bar{u}_i \bar{u}_j}{\partial x_j} = -\frac{1}{\rho} \frac{\partial \bar{p}}{\partial x_i} + \frac{\partial}{\partial x_j} \left( \nu \frac{\partial \bar{u}_i}{\partial x_j} \right) - \frac{\partial \tau_{ij}}{\partial x_j}, \quad (6.5)$$

where  $\tau_{ij}$  is the subgrid scale (SGS from here on) stress tensor defined by

$$\tau_{ij} = \overline{u_i u_j} - \bar{u}_i \bar{u}_j. \quad (6.6)$$

The filtered equations are unclosed since the SGS stress tensor  $\tau_{ij}$  is unknown. The SGS stress tensor can be modelled based on isotropic eddy-viscosity as:

$$\tau_{ij} - \frac{1}{3} \delta_{ij} \tau_{kk} = -2\nu_t \bar{S}_{ij}, \quad (6.7)$$

where  $\nu_t$  is the SGS eddy viscosity,  $\bar{S}_{ij}$  is the resolved rate of strain tensor given by

$$\bar{S}_{ij} = \frac{1}{2} \left( \frac{\partial \bar{u}_i}{\partial x_j} + \frac{\partial \bar{u}_j}{\partial x_i} \right), \quad (6.8)$$

where  $\nu_t$  is computed in terms of the Smagorinsky (1963) type eddy-viscosity model using

$$\nu_t = (C_\nu \bar{\Delta})^2 |\bar{S}|. \quad (6.9)$$

Here  $C_\nu$  is the Smagorinsky coefficient,  $|\bar{S}|$  is the modulus of rate of strain tensor for the resolved scales,

$$|\bar{S}| = \sqrt{2\bar{S}_{ij}\bar{S}_{ij}}, \quad (6.10)$$

and  $\bar{\Delta}$  is the grid filter length obtained from

$$\bar{\Delta} = V^{1/3}. \quad (6.11)$$

Consequently, the SGS stress tensor is computed as follows

$$\tau_{ij} - \frac{1}{3}\delta_{ij}\tau_{ij} = -2(C_v\bar{\Delta})^2|\bar{S}|\bar{S}_{ij}. \quad (6.12)$$

This model claims to be simple and efficient. It needs merely a constant *in priori* value for  $C_v$ . Nevertheless, work from previous researchers (see Lilly (1966); Deardorff (1970); Piomelli et al. (1988)) has shown different values of  $C_v$  are required for distinct flows. Hence, the major drawback of this model used in LES is that there is an inherent inability to represent a wide range of turbulent flows with a single value of the model coefficient  $C_v$ . Given that the turbulent flow over tube-banks in the current study is fully three-dimensional, and a universally accepted value for  $C_v$  is not known for this case, the standard Smagorinsky SGS model is not employed.

Germano et al. (1991) proposed a new procedure to dynamically compute the model coefficient  $C_v$  based on the information obtained from the resolved large scales of motion. The new procedure employs another, coarser filter  $\tilde{\Delta}$  (test filter) whose width is greater than that of the default grid filter. Applying the test filter to the filtered Navier-Stokes equations, one obtains the following equations

$$\frac{\partial \tilde{u}_i}{\partial t} + \frac{\partial \tilde{u}_i \tilde{u}_j}{\partial x_j} = -\frac{1}{\rho} \frac{\partial \tilde{p}}{\partial x_i} + \frac{\partial}{\partial x_j} \left( \nu \frac{\partial \tilde{u}_i}{\partial x_j} \right) - \frac{\partial T_{ij}}{\partial x_j}, \quad (6.13)$$

where the tilde denotes the test-filtered quantities.  $T_{ij}$  represents the subgrid scale stress tensor from the resolved large scales of motion and is given by

$$T_{ij} = \widetilde{u_i u_j} - \tilde{u}_i \tilde{u}_j. \quad (6.14)$$

The quantities given in equations (6.6) and (6.14) are related by the Germano identity:

$$\mathcal{L}_{ij} = T_{ij} - \tilde{\tau}_{ij}, \quad (6.15)$$

which represents the resolved turbulent stress tensor from the SGS tensor between the test and grid filters. It can be computed directly from the resolved field through

$$\mathcal{L}_{ij} = \widetilde{\overline{u_i u_j}} - \widetilde{\overline{u_i}} \widetilde{\overline{u_j}}. \quad (6.16)$$

Applying the same Smagorinsky model to  $T_{ij}$  and  $\tau_{ij}$ , the anisotropic parts of  $\mathcal{L}_{ij}$  can be written as

$$\mathcal{L}_{ij} - \frac{1}{3} \delta_{ij} \mathcal{L}_{kk} = -2CM_{ij}, \quad (6.17)$$

where  $C = C_v^2$  and

$$M_{ij} = \widetilde{\Delta^2 |\widetilde{S}| \widetilde{S}_{ij}} - \widetilde{\Delta^2 |\widetilde{S}|} \widetilde{S}_{ij}. \quad (6.18)$$

One hence can obtain the value of  $C$  from equation (6.17). The model value of  $C$  is obtained via the least squares approach proposed by Lilly (1992), since expression (6.17) is an overdetermined system of equations for the unknown variable  $C$ . Lilly (1992) defined a criterion for minimizing the square of the error as

$$E = (L_{ij} - \frac{\delta_{ij}}{3} L_{kk} + 2CM_{ij})^2. \quad (6.19)$$

In order to obtain a local value, varying in time and space in a fairly wide range, for the model constant  $C$ , one takes  $\frac{\partial E}{\partial C}$  and sets it zero to get

$$C = -\frac{1}{2} \frac{L_{ij} M_{ij}}{M_{ij} M_{ij}}. \quad (6.20)$$

A negative  $C$  represents the transfer of flow energy from the subgrid-scale eddies to the resolved eddies, which is known as "back-scatter" and is regarded as a desirable attribute of the dynamic model, since this phenomenon has been shown to occur in practice (see Leslie and Quarini (1979)). The Smagorinsky constant  $C_v$ , as defined earlier, is given by the square root of  $C$ , but the possibility of negative  $C$  values presents no difficulty in practice, since the equation for eddy viscosity 6.9 involves  $C_v$  squared.

### 6.2.2 The Werner and Wengle wall layer model

The Large Eddy Simulation (LES) of turbulent flows over tube-banks is hampered by the excessive computational cost incurred when the dynamic and thin near-wall layer is fully resolved. To obviate the computational cost associated with calculating the wall shear stress from the laminar stress-strain relationship that requires the first cell to be put within the range of  $y^+ \approx 1$ , [Werner et al. \(1993\)](#) propose a simple power-law to replace the law of the wall, in which the velocity profile on a solid wall is given as following,

$$u^+ = \begin{cases} y^+ & \text{for } y^+ \leq 11.81 \\ A(y^+)^B & \text{for } y^+ > 11.81 \end{cases} \quad (6.21)$$

where  $A = 8.3$  and  $B = 1/7$ . An analytical integration of (6.21) results in the following relations for the wall shear stress

$$|\tau_w| = \begin{cases} \frac{2\mu|u_p|}{\Delta y} & \text{for } y^+ \leq 11.81 \\ \rho \left[ \frac{1-B}{2} A^{\frac{1+B}{1-B}} \left( \frac{\mu}{\rho\Delta y} \right)^{1+B} + \frac{1+B}{A} \left( \frac{\mu}{\rho\Delta y} \right)^B |u_p| \right]^{\frac{2}{1+B}} & \text{for } y^+ > 11.81 \end{cases} \quad (6.22)$$

where  $u_p$  is the velocity component parallel to the wall and given by:

$$|u_p| = \frac{\mu}{2\rho\Delta y} A^{\frac{2}{1-B}} \quad (6.23)$$

where  $\Delta y$  is the wall-normal dimension of the near-wall control volume. The Werner-Wengle form of wall function is more computationally efficient than the standard form and is more flexible in terms of applicable  $y^+$  range.

### 6.2.3 Flow configuration of in-line tube banks

The flow configuration is shown in figure 6.1 and the coordinate system is defined in figure 6.2. Flow is from left to right and normal to the cylinder axis. The computational domain is of size  $L_x \times L_y \times L_z = 28D \times 16D \times 2D$ , where  $D$  is the cylinder diameter. This configuration is based on the second test case considered in [Shim \(1985\)](#) which

measures surface pressure distributions and fluctuating lift forces and was performed in a suction-type wind tunnel. It consists of four-column in-line tube bundles with transverse pitch-to-diameter ratio  $S_T$  ( $P_T/D$ ) of 2.67 and longitudinal pitch-to-diameter ratio  $S_L$  ( $P_L/D$ ) of 2.31, respectively. The Reynolds number  $Re_o$  based on the free stream velocity  $U_o$  and the cylinder diameter  $D$  equals 9600, and  $Re_g$  based on the gap streamwise velocity between two cylinders is equal to 15200.

The Navier-Stokes solver used in this work, ANSYS FLUENT v12.0, uses a cell-centered, collocated grid arrangement finite-volume (FV) discretization method. All spatial terms in the momentum equations are discretized by the bounded central differencing scheme, which not only offers the advantage of low numerical diffusion of central-differencing scheme but also eliminates unphysical oscillations in the solution fields. Furthermore, the spatial discretization scheme is based on a multi-dimensional, least squares cell-based gradient reconstruction scheme to guarantee a second-order spatial accuracy. In order to prevent unphysical checker-board pressure field, ANSYS FLUENT employs a procedure similar to that proposed by [Rhie and Chow \(1983\)](#). Gear's implicit, three-level second-order accurate scheme is employed for temporal discretization. A generalized fractional-step method is employed for the overall time-advancement.

The computational grid is evident in figure 6.3. The total number of grid elements used for the present simulation is 2730240, and has an embedded region of fine cells local to the tube array in order to enhance the mesh resolution near the cylinders without incurring too large an increase in the total number of mesh elements. 96 grid points are allocated around the circumference of each cylinder. The grid spacing adjacent to the cylinder in the radial, circumferential, and spanwise direction are  $\Delta r/D = 1.4 \times 10^{-2}$ ,  $\Delta \theta = 3.27 \times 10^{-2}$ ,  $\Delta z/D = 5.0 \times 10^{-2}$ , respectively. The centroid of the first cell adjacent to the cylinder is within the range  $\Delta y^+ < 11.8$  in wall units<sup>1</sup> that satisfies the requirements of the Wener-Wengle wall-layer model for LES. Prior to the present simulation, with the standard Smagorinsky subgrid scale model, coarser grid simulations were carried out to determine the grid resolution necessary to obtain realistic solutions.

<sup>1</sup>The superscript + denotes a non-dimensional quantity scaled using the wall variables, e.g.  $y^+ = yu_\tau/\nu$ , where  $\nu$  is the kinematic viscosity and  $u_\tau = \sqrt{\tau_w/\rho}$  is the wall friction velocity based on the wall shear stress  $\tau_w$ , and which is a velocity scale representative of velocities close to a solid boundary.

It should be noted, however, that demonstration of grid independence is notoriously difficult with LES solutions.

With fully developed turbulent flows, periodic boundary conditions are justifiable for using along the normal ( $y$ ) and spanwise ( $z$ ) direction. This assumption is strained in the present case, as the wide pitching of the cylinder array results in significant coherent vortex shedding. However, it is considered that the dimensions of the computational domain in the pitch-wise and span-wise directions are sufficiently large to obtain realistic solutions for the centre cylinders. For the inlet boundary condition, a simple uniform velocity profile is assumed and the turbulent intensity set to zero. Hence, the turbulence fluctuations at the inlet was not accounted for temporally and spatially. Nevertheless, a length  $5D$  before the first column bank is used to allow the development of turbulence. At the exit boundary, the solution variables from the adjacent interior cells are extrapolated to satisfy the mass conservation.

The simulation is advanced with a non-dimensional time step  $\Delta t U_o/D \approx 2 \times 10^{-3}$  that yields a maximum Courant-Friedrichs-Lewy (CFL) number 0.5. For the results presented here, the first-order statistics are collected by integrating the unsteady solutions over an interval of  $30D/U_o$ , and all the statistics are averaged over the 40 sampling points across the spanwise direction.

### 6.3 Results and discussion

To provide an overview of the turbulent flow development across the four-column in-line tube banks, wake vortices visualized using the  $Q$  criterion proposed by [Hunt et al. \(1988\)](#) are presented first. Then, time-resolved pressure distributions provide quantitative information on surface pressure fluctuations, which are compared with the experimental measurements of [Shim \(1985\)](#). Following this, the time histories of coefficient of drag  $C_D$  and lift are given. The developments of vortex shedding behind the cylinder in the middle column are studied by examining the corresponding energy spectrum in the wake. The coherence of vortex shedding along the length of the middle cylinder is investigated through computing the auto-correlation function of each velocity

fluctuation component. In the present work, the turbulent flow across tube banks has been considered to have reached the statistically stationary state after a simulation time of  $T = 200D/U_o$ . All the statistics presented here are computed after this transient stage. Further, the statistics (apart from the spanwise auto-correlation) are averaged in the periodic spanwise direction.

### 6.3.1 Instantaneous flow field

Vortex structures in the flow field around the four-in-line tube bank array are revealed in figure 6.4 by plotting iso-surfaces of normalised  $Q$  – criterion  $= 8 \times 10^{-2}$ . The  $Q$  – criterion, proposed by Hunt et al. (1988), is defined as a positive second invariant of velocity gradient tensor  $\nabla \mathbf{u}$  for incompressible flows by the following expression

$$Q = \frac{\partial u_i}{\partial x_j} \frac{\partial u_j}{\partial x_i} = \frac{1}{2} (\|\boldsymbol{\omega}_{ij}\|^2 - \|e_{ij}\|^2), \quad (6.24)$$

where  $e_{ij}$  and  $\boldsymbol{\omega}_{ij}$  denotes the symmetric and antisymmetric parts of  $\nabla \mathbf{u}$ ; i.e.  $\boldsymbol{\omega}_{ij} = \frac{1}{2}(u_{i,j} - u_{j,i})$  and  $e_{ij} = \frac{1}{2}(u_{i,j} + u_{j,i})$ , respectively. The iso-surfaces are coloured according to the magnitude of the local resolved turbulence kinetic energy (TKE), whilst Figure 6.5 shows the corresponding contours of TKE on the mid-span plane through the domain.

The instantaneous flow field shows the salient feature of the wake dynamics where a wide, yet different range of scales behind every column of cylinders can be observed. As far as the first column cylinders are concerned, the flow shows no unexpected properties, but a few points are worth noting for comparison with flow patterns behind other cylinders.

Firstly, the boundary layer on each individual cylinders of the first column remains laminar up to the separation point, and it undergoes transition to turbulence in the separated shear layer. The boundary layer separation on the cylinders from the downstream columns is much delayed so that the wake is much narrower, resulting in a much smaller coefficient of drag. This results principally from the significantly increased inflow turbulence level for the downstream cylinders. Figure 6.5 shows a close-up of the vortex motion around the cylinders across the middle plane, again shown contours of TKE in terms of the same normalized-Q criterion. It is evident that the turbulence level is

quite high at the front side of the downstream cylinders , and has reached approximately equilibrium levels by the third and fourth column of cylinders..

Secondly, figure 6.4 illustrates different flow pattern of vortex travelling downstream each column of cylinders. Large coherent structures are visible in the wake of first column of cylinders. Nevertheless, the classical von Karman vortex street does not persist because the second cylinder column lies within the range of the recirculation region of flow behind the first column and hence breaks up the vortex street in the wake. Another effect of the downstream cylinder is to increase the wake instabilities further. Large flow structures are lost and broken into small eddies, producing ultimately a fully developed grid turbulence after the final cylinder column.

### 6.3.2 Surface pressure characteristics

Figure 6.6a presents time-averaged surface pressure distributions against angle  $\theta$  from the front stagnation point for the middle circular cylinder, taken from the first column to the fourth column, respectively. The experimental results of Shim (1985) are shown for comparison.

The mean surface pressures are presented in terms of the coefficient of pressure

$$\bar{C}_p = \frac{\langle p \rangle_T - p_{ref}}{q_{ref}}, \quad (6.25)$$

where  $\langle p \rangle_T$  denotes an ensemble average across the spanwise direction for all the sampling points on the cylinder surface over the sampling time interval T. Although the vortex shedding does not necessarily occur in phase over the whole spanwise direction, the time-averaged boundary layers on either side of each circular cylinder are assumed to be symmetrical.  $q_{ref}$  is the dynamic pressure in terms of gap velocity  $u_g$  and fluid density  $\rho$ , which is given by

$$q_{ref} = \frac{1}{2} \rho u_g^2. \quad (6.26)$$

In order to make  $\bar{C}_p$  equal to unity at the front stagnation point for every cylinder, the corresponding static pressure  $p_{ref}$  is calculated by applying equation 6.25 to enforce

$\bar{C}_p = 1.0$  at  $\theta = 0^\circ$ . This value of  $p_{ref}$  is then used to determine  $\bar{C}_p$  around the rest of the cylinder surface. This procedure was also used in the work of Shim (1985) for calculating  $\bar{C}_p$ .

Excellent agreements for the time-averaged surface pressure distribution around the four cylinders are observed between the present LES calculations and the experimental measurements of Shim (1985) among the four plots of figure 6.6. Other quantities, for example, the r.m.s pressure distribution and vortex shedding frequency are also very comparable. They shall be shown in later figures in this chapter. For the central cylinder in the first column, it may be seen that the LES data in figure 6.6a contains a kink near  $\theta = 85^\circ$ , which indicates the presence of the laminar boundary layer separation from the upper and lower surfaces of the cylinder. This transition region from the experimental data of Shim (1985) is not as readily perceived as in the LES computation, in that the measurements were taken in 10-degree increments from the forward stagnation point to each side of the cylinder. For the discernible wiggle from the present calculations in the range of  $\theta \in [80^\circ, 120^\circ]$ , the likely reason is entrainment of shear layer fluid on to the cylinder surface owing to the interference from the close arrangement of cylinders.

To the best of the author's knowledge, there is so far no information available on the pressure distribution around the surfaces of cylinders in a tube bank from LES. It is of interest, thus, to show mean pressure distributions around the surface of the downstream cylinders in terms of the equation 6.25, and to further compare the results measured by Shim (1985). As far as the positive values of base  $\bar{C}_p$  obtained from the downstream cylinders are concerned, this results from the definition of  $\bar{C}_p$  in this work. It can be observed that the results from LES and experiment are very comparable across the figure 6.6b, c, d. Because of the wake from the first column of cylinders which impinges upon the downstream second column of cylinders, there is a dip in total pressure towards the row centre line, which explains the non-intuitive rise in surface pressure from the stagnation point,  $\theta = 0^\circ$ , on the second row cylinder. In particular, as can be observed from the figure 6.6a and 6.6b, they display distinct shapes for mean pressure distribution. The rise of mean pressure distribution is clearly discernible within the range of  $\theta \in [0^\circ, 40^\circ]$  in figure 6.6b. It is interesting to note that the peaks indicated by LES and experiment lie almost exactly at the same position around  $\theta = 40^\circ$  in

figure 6.6b. Moreover, it is worthwhile noting that the difference from the pressure of front stagnation point and the base pressure is reduced significantly compared to the corresponding cylinder from the first column. This is because a “laned” total pressure profile is developed as a result of the stream-wise alignment of the cylinder wakes. In contrast to figure 6.6b, the rise is barely discernible for  $\bar{C}_p$  from the third and fourth column in figure 6.6c,d. This can be explained as the wake from downstream cylinders is much more mixed than the one behind the first column.

The r.m.s value of the fluctuating pressure around the surfaces of the centre cylinders in the four columns are shown in the four figures 6.7a, b, c, d along with the experimental data of Shim (1985). The first feature to note is that the pressure fluctuates more than 50% for the downstream cylinders. This indicates that the instantaneous surface pressure is significantly different from the time-averaged value and further demonstrates that the URANS methodology is not suitable for the present work. Figure 6.7a exhibits relatively high and uniform values of fluctuating pressure distributions around the first cylinder from the findings of Shim (1985). The experimental result must be suspected to be in error here since according to the work of Norberg (2003) at a comparable Reynolds number  $C'_p$  exhibits a very low level at the frontal stagnation line ( $\theta = 0^\circ$ ). Considering the LES prediction, the position of first peak as shown in the figure 6.7a corresponds to the same angle in the figure 6.6a that indicates the laminar boundary layer separation. Moreover, the second peak after the shoulder of the cylinder is probably associated with influence of shed vortices. It can be observed that the general trend of the LES results is in reasonably good agreement with the measurements of Shim (1985) except for the first column cylinder.

Table 6.1 shows a comparison of maximum value of r.m.s pressure fluctuation from the present LES computation with the experimental values of Shim (1985) and Norberg (2003). It can be observed that the values from the present calculations match very well with the measurements, especially for the angular position within the upwind side at which the maximum r.m.s value of fluctuating pressure occurs. In addition, one interesting point is that the width of wakes from the second, third and fourth column cylinder is very close. The maximums on downstream cylinders are caused by the impingement of shedding-vortex from the upstream cylinders. The low r.m.s values of

Case		Maximum of $C'_p$	$C'_p(90^\circ)$
Present LES ( $Re_g = 15270$ )	C1	0.236 ( $110^\circ$ )	0.159
	C2	0.584 ( $40.4^\circ$ )	0.425
	C3	0.640 ( $40.4^\circ$ )	0.441
	C4	0.544 ( $36.7^\circ$ )	0.377
Experiments (Shim, 1985)	C1	0.457 ( $110^\circ$ )	0.438
	C2	0.641 ( $40^\circ$ )	0.539
	C3	0.658 ( $40^\circ$ )	0.592
	C4	0.658 ( $40^\circ$ )	0.582
Experiments (Norberg, 2003) Single cylinder $Re = 10k$		0.292	0.282

 Table 6.1: Comparison of results for r.m.s pressure distribution  $C'_p$ 

pressure fluctuation compared with experimental measurements on the downwind side may possibly result from the relatively weak wake predicted by the present LES with wall-layer modelling. It is also worthwhile emphasizing that the calculated results at  $\theta = 90^\circ$  are significantly higher than the value at a comparable  $Re = 10k$  compiled in Norberg (2003) for a single circular cylinder, except for the first row.

Finally, judging from the shape of mean and r.m.s pressure distribution around the surface in the two figures 6.6, 6.7, it may be concluded that the present calculation is capable of accurately predicting the pattern and dynamics of turbulent flow across the tube bank.

### 6.3.3 Drag and lift coefficients

To further validate the present study with experiments, table 6.2 summarizes the flow parameters  $\bar{C}_D$  and  $C'_L$  along with experimental measurements. The coefficient of mean drag per unit span is defined by:

$$\bar{C}_D = \frac{\bar{F}_D}{ld\rho u_g^2/2}, \quad (6.27)$$

where  $l$  is the spanwise length of the cylinder;  $\bar{F}_D$  denotes the form drag force caused by the surface pressure distribution through ignoring the viscous drag force, which is obtained by an integration of mean pressure distribution around the cylinder. Thus,  $\bar{C}_D$  is

given by

$$\bar{C}_D = \int_{0^\circ}^{180^\circ} \bar{C}_P \cos(\theta) d\theta. \quad (6.28)$$

It is evident that the results of  $\bar{C}_D$  predicted by the present LES study agree favorably well with the experimental measurements of Shim (1985) except for over-prediction of  $\bar{C}_D$  for the second column cylinder. The magnitudes of  $C'_L$  obtained from this work show reasonable agreement with experimentally measured values except for the first column cylinder due to the reason discussed before. The results for  $\bar{C}_D$  and  $C'_L$  are also presented in terms of the free stream velocity  $u_o$ , based on the conversion factor discussed in section 6.3.2. Changing the non-dimensionalising factor clearly increases all the coefficient values, and is done to facilitate comparison with data for an isolated single cylinder.

Comparing this modified value of  $\bar{C}_D = 1.941$  in terms of  $Re_g = 15270$  with  $\bar{C}_D = 1.185$  (see Schlichting et al. (2000)) for a comparable Reynolds number, it can be observed that  $\bar{C}_D$  for the first column cylinder predicted in this LES study is considerably higher than the value for a unconfined single smooth circular cylinder. This discrepancy is undoubtedly a consequence of a higher pressure coefficient which principally results from higher separation velocities in confined flow situations (see Richter and Naudascher (1976)).

In the light of the foregoing discussion it might be thought that the  $\bar{C}_D$  values for the downstream cylinders would also be much higher than for an unconfined circular cylinder, due to blockage effects. However, compared with the standard isolated cylinder value  $\bar{C}_D = 1.185$  (see Schlichting et al. (2000)), table 6.2 shows comparable values for  $\bar{C}_D$ . This apparent anomaly is due to the lane-ing of total pressure created by the wakes of the in-line cylinder array. The first column of cylinders see a uniform value of total pressure upstream, and the corresponding high static pressure on much of the upstream surface of these cylinders, combined with a lower, approximately uniform static pressure in the wake gives rise to a high form drag. For cylinders in the subsequent columns the total pressure in the regions between stream-wise adjacent cylinders is significantly reduced, leading to the reduction in form drag seen in table 6.2 for the LES and tube array experiment.

Case		$\overline{C}_D$	$C'_L$	$\overline{C}_D$	$C'_L$
		Based on $u_g$		Based on $u_o$	
Present LES	C1	0.767	0.228	1.941	0.579
	C2	0.404	0.655	1.022	1.656
	C3	0.454	0.650	1.146	1.645
	C4	0.464	0.507	1.174	1.284
Experiments (Shim, 1985)		Estimated		Estimated	
	C1	0.799	0.05-0.08	2.022	0.127-0.202
	C2	0.324	0.55-0.65	0.820	1.391-1.645
	C3	0.465	0.60-0.70	1.176	1.518-1.771
	C4	0.476	0.52-0.60	1.204	1.316-1.518
Emp.correlation (Norberg, 2003)		$Re = 15270$		$Re = 9600$	
			0.520		0.520
Experiments (Richter and Naudascher, 1976)				Blockage ratio = 1/4	
				1.35-1.40	0.80-0.90

 Table 6.2: Comparison of results for  $\overline{C}_D$  and  $C'_L$ 

The remaining data in table 6.2 show comparisons for r.m.s. lift coefficient  $C'_L$  from isolated cylinder results due to Norberg (2003) and confined cylinder experimental data from Richter and Naudascher (1976). The data for  $C'_L$  from Norberg (2003) are determined from the following correlation

$$C'_L = 0.52 - 0.06 \times [\log(Re/1600)]^{-2.6} \quad (5.4 \times 10^3 < Re < 2.2 \times 10^5), \quad (6.29)$$

which covers the upper bound of sub-critical Reynolds number range.  $C'_L$  does not display much variation when the Reynolds remains below the critical value. The data from Richter and Naudascher (1976), which are extrapolated from their experimental observations performed for a smooth circular cylinder in a wind-tunnel with a blockage ratio of 1/4, comparable to that for the present cylinder array, are included for further comparisons.

Considering the r.m.s. values of  $C'_L$  non-dimensionalised using the free stream velocity  $u_0$ , the LES value for the first column of cylinders is around 3 times larger than that measured by Shim (1985), but not very much higher than that suggested by the correlation 6.29 for an isolated cylinder, whilst it is significantly lower than the confined cylinder value of Richter and Naudascher (1976). The LES values of  $C'_L$  for the downstream columns of

cylinders are almost three times as large as for the first column, and here the agreement with the experimental data of Shim (1985) is reasonably good. Both the experimental and LES data show fluctuating lift coefficient  $C'_L$  values significantly larger than the isolated cylinder values, even that of Richter and Naudascher (1976), which includes the effect of blockage. Overall, this suggests enhancement of the vortex shedding for columns downstream of the first for the in-line cylinder configuration.

Figures 6.8 and 6.9 show time histories of the instantaneous drag and lift coefficients from the LES respectively, again basing the non-dimensionalising factor on the uniform gap velocity  $u_g$ . For an isolated cylinder, the theoretically expected result for instantaneous drag coefficient  $\bar{C}_D$  would be a low-amplitude sinusoidal ripple at twice the Strouhal frequency, superimposed on a mean value of 1.35-1.4. In practice, the amount of noise on the low amplitude drag oscillation often makes the double frequency signal hard to discern. This type of behaviour is clearly seen for the first column cylinders C1 in figure 6.8a, though with a higher mean drag. For subsequent columns, the mean drag coefficient drops to around 1.1, but with a very much higher level of fluctuation, showing strong Strouhal frequency and double Strouhal frequency components, but with irregularly modulated amplitudes. The largest peak-to-peak excursions are shown in the second column of cylinders, C2, in figure 6.8a, probably due to the influence of the strong vortex shedding from the first column. Subsequent columns, C3 and C4 in figure 6.8b, show similar but less erratic and slightly lower amplitude variations in  $\bar{C}_D$ , but still with a peak-to-peak amplitude of over 5 times that expected for an isolated cylinder. Figure 6.9 shows the corresponding LES time histories for instantaneous lift coefficient  $C'_L$ . The predominant feature in all these plots is a sinusoidal variation in lift around a mean of zero, at the Strouhal vortex shedding frequency. After the first column of cylinders, the amplitude of the oscillation increases considerably, and the signal shows a greater level of random modulation. As indicated by the r.m.s. values in table 6.2, the amplitude is a maximum in the second and third columns, falling off slightly in the fourth, possibly because there is no further downstream column. A similar phenomenon was reported by Liang and Papadakis (2007).

### 6.3.4 Shear-layer instability and vortex shedding

Figure 6.10 presents close-up views of an instantaneous velocity vector map in the middle plane of the flow domain around the four cylinders C1, C2, C3 and C4. In accordance with the results of previous researchers (e.g. Bloor (1964)), in the sub-critical regimes, the laminar boundary layer separates near the shoulder of the cylinder, forming a laminar shear layer. Transition to turbulent flow occurs shortly afterwards, within this shear layer. In figure 6.10a, it can be observed that small-scale vortexes are being formed in the shear layers behind C1, which may indicate the unstable break-up of the shear layer and transition to turbulence, though it is unclear whether the resolution of the present model is sufficient to simulate this accurately. Nevertheless, such small vortexes appear not to be formed behind the downstream cylinders as shown in figure 6.10b c d. In the real flow, for cylinders in the second and subsequent columns, the upwind boundary layers would be turbulent almost from the stagnation point, due to the high level of background turbulence, and so this form of instability would not be seen.

Figure 6.11 presents a statistically significant sample of time histories of velocity fluctuations at a point,  $(x/D = 0.55, y/D = 0.65)$  with respect to the center, of the cylinder that lies in the near wake near of the central cylinder in the first column. The power spectrum density is obtained by an ensemble average across the 40 sampling stations in the homogeneous spanwise direction. The fairly sharp peak in the spectrum, indicated in figure 6.12b, corresponds to the Strouhal frequency  $f_{St}$ , which characterizes the predominant frequency of vortex shedding. There follows a plateau in the spectrum, until another possible peak, certainly in  $v'$ , again indicated on figure 6.12b. Following Dong et al. (2006), it is suggested that this peak may correspond to the frequency of the pre-transition shear layer vortices,  $f_{sl}$ . However, the value for  $f_{sl}$  predicted for the first central column cylinder does not match the well-known  $Re^{0.67}$  law for an unconfined circular cylinder (e.g. Prasad and Williamson (1997)). This is consistent with the observations from Brun et al. (2004) that indicate there is no universal Reynolds number dependence of  $f_{sl}/f_{St}$  for two cylinders placed side by side.

The time histories and corresponding power spectrum densities for the three downstream

cylinders, obtained in a similar way, are presented in figure 6.12, figure 6.13 and figure 6.14. The fundamental frequency of vortex shedding is well pronounced for the central cylinders in all three successive columns. Accord to Gerrard (1965, 1966), the fundamental shedding frequency depends primarily on the mean flow rather than the fluctuating quantities, because the strengths of the shed vortices depend most strongly on the mean rate of shedding of vorticity, which is governed by the mean behavior of the separated shear layer. Consequently, it is reasonable to expect that the fundamental shedding frequency will show little variation for downstream cylinders in the sub-critical range of Reynolds number. Finally, no second peak signature for shear layer vortices is observed in the spectra for any of the cylinder columns after the first. This is consistent with existence of laminar shear layers only for the first column cylinders, as discussed earlier.

The dominant Strouhal frequency of vortex shedding predicted in the present study is evaluated in terms of the mean velocity across the gap  $u_g$ . It is of interest to compare the predicted value with the experimental observations, especially with the universal Strouhal number  $St^*$  proposed by Roshko (1954) that is defined as  $fd^*/u^*$  in terms of the wake width between the rows of vortices  $d^*$  and the wake velocity  $u^*$  obtained from the free-streamline theory. These are summarized in the table 6.3 along with an extrapolated value from the measurements for a confined circular cylinder by Richter and Naudascher (1976). It can be observed that the present LES predictions of Strouhal number for all 4 columns are identical, and all are in excellent agreement with the experimental value of Shim (1985). Agreement with the universal Strouhal number number, based on the experimental measurements of Richter and Naudascher (1976) and the theoretical value from Roshko (1954) is also good, with a maximum discrepancy of less than 5%.

### 6.3.5 Correlation length for vortex shedding

To examine the spatial structure of vortex shedding behind the cylinders, figure 6.15 presents the auto-correlation functions for the streamwise and crosswise velocity components for the 40-sampling stations, at location  $(x/D = 0.55, y/D = 0.65)$  with respect to the axis of the cylinder, across the homogeneous spanwise direction. The auto-correlation

Case	$St$
Present LES ( $Re_g = 15270$ )	C1 0.153
	C2 0.153
	C3 0.153
	C4 0.153
Experiments (Shim, 1985)	0.152
Experiments (Richter and Naudascher, 1976) ( $Re = 1.5 \times 10^4$ )	$St^*$ 0.151
Theoretical Value (Roshko, 1954) ( $Re < 2 \times 10^5$ )	$St^*$ 0.16

 Table 6.3: Comparison of  $St$  with the universal Strouhal number

function is defined as

$$R_{ii}(\mathbf{x}; \mathbf{z}, t) = \frac{\overline{u'_i(\mathbf{x}; t) u'_i(\mathbf{x} + \mathbf{z}; t)}}{\overline{u'^2_i(\mathbf{x}; t)}} \quad (6.30)$$

From figure 6.15a, it can be observed for the first column cylinder C1 that  $R_{u'u'}$  and  $R_{v'v'}$  decreases monotonically to zero within the range of  $L/D = 1$ . This implies that the spanwise length of the biggest eddy from vortex shedding approximately equal to the diameter of the cylinder. This feature has been demonstrated for an unconfined single circular cylinder by previous researchers. The fact that  $R_{u'u'}$  and  $R_{v'v'}$  appear to show re-correlation between mid-span and  $z/D = 2.0$  is concerned with the periodic boundary condition employed for the homogeneous spanwise direction in the present LES study.

From figure 6.15b,c d, it can be observed that the downstream cylinders C2, C3 and C4 display different behavior with respect to the auto-correlation as a function of the spanwise length for the streamwise and crosswise velocity fluctuations. Firstly, within the length of  $L/D = 1$ ,  $R_{u'u'}$  and  $R_{v'v'}$  do not decrease to zero. Secondly,  $R_{v'v'}$  wiggles across the middle part of the cylinder  $L/D \in [0.5, 1.5]$ . Both of the discrepancies from the first column cylinder C1 behavior may result from the mixing of the shed vortices from different column cylinders, giving rise to complex eddy patterns in the wake.

## 6.4 Concluding remarks

A turbulent flow across tube banks with transverse and longitudinal pitch  $P_T/D = 2.67$ ,  $P_L/D = 2.31$ , respectively, has been simulated successfully by Large Eddy Simulation

(LES) based on the dynamic Smagorinsky subgrid scale model (SGS) with a wall-layer model. Flow structures within the tube bank based on the normalized  $Q$  criterion have been presented. Contours of  $Q$  criterion, coloured by turbulence intensity, indicate that turbulence intensity builds up to an equilibrium level by the third column of cylinders. The middle cylinder from each column was chosen to present results and compare with experiments. The mean surface pressure characteristics observed in the experiments of Shim (1985) are reproduced almost exactly. LES prediction of the fluctuating pressure measurements which, to the author's knowledge has never been previously shown, is generally in good agreement with experiment, apart from for the cylinder in the first column. Even here, based on separate published results for an isolated cylinder, the evidence is that the major error is probably in the experimental results, since the frontal surface fluctuation levels are unexpectedly high for undisturbed inflow. Quite satisfying agreement was observed between the present simulation and the experimental measurements of Shim (1985) for drag and lift coefficients, which indicate that the cylinders in the second column experience the minimum mean drag force and maximum lift force fluctuation. The LES shows that, for cylinder columns beyond the first, the mean drag coefficient is lower than that expected for an isolated cylinder at similar Reynolds number, whilst the fluctuations in both lift and drag coefficient are much higher. A frequency analysis for velocity signals at the position with respect to each cylinder axis ( $x/D = 0.55, y/D = 0.65$ ) is presented and compared with experimental as well as theoretical work. These results show that, for this relatively large-pitch tube bank, there is a constant dominant vortex shedding frequency throughout the cylinder array, corresponding to a Strouhal number of 0.153 based on gap velocity. Only for the first column of cylinders, where a laminar shear layer follows separation, is a shear layer instability frequency peak observed in the spectra. As far as the first column cylinder is concerned, the shear layer instability frequency observed does not agree with the universal value for an unconfined single circular cylinder, but this supports the recent experimental measurements for tandem cylinders by Brun et al. (2004). Finally, auto-correlation functions for streamwise and cross velocity fluctuations as a function of the spanwise length are investigated. For the first column cylinders the correlation function falls to zero over a spanwise length of  $\pm$  one diameter, as is generally observed for

an isolated cylinder. The turbulent eddies behind downstream cylinders are of more complex structure than for the first column cylinders, as a result of the mixing of shed vortices from different column cylinders, and the spanwise correlation function does not fall below 0.3.

## REFERENCES

- H. R. Barsamian and Y. A. Hassan. Large eddy simulation of turbulent crossflow in tube bundles. *Nuclear Engineering and Design*, 172(1-2):103–122, 1997.
- S. Beale and D. B. Spalding. A numerical study of unsteady fluid flow in in-line and staggered tube banks. *Journal of Fluids and Structures*, 13(6):723–754, 1999.
- S. Benhamadouche and D. Laurence. LES, coarse LES, and transient RANS comparisons on the flow across a tube bundle. *International Journal of Heat and Fluid Flow*, 24(4):470–479, 2003.
- M. S. Bloor. The transition to turbulence in the wake of a circular cylinder. *Journal of Fluid Mechanics*, 19(02):290–304, 1964.
- D. Bouris and G. Bergeles. Two dimensional time dependent simulation of the subcritical flow in a staggered tube bundle using a subgrid scale model. *International Journal of Heat and Fluid Flow*, 20(2):105–114, 1999.
- M. Breuer. Large eddy simulation of the subcritical flow past a circular cylinder: numerical and modeling aspects. *International Journal for Numerical Methods in Fluids*, 28(9):1281–1302, 1998.
- M. Breuer. A challenging test case for large eddy simulation: high reynolds number circular cylinder flow. *International Journal of Heat and Fluid Flow*, 21(5):648–654, 2000.
- C. Brun, D. Tenchine, and E. J. Hopfinger. Role of the shear layer instability in the near wake behavior of two side-by-side circular cylinders. *Experiments in Fluids*, 36(2):334–343, 2004.

- L. Davidson. Large eddy simulations: how to evaluate resolution. *International Journal of Heat and Fluid Flow*, 30(5):1016–1025, 2009.
- J. W. Deardorff. A numerical study of three-dimensional turbulent channel flow at large reynolds numbers. *Journal of Fluid Mechanics*, 41(02):453–480, 1970.
- S. Dong, G. E. Karniadakis, A. Ekmekci, and D. Rockwell. A combined direct numerical simulation-particle image velocimetry study of the turbulent near wake. *Journal of Fluid Mechanics*, 569:185–208, 2006.
- M. Germano, U. Piomelli, P. Moin, and W. H. Cabot. A dynamic subgrid-scale eddy viscosity model. *Physics of Fluids A: Fluid Dynamics*, 3:1760, 1991.
- J. H. Gerrard. A disturbance-sensitive reynolds number range of the flow past a circular cylinder. *Journal of Fluid Mechanics*, 22(1):187–196, 1965.
- J. H. Gerrard. The mechanics of the formation region of vortices behind bluff bodies. *Journal of Fluid Mechanics*, 25(2):401–413, 1966.
- Y. A. Hassan and H. R. Barsamian. Tube bundle flows with the Large Eddy Simulation technique in curvilinear coordinates. *International Journal of Heat and Mass Transfer*, 47(14-16):3057–3071, 2004.
- R. S. Hill, K. C. Shim, and R. I. Lewis. Sources of excitation in tube banks due to vortex shedding. *ARCHIVE: Proceedings of the Institution of Mechanical Engineers, Part C: Mechanical Engineering Science 1983-1988 (vols 197-202)*, 200(43):293–301, 1986.
- J. C. R. Hunt, A. A. Wray, and P. Moin. Eddies, streams, and convergence zones in turbulent flows. In *Studying Turbulence Using Numerical Simulation Databases, 2*, volume 1, pages 193–208, 1988.
- S. A. Jordan. Resolving turbulent wakes. *Journal of Fluids Engineering*, 125:823, 2003.
- K. Lam, Y. F. Lin, L. Zou, and Y. Liu. Experimental study and large eddy simulation of turbulent flow around tube bundles composed of wavy and circular cylinders. *International Journal of Heat and Fluid Flow*, 31(1):32–44, 2010.

- A. Leonard. Energy cascade in large-eddy simulations of turbulent fluid flows. *Adv. Geophys*, 18:237–248, 1974.
- D. C. Leslie and G. L. Quarini. The application of turbulence theory to the formulation of subgrid modelling procedures. *Journal of Fluid Mechanics*, 91(01):65–91, 1979.
- C. Liang and G. Papadakis. Large eddy simulation of cross-flow through a staggered tube bundle at subcritical reynolds number. *Journal of Fluids and Structures*, 23(8): 1215–1230, 2007.
- D. K. Lilly. *On the application of the eddy viscosity concept in the inertial sub-range of turbulence*. National Center for Atmospheric Research, 1966.
- D. K. Lilly. A proposed modification of the germano subgrid-scale closure method. *Physics of Fluids A: Fluid Dynamics*, 4:633, 1992.
- P. J. Mason. Large-eddy simulation: A critical review of the technique. *Quarterly Journal of the Royal Meteorological Society*, 120(515):1–26, 1994.
- C. Moulinec, M. Pourquie, B. J. Boersma, and F. T. M. Nieuwstadt. Diagonal cartesian method on staggered grids for a dns in a tube bundle. *Direct and Large-Eddy Simulation IV*, page 221, 2002.
- C. Moulinec, J. C. R. Hunt, and F. T. M. Nieuwstadt. Disappearing wakes and dispersion in numerically simulated flows through tube bundles. *Flow, turbulence and combustion*, 73(2):95–116, 2004a.
- C. Moulinec, M. J. B Pourquié, Buchal T. Boersma, B. J, and F. T. M Nieuwstadt. Direct numerical simulation on a cartesian mesh of the flow through a tube bundle. *International Journal of Computational Fluid Dynamics*, 18(1):1–14, 2004b.
- C. Norberg. Fluctuating lift on a circular cylinder: review and new measurements. *Journal of Fluids and Structures*, 17(1):57–96, 2003.
- U. Piomelli, P. Moin, and J. H. Ferziger. Model consistency in large eddy simulation of turbulent channel flows. *Physics of Fluids*, 31:1884, 1988.

- A. Prasad and C. H. K. Williamson. The instability of the shear layer separating from a bluff body. *Journal of fluid mechanics*, 333(1):375–402, 1997.
- C. M. Rhie and W. L. Chow. Numerical study of the turbulent flow past an airfoil with trailing edge separation. *AIAA journal*, 21(11):1525–1532, 1983.
- A. Richter and E. Naudascher. Fluctuating forces on a rigid circular cylinder in confined flow. *Journal of Fluid Mechanics*, 78(Part 3):561–576, 1976.
- W. Rodi. Comparison of les and rans calculations of the flow around bluff bodies. *Journal of Wind Engineering and Industrial Aerodynamics*, 69:55–75, 1997.
- R. S. Rogallo and P. Moin. Numerical simulation of turbulent flows. *Annual Review of Fluid Mechanics*, 16(1):99–137, 1984.
- P. Rollet-Miet, D. Laurence, and J. Ferziger. Les and rans of turbulent flow in tube bundles. *International journal of heat and fluid flow*, 20(3):241–254, 1999.
- A. Roshko. On the drag and shedding frequency of two-dimensional bluff bodies. Technical report, DTIC Document, 1954.
- P. Sagaut. *Large eddy simulation for incompressible flows*, volume 20. Springer, 2001.
- H. Schlichting, K. Gersten, and K. Gersten. *Boundary-layer theory*. Springer Verlag, 2000.
- K. C. Shim. *Fluctuating Phenoema in tube banks in cross-flow*. PhD thesis, Newcastle University, 1985.
- K. C. Shim, R. S. Hill, and R. I. Lewis. Fluctuating lift forces and pressure distributions due to vortex shedding in tube banks. *International Journal of Heat and Fluid Flow*, 9(2):131–146, 1988.
- O. Simonin and M. Barcouda. Measurements and prediction of turbulent flow entering a staggered tube bundle. In *4th International Symposium on Applications of Laser Anemometry to Fluid Mechanics, Lisbon, Portugal, paper*, volume 5, 1988.
- J. Smagorinsky. General circulation experiments with the primitive equations. *Monthly weather review*, 91(3):99–164, 1963.

- Y. Q. Wang, P. Jackson, and T. J. Phaneuf. Turbulent flow through a staggered tube bank. *Journal of Thermophysics and Heat Transfer*, 20(4):738, 2006.
- J. K. Watterson, W. N. Dawes, A. M. Savill, and A. J. White. Predicting turbulent flow in a staggered tube bundle. *International Journal of Heat and Fluid Flow*, 20(6): 581–591, 1999.
- H. Werner, H. Wengle, et al. Large-eddy simulation of turbulent flow over and around a cube in a plate channel. *Turbulent Shear Flows*, 8:155–168, 1993.
- C. H. K. Williamson. Vortex dynamics in the cylinder wake. *Annual Review of Fluid Mechanics*, 28(1):477–539, 1996.

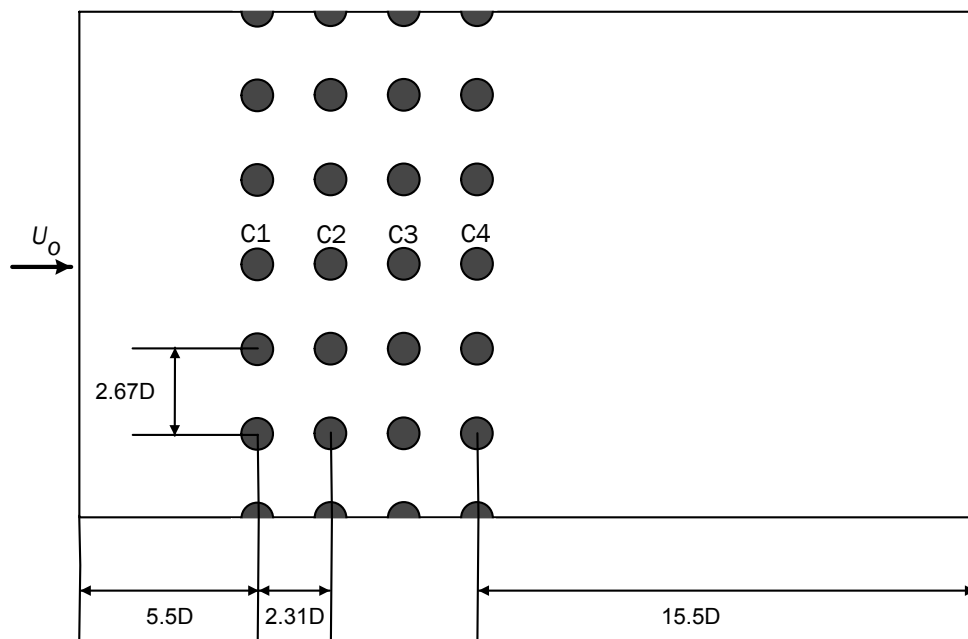


Figure 6.1: Configuration of the four-column in-line tube banks

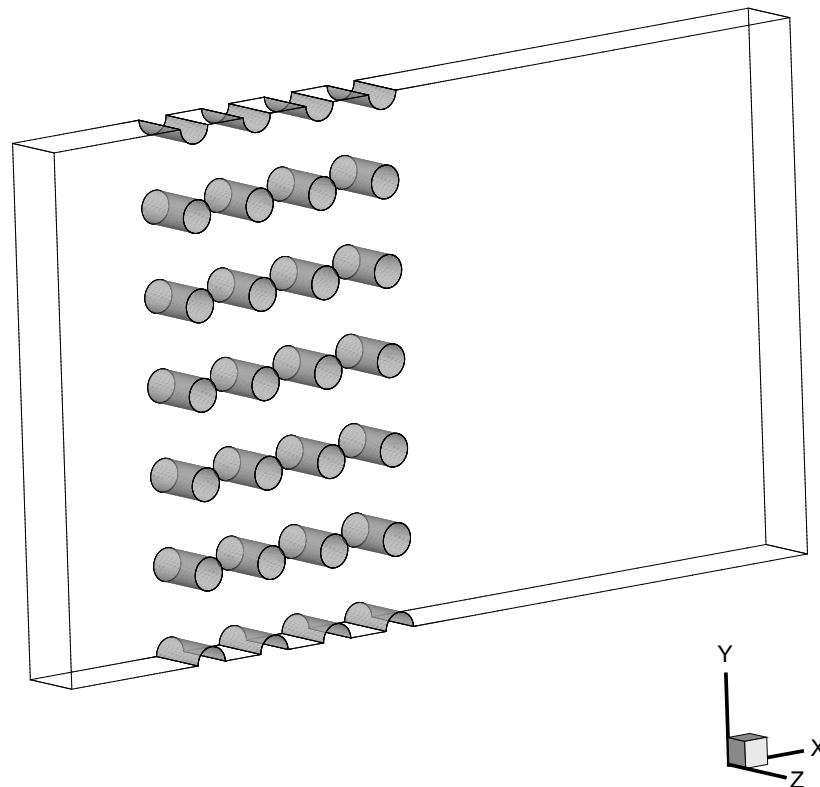


Figure 6.2: Configuration of the four-row in-line tube bank, The  $x$ -axis indicates the freestream flow direction;  $y$ - and  $z$ -axis respectively indicate the transverse and spanwise direction.

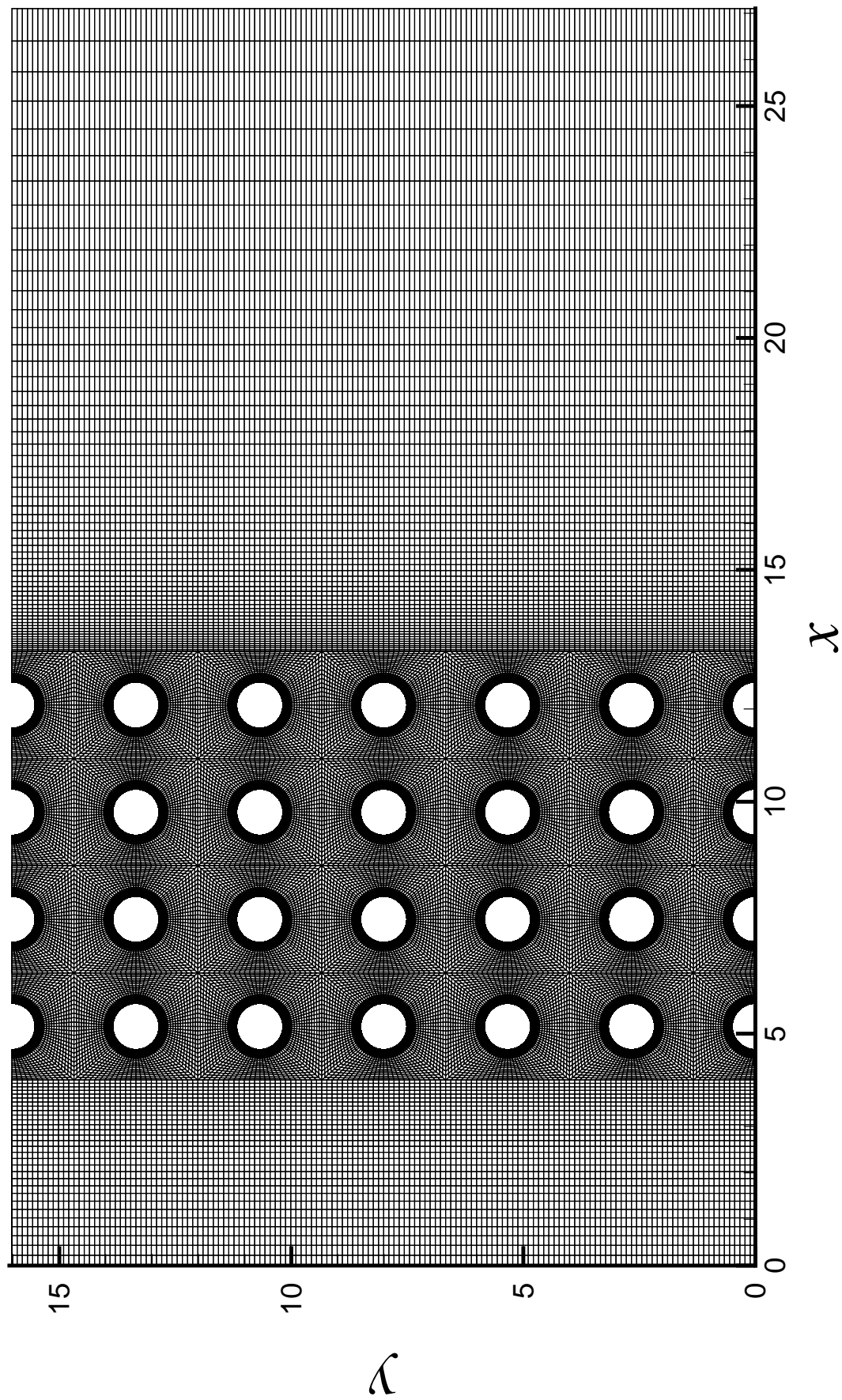


Figure 6.3: Computational domain and mesh in the  $x - y$  plane

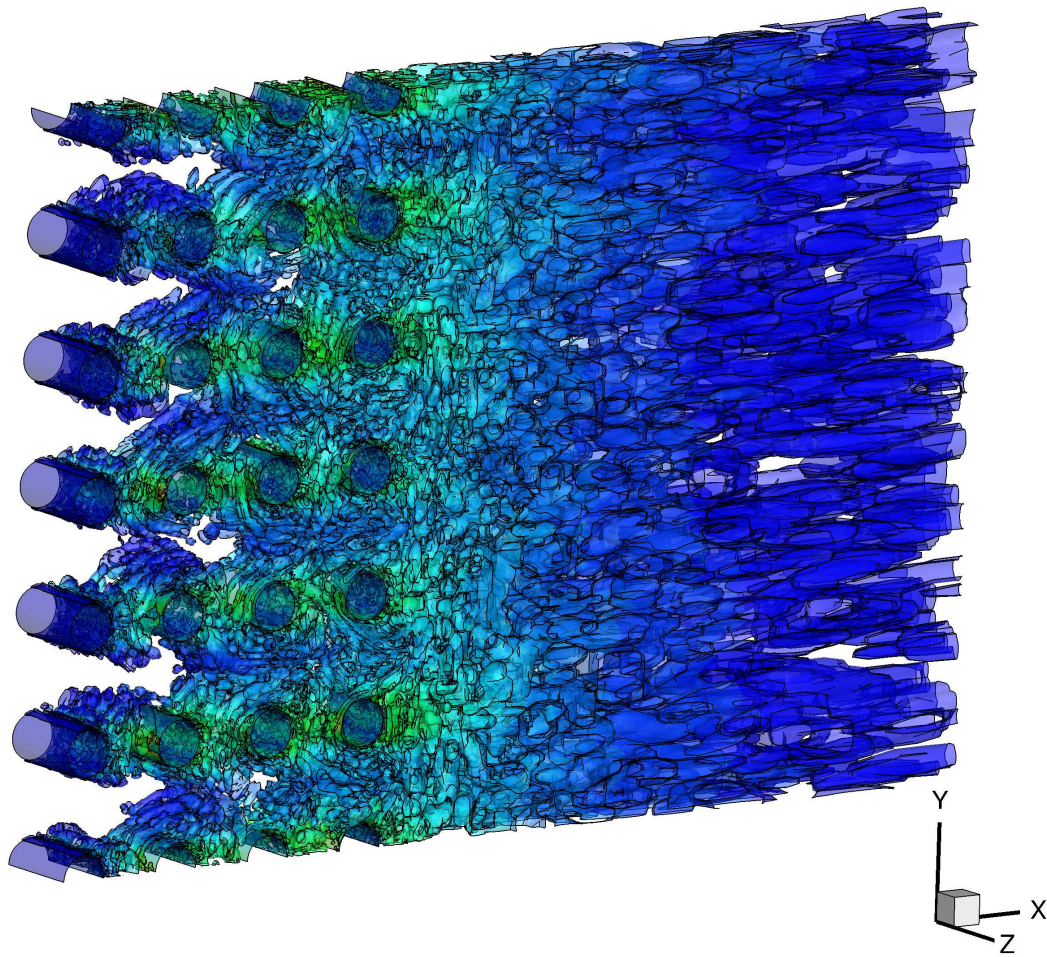


Figure 6.4: The filtered flow structure development across the four-in-line tube banks, iso-surface of the second invariant of velocity gradient tensor, colored by the resolved turbulent kinetic energy (TKE)

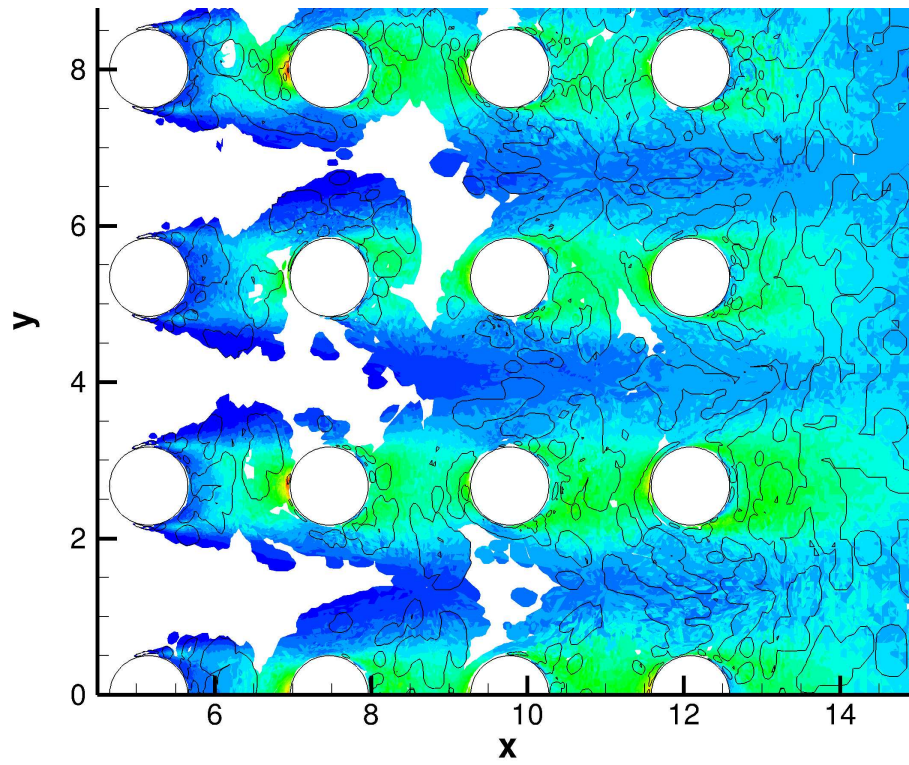


Figure 6.5: Vortex motion around cylinders at the middle plane cut

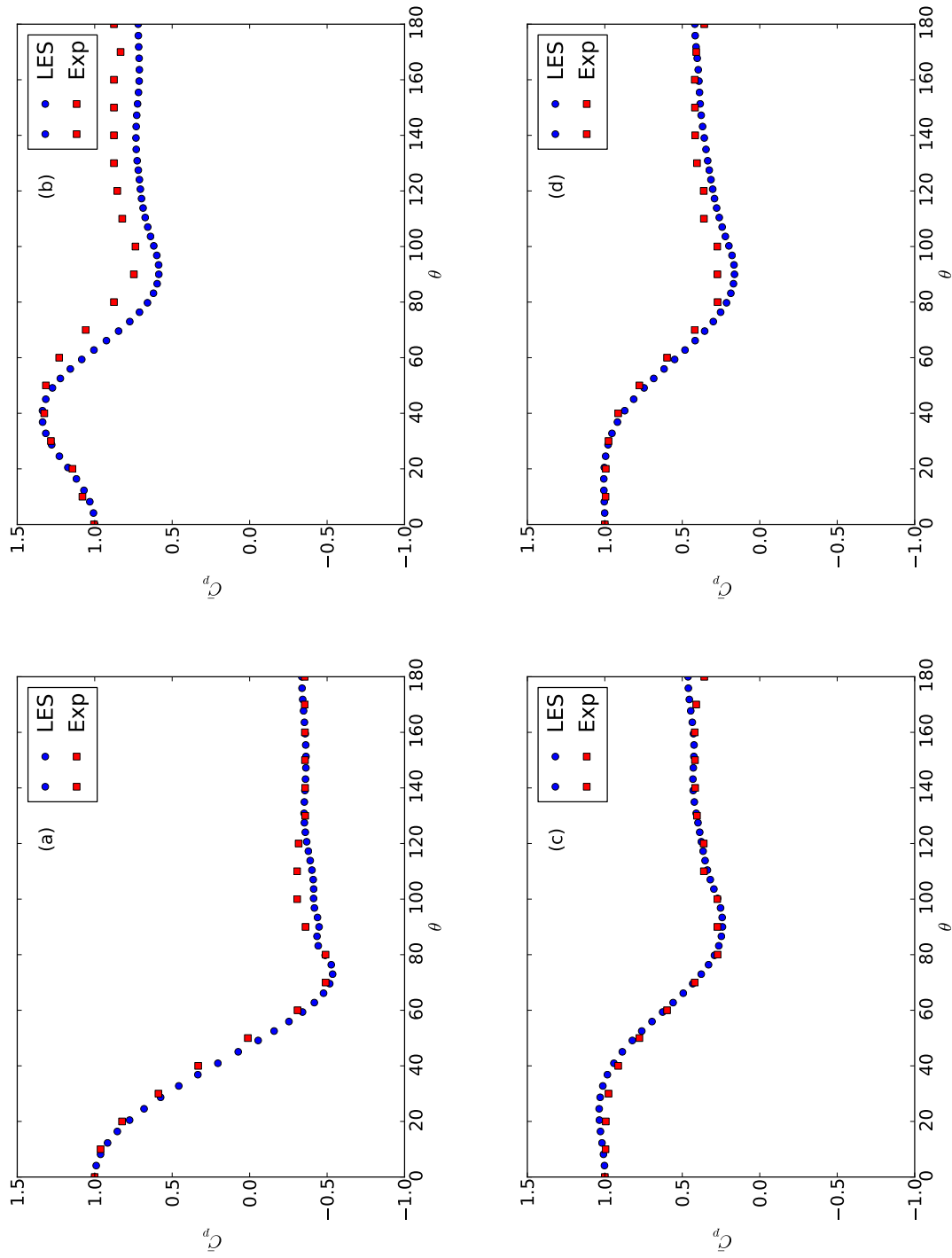


Figure 6.6: Averaged mean  $C_p$  as a function of angle from the front stagnation point, (a) C1, (b) C2, (c) C3, (d) C4  
 Averaged mean  $C_p$  as a function of angle from the front stagnation point, (a) C1, (b) C2, (c) C3, (d) C4

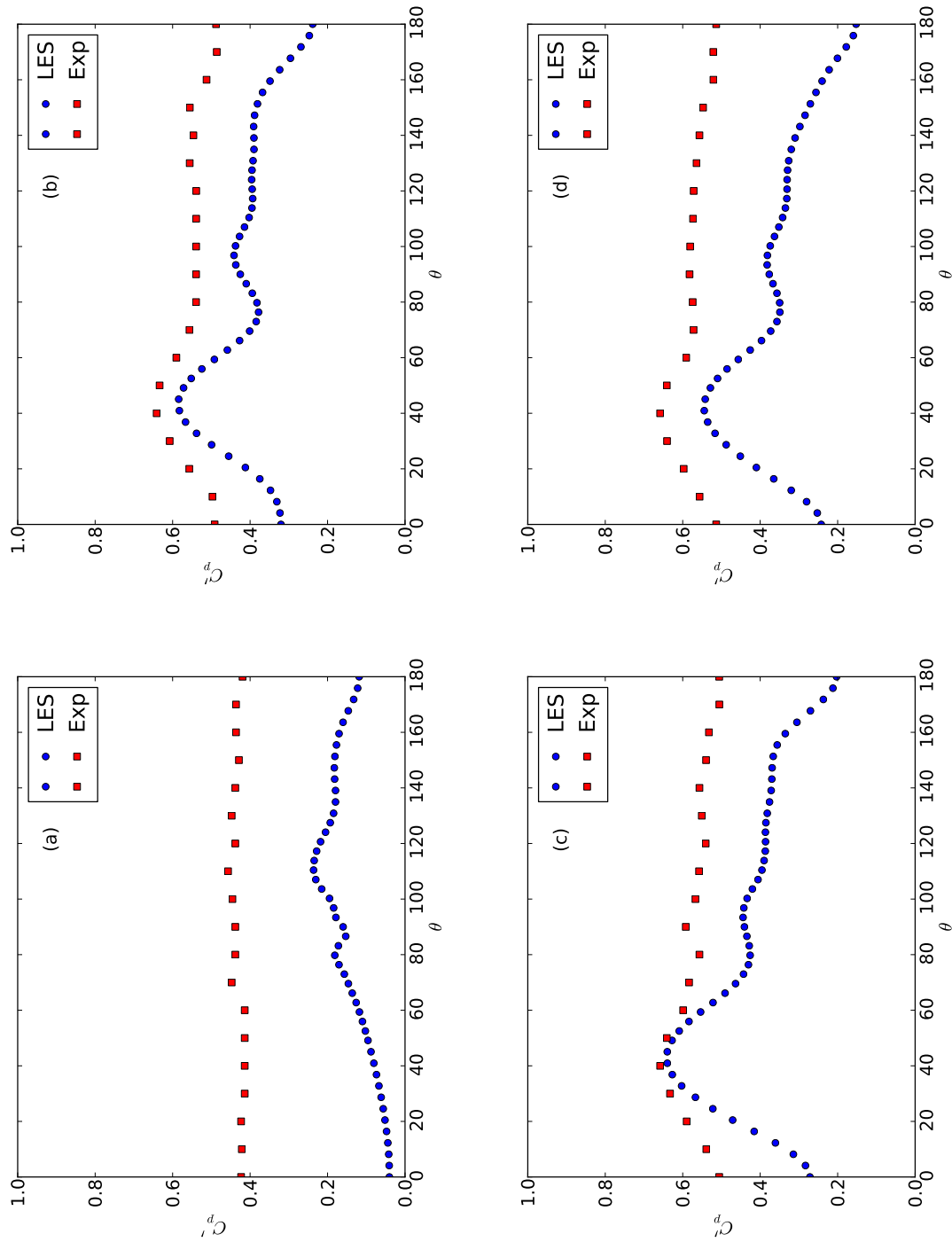


Figure 6.7: surface fluctuating pressure distribution as a function of angle from the front stagnation point over 30 non-dimensional time units, (a) **C1**, (b) **C2**, (c) **C3**, (d) **C4**

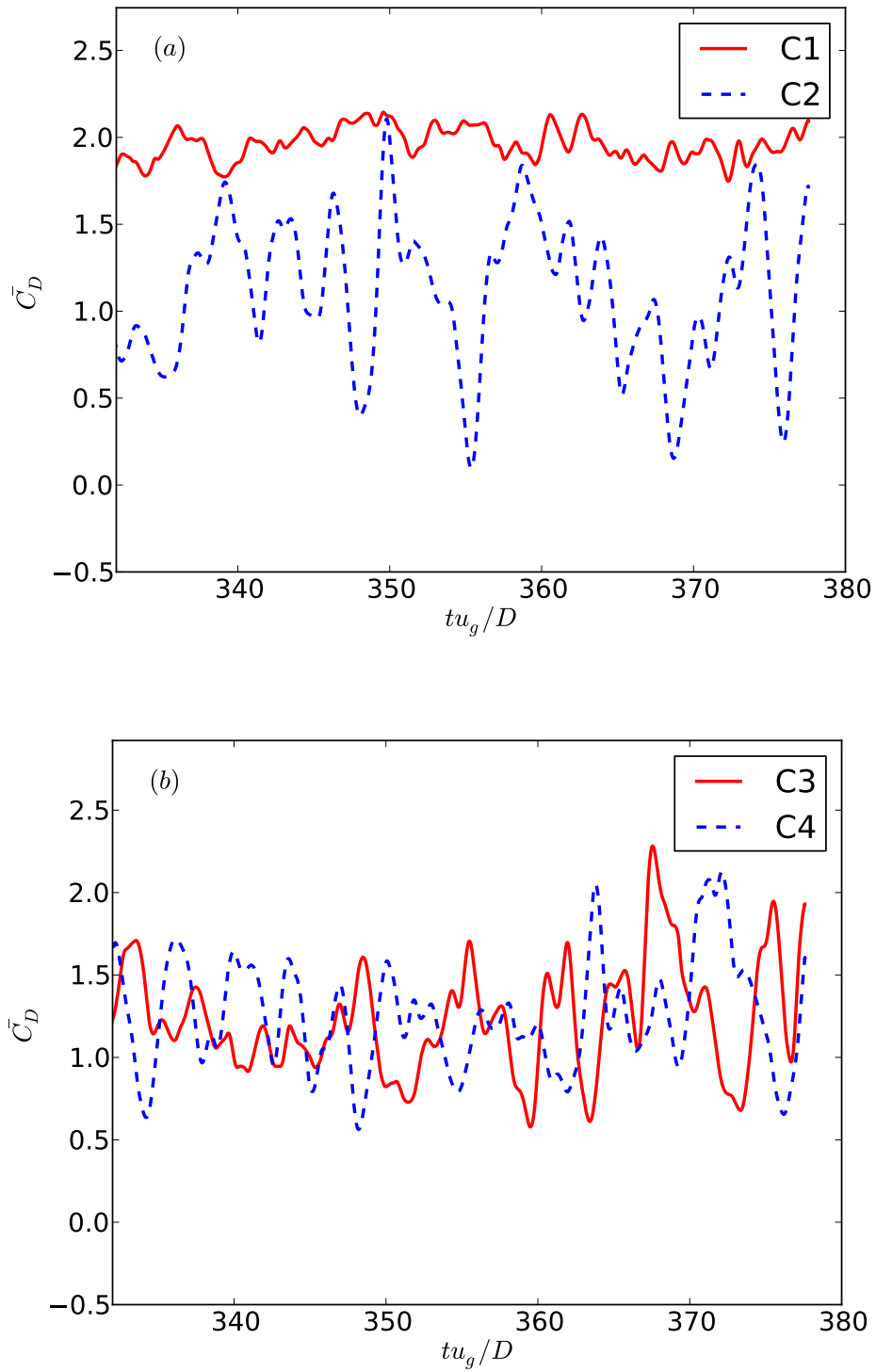


Figure 6.8: Time history of  $\bar{C}_D$ , (a) **C1,C2** (b) **C3,C4**

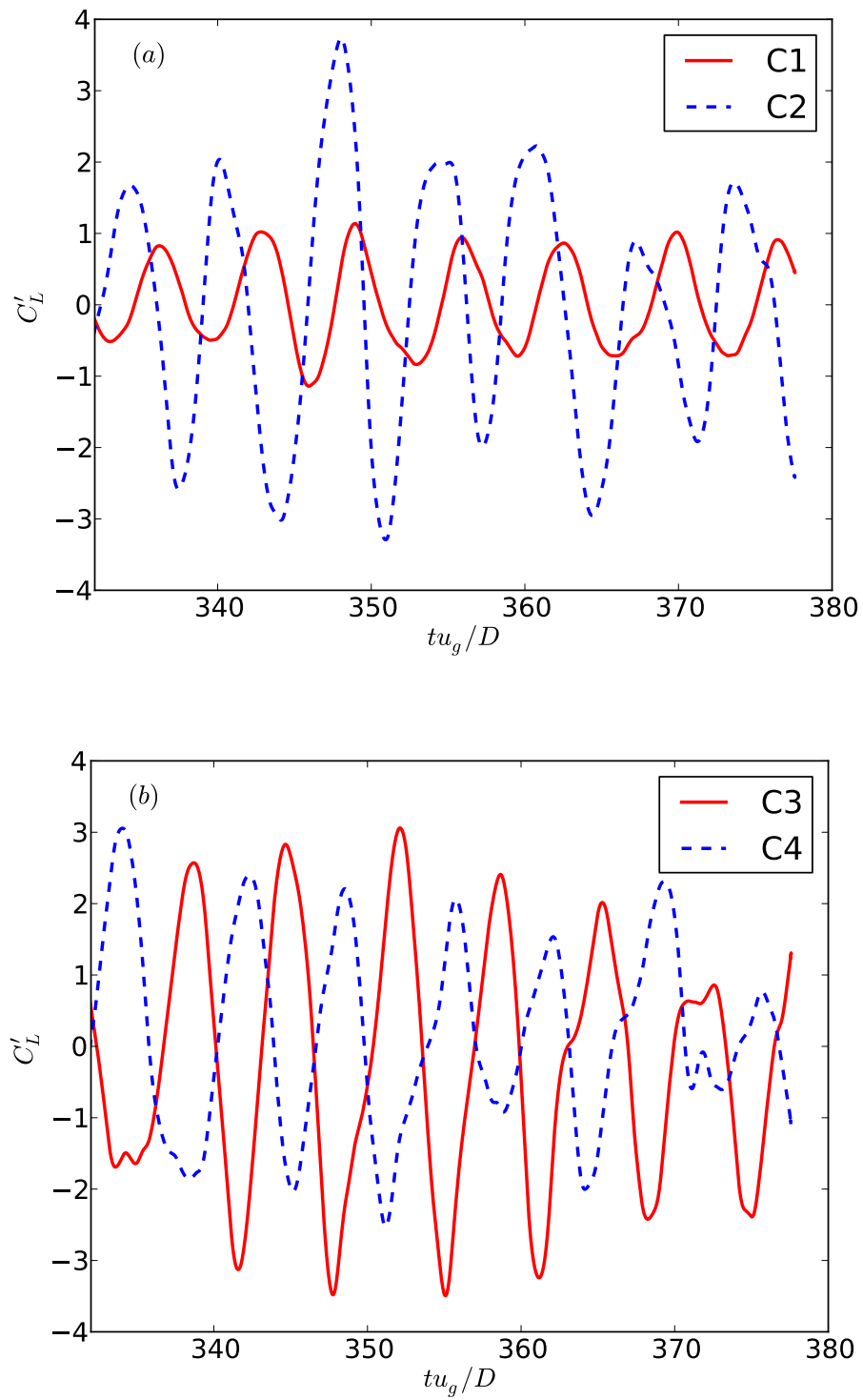


Figure 6.9: Time history of  $C'_L$ , (a) C1,C2 (b) C3,C4

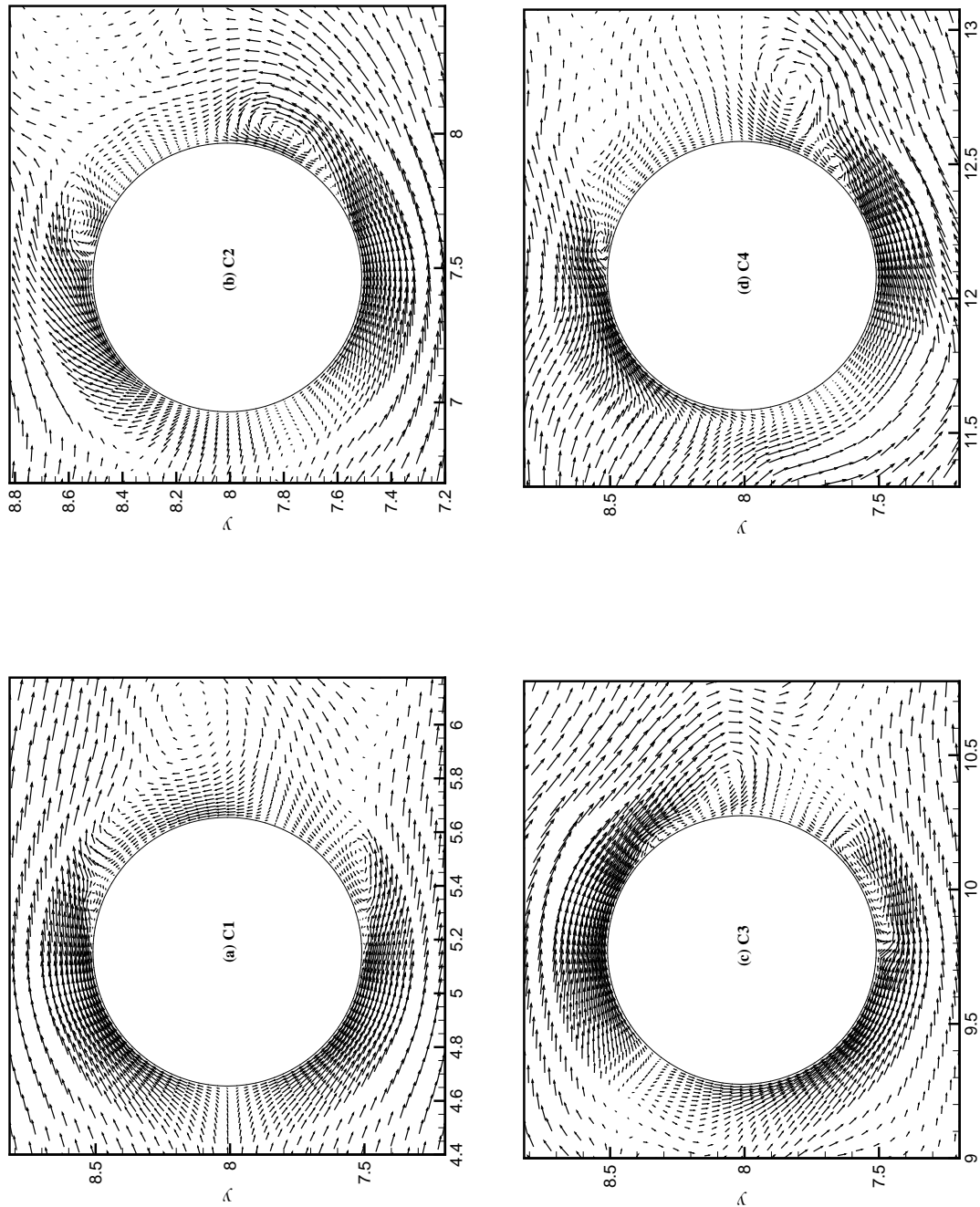


Figure 6.10: Instantaneous velocity vector map in the middle plane of flow domain (a) C1, (b) C2, (c) C3, (d) C4

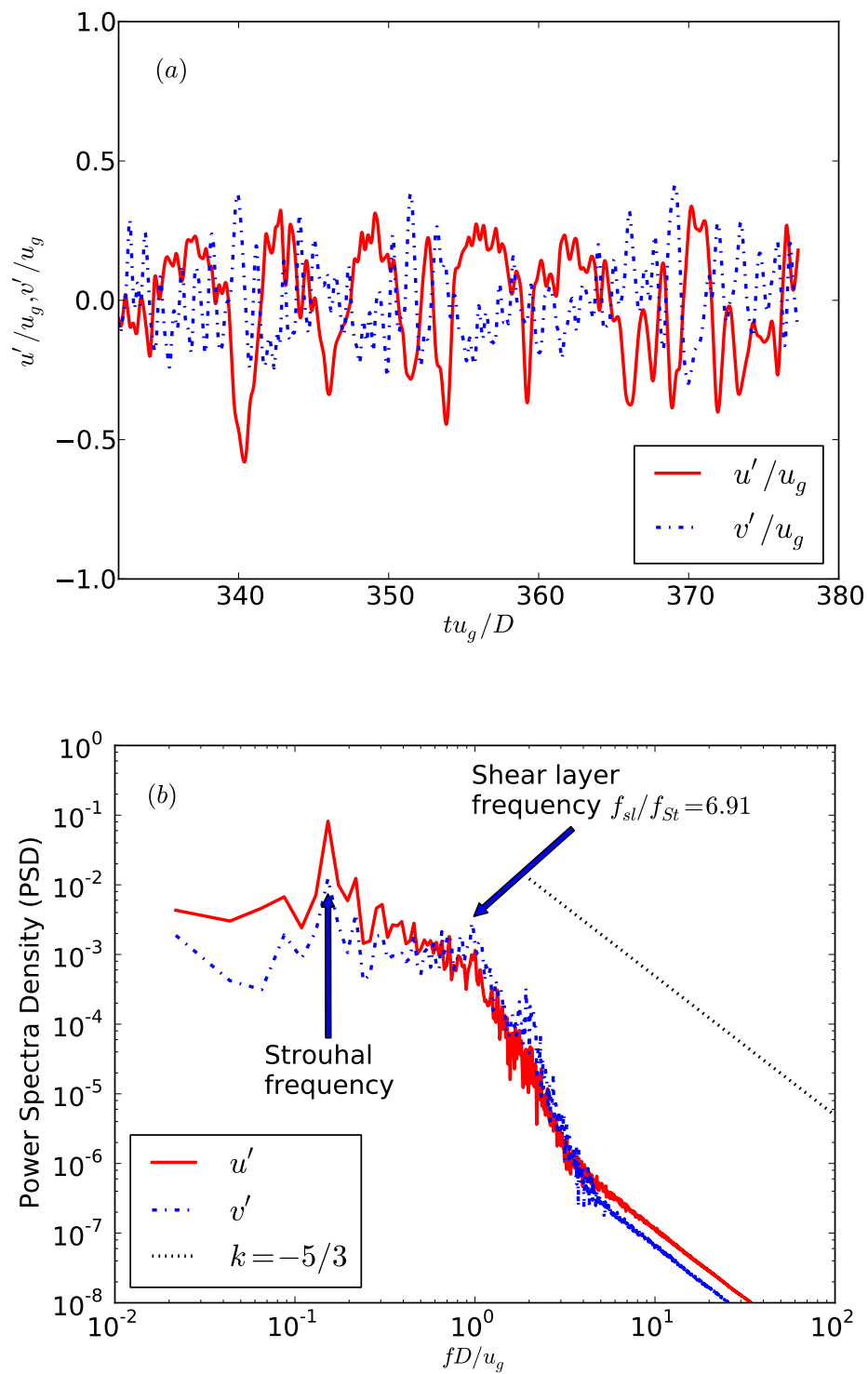


Figure 6.11: Time histories of velocity signal fluctuations behind cylinder C1 and the corresponding power spectrum density.

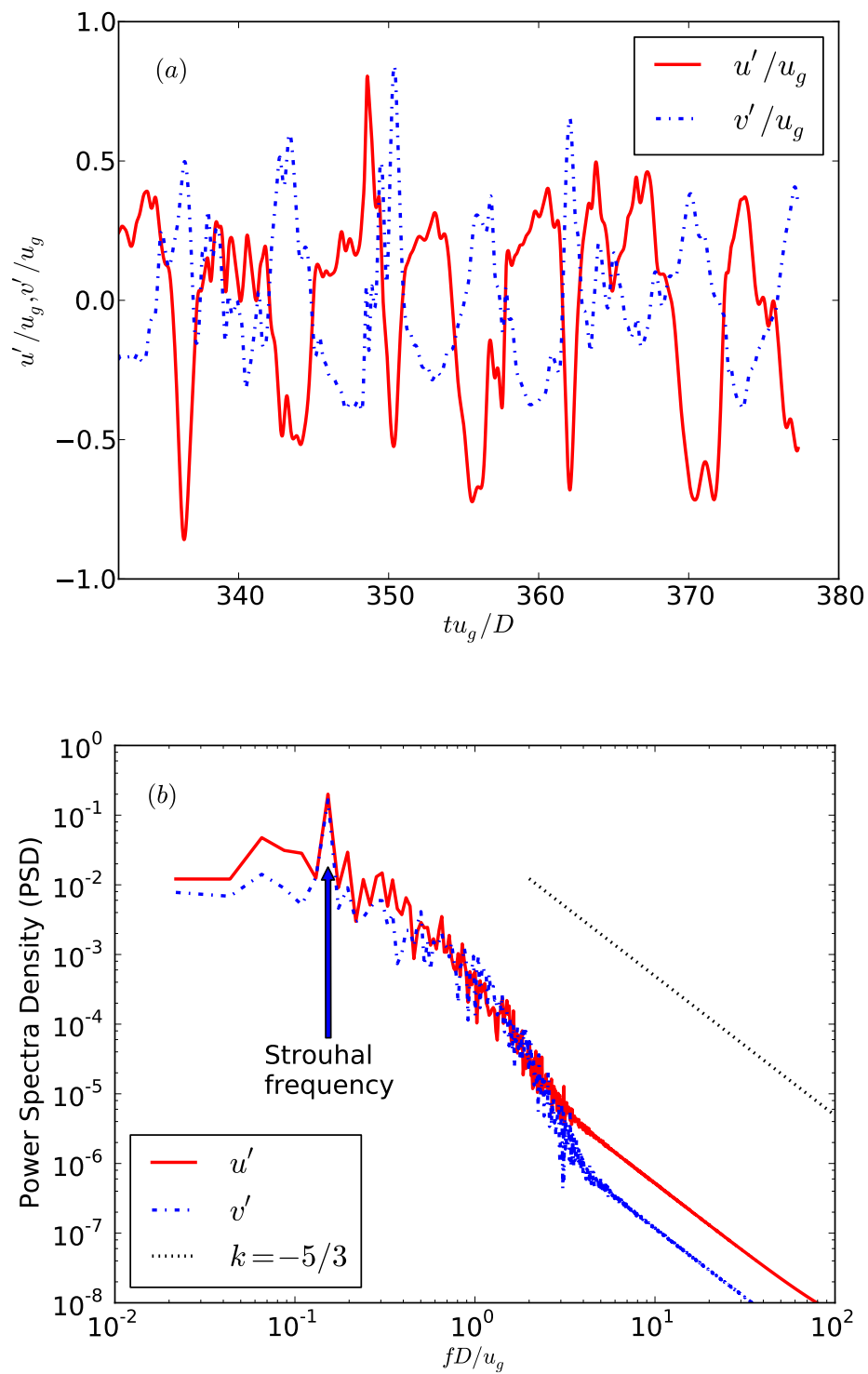


Figure 6.12: Time histories of velocity signal fluctuations behind cylinder C2 and the corresponding power spectrum density.

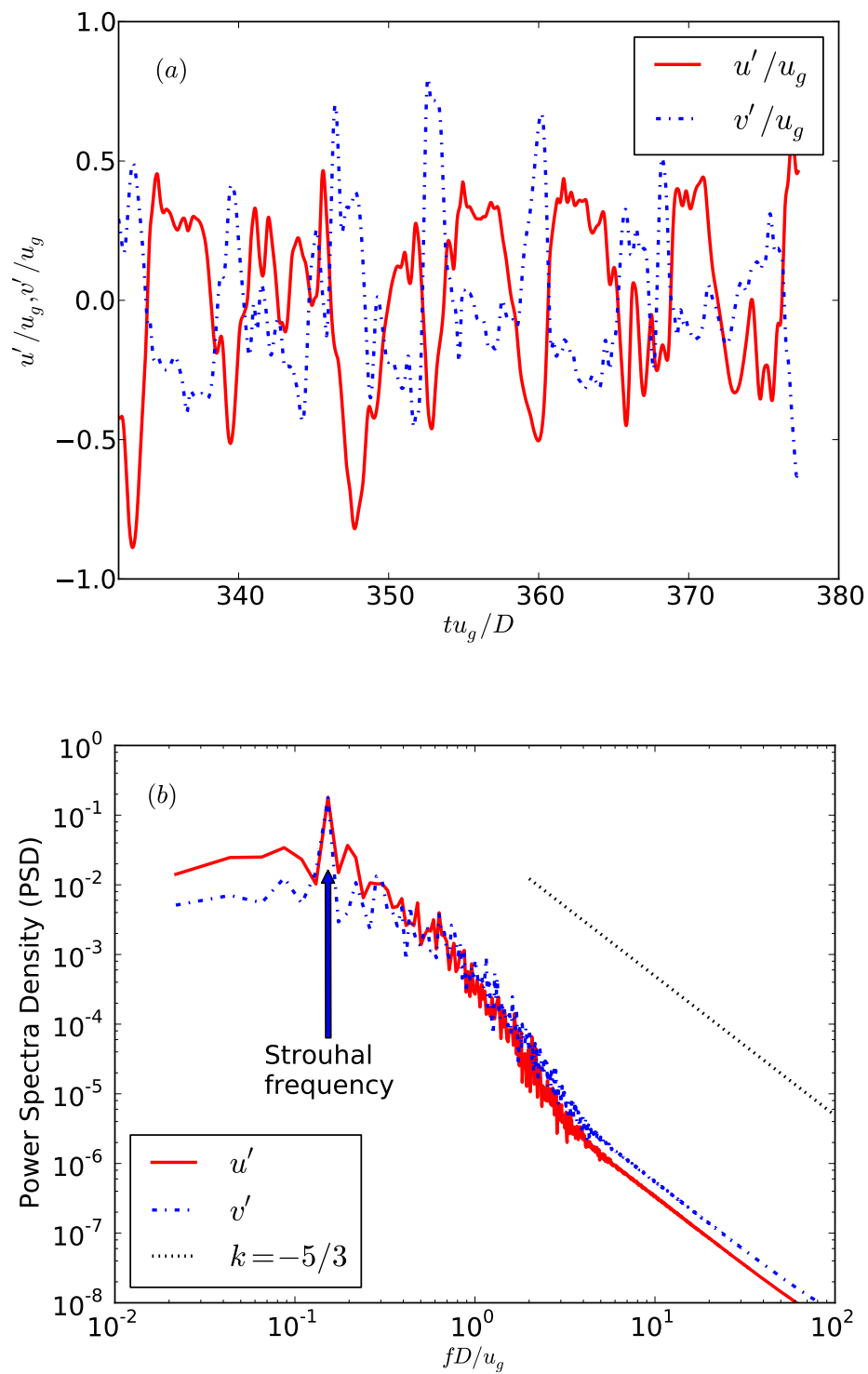


Figure 6.13: Time histories of velocity signal fluctuations behind cylinder C3 and the corresponding power spectrum density.

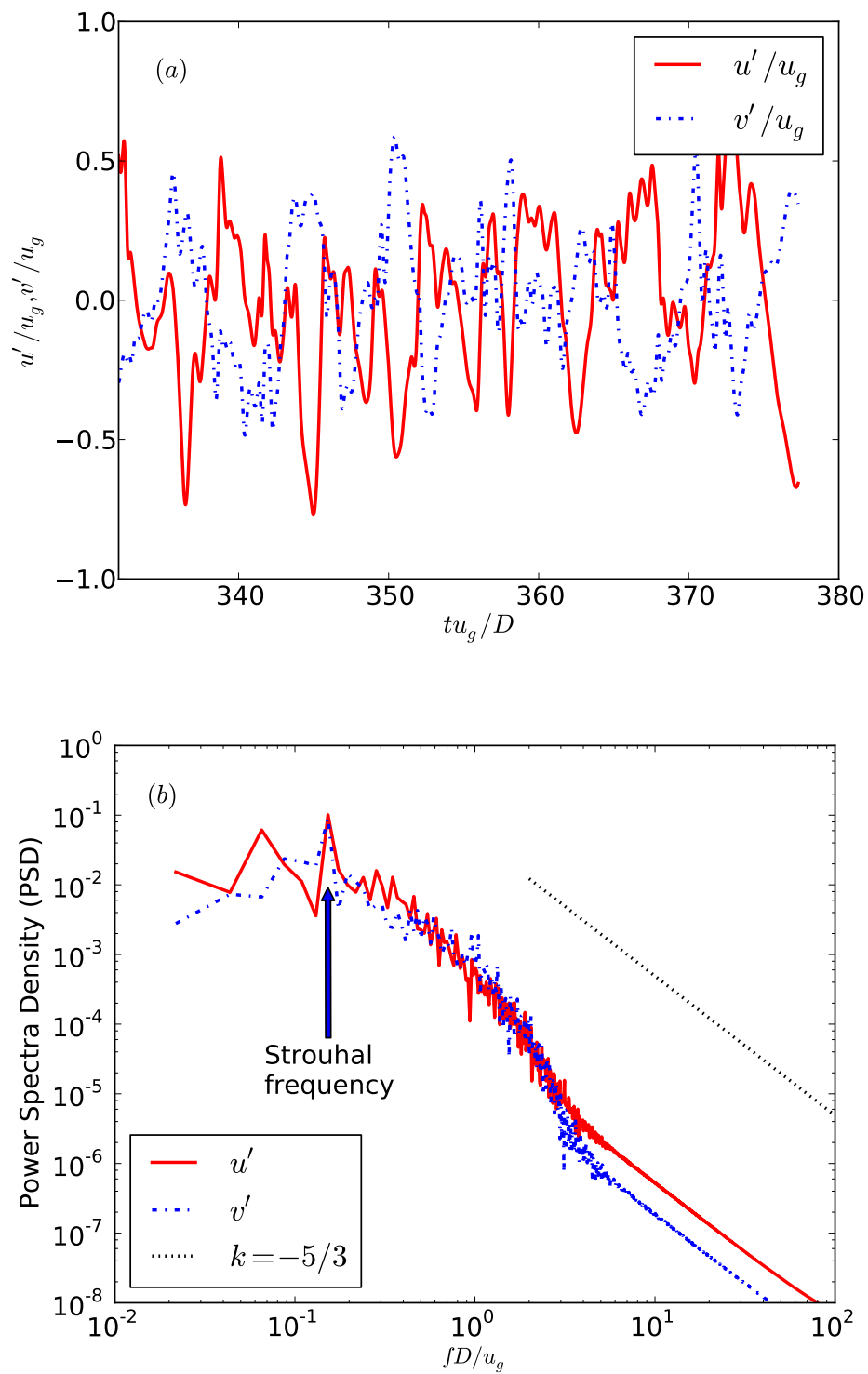


Figure 6.14: Time histories of velocity signal fluctuations behind cylinder C4 and the corresponding power spectrum density.

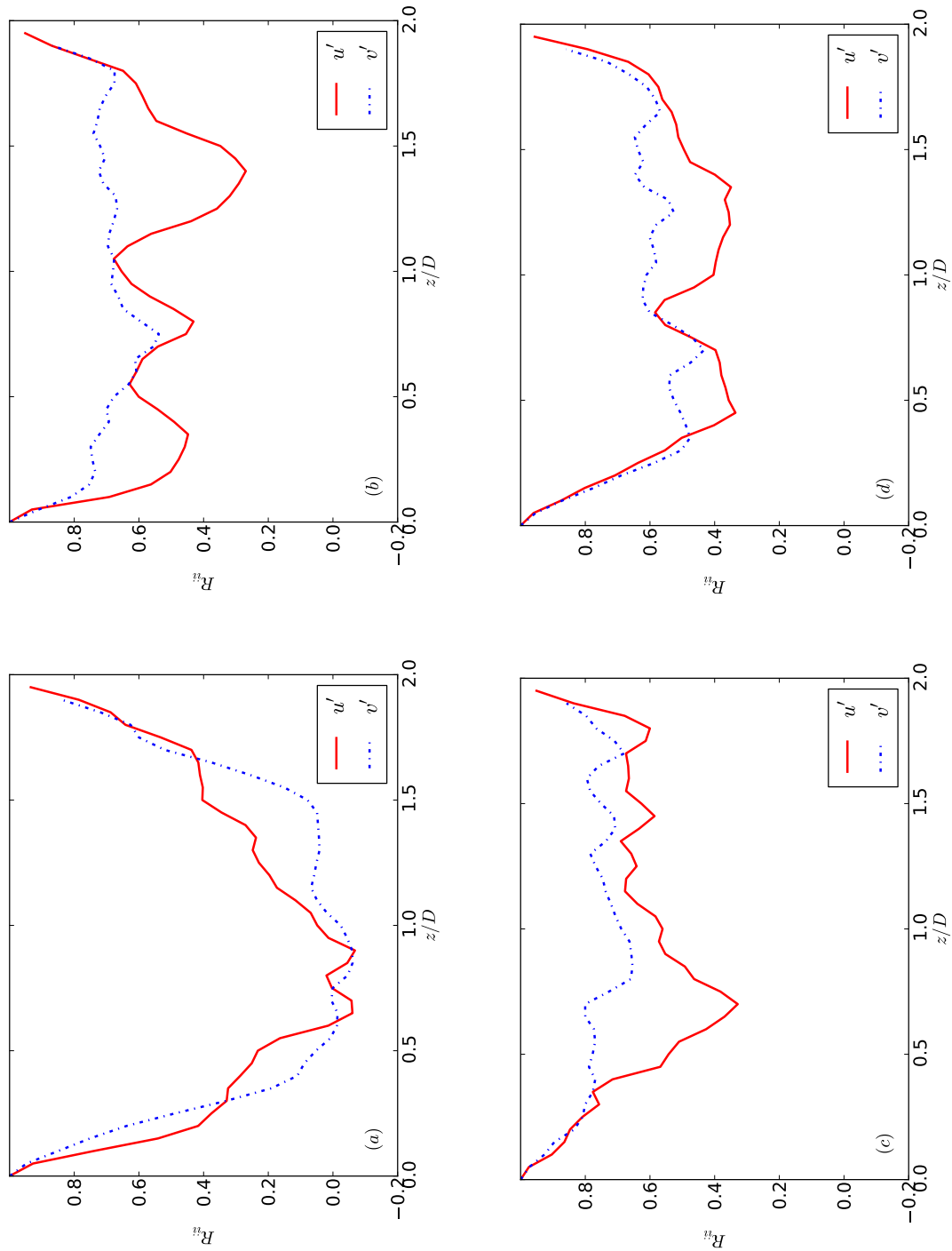


Figure 6.15: Auto-correlation of streamwise and crosswise velocity fluctuations as a function of spanwise length (a) **C1**, (b) **C2**, (c) **C3**, (c) **C4**,

# Chapter 7

## An LES study of particle deposition within an in-line array tube-banks

### 7.1 Introduction

An investigation of the deposition and impact of aerosol particles to heat exchangers is of importance in the design and operation of heat exchanger tube banks used in a wide range of industrial applications, e.g., civil advanced gas-cooled reactor (CAGR) boilers, oil-fired steam boilers of thermal power stations and process plants. In many safety cases involving dropped fuel in CAGRs a significant proportion of the activity will be associated with small aerosol  $U_3O_8$  particles. The main mechanisms by which aerosol particulates deposit and impact on wall surfaces include gradient/diffusion or free-flight to the wall, inertial deposition, interception, and turbulent eddy-diffusion, Brownian diffusion and thermophoresis, gravitational setting, etc. The mechanisms that are responsible for the deposition of heavy particles in fully developed turbulent boundary layers are gradient/diffusion and free flight to the wall ([Friedlander and Johnstone \(1957\)](#)) and by turbophoresis ([Reeks \(1983\)](#)) with turbulent eddy-diffusion ([Kallio and Reeks \(1989\)](#)). However, under the conditions of high volume flow rate low pressure drop filtration, inertial impact becomes the dominant mechanism governing

deposition among all the competing ones that contribute to the deposition of aerosol particulates on cylindrical surfaces (see [Helgesen and Matteson \(1991, 1994\)](#)).

There has been extensive research regarding the inertial deposition of heavy particles or droplets from flowing gas streams by impact on a single cylinder surfaces through theory and experiments. For example, [Brun et al. \(1955\)](#) reported three impingement characteristics of water droplets on a cylinder surface, which are total rate of water droplet impingement, extent of droplet impingement zone and local distribution of impinging water on the cylinder surface. The results for the collection efficiency of a cylinder in [Brun et al. \(1955\)](#) were presented as a function of a combination of the Stokes and Reynolds number of the droplets considered. This treatment was extended to use a generalized Stokes number to determine the collection efficiency of a cylinder for non-Stokesian particles by [Israel and Rosner \(1982\)](#). This generalized Stokes number is normally referred to as the effective Stokes number and defined as

$$St_{\text{eff}} = \psi(Re_p)St, \quad (7.1)$$

where  $\psi(Re_p)$  is the non-Stokes drag correction factor and given by

$$\psi(Re_p) = \frac{24}{Re_p} \int_0^{Re_p} \frac{1}{C_D(Re') Re'} dRe', \quad (7.2)$$

and

$$St = \frac{\rho_p d_p^2 U_o}{18\mu D}. \quad (7.3)$$

More recently, the collection efficiency was examined through directly solving the incompressible Navier-Stokes equations coupled with the Lagrangian point particle tracking approach in a relatively low Reynolds number cross flow across a cylinder by [Haugen et al. \(2010\)](#).

There have been a number of numerical studies on the deposition and impact of heavy particles on tube-banks surfaces, and they focused on the two-dimensional simulations. [Jun and Tabakoff \(1994\)](#) carried out a two-dimensional numerical simulation for a dilute particle laden laminar flow over in-line tube-banks in order to study particle impact and erosion of cylinders. Rebound phenomena of particles from cylinder surfaces were taken

into account as well in the above work. [Bouris et al. \(2001\)](#) performed a two-dimensional large eddy simulation to evaluate different tube configurations for particle deposition rate reduction on heat exchanger tube bundles, in which an energy balance model was implemented to account for the adhesion or rebound of particles upon hitting a tube. [Tian et al. \(2007\)](#) made use of the two-dimensional RANS (Reynolds-averaged Navier-Stokes) modelling framework and embedded particle tracking model in ANSYS FLUENT to study the characteristics of particle-wall collisions. An algebraic particle-wall collision and stochastic wall roughness model was also implemented by these authors.

Engineering predictions of the deposition of heavy particles on bluff bodies depends primarily on the accurate prediction of the mean flow and the turbulence based on RANS. The methodology of three-dimensional RANS modelling frameworks coupled with a separate boundary layer model, which supplies fluctuating fluid velocity fluctuations seen by heavy particles, has been extended to study the prediction of deposition rates of heavy particles (e.g. [Dehbi \(2008\)](#)) in complex geometries. [Dehbi and Martin \(2011\)](#) further employed this method to study particulate flows around linear arrays of spheres and got good predictions of deposition rates when compared with experimental measurements. However, for a turbulent flow across bluff bodies, e.g. spheres or cylinders, the dominant feature of such a flow is that it has strongly unsteady, three-dimensional vortex shedding [Williamson \(1996\)](#). This requires solving the Navier-Stokes equations with the time-dependent term, i.e. unsteady RANS (URANS) or LES, in order to resolve the unsteady phenomena of vortex shedding as accurately as possible. In this study, first a URANS simulation was carried out for a turbulent flow across in-line tube-banks. The approach presented in [Dehbi \(2008\)](#) was used to determine the  $y^+$  value of each cell associated with its correspondingly nearest wall-adjacent cell face. However, as shown in figure 7.1 for the contour of constant  $y^+$  for each cell associated with its correspondingly nearest wall-adjacent cell face, the boundary layer around every cylinder based on a threshold  $y^+$  value 100 doesn't have a regular shape. This irregular boundary layer shape as a result of the unsteadiness of vortex shedding makes the application of RANS using wall-functions for near wall behaviour, problematic.

LES has been convincingly demonstrated to be superior to unsteady RANS (URANS) in accurately predicting the flow and vortex dynamics of a turbulent cross-flow in a

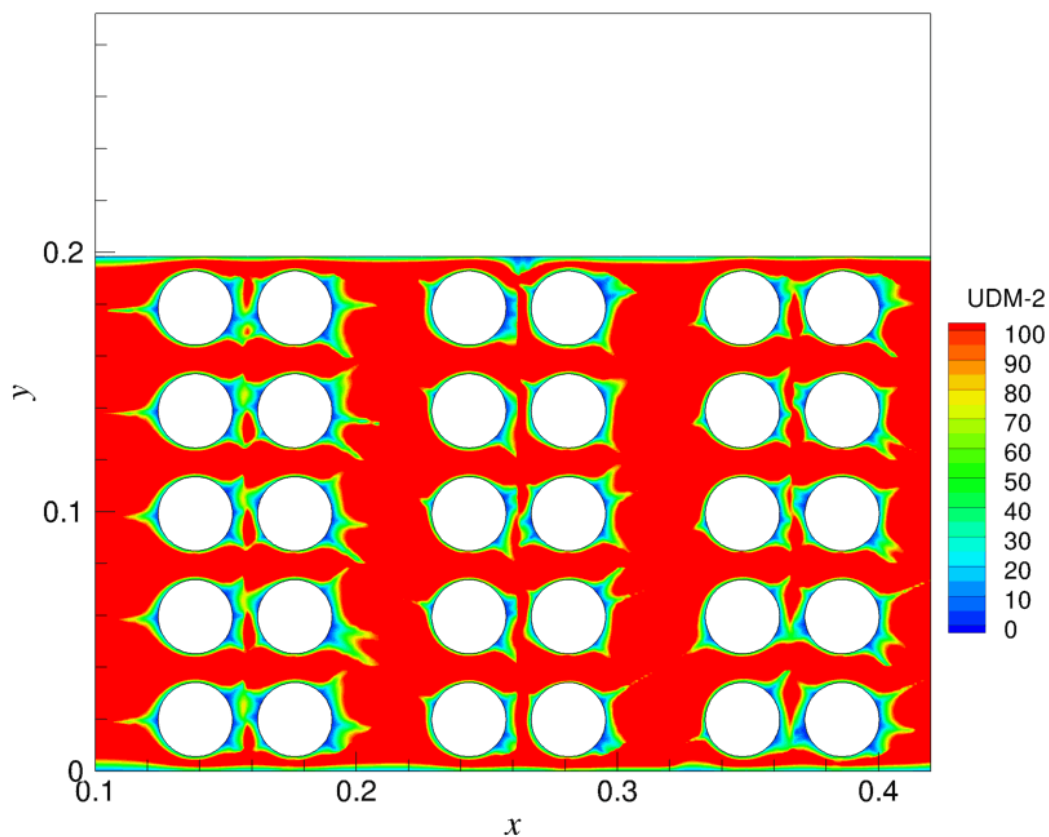


Figure 7.1: Contour of the  $y^+$  value of each cell associated with its correspondingly nearest wall-adjacent cell face in a turbulent flow across in-line tube-banks. UDM-2 stands for  $y^+$ .

staggered tube bundle (see [Benhamadouche and Laurence \(2003\)](#)). This is because LES is capable of providing details of the large scales structures and in particular resolving a significant part of the vortex shedding physics and hence reducing the reliance on modelling. The success of LES for single-phase turbulent flows across complex geometries has been extended to two-phase flows over complex geometries. [Apte et al. \(2003\)](#) performed an LES study of particle-laden swirling flow in a coaxial-jet combustor. They demonstrated that results obtained from LES are significantly more accurate than the results by RANS applied to the same problem. [Riber et al. \(2009\)](#) conducted a comparison study of numerical strategies for LES of particulate two-phase recirculating flows and observed that the dispersed phase is predicted more accurately by the Lagrangian point particle approach than the Eulerian approach. Therefore, the Lagrangian point particle approach coupled with the LES technique is employed in this

study.

The principal objective of this work is to investigate inertial deposition and impaction of heavy particles on in-line array tube-banks in a turbulent cross flow. The numerical technique used for the underlying flow field is large eddy simulation, whilst the Lagrangian point particle tracking approach is employed to obtain particles trajectories.

## 7.2 Overview of numerical simulations

### 7.2.1 Mathematical formulation of LES

The mathematical formulation of LES for the continuous phase has already been described in the previous chapter, section 6.2.

### 7.2.2 Flow configuration of in-line tube banks

Figure 7.2 shows the flow configuration with the corresponding coordinate system, which is based on the experiments involving particle deposition on heat exchanger tube-banks from Hall (1994). Flow is from left to right and normal to the cylinder axis. The computational domain is of size  $L_x \times L_y \times L_z = 36.16D \times 6.94D \times 2D$ , where  $D$  is the cylinder diameter. The configuration of this tube-banks is different from the tube-bank considered in Chapter 6. It consists of four by five pairs of in-line tube banks. Every pair has the transverse pitch that is of the ratio of pitch-to-diameter  $S_T(P_T/D) = 1.388$  and the longitudinal pitch that is of the ratio of pitch-to-diameter  $S_{L0}(P_L/D) = 1.331$ , respectively. The longitudinal pitch between the two adjacent cylinders from two adjacent tube-banks is of the ratio of pitch-to-diameter  $S_{L1}(P_L/D) = 2.331$ . The Reynolds number  $Re_o$  based on the free stream velocity  $U_o$  and the cylinder diameter  $D$  equals to 9500, and a Reynolds number  $Re_g$  based on the gap velocity  $U_g$  in the  $x$ - direction between two cylinders of 33960.

Figure 7.3 shows a side view of the computational grid with a close-up around a cylinder. The total number of grid elements used for the present simulation is around 3.4 million.

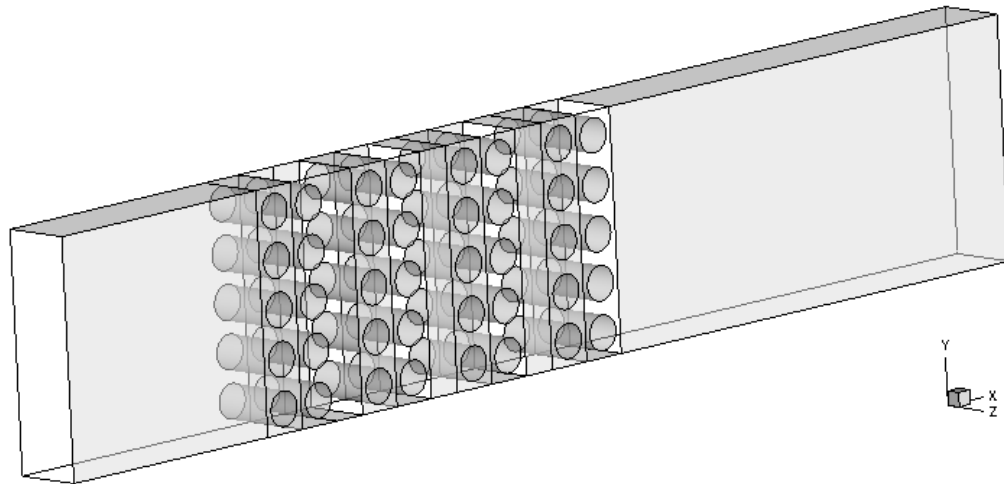


Figure 7.2: Configuration of four by five pairs of in-line tube banks.

The mesh has an embedded region of fine mesh designed for each cylinder in order to enhance the mesh resolution near the cylinder without incurring too large an increase in the total number of mesh elements. The first cell adjacent to the cylinder is within the range  $\Delta y^+ < 11.8$  in wall units<sup>1</sup>, which satisfies the requirements of the Wener-Wengle wall-layer model used for wall-modelling LES. Prior to the present simulation, with the standard Smagorinsky subgrid scale model, a simulation based coarse grid resolution was carried out to determine the resolution.

With fully developed turbulent flows, the use of periodic boundary conditions is justified to use along the normal ( $y$ ) and spanwise ( $z$ ) direction. For the inlet boundary condition, a simple uniform velocity profile is assumed and the turbulent intensity set to zero. Hence, the turbulence fluctuations at the inlet was not accounted for temporally and spatially. Nevertheless, a length of  $7.5D$  before the first column bank is used to allow the development of turbulence. At the exit boundary, the solution variables from the adjacent interior cells are extrapolated to satisfy the mass conservation.

The simulation is advanced with non-dimensional time step  $\Delta t U_o / D \approx 1.4 \times 10^{-3}$  that yields a maximum Courant-Friedrichs-Lewy (CFL) number 0.7. For the carrier phase, the first-order statistics are collected by integrating the governing equations over a time

<sup>1</sup>The superscript + denotes a non-dimensional quantity scaled using the wall variables, e.g.  $y^+ = yu_\tau/\nu$ , where  $\nu$  is the kinematic viscosity and  $u_\tau = \sqrt{\tau_w/\rho}$  is the wall friction velocity based on the wall shear stress  $\tau_w$ , and which is a velocity scale representative of velocities close to a solid boundary.

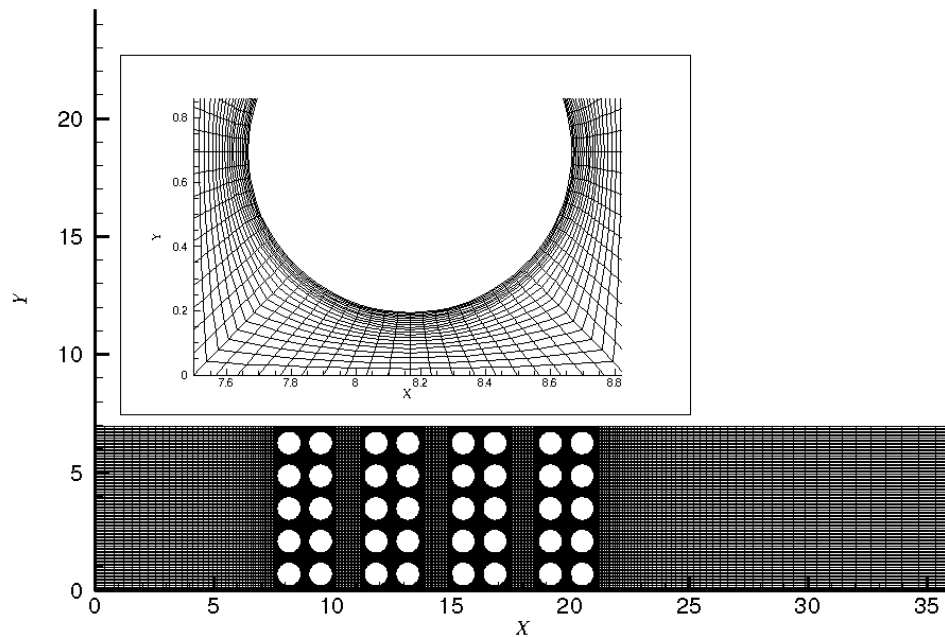


Figure 7.3: A side view of computational mesh used for the LES with a close look-up around a cylinder.

interval of  $25D/U_o$ , and all the statistics are averaged over the 40 sampling points across in the spanwise direction.

### 7.2.3 Calculation of particle trajectories

A parallel Lagrangian particle tracking module was developed and fully coupled with ANSYS FLUENT to calculate trajectories of heavy particles in flow fields (see Chapter 3). The particle localization algorithm on unstructured grids proposed by [Haselbacher et al. \(2007\)](#) was used to locate the cell which contains the current particle position. In this study, the focus is on the impaction and deposition of non-inter-collision, rigid, spherical and heavy particles on in-line tube-banks ; the concentration of particles is dilute enough to assume one-way coupling. The momentum balance equation of particles discussed by [Maxey and Riley \(1983\)](#) is simplified in this work by taking into account only the drag force. We thus can write the particle equation of motion involving the non-linear form of

the drag law with the point particle approximation

$$\frac{d\mathbf{u}_p}{dt} = \frac{1}{\tau_p} C_D \frac{Re_p}{24} (\mathbf{u} - \mathbf{u}_p), \quad (7.4)$$

where  $\mathbf{u}_p$  is the particle velocity and  $\mathbf{u}$  the instantaneous fluid velocity at the particle location,  $\tau_p$  is the particle response time. An empirical relation for  $C_D$  from [Morsi and Alexander \(1972\)](#), which is applicable to a wide range of particle Reynolds number with sufficiently high accuracy, is employed, namely

$$C_D = c_1 + \frac{c_2}{Re_p} + \frac{c_3}{Re_p^2}, \quad (7.5)$$

where  $c_1, c_2, c_3$  are constants and provided by [Morsi and Alexander \(1972\)](#). The above empirical expression exhibits the correct asymptotic behavior at low as well as high values of  $Re_p$ .

The position  $\mathbf{x}_p$  of particles is obtained from the kinematic relationship

$$\frac{d\mathbf{x}_p}{dt} = \mathbf{u}_p \quad (7.6)$$

The boundary condition for the above equation is that the particle is captured by the wall when its center away the nearest wall surface is less than its radius. This is not properly treated in the default discrete phase model (DPM) provided by ANSYS FLUENT. Furthermore, this error has a significant effect upon predictions concerning the deposition of heavy particles under investigation.

From a statistically stationary LES flow field, equation: (7.6) is integrated in time using the second-order Adams-Bashforth scheme to get particle trajectories, whilst equation: (7.4) is integrated with the second-order accurate Gear2 (backward differentiation formulae) scheme that is applicable to stiff systems. Fluid velocities are stored at the cell centroid. Since it is only by chance that a particle coincides with the cell centroid, a quadratic scheme based on fluid velocity gradient is used to interpolate the fluid velocity to the particle location.

Results on for three sets of particles ( $St = 0.35, 0.086, 0.0075$ ) are obtained by following the trajectories of  $10^7$  particles which are continuously released into the computational domain. Using this large number of particles trajectories is crucial in order to obtain statistically significant results on the particle phase, especially in the unsteady vortex shedding region. However, the particle accumulation on the tube-banks has not been taken into account, otherwise it is necessary to consider particle-particle interaction upon impacting on the cylinder.

#### 7.2.4 A particle-wall collision model

Particle-wall collisions play an important role in particle-laden two-phase flows because they affect the deposition and accumulation on wall surfaces. In this work, the aim is not to seek a new particle-wall-collision model; instead a well-known dry particle-wall-collision model from [Thornton and Ning \(1998\)](#) was implemented to account for the energy loss resulting from the particle-wall-collision. The energy loss resulting from impact upon a wall is normally characterized by the coefficient of restitution (CoR)  $e$  that is defined by

$$e = \frac{v_r^n}{v_i^n} \quad (7.7)$$

where  $v_r^n$  is the rebound normal velocity and  $v_i^n$  the incident normal velocity. Then, the loss of kinetic energy  $\Delta Q$  of a particle with mass  $m_p$  is given by

$$\Delta Q = \frac{1}{2} m_p (v_i^{n2} - v_r^{n2}) = \frac{1}{2} m_p v_i^{n2} (1 - e^2). \quad (7.8)$$

In the case of elastic impact,  $e = 1$  means no energy loss has occurred. When  $e = 0$ , the maximum incident normal velocity is normally referred to as the critical sticking (impact) velocity  $v_s$ . Then from

$$\Delta Q = \frac{1}{2} m_p v_s^2, \quad (7.9)$$

$e$  is given by

$$e = \left[ 1 - \left( \frac{v_s}{v_i^n} \right)^2 \right]^{\frac{1}{2}}. \quad (7.10)$$

If  $v_i^n$  is higher than  $v_s$  then  $e > 0$  and the particle can bounce off the wall upon impact; if not, the particle sticks the wall and  $e = 0$ . For adhesive and elastic particles, the energy loss may be calculated according to

$$\Delta Q = \left( \frac{14.18}{m^*} \right)^{\frac{1}{2}} \left( \frac{\Gamma^5 R^*}{E^{*2}} \right)^{\frac{1}{6}}, \quad (7.11)$$

where  $R^* = 0.5 d_p$ ,  $m^* = \frac{1}{6} \pi \rho_p d_p^3$ ,  $\Gamma$  is the inter-facial surface energy, and

$$\frac{1}{E^*} = \frac{1 - \nu_1^2}{E_1} + \frac{1 - \nu_2^2}{E_2}, \quad (7.12)$$

where  $E_1$  and  $E_2$  are Young modulus of the particle and cylinder, and  $\nu_1$  and  $\nu_2$  Poisson coefficients. The critical sticking velocity  $v_s$  then can be determined by the properties of the particle and cylinder wall surface. In this study, the material properties used for the particles and cylinder are based on alumina particles impacting on steel substrate. Figure 7.4 shows the variation of critical sticking velocity on steel cylinder for a wide range of alumina particle radii. It can be observed that the smaller the particle radius, the larger the critical sticking velocity, i.e. it is easier for larger particles to get bounce upon impact. Figure 7.5 illustrates how the coefficient of restitution varies with the particle incident normal velocity. When the particle incident normal velocity is approaching 0.2 m/s the coefficient of restitution is close to 0.985.

In this study, the critical sticking velocities for three sets of particles considered are calculated and input as parameters before starting particle tracking. Therefore, this model can be used to determine whether a particle sticks to or rebound from a wall upon impact with the wall.

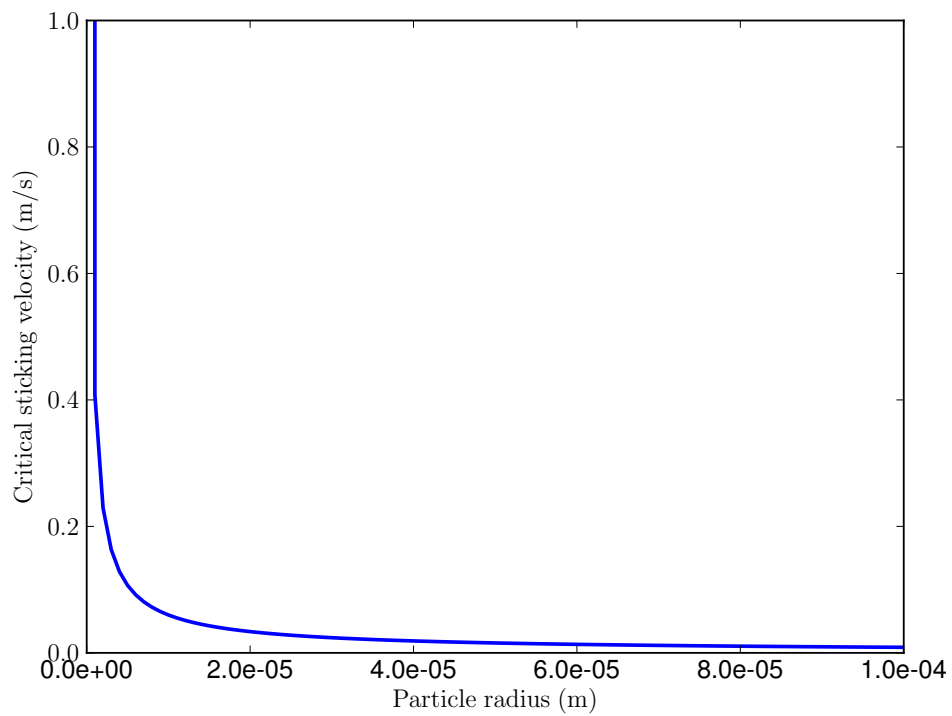


Figure 7.4: Critical sticking velocity on a steel cylinder as a function of alumina particle radius.

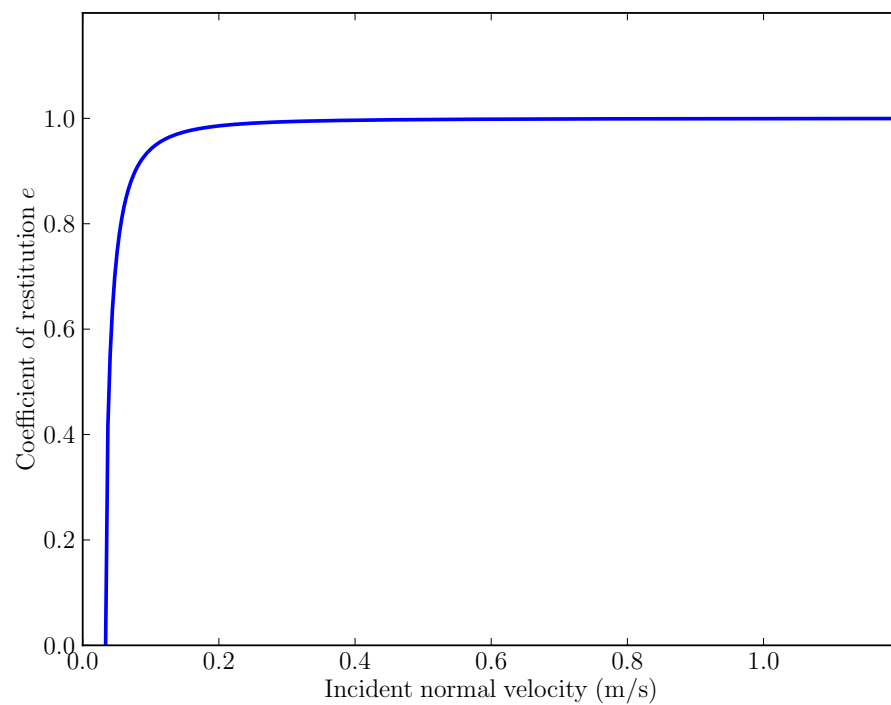


Figure 7.5: Coefficient of restitution  $e$  as a function of alumina particle incident normal velocity upon a steel cylinder.

## 7.3 Results and discussion

### 7.3.1 Results on the carrier phase

Vortex structures in the flow field around the in-line tube-banks are revealed in figure 7.6 by plotting iso-surfaces of normalised  $Q$  – criterion =  $8 \times 10^{-2}$  (see Hunt et al. (1988)). As can be seen, the top cylinder in the first column develops a laminar boundary layer and has some kind of laminar vortex shedding. However, this is not observed from the downstream cylinders. Large coherent structures are visible in the gaps between tube-banks, but they are not as well organized and periodic as in typical Karman vortex streets for a single cylinder at the similar Reynolds number. Large coherent structures between two adjacent column cylinders in the same pair are not as obvious as those in the gaps. This may result from the relatively small axial gap between the cylinders in every pair, destroying the development of the wake. Finally, the flow is evolving into a turbulent flow like a grid turbulence from the final pair of tube-banks.

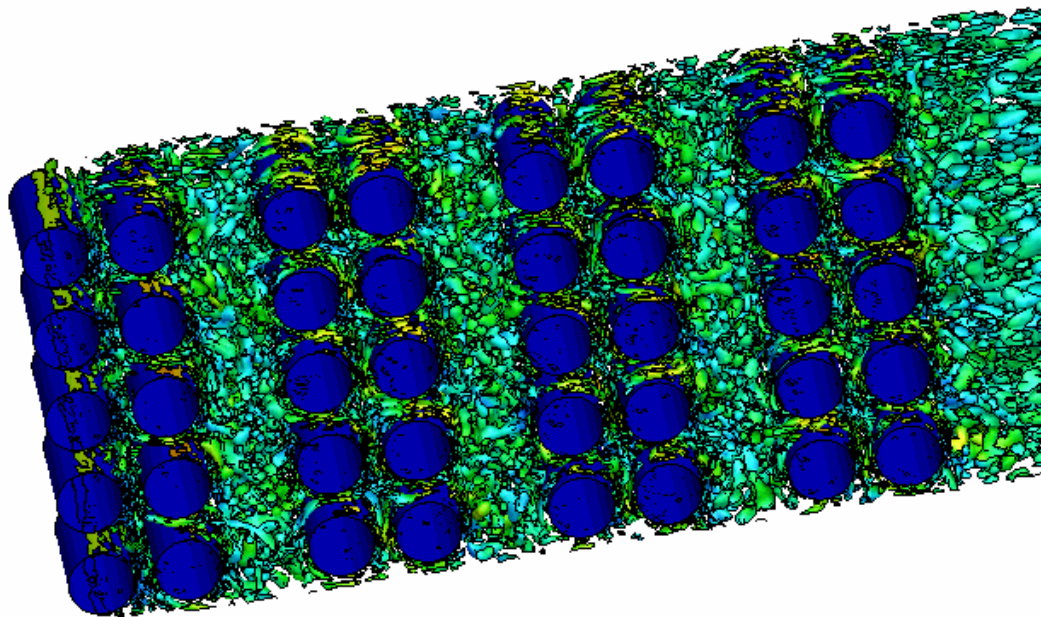
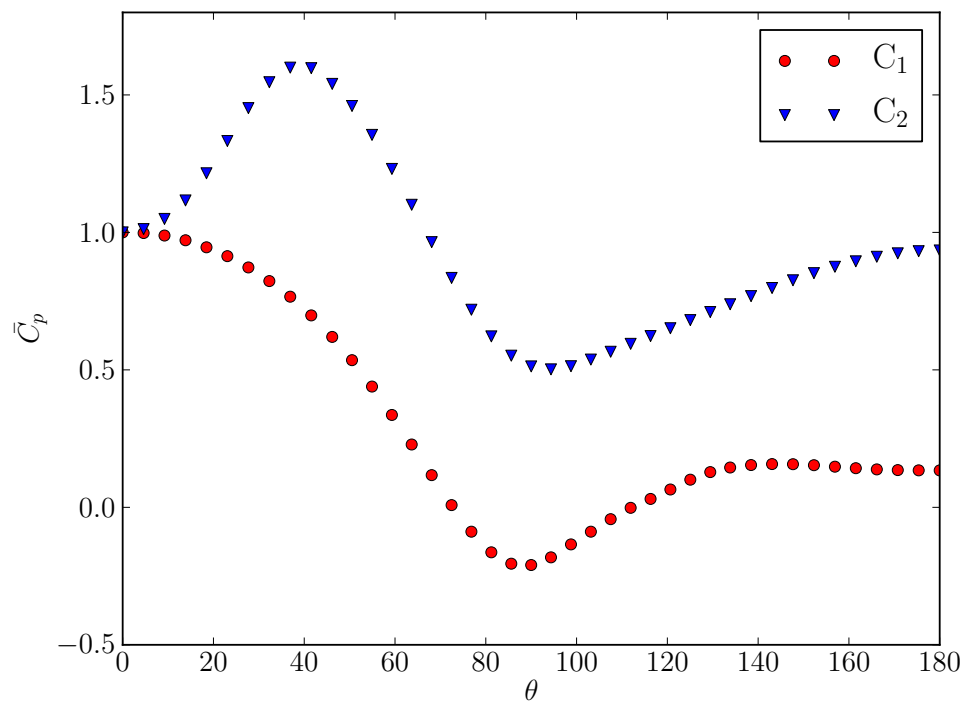
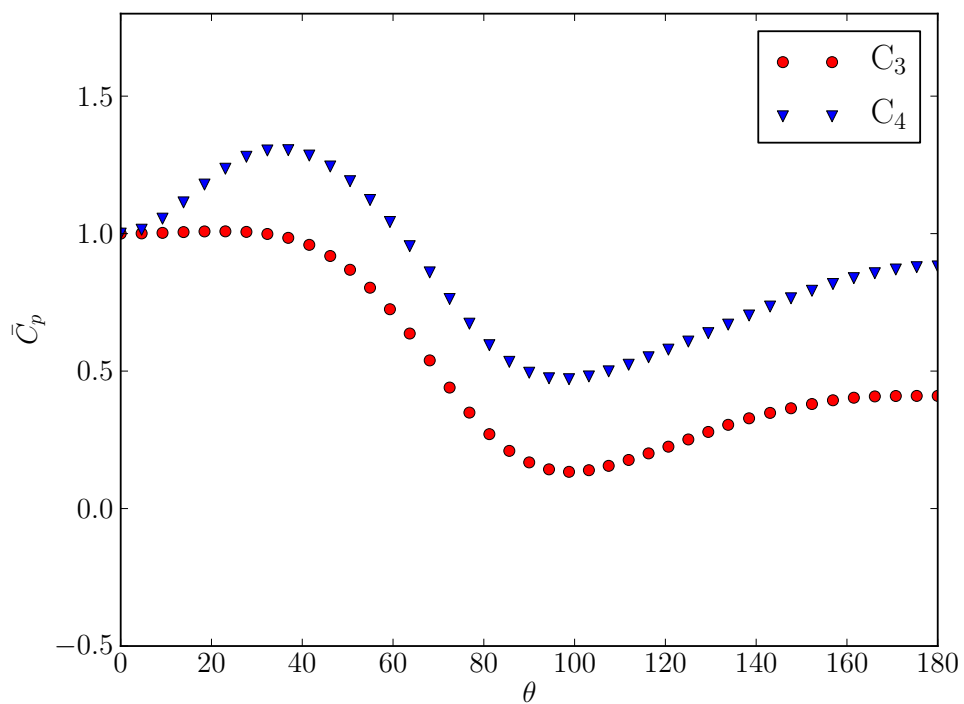


Figure 7.6: Instantaneous velocity magnitude based on the normalised  $Q$  – criterion =  $8 \times 10^{-2}$ .

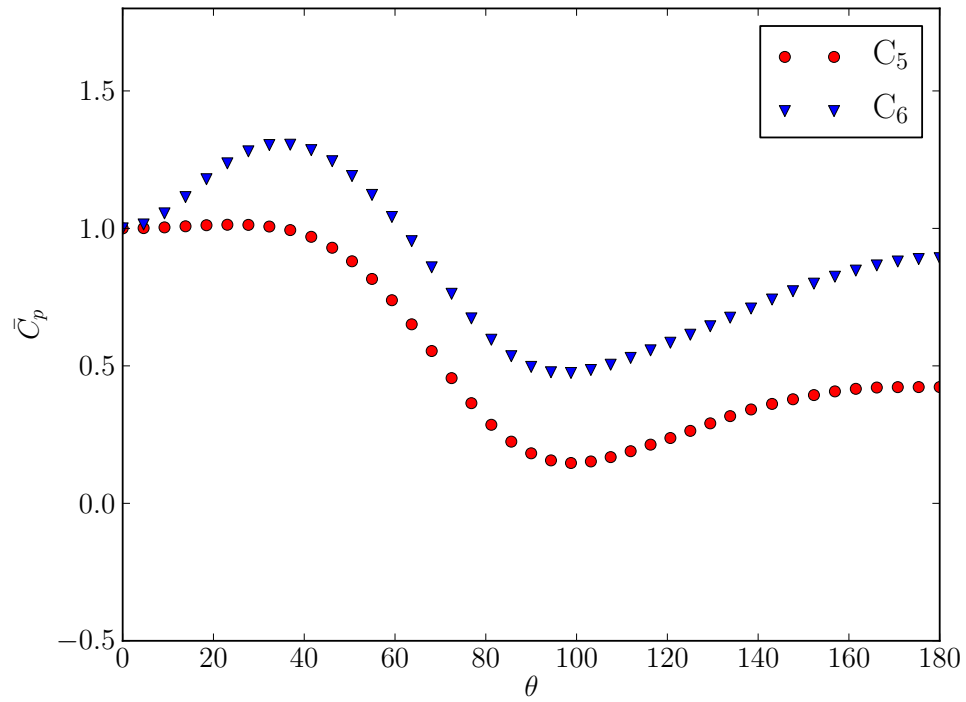


(a)

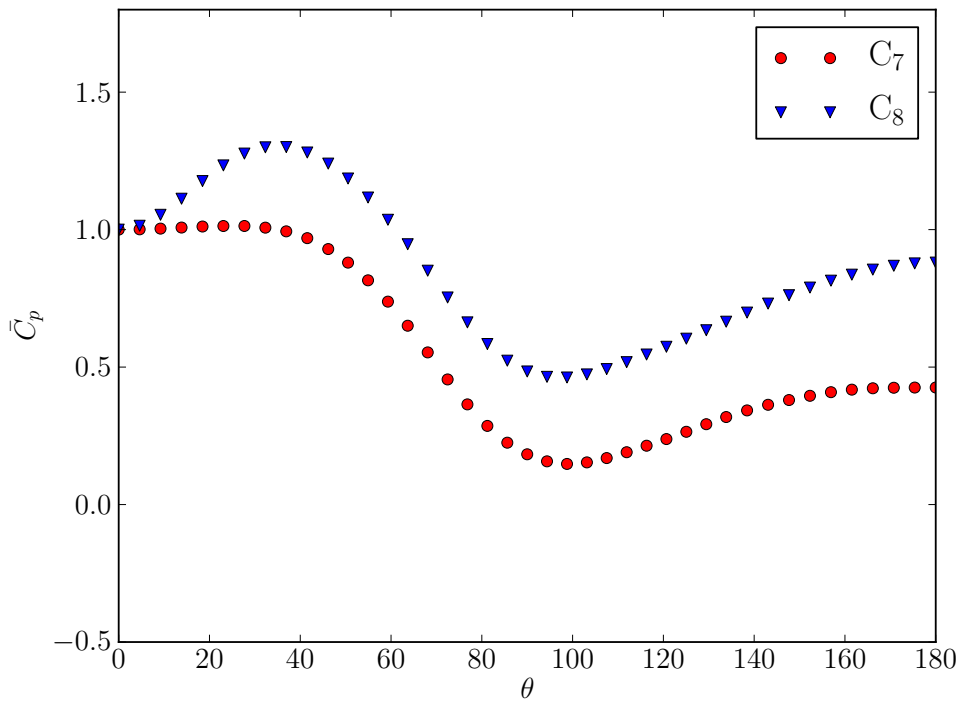


(b)

Figure 7.7: Mean pressure distribution on the middle cylinder surface. Definition of  $\bar{C}_p$  based on Shim et al. (1988). (a) the first pair tube banks, (b) the second pair tube banks.



(a)



(b)

Figure 7.8: Mean pressure distribution on the middle cylinder surface. Definition of  $\bar{C}_p$  based on Shim et al. (1988). (a) the third pair tube banks, (b) the fourth pair tube banks.

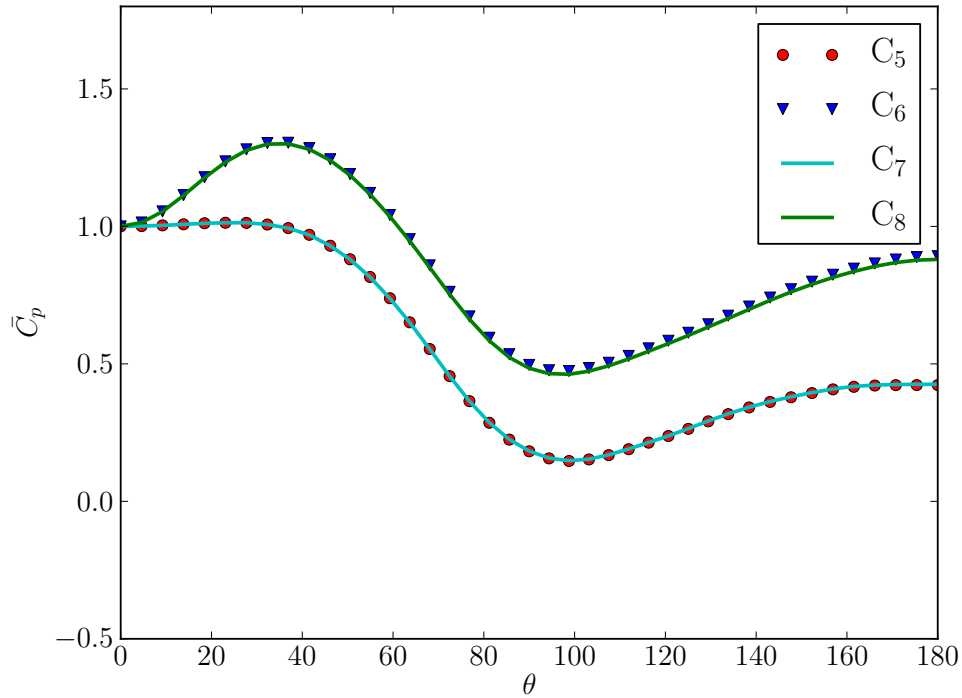


Figure 7.9: Comparison of mean pressure distribution on the middle cylinder surface from the second, third and fourth pair of tube-banks

Following [Shim et al. \(1988\)](#), the coefficient for the mean pressure distribution on the cylinder surface is define as

$$\bar{C}_p = \frac{\langle p \rangle_T - p_{ref}}{q_{ref}}, \quad (7.13)$$

where  $\langle p \rangle_T$  denotes an ensemble average across the spanwise direction for all the sampling points on the cylinder surface over the sampling time interval  $T$ , and

$$q_{ref} = \frac{1}{2} \rho U_g^2. \quad (7.14)$$

In order to make  $\bar{C}_p$  equal to unity at the front stagnation point for every cylinder, the corresponding static pressure  $p_{ref}$  is calculated according to equation 7.13;  $\bar{C}_p$  is hence determined around the cylinder surface.

Comparisons of  $\bar{C}_p$  on the middle cylinders surface from the first and second pair of tube-banks are shown in figure 7.7. It can be observed that  $\bar{C}_p$  has the standard shape associated with that on a single circular cylinder on  $C_1$ . However,  $\bar{C}_p$  on the second

cylinder  $C_2$  is of an **S** shape, indicating there is a region in the front side of the cylinder that has a higher pressure than the front stagnation point. This effect is due to the reduced total pressure in the small gap between the cylinders in the pair. The phenomena was also observed in the experimental measurements for tube-banks with a close longitudinal pitch from Shim et al. (1988). From 7.7b, It can be observed that  $\bar{C}_p$  on  $C_3$  is also of the standard shape for a single cylinder, but it has a relatively high base pressure.  $\bar{C}_p$  on the following cylinder  $C_4$  has the similar shape like to the one on  $C_2$ , implying that the shedding vortex from  $C_3$  impacts on the front side of  $C_4$ .

Figure 7.8 shows  $\bar{C}_p$  on the middle cylinders from the third and fourth pair of tube-banks. As can be seen, the shapes of  $\bar{C}_p$  on the front and back cylinder within these two pairs are consistent with the shapes of  $\bar{C}_p$  on the cylinders within the first and second pair tube-banks. For instance,  $\bar{C}_p$  on the front cylinder is of the standard shape of  $\bar{C}_p$  on a single cylinder;  $\bar{C}_p$  on the back cylinder develops an **S** shape from the front stagnation point to the back point due to the vortex impingement on the front side from the upstream cylinder.

Figure 7.9 shows a comparison of  $\bar{C}_p$  from cylinders within the third and fourth pair of tube-banks. Interestingly, there is no discernible discrepancy between the same cylinder from these two pairs. This indicates that the turbulent flow within the tube-bank has reached approximately equilibrium and become stream-wise periodic by the third and fourth column pairs.

## 7.3.2 Results for the particle phase

### 7.3.2.1 Sample particle trajectories and bounce upon impact

Figure 7.10 shows some sample trajectories of alumina particles with diameter  $2 \times 10^{-5}$  ( $St = 0.345$ ) across the tube-banks. With the present particle-wall collision model, it can be clearly observed that some particles rebound upon impact on the cylinders. This normally results in a smaller rebound velocity as a result of energy loss.

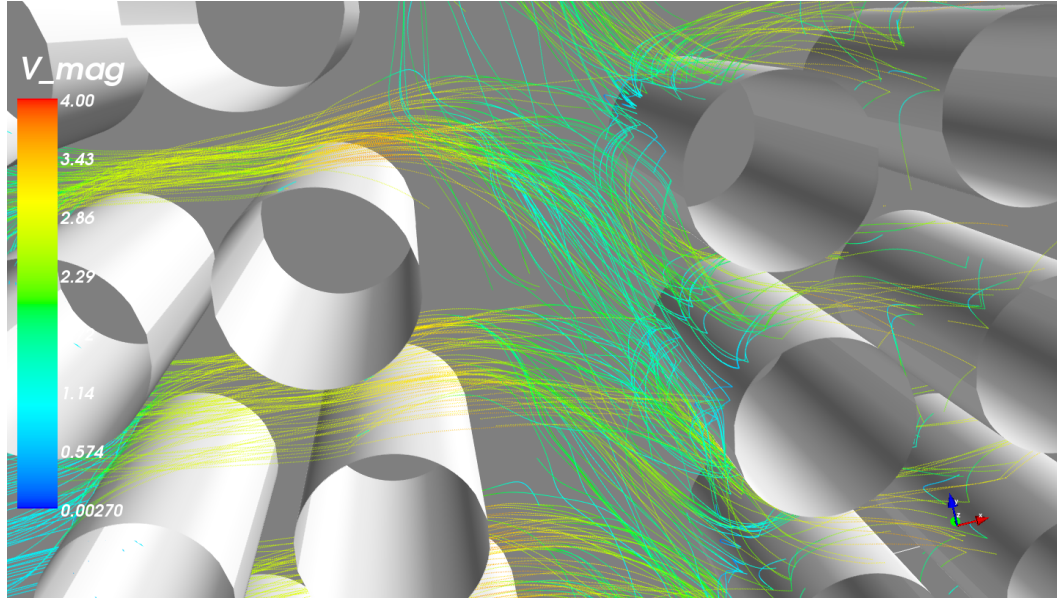


Figure 7.10: Sample particle trajectories and bounce upon impact on cylinders for particles  $St = 0.35$

### 7.3.2.2 Deposition efficiency on tube-banks

The deposition efficiency for a single cylinder (known as collection efficiency) is normally defined as

$$\eta_{sc} = \frac{N_{dep}}{N_{tot}}, \quad (7.15)$$

where  $N_{dep}$  is the number of deposition particles on the cylinder, and  $N_{tot}$  is the number of uniformly distributed particles in the upstream cross-sectional area of the cylinders.

Table 7.1 shows the deposition efficiency of particles of Stokes number  $St = 0.35$  onto the individual cylinders from the first column. C1a denotes the top cylinder and C1e the bottom cylinder shown in figure 7.2 within the first column. The present particle of Stokes number  $St = 0.35$  corresponds to an effective Stokes number  $St_{eff} = 0.21$  based on equation 7.2, which is in the valid range of particle Stokes number considered by Israel and Rosner (1982). Hence, the computed results are compared with the deposition efficiency of particles of an effective Stokes number 0.21 onto an isolated single cylinder from Israel and Rosner (1982). As can be seen, within the first column cylinders the deposition efficiencies of particles onto individual cylinders are significant lower than onto an isolated single cylinder. This may result from the fact that particles bounce upon impaction is taken into account in this study, which reduces the deposition efficiency.

Case	$\eta$ (individuals)	
Present LES ( $St_{\text{eff}} = 0.21$ )	C1a	0.00865058
	C1b	0.00728681
	C1c	0.00678809
	C1d	0.00656457
	C1e	0.00729435
Experiments (Israel and Rosner, 1982)	0.06869	

Table 7.1: Comparison of deposition efficiency of particles of  $St = 0.35$  onto the individual cylinders from the first column tube-banks with the deposition efficiency on a single cylinder

Moreover, the reduction of deposition efficiency might also due to a “laned” stream-wise velocity profile is developed in the longitudinal gap between two cylinders as a result of the stream-wise in-line alignment of the cylinders, which accelerates the particles to higher velocities when they are approaching the cylinders. The combined effects from both bounce and acceleration reduces the deposition efficiency of particles significantly.

However, when it comes to particles depositing on in-line tube-banks, overall deposition efficiencies for each tube-bank pair has to be defined differently. The deposition efficiency for the first pair is determined by taking the number of particles in the upstream cross-sectional area of the first column cylinders, and comparing that number to the number of particles actually deposited on the first tube-bank pair. This reads

$$\eta_{\text{pair1}} = \frac{N_{\text{pair1}}}{\frac{5D}{6.94D} N_{\text{tot}}}, \quad (7.16)$$

where  $N_{\text{pair1}}$  is the number of deposition particles on the first tube-bank pair,  $N_{\text{tot}}$  is the total number released from the upstream,  $5D/6.94D$  is ratio of the cross-sectional area of the first column cylinders to the cross-sectional area of the computational domain. However, since it is difficult to define how many particles are in the upstream cross-sectional area of the succeeding tube-banks, the number is assumed to be simply the number in the particle release plane cross-sectional area  $5N_{\text{tot}}/6.94$  minus the number of particles deposited on the preceding tube-banks. For example, the deposition efficiency

Case		$\eta$ (pair of tube-banks)
LES ( $St = 0.35$ )	Pair1	7.317e-03
	Pair2	6.012e-03
	Pair3	1.502e-03
	Pair4	2.824e-04
LES ( $St = 0.086$ )	Pair1	2.882e-02
	Pair2	3.764e-02
	Pair3	8.537e-03
	Pair4	6.362e-04
LES ( $St = 0.0075$ )	Pair1	1.187e-02
	Pair2	7.502e-03
	Pair3	7.137e-04
	Pair4	4.409e-05

Table 7.2: Comparison of deposition efficiency of particles of  $St = 0.35, 0.086$  and  $0.0075$  onto each pair of the tube-banks

of the fourth tube-bank pair can be written as

$$\eta_{pair_4} = \frac{N_{pair_4}}{\left( \frac{5D}{6.94D} N_{tot} - \sum_{i=1}^3 N_{pair_i} \right)}. \quad (7.17)$$

The computed results for deposition efficiency of the three sets of particles ( $St = 0.35, 0.086$  and  $0.0075$ ) considered across the tube-banks are shown in Table 7.2.

Comparing the particle of Stokes number  $St = 0.35$ , it can be observed from Table 7.2 that there is a considerable increase of the deposition efficiency for particles of Stokes number  $St = 0.086$  and  $0.0075$ , which is not consistent with theoretical results for a single cylinder. A possible explanation is that a large amount of particles are entrained into the wake of the back-columns of each pair of tube-banks and get deposited by impaction on the downstream face (see Haugen et al. (2010)). In addition, for all the three sets of particles, the deposition efficiency onto the downstream pairs of tube-banks is considerably lower than onto the first pair of tube-banks.

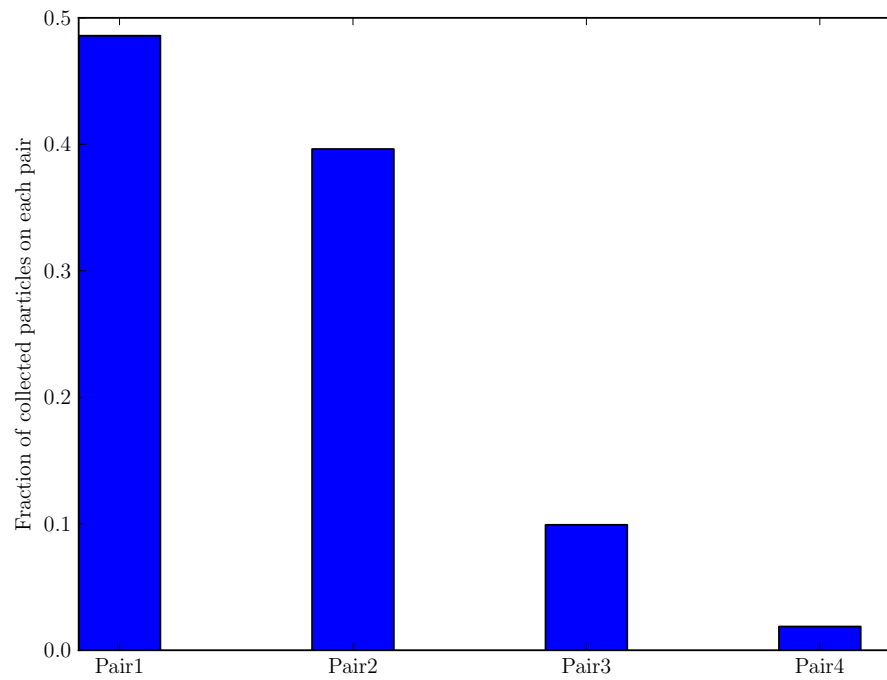
### 7.3.2.3 Deposition fraction across the tube-banks

Deposition data for three sets of particles ( $St = 0.35, 0.086, 0.0075$ ) on tube-banks are presented here. The pairs of tube-banks shown in figure 7.2 are designated by pair1

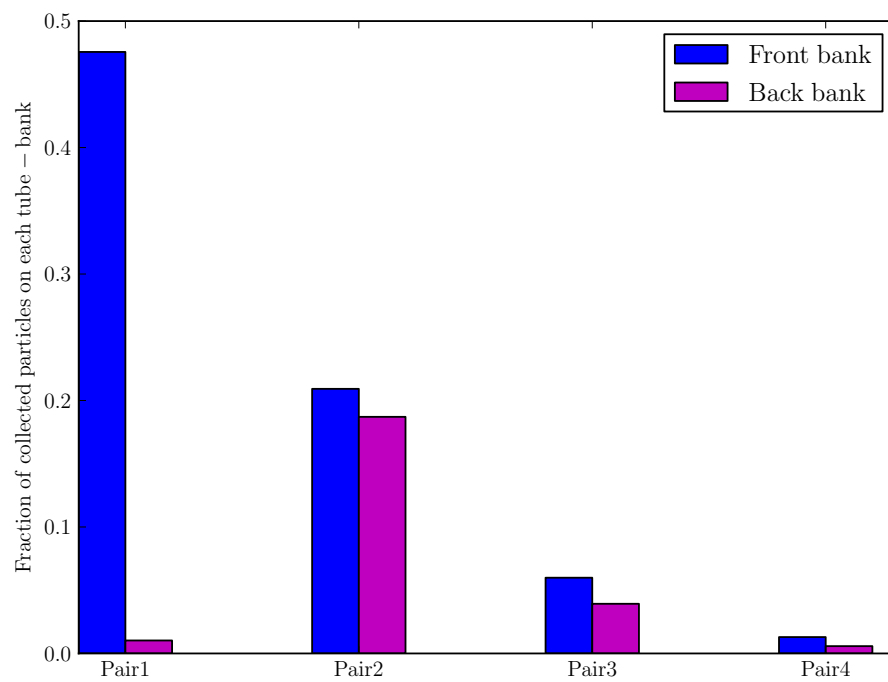
(upstream) through pair4 (downstream); the upstream and downstream column of tube-banks in each pair are designated by front bank and back bank.  $10^7$  particles are released into the computational domain continuously for an interval of 1000 continuous time steps, in order to collect enough particles and account for the unsteady flows.

Figure 7.11, 7.12 and 7.13 show variation in the deposition fraction (as a fraction of the total number of particles) across the whole set of tube-banks, for the three sets particles. As can be seen from figure 7.11, for the particles with Stokes number  $St = 0.35$ , across the four pairs of the tube-banks the fraction of deposition particles on the pair1 is significantly higher than on the downstream pair of tube-banks, pair2, pair3 and pair4. In addition, the fraction of deposition on the front cylinders in the same pair of tube-banks is higher than on the back cylinders, especially for the pair1. This may result from the fact that a significant part of this set of particles is entrained in the bulk flow between cylinders and not within the vortices shed vortex from the preceding cylinders (see figure 7.10). However, the computed results for particles  $St = 0.086, 0.0075$  are not consistent with those results for  $St = 0.35$ . Although the fraction of deposition on the pair3 and pair4 are lower than the preceding two pairs, a striking difference is noted when compared to the particles with  $St = 0.35$ .

It can be observed from figure 7.14a that the downstream surface deposition on the back cylinders of pair1 and pair2, for particles  $St = 0.0075$  results in a considerably higher fraction of deposition. For the downstream surface deposition, Haugen et al. (2010) argued that when particle with response time  $\tau_p$  is close to the eddy time  $\tau_{eddy}$ , they normally follow the eddies in the wake of the tube-banks and gain enough momentum to impact on the cylinders.

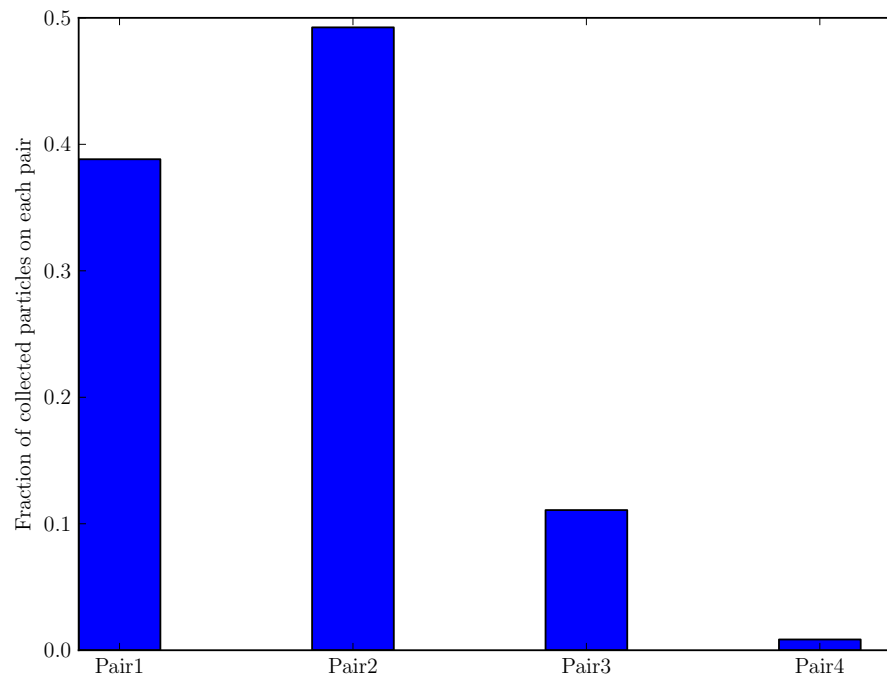


(a)

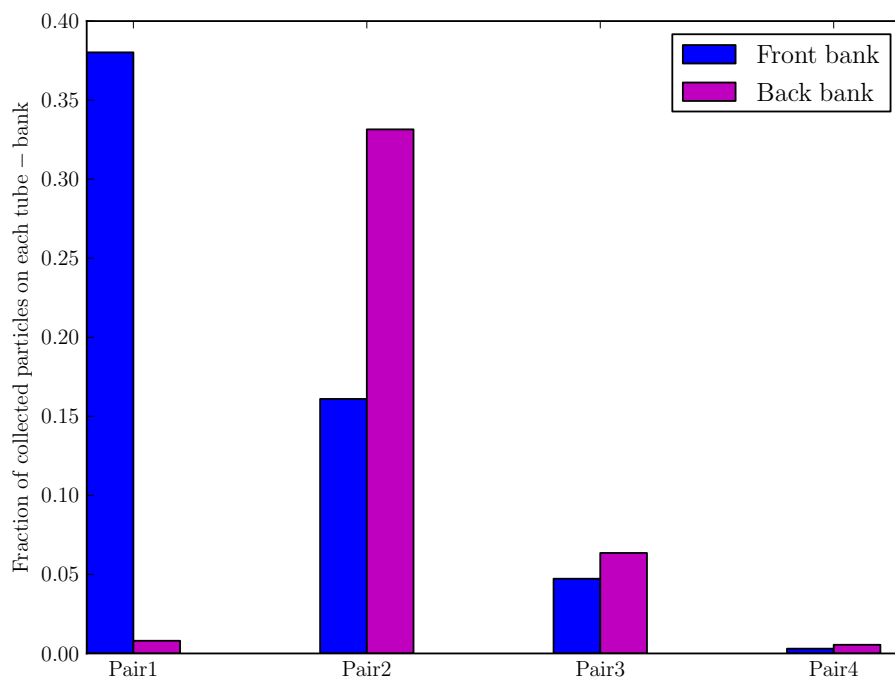


(b)

Figure 7.11: Fraction of total deposition particles across tube-banks for particles  $St = 0.35$  (a) each pair of tube-banks, (b) each tube-banks.

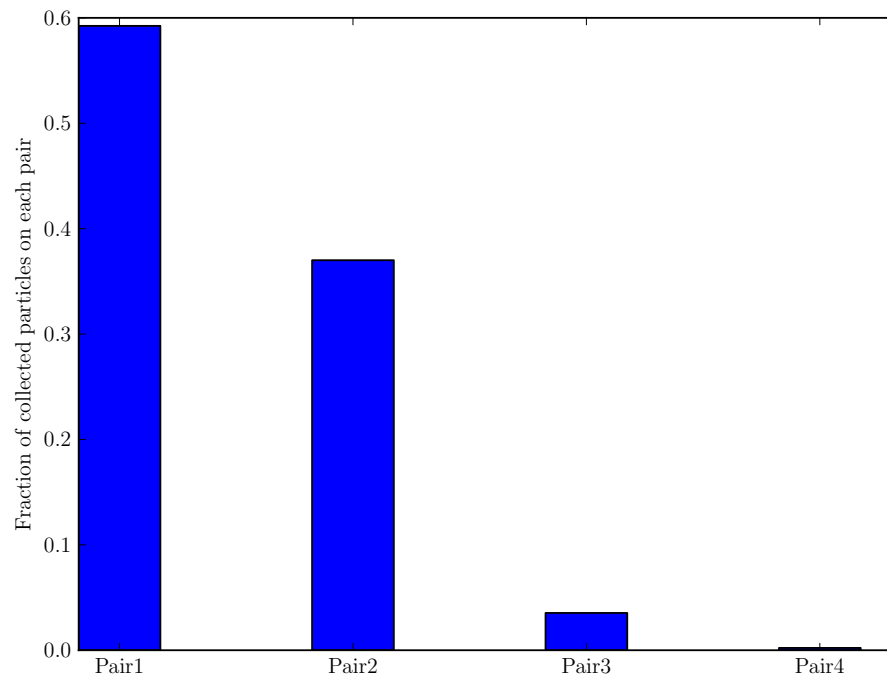


(a)

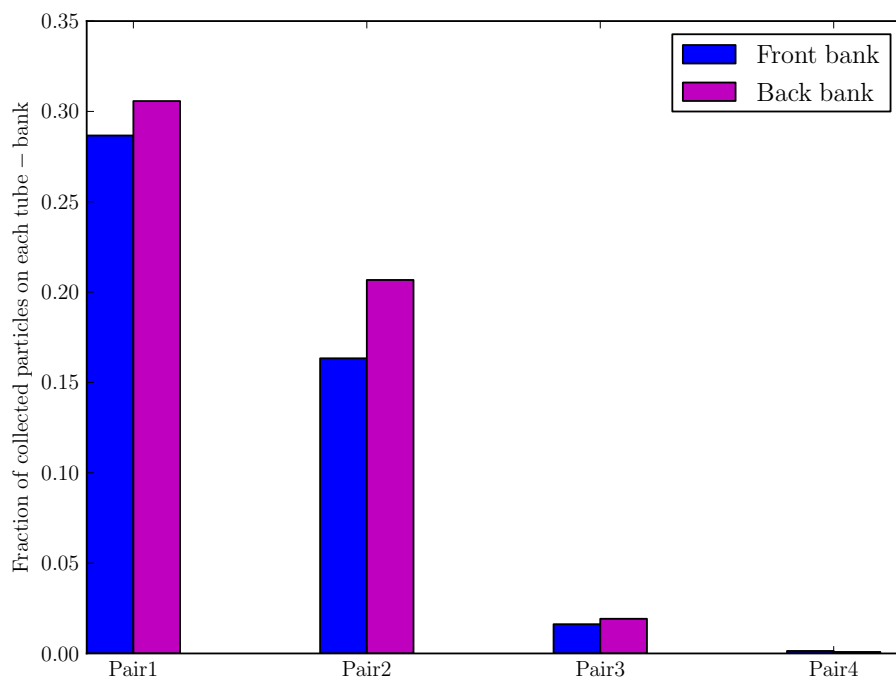


(b)

Figure 7.12: Fraction of total deposition particles across tube-banks for particles  $St = 0.086$  (a) each pair of tube-banks, (b) each tube-banks.

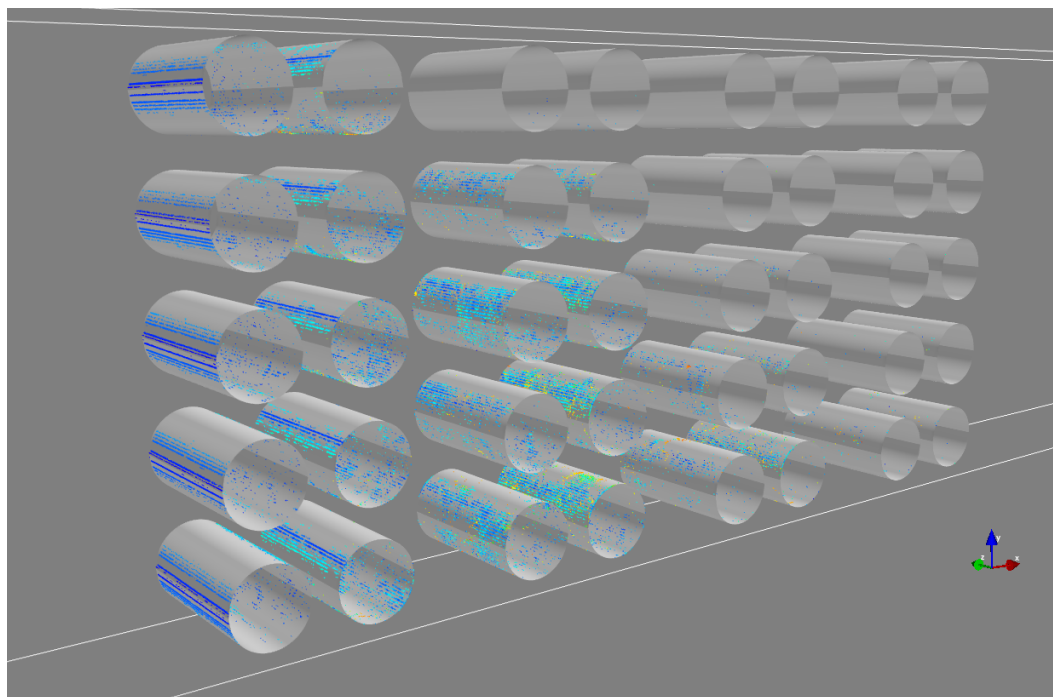


(a)

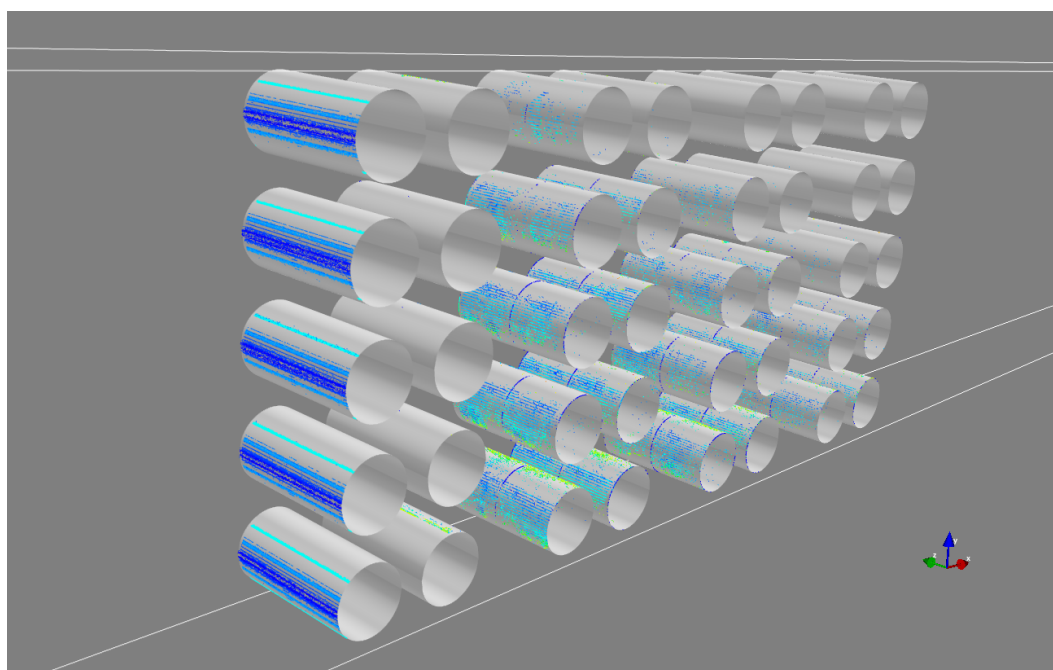


(b)

Figure 7.13: Fraction of total deposition particles across tube-banks for particles  $St = 0.0075$  (a) each pair of tube-banks, (b) each tube-banks.



(a)



(b)

Figure 7.14: Deposition particles on tube-banks (a)  $St = 0.0075$ , (b)  $St = 0.35$ .

## 7.4 Concluding remarks

Deposition and impact of heavy particles to an in-line array of tube-banks has been studied using Lagrangian particle tracking with an LES of the underlying carrier flow. The flow Reynolds number, based on the cylinder diameter  $D$  and flow velocity between the gap of two vertically adjacent cylinders, was 33960. Flow structures across the tube bank based on the normalized  $Q$  criterion have been presented. Using the formula for mean pressure distribution for cylinders in tube-banks proposed by Shim et al. (1988), mean pressure distribution on the middle cylinder from each tube-bank was calculated. The  $S$  shape of mean pressure distribution was observed on the back-bank of the first pair and second pair of tube-banks. Further, the mean pressure distribution on the each tube-bank within the third and fourth pair of tube-banks displays almost exactly the same behavior. This confirms the turbulent flow has reached equilibrium from the third pair of tube-banks.

The results for three sets of particles ( $St = 0.35, 0.086, 0.0075$ ) are based on  $10^7$  particles tracked using the Lagrangian point particle tracking approach. The particle bounce upon impact is taken into account through a particle-wall collision model. Sample trajectories of particle with diameter 20 $\mu\text{m}$  across tube-banks were shown, indicating that some particles rebound from the cylinder surface upon impact. The deposition efficiency for the three sets of particles was presented across the tube-banks together with the fraction of particles deposited across each tube-bank pairs. It was observed that for particles with a  $St = 0.35$  most get deposited on the first cylinders in each pair,, especially on the first column. This is consistent with practical experience that the first column of tubes plays a protection role on mitigating fouling on the succeeding tube-banks. Based on the effective Stokes number proposed by Israel and Rosner (1982), the overall deposition efficiency of the particle  $St = 0.35$  on the first tube-bank pair is significantly lower than that of a single circular cylinder. The results on deposition efficiency for particles  $St = 0.086, 0.0075$  are different from those for particles of Stokes number  $St = 0.35$ . The charts showing particle deposition fraction on each cylinder within each tube bank pair indicate that many more of the smaller particles get deposited on the downstream surfaces of the rear cylinders within each pair. This is attributed to the fact that the

smaller particles are more easily entrained into the wake and impact onto the downstream faces of the rear cylinders within each pair.

## REFERENCES

- S. V. Apte, K. Mahesh, P. Moin, and J. C. Oefelein. Large-eddy simulation of swirling particle-laden flows in a coaxial-jet combustor. *International Journal of Multiphase Flow*, 29(8):1311–1331, 2003.
- S. Benhamadouche and D. Laurence. LES, coarse LES, and transient RANS comparisons on the flow across a tube bundle. *International Journal of Heat and Fluid Flow*, 24(4): 470–479, 2003.
- D. Bouris, G. Papadakis, and G. Bergeles. Numerical evaluation of alternate tube configurations for particle deposition rate reduction in heat exchanger tube bundles. *International Journal of Heat and Fluid Flow*, 22(5):525–536, 2001.
- R. J. Brun, W. Lewis, P. J. Perkins, and J. S. Serafini. Impingement of cloud droplets on a cylinder and procedure for measuring liquid-water content and droplet sizes in supercooled clouds by rotating multicylinder method. 1955.
- A. Dehbi. Turbulent particle dispersion in arbitrary wall-bounded geometries: A coupled CFD-Langevin-equation based approach. *International Journal of Multiphase Flow*, 34(9):819–828, 2008.
- A. Dehbi and S. Martin. Cfd simulation of particle deposition on an array of spheres using an euler/lagrange approach. *Nuclear Engineering and Design*, 2011.
- S. K. Friedlander and H. F. Johnstone. Deposition of suspended particles from turbulent gas streams. *Industrial & Engineering Chemistry*, 49(7):1151–1156, 1957.
- D. Hall. The transport of particles through CAGR boilers, 1994.

- A. Haselbacher, F. M. Najjar, and J. P. Ferry. An efficient and robust particle-localization algorithm for unstructured grids. *Journal of Computational Physics*, 225(2):2198–2213, 2007.
- N. E. L. Haugen, S. Kragset, M. Bugge, R. Warnecke, and M. Weghaus. Particle impaction efficiency and size distribution in a mswi super heater tube bundle. *Arxiv preprint arXiv:1008.5040*, 2010.
- J. K. Helgesen and M. J. Matteson. Particle mixing and diffusion in the turbulent wake of cylinder arrays. *Experiments in Fluids*, 10(6):333–340, 1991.
- J. K. Helgesen and M. J. Matteson. Particle mixing and diffusion in the turbulent wake of a single cylinder. *Aerosol Science and Technology*, 20(1):111–126, 1994.
- J. C. R. Hunt, A. A. Wray, and P. Moin. Eddies, streams, and convergence zones in turbulent flows. In *Studying Turbulence Using Numerical Simulation Databases, 2*, volume 1, pages 193–208, 1988.
- R. Israel and D. E. Rosner. Use of a generalized stokes number to determine the aerodynamic capture efficiency of non-stokesian particles from a compressible gas flow. *Aerosol Science and Technology*, 2(1):45–51, 1982.
- Y. D. Jun and W. Tabakoff. Numerical simulation of a dilute particulate flow (laminar) over tube banks. *Journal of Fluids Engineering*, 116(4):770–777, 1994.
- G. A. Kallio and M. W. Reeks. A numerical simulation of particle deposition in turbulent boundary layers. *International Journal of Multiphase Flow*, 15(3):433–446, 1989.
- M. R. Maxey and J. J. Riley. Equation of motion for a small rigid sphere in a nonuniform flow. *Physics of Fluids*, 26:883, 1983.
- S. A. Morsi and A. J. Alexander. An investigation of particle trajectories in two-phase flow systems. *Journal of Fluid Mechanics*, 55(02):193–208, 1972.
- M. W. Reeks. The transport of discrete particles in inhomogeneous turbulence. *Journal of Aerosol Science*, 14(6):729–739, 1983.

- E. Riber, V. Moureau, Garc M., T. Poinot, and O. Simonin. Evaluation of numerical strategies for large eddy simulation of particulate two-phase recirculating flows. *Journal of Computational Physics*, 228(2):539–564, 2009.
- K. C. Shim, R. S. Hill, and R. I. Lewis. Fluctuating lift forces and pressure distributions due to vortex shedding in tube banks. *International Journal of Heat and Fluid Flow*, 9(2):131–146, 1988.
- C. Thornton and Z. Ning. A theoretical model for the stick/bounce behaviour of adhesive, elastic-plastic spheres. *Powder technology*, 99(2):154–162, 1998.
- Z. F. Tian, J. Y. Tu, and G. H. Yeoh. Numerical modelling and validation of gas-particle flow in an in-line tube bank. *Computers & chemical engineering*, 31(9):1064–1072, 2007.
- C. H. K. Williamson. Vortex dynamics in the cylinder wake. *Annual Review of Fluid Mechanics*, 28(1):477–539, 1996.

# Chapter 8

## Conclusions and future work

### 8.1 Conclusions

The inertial deposition of heavy particles from turbulent flows has been investigated through Lagrangian particle tracking in a CFD modelling framework. The principal goal of this study was to underpin the idea both used in the British Energy Nuclear code CIRCD (Reeks (1991)) and proposed by Kallio and Reeks (1989), and to further develop a simple but more complete engineering model that can be used in future simulations of inertia deposition of heavy particles.

Through investigations of the discrete random walk (DRW) eddy-interaction model, implemented within the commercial CFD code ANSYS FLUENT v12.0 using a RANS modelling framework, multiple deficiencies associated with the discrete particle phase (DPM) model were discovered, which have a significant effect on the predictions of particle deposition in turbulent boundary layers. It should be emphasised that these deficiencies are typical of most, if not all, of the present generation of general purpose CFD codes, and are not directed as a specific criticism of FLUENT's DPM implementation. Some of these deficiencies were addressed by the author by additional code, implemented via the standard User Defined Function templates (DPM UDFs), but limitations in access to the main solver using this approach made it impractical to completely resolve the underlying problems. As a result, a complete new Lagrangian particle tracking module

was written and implemented as a high level UDF within FLUENT, replacing the native tracking code entirely. Development of this model made it possible to predict particle deposition within a turbulent boundary layer, using FLUENT, to the same level of accuracy as a stand-alone C code based on the method of [Kallio and Reeks \(1989\)](#), but with the advantage that deposition in complex geometries could be modelled. This new model has been extensively tested and validated. Nevertheless the agreement with the experimental data of [Liu and Agarwal \(1974\)](#) is not quite as good as that shown in the original paper of [Kallio and Reeks \(1989\)](#), though no explanation for this has been found. The new implementation allows prediction of the transport and deposition of heavy particles suspended in steady and unsteady turbulent flows. Unlike the own Discrete Phase Model in FLUENT (see [Fluent \(2009\)](#)), it is compatible with LES modelling, though sub-grid scale effects are not currently included in the tracking algorithm. In addition, parallelization of the Lagrangian particle tracking module is achieved using the public domain MPI (Message Passing Interface) library.

### 8.1.1 Conclusions on the stochastic quadrant model

The CFD implementation of the DRW model of [Kallio and Reeks \(1989\)](#) produced a dramatic improvement in the prediction of deposition of heavy particles in a fully developed turbulent boundary layers compared to FLUENT's base DPM model, but the predictions still showed over-prediction of deposition in the diffusion/impaction region, compared to available experimental data. Further enhancements of the DRW model of [Kallio and Reeks \(1989\)](#) were therefore investigated leading to a simple, but more complete, stochastic quadrant model, which attempts to account for the effect of turbulent structures (sweeps and ejections) on particle transport within the boundary layer. This quadrant model was inspired by the quadrant analysis proposed by [Willmarth and Lu \(1972\)](#). The corresponding detailed statistics of the wall-normal velocity fluctuations in each quadrant are extracted from an LES of a fully developed channel flow, using the quadrant analysis. The turbulent dispersion of heavy particles in fully developed turbulent boundary layers is then modelled as interactions of heavy particles with a succession of random eddies found from four quadrants in a homogeneous Markov process way.

This model was fully coupled with the steady Navier-Stokes solver in ANSYS FLUENT v.12.0 via the stand-alone Lagrangian stochastic particle tracking described previously. Deposition rates of heavy particles from turbulent flows is of particular interest to the present stochastic model. This model yields very good predictions of deposition rate for particles with Stokes number  $St > 5$  when compared against benchmark experimental measurements from [Liu and Agarwal \(1974\)](#). Prediction of deposition rates at lower values of Stokes number gives under-estimation, and may need further improvement or the addition of Brownian motion effects. However, the deposition rates predicted by the present model compare favorably with the results reported by other researchers. Of particular significance is the comparison of the present model with a more complex stochastic model which is based on the Langevin equation to account explicitly for the strong sweeps and ejections in boundary layer turbulence.

The good agreement between the simulated and experimental results demonstrates that the proposed stochastic quadrant model realistically reproduces the dynamic behaviour of particles within turbulent boundary layers. It is concluded that the present model appropriately incorporates the skewness of wall-normal velocity fluctuations in a numerical simulation without either using too complex mathematical models, or needing to "tune" model parameters.

### **8.1.2 Conclusions on the wall effects on particle deposition**

Prior to the current work no systematic investigation of the potential errors in particle deposition in turbulent boundary layers due to the modified hydrodynamic forces experienced by particles when very close to the wall has been carried out, possibly because of the complexity of the correlations involved. The effect is studied with the proposed stochastic quadrant model, using recently published composite correlations for the drag coefficient  $C_D$  and lift coefficient  $C_L$  from [Zeng et al. \(2009\)](#). The computed results indicate that for practical cases hydrodynamic effects can reasonably be neglected for particle deposition in turbulent boundary layers.

### 8.1.3 Conclusions on the LES study of inertial deposition of heavy particles onto tube-banks

One of the aims of the present work was to investigate methods for the prediction of inertial particle deposition in complex geometries, such as the heat exchanger tube banks of CAGR boilers; a potential application of significant importance in nuclear safety studies. Initially it was hoped to apply the RANS flow analysis and Lagrangian tracking scheme of described in Chapter 2 to Chapter 5 of the present thesis to this problem. As illustrated in Chapter 7, however, vortex shedding within tube banks results in extremely irregular, fluctuating  $y^+$  fields, which make this methodology unsuitable. Also the high turbulence levels within tube banks, mean that boundary layer effects have less impact on deposition than direct impaction. As a result, Large Eddy Simulation (LES) was considered to be the most appropriate tool to investigate deposition of heavy particles within tube banks.

Firstly, it was necessary to validate the flow predictions given by ANSYS FLUENT v12.0, using LES with the dynamic Smagorinsky SGS model and a wall-layer representation of the boundary layer, for the carrier phase turbulent flow across a tube-bank, through comparison with experiments. The experimental measurement of Shim et al. (1988) provided a suitable benchmark case, giving mean and fluctuating pressure distribution data for a widely pitched array of 4 columns of cylinders in a square, in-line arrangement, together with measurements of vortex shedding frequencies. The LES model was based on a domain including 4 columns of 6 cylinders each, with aspect ratio 2, between pitch-wise and spanwise periodic boundaries, and comprised 2.7 million cells. The Reynolds number, based on gap velocity, was  $1.5 \times 10^4$ . Agreement with experimental data for mean pressure distribution for all columns was almost exact, whilst satisfactory agreement with the fluctuating pressure distributions was achieved for all except the first column. Even here, alternative comparative evidence suggests that the LES results may be more reliable. Vortex shedding was correctly predicted for all columns within the tube bank, with the correct Strouhal number. The results confirmed the importance of vortex shedding and the high levels of turbulence seen in tube banks, and confirmed LES to be an accurate predictive tool for this type of flow.

Having established the reliability of LES for the prediction of turbulent carrier flow field, the modelling was extended to investigate heavy particle deposition within tube banks. At version 12.0, ANSYS FLUENT (see [Fluent \(2009\)](#)) does not support discrete phase particle tracking in combination with LES turbulence modelling, but the use of the complete new particle tracking UDF developed in this study, described in Chapter 3, removed this basic limitation, though the effect of sub-grid scale turbulence on particle motion is not included. Parallelization of the tracking code was essential to enable statistically meaningful numbers of particles to be tracked through the computational domain of around 3.5 million cells.

For the dispersed particle phase, prior work has documented the deposition efficiency of heavy particles onto a single cylinder in turbulent flows. For example, [Israel and Rosner \(1982\)](#) reported that the deposition efficiency depends on the effective particle Stokes number. The tube bank geometry studied in the present work was based on a partial model of a CAGR tube array, used in an experimental investigation of particle deposition by [Hall \(1994\)](#). Here the tube columns were arranged in closely pitched in-line pairs, with a wider gap separating each pair. Test rig used in [Hall \(1994\)](#) consisted of 10 pairs of columns, each of 5 tubes, but the present computational domain modelled only 4 column pairs because of limited computational resources. Nevertheless it was demonstrated from the LES that the mean flow had become stream-wise periodic by the third and fourth column pairs. The Reynolds number for simulations was 33960 based on the gap velocity in the streamwise direction.

The Lagrangian point particle approach, coupled with LES of the carrier flow, was used to study the inertial deposition of heavy particles onto this in-line tube bank for three sets of heavy particles. An energy based model for possible particle bounce on impact was included in the deposition algorithm. The deposition efficiency of heavy particles on each pair of tube-columns across the bank was computed, and the results for the largest particles, of Stokes number  $St = 0.345$ , were compared with theoretical values for an isolated single circular cylinder. It was observed that the deposition efficiency onto the first tube-bank pair was significantly lower than that onto an isolated circular cylinder. In addition, the fractional deposition of particles across each of the tube-column pairs was determined. For the particle Stokes number  $St = 0.345$ , most of

particles were deposited on the upstream column of each pair, especially on the first column. This is consistent with practical experience that the first column of tubes plays a protection role in mitigating fouling on the succeeding tube columns. In contrast, the results for deposition efficiency for particles of Stokes number  $St = 0.086$  and  $0.0075$  are significantly different from those for particles of  $St = 0.345$ , based on the present simulations. A display of particle deposition location on tube-bank suggests that far more of the smaller particles get deposited on the downstream cylinders of each column pair, with significant numbers being deposited on the rear surfaces. A possible explanation is that the smaller particles are more easily entrained into the wake, and impact onto the rear surfaces of the cylinders. This issue calls for further investigation.

## 8.2 Future work

Most notably, this is the first study to the author's knowledge to propose a simple stochastic engineering model embodying the effects of near-wall coherent-structures on the inertial deposition of heavy particles. However, some limitations are worth noting and need further research of the proposed stochastic quadrant model and particle deposition onto tube-banks.

First, although the hypotheses in the mode are supported statistically, the stochastic model is not assessed through the well-mixed criterion (see [Thomson \(1987\)](#)). Future work should therefore include follow-up work designed to evaluate whether the model satisfies the above criterion and also whether it results in spurious drift (see [MacInnes and Bracco \(1992\)](#)) following the turbulence gradient and, if so, how to address this. In addition, the one-dimension nature of the present model fails to account for the prominence of longitudinal vortices. Future work should therefore include the streamwise fluid velocity fluctuations simultaneously. In addition, the present quadrant model considers only wall-normal fluid velocity fluctuations,  $v'$ , as in the previous work of [Kallio and Reeks \(1989\)](#). [Pope \(2000\)](#) discusses the work of [Willmarth and Lu \(1972\)](#) in Section 7.4 of his book, and points out that the simple fact that the  $u$ - $v$  correlation coefficient is around  $-0.5$  suggests that quadrant II and quadrant IV events are twice as likely as quadrant I

and quadrant V events, irrespective of the turbulence structure. Including stream-wise  $u'$  fluctuations, correctly correlated with the wall-normal  $v'$  fluctuations may therefore offer an alternative modelling approach. The author did some preliminary work on this concept, but abandoned it due to lack of time. Completion of this work might prove a useful avenue of further research. The integral Lagrangian time scales used for the eddies in four quadrants in the present quadrant method may also need further scrutiny. Finally, the use of the Langevin equation as an alternative to the discrete random walk approach should also be investigated.

Although the computed deposition rates based on the composite correlation for  $C_D$  and  $C_L$  indicate that they have only a minor effects on particle deposition, future work may consider the more general composite but more complex correlation proposed by [Lee and Balachandar \(2010\)](#). On the other hand, the more general composite correlations are much more computationally expensive, and correspondingly less robust than those employed in the present study.

The new Lagrangian particle tracking algorithm, described in chapter 3, is compatible with ANSYS FLUENTs LES turbulence model but, at present, does not include the effects of sub grid scale turbulence on the particles. For the application to large scale separated flows in tube banks, considered in chapter 7, this is not a major consideration, but extending the model to account for SGS effects would increase its utility for the boundary layer type problems considered in the earlier chapters of this thesis. The approach suggested would be to combine FLUENTs turbulent kinetic energy transport LES to generate the white noise term for a Langevin tracking model. The final topic considered in the present work was prediction of the deposition of inertial particles in the flow through tube banks; a subject of some importance in the nuclear industry. This was the last piece of work to be completed and, although the work presented demonstrates well the potential of combined LES and particle tracking for this demanding application, time constraints prevented a more detailed comparison of results with the earlier experimental work of [Hall \(1994\)](#). A more complete analysis of the generated data would be a valuable extension of this work. It should be noted that, to the authors knowledge, [Hall \(1994\)](#) measurements provide the only experimental data available for this important application. With the recent developments in experimental techniques such

as Particle Image Velocimetry, it would be valuable if further experimental data could also be generated. Finally there are a number of related problems of direct relevance to the nuclear industry which could be investigated using this approach, such as the difference in particle deposition for tube banks with finned tubes.

## REFERENCES

- A. Fluent. 12.0 documentation. *ANSYS Inc*, 2009.
- D. Hall. The transport of particles through CAGR boilers, 1994.
- R. Israel and D. E. Rosner. Use of a generalized stokes number to determine the aerodynamic capture efficiency of non-stokesian particles from a compressible gas flow. *Aerosol Science and Technology*, 2(1):45–51, 1982.
- G. A. Kallio and M. W. Reeks. A numerical simulation of particle deposition in turbulent boundary layers. *International Journal of Multiphase Flow*, 15(3):433–446, 1989.
- H. Lee and S. Balachandar. Drag and lift forces on a spherical particle moving on a wall in a shear flow at finite Re. *Journal of Fluid Mechanics*, 657:89–125, 2010.
- B. Y. H. Liu and J. K. Agarwal. Experimental observation of aerosol deposition in turbulent flow. *Journal of Aerosol Science*, 5(2):145–148, IN1–IN2, 149–155, 1974.
- J. M. MacInnes and F. V. Bracco. Stochastic particle dispersion modeling and the tracer-particle limit. *Physics of Fluids A: Fluid Dynamics*, 4:2809, 1992.
- S. B. Pope. *Turbulent Flows*. Cambridge University Press, 2000.
- M. W. Reeks. CIRCD a computer code for calculating the deposition half-lives of gas borne particles in gas-cooled reactor circuits. *TD/STB/REP/0268, RPTG/P(91)18*, 1991.
- K. C. Shim, R. S. Hill, and R. I. Lewis. Fluctuating lift forces and pressure distributions due to vortex shedding in tube banks. *International Journal of Heat and Fluid Flow*, 9(2):131–146, 1988.

- D. J. Thomson. Criteria for the selection of stochastic models of particle trajectories in turbulent flows. *Journal of Fluid Mechanics*, 180(7):529–556, 1987.
- W. W. Willmarth and S. S. Lu. Structure of the reynolds stress near the wall. *Journal of Fluid Mechanics*, 55(01):65–92, 1972.
- L. Zeng, F. Najjar, S. Balachandar, and P. Fischer. Forces on a finite-sized particle located close to a wall in a linear shear flow. *Physics of Fluids*, 21:033302, 2009.